

CHALCOPHILE ELEMENT PROCESSING AND
DISTRIBUTION BENEATH A CONTINENTAL VOLCANIC ARC

by

DANIEL COX

A thesis submitted to the University of Birmingham for the degree of
DOCTOR OF PHILOSOPHY

Department of Earth Sciences
School of Geography, Earth and Environmental Sciences
College of Life and Environmental Sciences
University of Birmingham

September 2019

UNIVERSITY OF
BIRMINGHAM

University of Birmingham Research Archive

e-theses repository

This unpublished thesis/dissertation is copyright of the author and/or third parties. The intellectual property rights of the author or third parties in respect of this work are as defined by The Copyright Designs and Patents Act 1988 or as modified by any successor legislation.

Any use made of information contained in this thesis/dissertation must be in accordance with that legislation and must be properly acknowledged. Further distribution or reproduction in any format is prohibited without the permission of the copyright holder.

Abstract

Chalcophile Element Processing and Distribution beneath a Continental Volcanic Arc

Daniel Cox

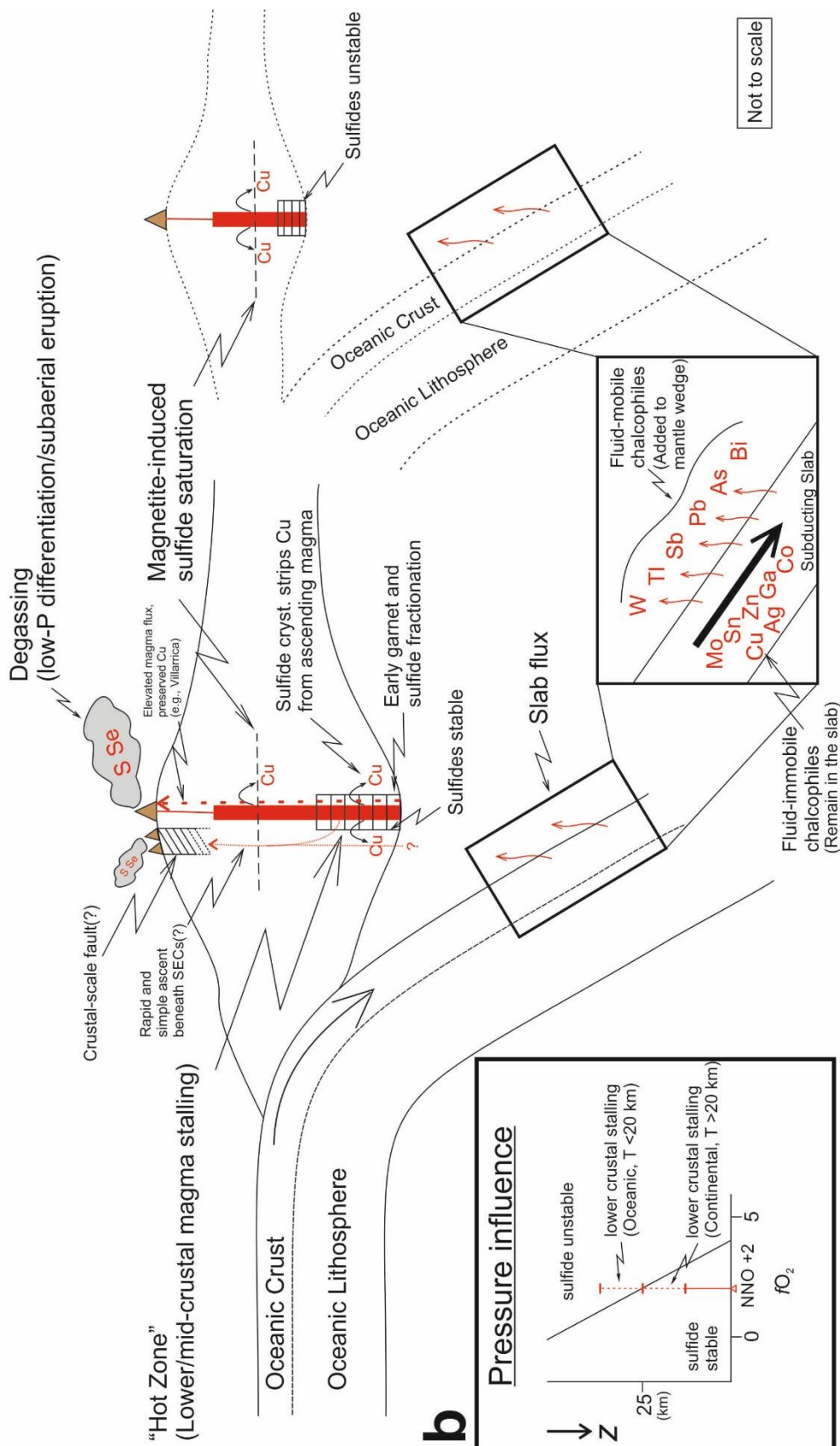
Published datasets of the concentrations of the chalcophile elements in volcanic rocks are rare, and most of our knowledge of their behaviour is based on oceanic arc-like settings, rather than continental arcs, where economically viable deposits of the chalcophiles are generally associated. This thesis, therefore, investigates the processing and distribution of the chalcophile elements within a continental volcanic arc, by presenting novel whole rock analyses of the near complete suite of chalcophile elements in volcanic rock samples collected from several edifices along the Chilean Andes. The data presented demonstrates that continental arc magmas typically achieve saturation in a crystalline sulfide phase early during magmatic evolution, likely at or near the base of the overriding continental crust, prior to ascent and low-pressure fractional crystallisation, and before magnetite fractionation, in contrast to oceanic arc-like settings. Observations are replicated at stratovolcanoes and small eruptive centres. The degree of crystalline sulfide fractionated is modelled to be minimal (≤ 0.6 wt.%). The thickness of the overriding crust at convergent margins is argued to be the dominant control on the distribution of the chalcophile elements. The implication of these findings is that either secondary processes are required to transport chalcophile elements to the sites of ore deposit formation, or such ore deposits are generated in atypical scenarios (e.g., high magma throughput).

Graphical abstract

a

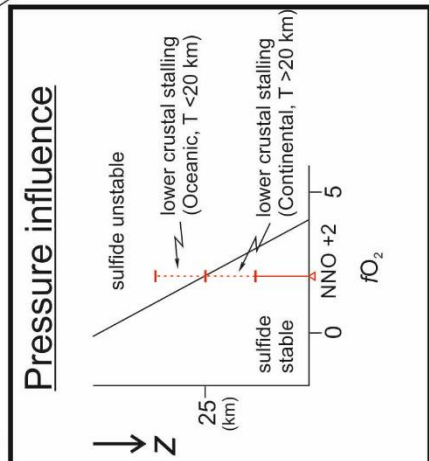
Thinner overriding crust (≤ 20 km)
(IA/BAB?)

Thick overriding crust (30+ km)
(CtA)



Not to scale

b



ii

Dedicated to Tim Lyons

My 'Father of Geology'

Acknowledgements

A thesis completed over a roller coaster ride of four years!

My first thanks has to go to my supervisors, Sebastian Watt, Alan Hastie and Frances Jenner, who, over the course of my Ph. D., have been instrumental in making this thesis come together, providing invaluable feedback on data interpretation, manuscript and chapter drafts and general Ph. D. queries. I am grateful for the hours Samantha Hammond put in in helping acquire accurate analyses of the chalcophile elements; without Sam, I would not have made it this far – thank you! There is no doubt that thanks to Seb, Alan, Fran and Sam, I have achieved my dreams of working on active and topical research and publishing a scientific article – I even managed to squeeze a second article out! I would also like to thank Iain McDonald, Nic Odling, Lin Marvin-Dorland, Andy Rees and Barbara Kunz for their help with the preparatory and analytical aspects of the current project. Thank you to the Natural Environment Research Council (NERC) consortia [Deep Volatiles, Tellurium and Selenium Cycling and Supply ('TeASe') and From Arc Magmas to Ore Systems ('FAMOS')] and the University of Birmingham for providing funding for the project, allowing me to conduct this fascinating research.

I must also thank David 'Davey' Cavell, David Buchs, Ginevra Chelli, Alvaro Amigo Ramos (Servicio Nacional de Geología y Minería; SERNAGEOMIN) and the Servicio Geológico Colombiano (SGC) for their input and expertise during our field season to Panama, Colombia and Chile. Without their help and advice, the field season would not have been as successful as it was. I am also grateful to all the hotel and hostel owners across the three countries who put us up and made us feel very

welcome. A special thank you goes to Alavro Nivia, of the SGC, for putting us up in his family home and taking us out to get involved in the true salsa experience in Cali!

Family have always been a massive part of life and something I have held, and will continue to hold, close to my heart. My parents (Sarah and David), sister (Sophie) and grandparents (Pat and Brian) have supported me endlessly in helping me achieve my dreams, not only over the past four years, but also during school and my Undergraduate Degree. Without them by my side, I would not have progressed this far. Not only that, but they have provided a welcome distraction when times have gotten tough...sorry for the burden! The travelling and stresses of the Ph. D. have meant that I have gone long periods without seeing you all, something I will be certain to make up to you all in the coming months – you'll have your chirpy and sarcastic son/brother/grandson back now that this thesis is complete!

A special thanks must to go to Davey, Emma, Ben and Alastair for being 'rocks' (pun intended) and really helping me push through some difficult times. Coffee breaks, lunch breaks, visits to the gin bar and meals out have been welcomed with open arms over the years and have made us a close knit group – friends I will cherish and forever stay in touch with! To my fellow 'BIG' boys, Davey and Ally, cheers! You two have been sound lads, always willing to enjoy a cuppa/beer over a few hours on the Xbox or a curry. Good luck with your Ph. D.'s boys, you've got this! We'll have that 'BIG' publication before long!

A very special thank you to my fellow countryman, Davey, who has not only made the past four years exciting, but made the three months in Central – South America interesting, exhilarating and some of the best months of my life – the stories

we took home from that trip will stay with me forever! And hopefully we can do something similar in the future. If you ever need a favour, boyo, you know where to find me.

My fellow Ph. D. colleagues have been fantastic during my time at the University of Birmingham, being great friends, supportive and providing endless banter throughout the office, so thank you. Both the biscuit and microwave funds and 'Games Nights' have been great fun to organise! The atmosphere throughout ES has also been amazing and has no doubt cemented us all as good friends and feeling like a family. Residential fieldtrips to Tenerife, Pembrokeshire and Northern Ireland have been welcome breaks from the monotony of writing. Also, thank you to Stephan Lautenschlager for awarding me the title of 'Honorary Palaeontologist' during the Pembrokeshire 2019 fieldtrip. Gretchel and Aruna have been fantastic during my time here, helping me with everything and anything, from finance queries, through teaching, future jobs, and just general chitchat to calm the stresses of Ph. D. life – thank you, you are both stars! Thank you to Gary and Steve for our early morning chats, always brightening up my day from first thing. Oh, and Sarah, it certainly was “darkest before the storm!”

Here's to the next chapter...

Good luck with your Ph. D., Soph!

Contents

Abstract	i
Graphical Abstract	ii
Dedication	iii
Acknowledgments	iv
Project overview	1
<u>Chapter 1</u>	
Introduction	6
1.1. The Chalcophile Elements	6
1.2. The Current Thesis	9
1.2.1. Motivations and aims of the study	9
<u>Chapter 2</u>	
Study region	12
2.1. The Andean Cordillera	12
2.2. Southern Volcanic Zone	14
2.2.1. Antuco	18
2.2.2. Villarrica – Quetrupillán – Lanín	20
2.2.2.1. Villarrica Volcano.....	23
2.2.2.2. Quetrupillán and Lanín Volcanoes	24
2.2.3. Chilean small eruptive centres	25
2.2.3.1. The Caburgua – Huelemolle Complex and Huililco	26
2.2.4. Yate – Hornopirén – Apagado	27
2.2.4.1. Yate Volcano.....	29
2.2.4.2. Hornopirén and Apagado Volcanoes	29
2.3. Central Volcanic Zone	30
2.3.1. Ollagüe	34
2.3.2. La Poruñita	37
2.3.3. San Pedro	37
<u>Chapter 3</u>	
Sample descriptions	40
3.1. Southern Volcanic Zone samples	41

3.1.1. Antuco	41
3.1.2. Yate	41
3.1.3. Hornopirén	43
3.1.4. Apagado.....	44
3.1.5. Villarrica.....	45
3.1.6. Quetrupillán	46
3.1.7. Lanín	47
3.2. Central Volcanic Zone samples	47
3.2.1. Ollagüe.....	47
3.2.2. La Poruñita.....	49
3.2.3. San Pedro	49
3.3. Petrographic summary.....	50

Chapter 4

Method development: acquiring chalcophile element analyses through ICP-tandem mass spectrometry.....53

4.1. Introduction.....	53
4.1.1. XRF analysis.....	53
4.1.2. ICP-OES analysis	54
4.1.3. ICP-MS and ICP-MS/MS analysis.....	54
4.1.3.1. ICP-MS analysis.....	54
4.1.3.2. ICP-MS/MS	57
4.2. Analytical methods	60
4.2.1. ICP-OES and MS analysis, Cardiff University.....	60
4.2.2. XRF analysis.....	61
4.2.3. ICP-MS/MS analysis, Open University.....	62
4.2.4. Data accuracy.....	64
4.2.4.1. Silver (Ag) standard addition method and subsequent offline ZrO interference correction	70
4.2.4.2. Further assessment of data repeatability	71
4.3. Summary.....	75

Chapter 5

Chalcophile element processing beneath a continental arc stratovolcano77

5.1. Introduction.....	77
5.2. Geochemical results.....	82
5.2.1. Major elements.....	82

5.2.2. Trace elements.....	86
5.3. Discussion.....	90
5.3.1. Subduction mobile chalcophile elements	90
5.3.2. Degassing of S and Se.....	91
5.3.3. Crustal processing of the chalcophile elements	93
5.3.4. A role for garnet fractionation?	98
5.3.5. Sulfide fractionation and Cu – Ag systematics.....	100
5.4. Conclusion	103

Chapter 6

Arc-scale processing of the chalcophile elements: implications for the formation of ore deposits	105
6.1. Introduction.....	105
6.2. Geological context	106
6.3. Geochemical Results.....	107
6.3.1. Major elements.....	107
6.3.2. Trace elements.....	113
6.4. Discussion.....	117
6.4.1. Crustal processing of the chalcophile elements	117
6.4.1.1. The role of pressure on the chalcophile elements during the petrogenesis of continental arc magmas	119
6.4.2. Implications for the formation of ore deposits.....	125
6.4.2.1. Summary of the potential mechanism(s) for ore deposit formation.....	130
6.5. Conclusions	130

Chapter 7

Chalcophile element systematics beneath small eruptive centres.....	133
7.1. Introduction.....	133
7.2. Monogenetic volcanic centres	135
7.2.1. Geological context of the Chilean small eruptive centres	137
7.3. Geochemical results	139
7.3.1. Major elements.....	139
7.3.2. Trace elements.....	143
7.4. Discussion.....	147
7.4.1. A similar crustal processing beneath small eruptive centres and stratovolcanoes	147
7.4.1.1. Sulfide saturation beneath small eruptive centres	148

7.4.1.2. Quantifying the degree of sulfide fractionation from small eruptive centre magmas	148
7.4.1.3. Pressure induced sulfide saturation in SEC magmas	151
7.4.2. Consistent Cu-rich (ore?) source at the base of the continental crust	156
7.4.2.1. A deep, pyroxenite source for Cu	156
7.5. Conclusion	158
<u>Chapter 8</u>	
Subduction mobile chalcophile elements	160
8.1. Introduction.....	160
8.2. Geochemical results	164
8.3. Discussion.....	169
8.3.1. Estimating the flux of the subduction mobile chalcophile elements	170
8.4. Conclusion	177
<u>Chapter 9</u>	
A synthesis of the processing and distribution of the chalcophile elements in a continental volcanic arc setting.....	178
9.1. Overall crustal processing of the chalcophile elements.....	179
9.2. On the formation of ore deposits	183
9.2.1. Elevated Cu contents at Villarrica.....	184
9.3. Subduction mobile chalcophile elements.....	185
9.4. Avenues for further investigation	186
Bibliography.....	188
Appendix A.....	211
Appendix B.....	230
Appendix C.....	259
Appendix D.....	272
Appendix E.....	277
Appendix F.....	279

Figure list

Fig. 1.1. Periodic Table of Elements.....	7
Fig. 1.2. World map highlighting global distribution of porphyry Cu ore deposits.....	8
Fig. 2.1. Volcanic zones of the Andean Cordillera.....	13
Fig. 2.2. Southern Volcanic Zone.....	16
Fig. 2.3. Location map of Antuco stratovolcano.....	19
Fig. 2.4. Villarrica – Quetrupillán – Lanín volcanic chain.....	22
Fig. 2.5. Hualaihué Peninsula.....	28
Fig. 2.6. Central Volcanic Zone.....	33
Fig. 2.7. Ollagüe stratovolcano.....	36
Fig. 2.8. San Pedro stratovolcano.....	38
Fig. 3.1. Thin section photomicrograph plate.....	52
Fig. 4.1. Schematic profile of ICP-MS/MS.....	57
Fig. 4.2. ISRM analyses, ICP-OES, Cardiff University, 2017.....	66
Fig. 4.3. ISRM analyses, XRF, University of Leicester, 2018.....	67
Fig. 4.4. Multi-element plot depicting accuracy of BHVO-2 monitor analyses.....	68
Fig. 4.5. Repeat Antuco sample analyses.....	72
Fig. 4.6. Repeat Yate, Hornopirén, Apagado analyses.....	73
Fig. 4.7. ISRM analyses, XRF, University of Edinburgh, 2017.....	74
Fig. 5.1. TAS-AFM plots of Antuco samples.....	82
Fig. 5.2. Ti-Fe-V bivariate plots of Antuco samples.....	83
Fig. 5.3. Major element bivariate plots of Antuco samples.....	84
Fig. 5.4. Select chalcophile element bivariate plots of Antuco samples.....	86
Fig. 5.5. Cu, Ag, Cu/Ag bivariate plots of Antuco samples.....	87
Fig. 5.6. Parental-MORB normalised multi-element plots of Antuco samples.....	88
Fig. 5.7. Schematic illustration of Cu processing beneath thick and thin crust arcs.....	96
Fig. 5.8. REE systematics of Antuco samples.....	98
Fig. 5.9. Trace element modelling of fractional crystallisation.....	101
Fig. 6.1. TAS-AFM plots of Chilean stratovolcano samples.....	108
Fig. 6.2. Major element bivariate plots of Chilean stratovolcano samples.....	111
Fig. 6.3. Cu-Ag-S-Se systematics of Chilean stratovolcanoes.....	113
Fig. 6.4. (C1) Chondrite normalised REE plot of Chilean stratovolcano samples.....	115
Fig. 6.5. REE systematics of Chilean stratovolcano samples.....	119

Fig. 6.6. ‘Shape coefficients’ of the REE of Chilean stratovolcano samples.....	121
Fig. 6.7. Cu and REE systematics of high flux Chilean stratovolcanoes.....	126
Fig. 7.1. TAS-AFM plots of Chilean SECs samples.....	140
Fig. 7.2. Major element bivariate plots of Chilean SECs samples.....	141
Fig. 7.3. S-Se systematics of Chilean SECs.....	144
Fig. 7.4. Cu-Ag systematics of Chilean SECs.....	145
Fig. 7.5. (C1) Chondrite normalised REE plot of Chilean SECs.....	145
Fig. 7.6. Trace element modelling of fractional crystallisation.....	149
Fig. 7.7. REE systematics of Chilean SECs.....	152
Fig. 7.8. ‘Shape coefficients’ of the REE of Chilean SECs.....	154
Fig. 8.1. Slab depth map of the Chilean Andes.....	162
Fig. 8.2. Select chalcophile element bivariate plots of Chilean stratovolcano and SEC samples.....	164
Fig. 8.3. Parental-MORB normalised multi-element plot of Chilean stratovolcanoes....	166
Fig. 8.4. Parental-MORB normalised multi-element plot of Chilean SECs.....	167
Fig. 8.5. Nb/Zr versus volcano-trench distance and slab depth.....	170
Fig. 8.6. Constructed baselines for samples from Antuco and Yate stratovolcanoes....	173
Fig. 8.7. Estimated percentage contribution of W-Tl-As-Pb-Sb versus volcano-trench distance and slab depth.....	174
Fig. 9.1. Overall schematic model of the processing and distribution of the chalcophile elements beneath thick and thin crust arcs.....	181

Table list

Table 4.1. Average of BHVO-2 monitor analyses during ICP-MS/MS analysis...	64
Table 4.2. Newly determined Ag contents of select ISRM.....	69
Table 4.3. Data sources for samples presented in the current project.....	75
Table 5.1. Fractional crystallization modelling parameters.....	100
Table 7.1. Fractional crystallization modelling parameters.....	149
Table 8.1. Estimated percentage contribution of W-Tl-As-Pb-Sb.....	171

Project overview

The 'Sulfur-loving' chalcophile elements – e.g., S, Cu, Ag, Au, Se, Tl, Bi, Pb (Goldschmidt, 1929, 1937) – are a very important suite of elements, both in terms of their economic value (Sillitoe, 2010; Mutschler et al., 2010; Kiseeva et al., 2017) and in their ability to investigate magmatic processes in a range of tectonic settings (e.g., Noll Jr et al., 1996; Sun et al., 2004; Jenner et al., 2010; Timm et al., 2012; Chiaradia, 2014; Jenner, 2017; Georgatou et al., 2018). However, despite their importance, the entire suite of chalcophile elements are relatively understudied, with a general lack of whole rock analyses of the complete suite of chalcophile elements present in the literature. The reasoning for this lack in whole rock chalcophile element analyses is probably due to the challenges faced when analysing for them. Their low whole rock concentrations (e.g., Ag and Se, ppb), plentiful analytical interferences and a lack of accurate International Standard Reference Material values make obtaining accurate analyses challenging.

Most studies to date have utilised glass analyses, focussing on investigating the processing and distribution of the chalcophile elements in mid-ocean ridge or oceanic (island) arc-like settings (e.g., Sun et al., 2004; Jenner et al., 2010, 2012; Timm et al., 2012). In contrast, although Cu analyses are in abundance for erupted products of continental volcanic arcs (Lee et al., 2012; Chiaradia, 2014; Georgatou et al., 2018), published analyses of the entire suite of chalcophile elements are limited. Therefore,

the current thesis aims to address the lack of whole rock chalcophile element analyses in the literature and better understand the processing and distribution of a greater number of chalcophile elements beneath stratovolcanoes within a typical continental volcanic arc setting (Central and Southern Volcanic Zones of South America). Additionally, the thesis compares the behaviour of the chalcophile elements between stratovolcanoes set on a range of overriding crustal thicknesses (e.g., 25 to $\sim\geq 70$ km), and between stratovolcanoes and several small eruptive centres.

The subsequent chapters of this thesis, each presented and briefly summarised below, explain how accurate whole rock chalcophile element analyses were obtained, and how their concentrations have been used to investigate their behaviour within this typical continental volcanic arc setting.

Chapter 1: Introduction

The introduction begins by defining the chalcophile elements, before proceeding to outline their importance, both economically and as geochemical tracers. Subsequently, the introduction explores the areas in which further research is required to better understand the processing and distribution of the chalcophile elements in a continental volcanic arc setting. Finally, the motivations and aims of the current project are outlined.

Chapter 2: Study region

Chapter 2 summarises the geological setting of the Andean Cordillera, before focussing on the specific study regions of this thesis, situated in the Central and Southern Volcanic Zones. The reasons for selecting these study regions is also discussed.

Chapter 3: Sample descriptions

Chapter 3 details the number and type of samples collected from each of the volcanic edifices investigated in the current project. In addition, overall summaries of the petrological characteristics of each sample suite are provided.

Chapter 4: Method development: acquiring chalcophile element analyses through ICP-tandem mass spectrometry

In this chapter, a brief description of each of the analytical techniques (XRF, ICP-OES, ICP-MS) utilised throughout the current project is first provided. The difficulties in analysing for the chalcophile elements are subsequently highlighted, before discussing the analytical techniques employed (e.g., ICP-tandem mass spectrometry, standard addition and offline interference corrections) to overcome these issues. The repeatability and accuracy of the geochemical data obtained are also commented on.

Chapter 5: Chalcophile element processing beneath a continental arc stratovolcano

The bulk of material presented in this chapter is published in Earth and Planetary Science Letters [Cox et al., 2019. Earth. Planet. Sci. Lett., Vol. 522, p. 1-11].

The majority of our knowledge of the processing of the chalcophile elements within continental volcanic arcs is based on our understanding of their behaviour in oceanic volcanic arc-like settings. Thus, chapter 5 presents a near complete suite of novel chalcophile element analyses for a typical continental volcanic arc stratovolcano

in southern Chile (Antuco), with the aim of refining our understanding of chalcophile element behaviour within a continental volcanic arc setting.

Chapter 6: Arc-scale processing of the chalcophile elements: implications for the formation of ore deposits

Building on chapter 5, chapter 6 presents further novel datasets of chalcophile element analyses for several stratovolcanoes along the Chilean arc segments. The broad range of crustal thicknesses (~25 to >70 km) on which the stratovolcanoes are situated allows this chapter to test previously presented hypotheses of the role of overriding crustal thickness, pressure and/or garnet fractionation on controlling the behaviour of the chalcophile elements.

Chapter 7: Chalcophile element systematics beneath small eruptive centres

Although small eruptive centres are the most common volcano type on Earth, there has been a lack of attention paid to the processing of the chalcophile elements beneath them. Thus, chapter 7 presents new chalcophile element analyses for several small eruptive centres in the Chilean Andes. Additionally, their processing is compared to that concluded beneath continental volcanic arc stratovolcanoes presented previously.

Chapter 8: Subduction mobile chalcophile elements

Chapter 8 presents and discusses analyses of the remaining chalcophile elements (W, Tl, As, Pb, Mo, Sb, Sn, Zn, Ga and Co) that are not as instructive on the behaviour of sulfides as Cu, Ag and Se. This chapter seeks to confirm which, if any,

chalcophile elements are subduction mobile, and provide estimates of their contribution to the sub-arc mantle wedge in a slab-derived flux.

Chapter 9: A synthesis of the processing and distribution of the chalcophile elements in a continental volcanic arc setting

By presenting a schematic model, the final chapter of this thesis discusses the overall findings of the current project on how the chalcophile elements are processed and distributed within a continental volcanic arc setting. This chapter aims to highlight the main controls on the behaviour of the chalcophile elements and the implications these have for the cycling of S in a subduction zone and the generation of economically viable ore deposits. Future avenues of investigation are also detailed.

Chapter 1

Introduction

1.1. The Chalcophile Elements

Through the formation of Earth's 'shells' (i.e., layers), Goldschmidt (1929) defined four groups of elements – atmophile, lithophile, chalcophile and siderophile – terms which remain in constant use today. The chalcophile elements were originally defined as those that partitioned into molten iron sulfides, hosted in what is now referred to as the outer core (Goldschmidt, 1929). Subsequently, Goldschmidt (1937) classified the chalcophile element suite (S, Se, Te, Fe, Cr, Cu, Zn, Cd, Pb, Sn, Ge, Mo, As, Sb, Bi, Ag, Au, Hg, Pd, Ru, Pt, Ga, In and Tl), as highlighted in the Periodic Table of Elements in **Fig. 1.1**. Since the chalcophile elements were first defined, the term 'chalcophile element' has been commonly used to refer to those elements that have an affinity for S ('S-loving'), and more specifically sulfides. Thus, the term 'chalcophile element' is used throughout this thesis to refer to those elements that are 'S-loving', keeping in line with the common usage of the term in the wider literature.

The chalcophile elements are of very significant economic value. Although Cu, Ag, Se and Au are all depleted in the continental crust (Jenner, 2017), these, and other chalcophile elements (e.g., Mo, Re, Zn, Bi, Pb, Te, Pd) are highly enriched in porphyry Cu-Au deposits that are globally associated with active convergent margins (**Fig. 1.2**),

Periodic Table of Elements

H																	He
Li	Be											B	C	N	O	F	Ne
Na	Mg											Al	Si	P	S	Cl	Ar
K	Ca	Sc	Ti	V	Cr	Mn	Fe	Co	Ni	Cu	Zn	Ga	Ge	As	Se	Br	Kr
Rb	Sr	Y	Zr	Nb	Mo	Tc	Ru	Rh	Pd	Ag	Cd	In	Sn	Sb	Te	I	Xe
Cs	Ba	L	Hf	Ta	W	Re	Os	Ir	Pt	Au	Hg	Tl	Pb	Bi	Po	At	Rn
Fr	Ra	A	Rf	Db	Sg	Bh	Hs	Mt	Ds	Rg							

s Goldschmidt classification (1937)

L	La	Ce	Pr	Nd	Pm	Sm	Eu	Gd	Tb	Dy	Ho	Er	Tm	Yb	Lu
A	Ac	Th	Pa	U	Np	Pu	Am	Cm	Bk	Cf	Es	Fm	Md	No	Lr

Figure 1.1. Periodic Table of Elements. Elements highlighted in red text are those originally defined as chalcophile by Goldschmidt (1937). The chalcophile elements in bold, red text are those focussed on in the current project.

such as those of the porphyry Cu belts of northern Chile (Sillitoe, 1988, 2010; Mutschler et al., 2010; Sun et al., 2013). However, despite this global association of ore deposits with convergent margins, their spatial occurrence within convergent margins is irregular (Sillitoe, 1997), and the controls on porphyry deposit formation remain incompletely understood. Porphyry Cu-Au deposits are not solely constrained to sites above active subduction zones, and have been identified in other tectonic settings, including post-collisional (or post-subduction) settings (Richards, 2009). Although chalcophile-enriched porphyry deposits are associated with convergent margins, several studies have demonstrated that primitive convergent margin magmas are not

systematically enriched in the chalcophile elements when compared to mid-ocean ridge basalts (MORB) (Sun et al., 2004; Jenner et al., 2010; Lee et al., 2012; Timm et al., 2012). Thus, there has been much debate over the process(es) that fuel the formation of chalcophile-rich ore deposits (Mungall, 2002; Richards, 2009; Jenner et al., 2010; Lee et al., 2012; Wilkinson, 2013; Chiaradia, 2014; Matjuschkin et al., 2016; Sun et al., 2017).

Further to their economic importance, several studies have demonstrated the ability of the chalcophile elements to track magmatic processes. These studies have highlighted the mobility of certain chalcophile elements during subduction (e.g., Noll Jr et al., 1996; Timm et al., 2012) and have investigated sulfide fractionation during magma ascent and evolution (Jenner et al., 2012, 2015; Williams et al., 2018; Reekie et al., 2019).

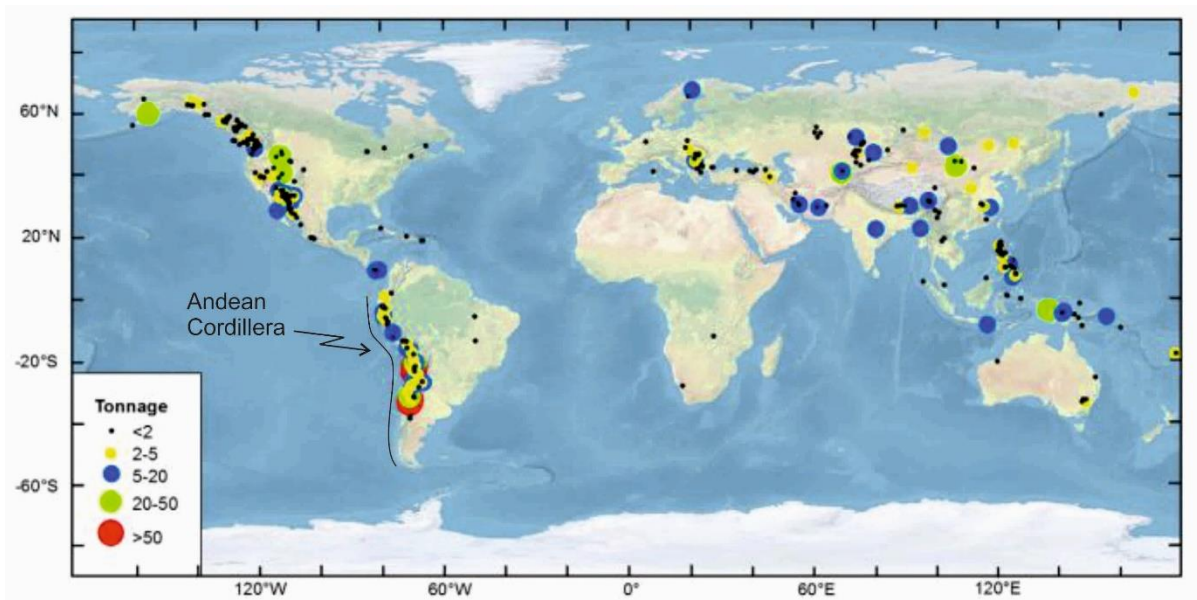


Figure 1.2. World map highlighting the global distribution of porphyry Cu ore deposits. The vast majority of deposits are associated with active convergent margins. Modified after Sun et al. (2015).

1.2. The Current Thesis

This thesis presents new whole rock major and trace element analyses, which include the near complete suite of chalcophile elements (S, Cu, Ag, Se, Pb, Tl, Bi, W, Mo, Ga, As, Sb, Sn, Zn, Co), for several volcanic centres in the Chilean segments of the Andean Cordillera, South America. Taking advantage of the presence of stratovolcanoes, small eruptive centres and varying crustal thicknesses across Chile, the data presented in this thesis has been used to systematically investigate the behaviour of the chalcophile elements in a typical continental volcanic arc setting. This thesis also comments on the implications the findings have for the cycling of S at convergent margins and the formation of chalcophile-rich ore deposits that are commonly associated with such settings.

1.2.1. Motivations and aims of the study

Although there are an abundance of Cu analyses present in the literature for continental volcanic arc settings, previous studies investigating other mantle-derived melts (i.e., oceanic arc-like settings, oceanic plateaux, mid-ocean ridges) have demonstrated the importance of the combined use of Cu, Ag, Au, Se and S for a more complete understanding of magmatic processes, such as tracking sulfide saturation (e.g., Jenner et al., 2010, 2012; Kurzawa et al., 2019; Reekie et al., 2019). Thus, the main motivation for conducting the research presented in this thesis is primarily centred around addressing the general lack of accurate whole rock analyses of the entire suite of chalcophile elements for a continental volcanic arc setting. Additionally, S represents a very important volatile element, and understanding how it is cycled within convergent margins has pronounced implications for the eruptive styles of volcanoes, their

associated hazards, the generation of ore deposits, and the climatic impact of volcanic SO₂ emissions (Wallace and Edmonds, 2011; Spandler and Pirard, 2013; Zellmer et al., 2015). However, despite these important and topical themes, the cycling of S at subduction zones is not fully constrained (Wallace, 2005; Spandler and Pirard, 2013). The 'S-loving' nature of the chalcophile elements means that gaining an understanding in how they are processed and distributed can provide insights into the cycling of S within a continental arc system (De Hoog et al., 2001a, 2001b; Lee et al., 2012).

The economic importance of the chalcophile elements (Sillitoe, 2010; Kiseeva et al., 2017), and the association of chalcophile-rich ore deposits with convergent margins (Sillitoe, 1997, 2010; Mutschler et al., 2010), makes understanding the processing and distribution of the chalcophile elements vital for attaining a more thorough grasp on what fuels the formation of porphyry Cu-Au deposits (Mungall, 2002; Richards, 2009; Jenner et al., 2010; Lee et al., 2012; Wilkinson, 2013; Chiaradia, 2014; Matjuschkin et al., 2016). Thus, it can aid in potentially identifying future exploration targets (e.g., Singer et al., 2002). Consequently, the aims and objectives of this thesis are as follows:

- 1) Obtain accurate chalcophile element analyses of volcanic rock samples by utilising the latest advancement in ICP-MS collision – reaction cell technology (i.e., the Agilent QQQ),
- 2) Constrain the behaviour of the chalcophile elements during magma genesis and the subsequent ascent and evolution of magmas in a continental volcanic arc setting, first using Antuco of the Southern Volcanic Zone, Chile as a case study,

3) Following on from above, compare the behaviour of the chalcophile elements beneath volcanic centres constructed on a range of crustal thicknesses (e.g., ~25 to ≥ 70 km), to identify if the thickness of the overriding crust at convergent margins exerts a strong control on chalcophile element processing,

4) Compare the processing and distribution of the chalcophile elements between large stratovolcanoes and small eruptive centres (SECs), to explore the relationship between the primitive magmas feeding SECs and the parental magmas of arc stratovolcanoes.

Overall, the goal of this thesis is to advance the understanding of how the chalcophile elements are processed and distributed within a continental volcanic arc, with the aim of helping to answer broader geological questions relating to ore deposit formation and the cycling of S in a subduction zone.

Chapter 2

Study region

2.1. The Andean Cordillera

The current study makes use of volcanic rock samples collected from several Chilean volcanic edifices, including both stratovolcanoes and small eruptive centres (SECs). This chapter summarises the geological setting of the study sites, on both a regional and more local scale, before introducing each of the volcanic edifices sampled.

The Andean Cordillera, which extends for $\geq 7,500$ km along the west coast of South America, from the northern Caribbean coast of Colombia to southern Chile (**Fig. 2.1**), represents the topographic expression of the oblique subduction of the Cocos, Nazca and Antarctic oceanic plates beneath the South American continental plate. Volcanism associated with the Andean Cordillera is not continuous; rather, it is constrained to four volcanically active arc segments – the Northern (NVZ, 5°N to 2°S), Central (CVZ, 14°S to 27°S), Southern (SVZ, 33°S to 46°S) and Austral (AVZ, 49°S to 55°S) Volcanic Zones – hosting more than 200 historically and recently active volcanoes, as well as hundreds of small eruptive centres (Stern, 2004). Volcanism in the N/C/SVZ is the manifestation of the subduction of the Cocos and Nazca Plates,

whereas volcanism in the AVZ is associated with the subduction of the Antarctic Plate (Stern, 2004). The discontinuous nature of volcanism in the Andean Cordillera is the

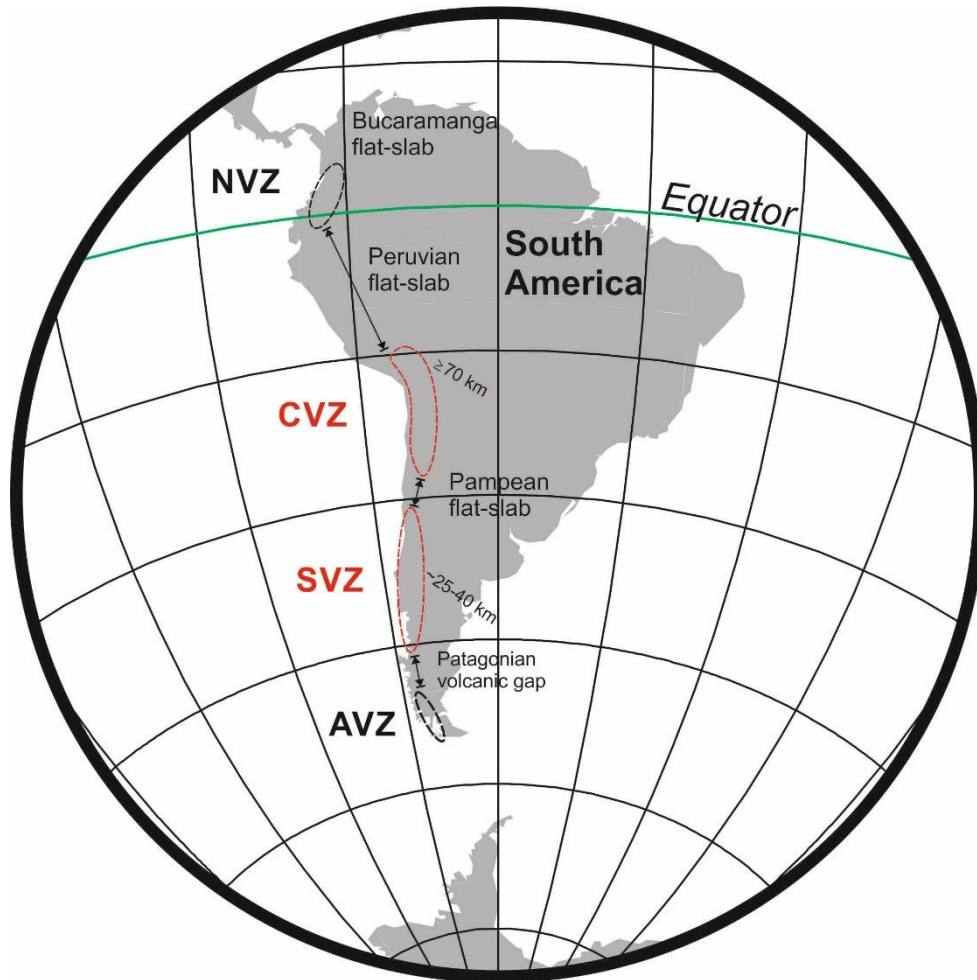


Figure 2.1. Volcanic zones of the Andean Cordillera. The Andean Cordillera extends for $\geq 7,500$ km along the western coast of South America, from the Caribbean coast of Colombia to southern Chile. N/C/S/AVZ: Northern/Central/Southern and Austral Volcanic Zones. The red zones highlight the zones of focus in the current project. The range of crustal thicknesses from where samples have been collected have also been highlighted [after Tassara and Echaurren (2012)]. Map constructed in Generic Mapping Tool, using a script written by Sebastian Watt.

result of four segments that lack recent volcanic activity. Three of these four segments, termed (north to south) the Bucaramanga, Peruvian and Pampean, are associated with so-called “flat slab” (or horizontal) subduction of thick and buoyant oceanic lithosphere (Barazangi and Isacks, 1976; Stern, 2004; Ramos and Folguera, 2009). The remaining non-volcanic segment, located between the SVZ and AVZ, is the Patagonian Volcanic Gap, where volcanism has ceased due to ridge (Chile Rise) subduction (Stern, 2004).

Density (Tassara et al., 2006; Tassara and Echaurren, 2012) and seismic refraction (Assumpção et al., 2013) models have demonstrated that the thickness of the continental crust varies along the length of the Andean Cordillera. These models have demonstrated the CVZ sits above the thickest continental crust, with the depth to the Moho in places being as great as ≥ 70 km. Continental crustal thickness generally decreases to the north and south of the CVZ, reaching ~ 40 km beneath the NVZ (Ecuador and southern Colombia) and as thin as ≤ 30 km beneath southernmost Chile. Additionally, the age of the subducting Nazca and Antarctic plates also vary along their length, increasing in age north and south of the Chile Rise, respectively (Stern, 2004).

Chilean volcanism is confined to the southernmost CVZ (northern Chile) and the SVZ (central to southern Chile), as well as the AVZ (which does not form part of the current study). The following sections outline the geological setting of both the CVZ and SVZ.

2.2. Southern Volcanic Zone

Located along central and southern Chile, the SVZ extends from 33°S to 46°S and is bounded to the north and south by the Pampean Flat Slab and Patagonian Volcanic Gap, respectively (**Fig. 2.2**). The SVZ hosts ≥ 60 volcanoes, most of which

have been active in the Holocene, plus numerous small eruptive centres (Stern, 2004; Wehrmann et al., 2014). Several sub-segments of the SVZ have been defined, with many iterations, based on either tectonic, petrologic and/or geochemical constraints [for a summary see Selles et al. (2004)]. However, the more commonly referred to divisions are (Hickey-Vargas et al., 2016a): the Northern (NSVZ, 33°S to 34.5°S), Transitional (TSVZ, 34.5°S to 37°S), Central (CSVZ, 37°S to 41.5°S) and Southern (SSVZ, 41.5°S to 46°S) Southern Volcanic Zones (**Fig. 2.2**).

Mirroring the broad scale of the Andean Cordillera, the overlying continental crustal thickness varies along the length of the SVZ, from ~60 km at the northern end, generally decreasing south to ~25 – 30 km at the southernmost point of the SVZ (Tassara and Echaurren, 2012). The age of the subducting Nazca Plate increases northward along the SVZ, from 0 Ma at the Chile Rise to ~37 Ma at the northern end (Wehrmann et al., 2014; Hickey-Vargas et al., 2016a).

The oceanic crust of the Nazca Plate subducting beneath southern Chile is cut by several transform faults, including (north to south) the Mocha, Valdivia, Chiloé and Guafo Fracture Zones (Contreras-Reyes and Carrizo, 2011; Dzierma et al., 2012; Hickey-Vargas et al., 2016a) (**Fig. 2.2**). The Mocha and Valdivia Fracture Zones dissect oceanic lithosphere generated at the East Pacific Rise (to the west), whereas the Chiloé and Guafo Fracture Zones dissect oceanic lithosphere generated at the Chile Rise, to the south (Hickey-Vargas et al., 2016a). These fracture zones intersect the Chile trench along the SVZ and are subsequently subducted beneath Chile. Contreras-Reyes and Carrizo (2011) have demonstrated that the subduction of these fracture zones is associated with the rupture-zone limits of large earthquakes along

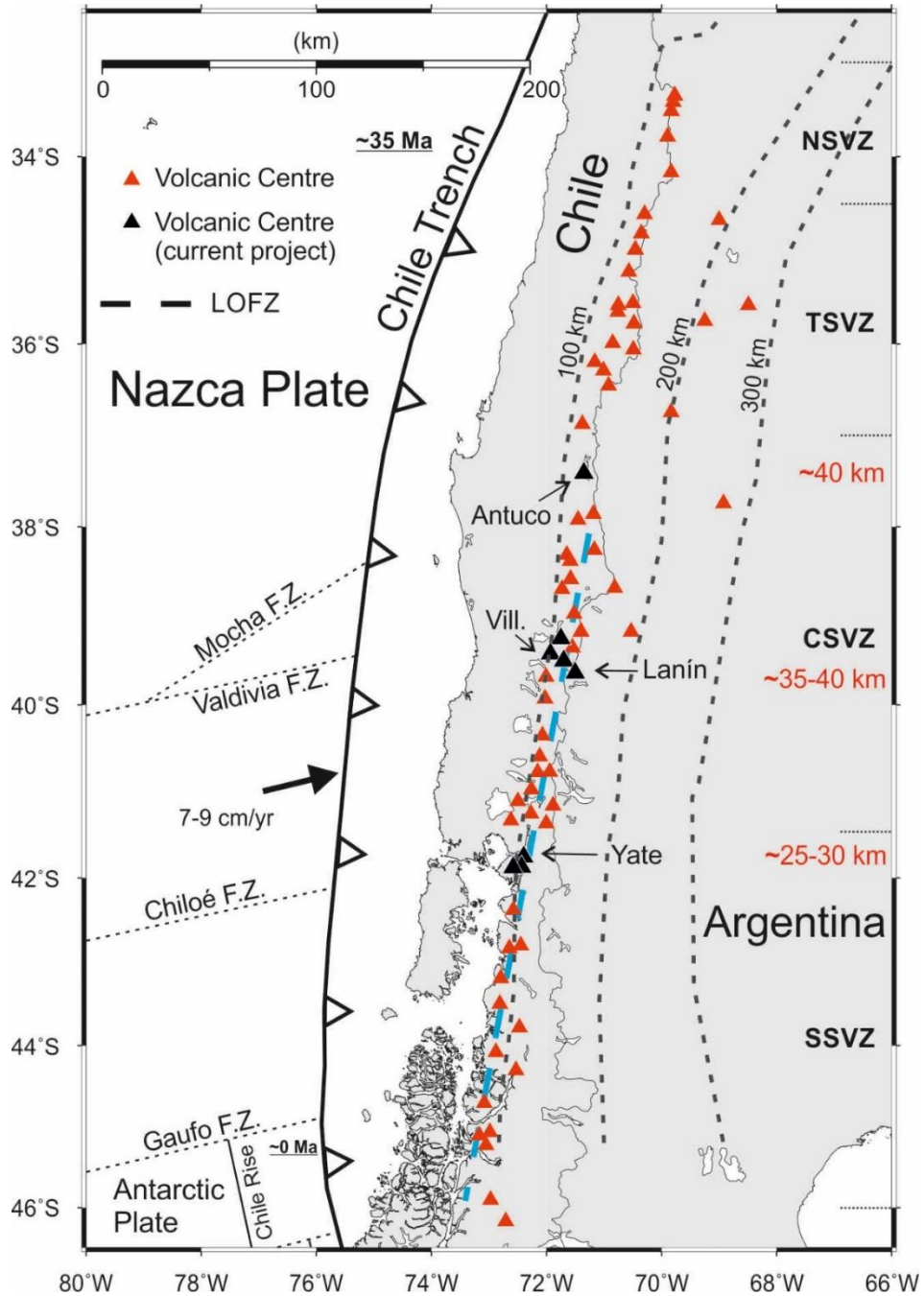


Figure 2.2. Southern Volcanic Zone. The Southern Volcanic Zone of Chile extends between 33°S and 46°S. Black triangles highlight the edifices discussed in the current study. Edifice locations compiled from the Holocene and Pleistocene volcano databases by the Global Volcanism Program, Smithsonian Institute (downloaded 28 June 2019). Location of fracture zones (F.Z.) and the Chile trench from Stern (2004) and Volker et al. (2011). Trace of the Liquiñe-Ofqui Fault Zone (LOFZ) from Hickey-Vargas et al. (2016a). Slab depth contours and estimated Moho depth at sample sites (red text) from Tassara and Echaurren (2012). Subducting slab age from Stern (2004). N/T/C/SSVZ: Northern/Transitional/Central and Southern Southern Volcanic Zones. Map constructed in Generic Mapping Tool, using a script written by Sebastian Watt.

the Chilean margin, and have subsequently argued that such fracture zones act as asperities and boundaries, controlling the extent of seismic behaviour. Additionally, Dzierma et al. (2012) have suggested that the subduction of the Valdivia Fracture Zone could explain why Villarrica and Llaima are amongst the most active volcanoes in South America (Volker et al., 2011). Dzierma et al. (2012) argue that the Valdivia Fracture Zone has facilitated fluid ingress into the subducting oceanic Nazca Plate, and as such, ultimately results in elevated fluid release into the sub-arc mantle wedge, and greater degrees of partial melting, beneath Villarrica and Llaima.

A prominent feature of the SVZ is the Liquiñe-Ofqui Fault Zone (LOFZ), a ~1,200 km long intra-arc fault zone that extends along the CSVZ and SSVZ (**Fig. 2.2**) (Lopez-Escobar et al., 1995a; Cembrano and Lara, 2009; Hickey-Vargas et al., 2016a). The positioning of a number of stratovolcanoes and a large proportion of SECs are influenced by the presence of the LOFZ, which is postulated to facilitate magma ascent (Lopez-Escobar et al., 1995a; Stern, 2004; Cembrano and Lara, 2009).

The SVZ represents an ideal foundation for investigating the processing and distribution of the chalcophile elements in a continental volcanic arc setting, because it has been demonstrated to be an archetypal arc segment (Syracuse et al., 2010), with a continental crustal thickness similar to the global average [~40 km; Assumpção et al. (2013)] and with other plate tectonic parameters (crustal age, subduction rate, subduction dip angle) within the typical range of global subduction zones. Additionally, although the crustal thickness (~25 – 40 km) between the field sites (i.e., CSVZ to SSVZ, Antuco to Hornopirén) varies, other parameters of the convergent margin (i.e., subducting slab age, convergence rate, subduction dip angle, distance to subducting slab and trench) do not alter considerably, and are within the typical ranges of global

subduction zones (Syracuse et al., 2010). Thus, in conjunction with the CVZ (outlined below), the role of crustal thickness, if any, in the processing of the chalcophile elements can be thoroughly investigated.

Volcanic rock samples used in the current study were collected from several volcanic centres along the SVZ, including Antuco, Villarrica, Quetrupillán, Lanín, SECs of the Caburgua – Huelemolle Complex and Huililco, Yate, Apagado and Hornopirén (**Fig. 2.2**). The local geological setting of each of these edifices is outlined below, with further location and descriptive details on the collected samples presented in **Chapter 3** and **Appendices A** and **B**.

2.2.1. Antuco¹

Antuco marks the northernmost point of the central part of the SVZ (**Fig. 2.3**) (Lopez-Escobar et al., 1995a; Hickey-Vargas et al., 2016a). Antuco is the younger (Pleistocene – Holocene age) of a pair of stratovolcanoes (the other being the Pleistocene Sierra Velluda Volcano) that form a volcanic complex at 37.2°S (Lopez-Escobar et al., 1981; Martínez et al., 2018) along an alignment oblique (50 - 70° E of N) to the main arc (Lopez-Escobar et al., 1995a). Antuco is the smaller of the two stratovolcanoes, with a basal diameter of ~11 km, rising to 2979 metres above sea level, and an estimated volume of 62 km³ (Martínez et al., 2018).

Volcanism at Antuco has been divided into two phases – Phase 1 and Phase 2 Antuco (**Fig. 2.3**) – separated by a westward directed, mid-Holocene sector collapse (Lopez-Escobar et al., 1981; Thiele et al., 1998) dated at 6.2 ka by Lohmar et al. (2005) and 4 ka by Clavero and Godoy (2010). Recently, Martínez et al. (2018) used a

¹ This section includes material published in *Earth Planet. Sci. Lett.* (Cox et al., 2019)

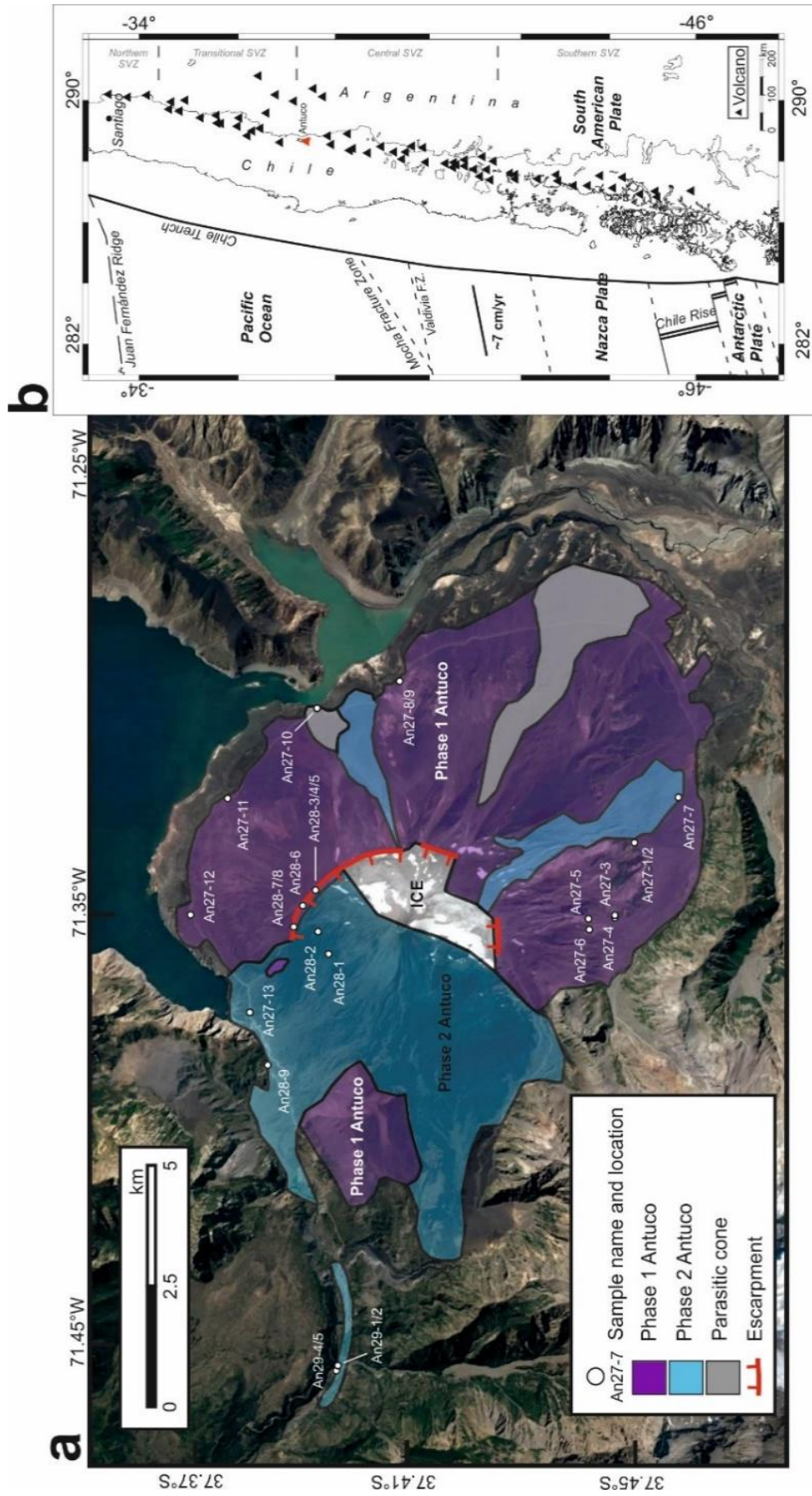


Figure 2.3. (a) Simplified geological map of Antuco Volcano, Chile. Sample locations highlighted with filled circles. Geological map adapted after Martínez et al. (2018). Base image from Google Earth (2018). (b) Location map of Antuco Volcano, highlighting its location at the northern end of the Central Southern Volcanic Zone.

comprehensive dataset of $^{40}\text{Ar} / ^{39}\text{Ar}$ dates to further define Early (commencing at 150.4 ka) and Late (~16.3 to 6.2 ka) periods of volcanism during Phase 1. Phase 1 lavas show a slightly broader compositional range (basalt to andesite) than Phase 2 lavas (basalt to basaltic andesite) (Lohmar et al., 1999, 2005; Martínez et al., 2018).

Antuco is typical of stratovolcanoes in the SVZ, both in terms of its dimensions (Volker et al., 2011) and range of erupted compositions, but is also amongst the most isotopically primitive volcanoes in the SVZ (Hildreth and Moorbath, 1988; Lohmar et al., 1999; Hickey-Vargas et al., 2016a). Primitive rock compositions at Antuco indicate a predominantly fluid enriched, depleted-MORB mantle source, typical of the central SVZ, which has been used as an endmember to explore additional crustal-derived source enrichment further north in the SVZ (Holm et al., 2014, 2016). In a global context, the parameters defining this segment of the SVZ (Syracuse et al., 2010), including a crustal thickness of 40 km (Hickey-Vargas et al., 2016a), suggest that it is representative of a 'typical' continental arc setting. The broad range in lava compositions and previous interpretations that the Antuco magmas stalled at the base of the continental crust prior to crystallisation at lower pressures (Martínez et al., 2018), make volcanic rocks from Antuco ideal for investigating the processing and distribution of the chalcophile elements during ascent of magmas through the continental crust.

2.2.2. Villarrica – Quetrupillán – Lanín

Villarrica, Quetrupillán and Lanín stratovolcanoes form a volcanic chain at 39°S in the CSVZ of the Andes, which extends for ~50 km in a NW – SE direction (Hickey-Vargas et al., 1989; Moreno R. et al., 1994b) toward the border between Chile and Argentina (**Fig. 2.2** and **2.4**). In addition to these stratovolcanoes, the Villarrica – Quetrupillán – Lanín volcanic chain also includes five eroded volcanic centres and >20

minor eruptive centres (e.g., the Caburgua – Huelemolle Complex small eruptive centres) that lie to the north – northeast of Villarrica (Lara et al., 2004). The Villarrica – Quetrupillán – Lanín volcanic chain is related to a N50 – 60°W trending lineament that runs oblique to the main volcanic arc axis and the LOFZ (**Fig. 2.4**). Unlike the orientation of Villarrica – Quetrupillán – Lanín, around 30 parasitic cones on the northeast and south flanks of Villarrica trend in a northeast direction, associated with the present-day maximum horizontal stress (Cembrano and Lara, 2009). The thickness of the overriding crust on which the Villarrica – Quetrupillán – Lanín chain is sat atop is ~35 – 40 km (Tassara and Echaurren, 2012).



Figure 2.4. Context of the Villarrica – Quetrupillán – Lanín volcanic chain. Black, dashed line highlights the orientation of the volcanic chain. Trace of the LOFZ, and associated sub-parallel faults and tension cracks from Sanchez et al. (2013) and Hickey-Vargas et al. (2016b). Sample IDs for the small eruptive centres have been omitted for clarity. Base image from Google Earth (2019).

2.2.2.1. Villarrica Volcano

Villarrica (39°25'S, 71°56'W, summit altitude 2847 m; Global Volcanism Program: <https://volcano.si.edu>, accessed 2019) is one of South America's most active and highest risk volcanoes, with 112 explosive eruptions over the last ~600 years (Van Daele et al., 2014). Villarrica is composed of volcanic products (lavas, pyroclastic, scoria and lahar deposits) that are Pleistocene to historic in age (Hickey-Vargas et al., 1989; Witter et al., 2004); the most recent eruption being that of March 2015 (Aiuppa et al., 2017; Delgado et al., 2017). Throughout its history, activity at Villarrica has been near constant (Van Daele et al., 2014) and dominantly effusive in nature, producing basaltic to basaltic andesite lavas (Hickey-Vargas et al., 1989; Moreno R. et al., 1994b). From a set of lake core records, Van Daele et al. (2014) concluded that Villarrica produced an explosive eruption of VEI ≥ 2 (Volcanic Explosive Index) roughly every 5 years, although recent historical records suggest a slightly lower frequency. The most recent (2015) eruption at Villarrica was generally characterised by explosive (strombolian/lava fountain) behaviour but also showed minor effusive (Hawaiian) behaviour (Delgado et al., 2017; Johnson et al., 2018). During Holocene times, Villarrica experienced two large, caldera forming eruptions, at ~14,300 and ~3,700 ka, that resulted in the Licán and Pucón ignimbrites, respectively (Moreno R. et al., 1994a). Lahar deposits are also associated with explosive eruptions at Villarrica (Moreno R. et al., 1994a; Van Daele et al., 2014). Present activity is restricted to degassing (also observed during the current project's fieldwork, March 2016) from its lava lake (Johnson and Palma, 2015; Aiuppa et al., 2017).

2.2.2.2. *Quetrupillán and Lanín Volcanoes*

Both Quetrupillán and Lanín stratovolcanoes are understudied, with very few geochemical analyses of their eruptive products (e.g., Hickey-Vargas et al., 1989; Lara et al., 2004). This is likely due to the high risk their near neighbour, Villarrica, poses to surrounding communities, consequently being paid more attention.

Quetrupillán (39°30'S, 71°43'W) sits ~25 km southeast of Villarrica (**Fig. 2.4**) and has a summit altitude of 2,360 m (Global Volcanism Program, accessed 2019). Van Daele et al. (2014) identified two eruptions from Quetrupillán in the lake cores, based on visible tephra fall out, both having occurred in the nineteenth century. Hickey-Vargas et al. (1989) presented geochemical analyses of seven lava samples from Quetrupillán, sampled from only the northern flank of the volcano, showing the lavas to range in composition from andesite to dacite.

Lanín (39°38'S, 71°30'W) sits further along the volcanic chain (**Fig. 2.4**), ~45 km southeast of Villarrica, with a summit altitude of 3,776 m (Global Volcanism Program, accessed 2019). Constructed since the Pliocene, Lanín has been inactive in historic times (Lara et al., 2004). This is supported by the lack of identifiable volcanic deposits from Lanín in the lake cores presented by Van Daele et al. (2014). Activity at Lanín has mostly been effusive, producing a bimodal distribution of lavas: basaltic and basaltic andesite, and dacitic (Hickey-Vargas et al., 1989; Lara et al., 2004). Pyroclastic flows and ash fall-out and lahar deposits have also been identified at Lanín (Lara et al., 2004).

2.2.3. Chilean small eruptive centres

The Chilean segments (C/SVZ) of the Andean Volcanic Arc play host to hundreds of SECs (Lopez-Escobar et al., 1995a; Stern, 2004). These SECs usually form clusters or alignments that are generally associated with the northeast – southwest trending LOFZ, and/or its subsidiary faults, or located near stratovolcanoes (Lopez-Escobar et al., 1995a, 1995b; Stern, 2004; Cembrano and Lara, 2009; Sánchez et al., 2013). The eruptive products (lavas and/or scoria deposits) of the Chilean SECs are generally basaltic to basaltic andesite in composition, and in conjunction with their association with the LOFZ, have been used to argue that this fault system has facilitated magma ascent (Lopez-Escobar et al., 1993, 1995a; Lara et al., 2006; Cembrano and Lara, 2009). Furthermore, Lopez-Escobar et al. (1995a) explained that SECs (and some stratovolcanoes) associated with either the LOFZ or its sub-parallel, master faults (i.e., faults trending roughly northeast) were generally basaltic in composition, compared to stratovolcano alignments associated with near east – west trending faults (e.g., Villarrica – Quetrupillán – Lanín), whose erupted products can span the entire compositional range, from basalt through rhyolite. Again, this was attributed to a more rapid ascent rate and shorter crustal residence times of magmas beneath centres along the LOFZ. However, Lopez-Escobar et al. (1995a) demonstrated that basalts and basaltic andesites of SECs, although amongst the most primitive in the SVZ, have MgO, Cr and Ni contents lower than mid-ocean ridge basalt (MORB) magmas. The volcanic products from SECs in Chile have been argued to represent the products closest to primary mantle melt compositions in the SVZ (e.g., López-Escobar and Moreno R., 1994; Lara et al., 2006; Watt et al., 2013), although the relationship between SEC magmas and magmas parental to those erupted at the

stratovolcanoes requires further investigation (Hickey-Vargas et al., 2016b; Rawson et al., 2016).

2.2.3.1. The Caburgua – Huelemolle Complex and Huililco

The SECs in the Pucón area of the CSVZ, which include the Caburgua – Huelemolle Complex (CHC), comprising several centres, and Huililco, are located ~10 – 25 km to the north/northeast of Villarrica and Quetrupillán stratovolcanoes (**Fig. 2.4**). The vast majority of these SECs are situated along either the main, northeast – southwest trending structure of the LOFZ, or sub-parallel lineaments to the LOFZ (Lopez-Escobar et al., 1995a; Cembrano and Lara, 2009; Sánchez et al., 2013). Huililco, however, located ~11 km to the northeast of Quetrupillán, is not situated along a fault structure (Sánchez et al., 2013; McGee et al., 2015). Based on tephrochronology and radiocarbon dating, the SECs are estimated to be aged between 4 and 16.5 ka (Morgado et al., 2015; Hickey-Vargas et al., 2016b). The SECs are of small volume (generally <0.5 km³), rise to heights no greater than 700 m and are heavily vegetated (Morgado et al., 2015).

Recently, these SECs have received attention in the literature in terms of their petrogenesis (e.g., Morgado et al., 2015, 2017; Hickey-Vargas et al., 2016b; McGee et al., 2017; Brahm et al., 2018). Although Huililco and the SECs of the CHC are all within close proximity of each other (~20 km), these recent studies have demonstrated that the compositions of erupted products vary between individual SECs and between the SECs and the neighbouring stratovolcano of Villarrica (Morgado et al., 2015, 2017; Hickey-Vargas et al., 2016b; McGee et al., 2017). Such compositional variations in this small region have been used to argue for discrete magma ascent pathways with varying magma histories (Hickey-Vargas et al., 2016b; McGee et al., 2017); an

interpretation previously suggested in a study of minor centres in the SVZ (Apagado, Hornopirén, Palena and South Minchinmávida) by Watt et al. (2013). Unlike Villarrica, which is postulated to have both a deep-seated and shallower magma chambers, magmas of the SECs are suggested to be sourced from a deep reservoir (Morgado et al., 2015), although Hickey-Vargas et al. (2016b) argued for a lower crustal pyroxenite source. However, the SEC magmas may still be subject to upper crustal storage (e.g., Morgado et al., 2017), and therefore a degree of fractional crystallisation.

In contrast to the SECs north of Villarrica, it has also been suggested that the SEC Huililco is genetically linked to its neighbouring stratovolcano Quetrupillán, having similar major and trace element and Sr and Nd isotope systematics, thus possibly sharing a plumbing system with Quetrupillán (McGee et al., 2017; Brahm et al., 2018). Furthermore, fractional crystallisation modelling presented by Brahm et al. (2018) suggested that Quetrupillán's magmas were generated from parental magmas comparable in composition to basalts from Huililco.

2.2.4. Yate – Hornopirén – Apagado

Yate, Hornopirén and Apagado are three volcanoes located on the heavily vegetated Hualaihué Peninsula of southern Chile (**Fig. 2.5**), at the northern end of the SSVZ (Stern, 2004). Both Yate and Hornopirén are located along the dextral strike-slip LOFZ, with Hornopirén situated ~13 km to the south of Yate. Apagado lies to the east of the LOFZ, ~20 km southwest of Yate and ~12 km east of Hornopirén. All three volcanoes have been active in the Holocene, however, the main focus of volcanic activity has been at Yate and Hornopirén, along the LOFZ (Watt et al., 2011). The overriding crustal thickness of the Hualaihué Peninsula is ~25 – 30 km (Tassara and Echaurren, 2012).

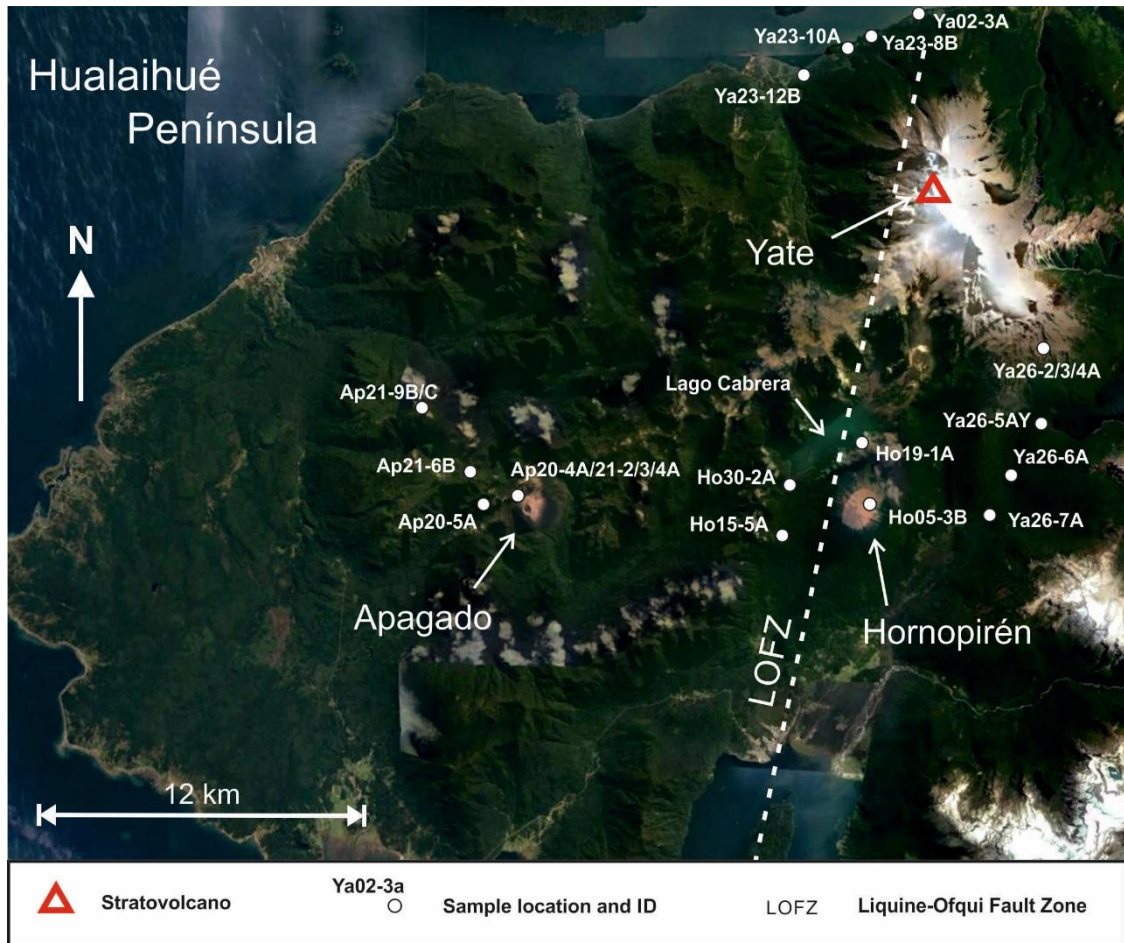


Figure 2.5. Volcanoes of the Hualaihué Península. Trace of the LOFZ from Watt et al. (2011). Base image from Google Earth (2019).

2.2.4.1. Yate Volcano

Yate is the largest of the three volcanic centres on the Hualaihué Peninsula, with a summit height of 2,187 m (Mella Barra, 2008; Global Volcanism Program, accessed 2019). Yate is a stratovolcano and is comprised of bedded Pleistocene lavas and pyroclastic units (Watt et al., 2009). Activity at Yate has mostly been effusive, however, explosive eruption events have recently been documented (e.g., Watt et al., 2011). Erupted volcanic products of Yate span a broad compositional range, from basalt to dacite (Mella Barra, 2008; Watt, 2010). Therefore, samples from Yate will allow a complete investigation into the behaviour of the chalcophile elements during magma evolution, providing a good counterpart to Antuco.

Yate is a hazardous volcano, posing a threat to local communities and has suffered numerous flank collapses during its history (Hauser Y., 1985; Watt et al., 2009). The subsequent debris avalanches have comprised volcanic rock and ice and have been documented to radiate both northwest and southeast from the summit, with one event (February 1965) resulting in the loss of life (Watt et al., 2009).

2.2.4.2. Hornopirén and Apagado Volcanoes

Hornopirén is a young, small (summit height of 1,572 m), symmetrical stratovolcano sat atop the LOFZ, directly south of Yate (Watt et al. 2011; Global Volcanism Program, accessed 2019). Activity at Hornopirén has been dominated by effusive behaviour, however, Watt et al. (2011) have documented several explosive eruptions, the largest at ~5.7 ka. In a detailed tephrochronological study of the volcanic centres on the peninsula, Watt et al. (2011) documented reduced activity at Yate in the Holocene, while the younger nature of Hornopirén suggested recent and rapid growth. Watt et al. (2011) therefore concluded that the locus of volcanic activity was transiting

southwards along the LOFZ toward Hornopirén, and away from Yate. In its current form, Apagado represents a scoria cone (i.e., SEC), positioned ahead of the active arc front (as defined by the much larger structures of Yate and Hornopirén). This cone is situated within the eroded remnants of an older stratovolcano, from which samples were collected, which may predate Yate (Watt et al., 2011).

Like the Villarrica – Quetupillán – Lanín volcanic chain, Apagado and Hornopirén – Yate form a short, across-arc traverse section, although it is unclear if the two sites were active at the same time (with the exception of the Holocene scoria cone at Apagado). In an across-arc study of olivine-hosted melt inclusions, including samples from the Apagado scoria cone and Hornopirén, Watt et al. (2013) demonstrated that near-primary melt compositions within melt inclusions from Apagado had elevated H₂O contents and low La/Yb when compared to those from Hornopirén, which had reduced water contents and higher La/Yb. Subsequently, Watt et al. (2013) suggested that due to its location at the arc front, the Apagado scoria cone was subject to a more H₂O-rich slab flux, whereas with increased distance from the arc front (toward Hornopirén), the slab flux became less H₂O-rich and dominated by hydrous melts, a consequence of increasing subducting slab temperature.

2.3. Central Volcanic Zone

The CVZ extends from 15°S to 27°S, across Peru and northern Chile (Stern, 2004), and is bounded by the Peruvian (north) and Pampean (south) Flat Slab segments (**Fig. 2.1**). The CVZ has the thickest (≥ 70 km) continental crust along the Andean Cordillera (Tassara et al., 2006; Tassara and Echaurren, 2012), considerably greater than the global continental average [~ 40 km; Assumpção et al. (2013)]. Along the length of the CVZ, the subducting Nazca Plate is $\sim 50 - 60$ Ma (Stern, 2004).

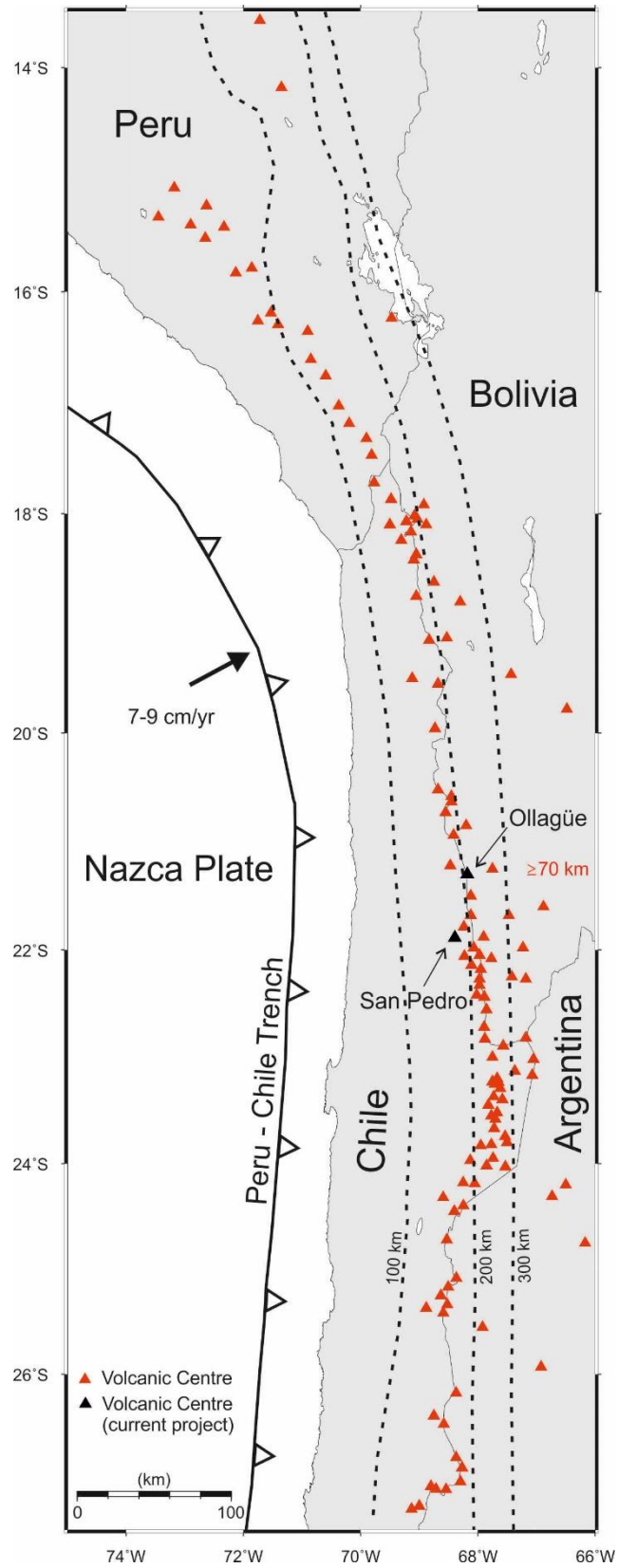
The CVZ of Chile provides an interesting comparison to sites in the SVZ for several reasons. First, the thickness of the overlying continental crust in the CVZ is nearly double that of the southernmost SVZ, and the range of crustal thicknesses spanned by the stratovolcanoes investigated in this thesis (i.e., ~25 – 80 km) covers the full range of crustal thicknesses in continental arcs globally (Syracuse et al., 2010). Thus, by comparing chalcophile element processing between the SVZ and CVZ, there is an opportunity to test the significance of the overriding crustal thickness in controlling the processing of the chalcophile elements (e.g., Chiaradia, 2014), with the results being applicable to continental volcanic arcs globally.

Several arc-parallel, linear belts of porphyry Cu-Au deposits extend for more than ~2,000 km along the CVZ, from southern Peru and into northern Chile (Sillitoe, 1988; Sillitoe et al., 2013). These belts host some of the world's largest Cu concentrations (Sillitoe, 2010). In addition to the porphyry Cu deposits of the CVZ, there are numerous iron oxide-copper-gold deposits, although they do not host the high chalcophile concentrations of the adjacent porphyry Cu-Au deposits (Sillitoe, 2003). In contrast with the Central Andes, there appears to be an absence of porphyry Cu deposits further south, at latitudes spanned by the SVZ. However, the major porphyry Cu deposits of the Central Andes are of Cenozoic age, and so much older than the current active volcanic arc (Sillitoe, 1988; Singer et al., 2002). Nevertheless, the ore deposits are spatially associated with thickened crust, and absent from the thinner crust to the south. It is therefore potentially informative to compare the processing of the chalcophile elements between the CVZ and SVZ – modern day arc segments constructed on thin and thick continental crust – to ascertain if crustal thickness is playing a fundamental role in controlling chalcophile element systematics

within continental volcanic arcs, and may therefore be implicated in the processes that ultimately give rise to the formation of porphyry Cu deposits.

Volcanic rock samples were collected from several sites in the CVZ; including Ollagüe, La Poruñita and San Pedro (**Fig. 2.6**). Again, the local geological settings of each edifice are outlined below, with further descriptive details on the samples collected presented in **Chapter 3** and **Appendices A** and **B**.

Figure 2.6. Central Volcanic Zone. The Central Volcanic Zone of Chile extends between 15°S and 27°S. Black triangles highlight the edifices discussed in the current study. Edifice locations compiled from the Holocene and Pleistocene volcano databases by the Global Volcanism Program, Smithsonian Institute (downloaded 28 June 2019). Location of the Peru – Chile trench from Stern (2004). Slab depth contours and estimated Moho depth at sample sites (red text) from Tassara and Echaurren (2012). Map constructed in Generic Mapping Tool, using a script written by Sebastian Watt.



2.3.1. Ollagüe

Ollagüe is an isolated, composite cone located on the border between Chile and Bolivia (**Fig. 2.7**), with a summit height of 5,863 m and an edifice volume of ~80 – 90 km³ (Feeley et al., 1993; Feeley and Davidson, 1994). The stratovolcano sits ~25 km East of the main Quaternary volcanic arc axis, on the western edge of the Bolivian Altiplano (Feeley et al., 1993). A Series of K/Ar and Ar/Ar dates from Ollagüe, which include dates obtained from both lavas and debris avalanche deposit material, constrain the activity at Ollagüe to <1.2 Ma (Worner et al., 2000; Clavero et al., 2004; Vezzoli et al., 2008). The pristine nature of lava flows on the flanks of Ollagüe are testament to its young age (Feeley et al., 1993). Additionally, present activity is visible as fumarolic emissions from the summit region (Feeley et al., 1993); such fumarolic emissions were also observed during the current project's field expedition to northern Chile in March 2016.

It must be noted that sampling in the Ollagüe – La Poruñita (below) region was challenging for several reasons. First, Ollagüe is an active volcano, with a history of collapse events (detailed below), and is situated at an extremely high altitude (>4,000 m). Additionally, Ollagüe is located along a dangerous section of the border between Chile and Bolivia, and is commonly surrounded by unmarked land-mine 'fields'.

The eruptive history of Ollagüe has been divided into four stages, each separated by a sector collapse (Feeley et al., 1993; Vezzoli et al., 2008). Detailed descriptions of each eruptive stage, and their associated volcanic rocks, are provided in the field and geochemical based studies of Feeley et al. (1993) and Vezzoli et al. (2008). Although Vezzoli et al. (2008) documented a sector collapse separating each eruptive stage, the scale of these collapses varied. The most prominent collapse was

that at ~300 ka (Clavero et al., 2004; Vezzoli et al., 2008); a westward directed sector collapse of the western flank of Ollagüe, extending up to ~16 km from the summit, and leaving a collapse amphitheatre of ~3.5 km in diameter (Feeley et al., 1993; Clavero et al., 2004). The resultant debris avalanche deposit filled the eastern perimeter of the Carcote Salar Basin and is characterised by hummocky terrain (≥ 150 hummocks); for a detailed description of the debris avalanche deposit, see Clavero et al. (2004). Since this sector collapse, the La Poruñita scoria cone (**Fig. 2.7**) has built atop the debris avalanche deposit [Feeley et al. (1993); see below].

Andesites represent the dominant composition of lavas erupted from Ollagüe, although erupted compositions range in composition from basaltic andesite to dacite (Feeley et al., 1993; Feeley and Davidson, 1994). Detailed geochemical studies of the entire compositional range of lavas at Ollagüe have postulated a two-stage model of crustal contamination during magma ascent, demonstrating, through trace element geochemistry and isotope (Sr, Nd and O) systematics, that the more primitive basaltic andesite magmas show a greater degree of crustal contamination compared to the more evolved andesite and dacite magmas (Feeley et al., 1993; Feeley and Hacker, 1995; Feeley and Sharp, 1995). The basaltic andesites have been argued to have acquired their contamination through the assimilation of lower crustal material, whereas the andesites and dacites have been argued to have acquired their contamination through assimilation of upper crustal material (Feeley et al., 1993; Feeley and Sharp, 1995).

In spite of the very thick continental crust in the Ollagüe region, Mattioli et al. (2006) provided evidence for rapid magma ascent beneath a Quaternary-aged(?), unnamed, shield-like monogenetic centre on the western flank of Ollagüe. Fast ascent

was postulated to have been associated with extensional structural features in the Ollagüe region, possibly related to a period of crustal relaxation during the Quaternary Period. Detailing the petrology and geochemistry of a near aphyric, high-K andesitic lava, Mattioli et al. (2006) demonstrated that the lava had a low modal abundance of phenocrysts (<3%, olivine and pyroxene) and rapidly cooled, skeletal olivine crystals. Additionally, although the magma was postulated to have ascended rapidly, avoiding storage and extensive crystallisation, it had still been contaminated by fertile crustal material, evidenced by the presence of xenocrysts (predominantly quartz, but also feldspar) and Sr-Nd-Pb isotope systematics.

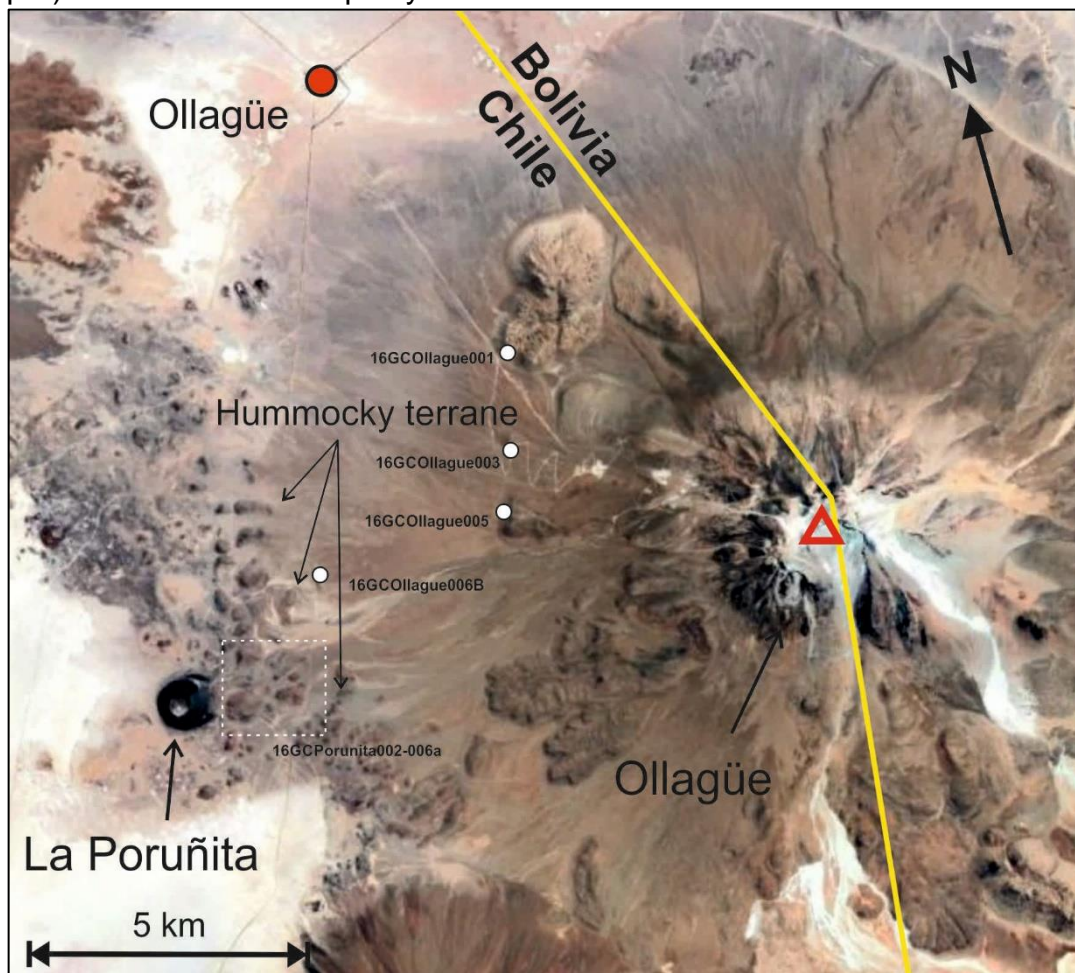


Figure 2.7. Ollagüe stratovolcano. The location and ID of samples collected from Ollagüe are marked with filled circles. However, for clarity, those samples collected from the debris avalanche deposit have been highlighted with a dashed box. Base image from Google Earth (2019).

2.3.2. La Poruñita

The La Poruñita SEC is situated in the CVZ on the western flank of Ollagüe stratovolcano, ~11 km to the west of Ollagüe's summit (**Fig. 2.7**). The cone represents one of a number of basaltic andesite scoria cones near to Ollagüe, most of which are unnamed (Vezzoli et al., 2008). The cone of La Poruñita is <100 m in height, with a basal diameter of ~700 m (Feeley et al., 1993). La Poruñita was dated between ~0.4 and 0.6 million years old by Worner et al. (2000), although these dates had large errors and are inconsistent with the age of the underlying debris avalanche deposit [~300 ka; Clavero et al. (2004)]. To date, a geochemical link, if any, between La Poruñita and Ollagüe is yet to be investigated.

2.3.3. San Pedro

San Pedro Volcano (21°53'S, 68°24'W) is roughly 100 km south of Ollagüe and is the westernmost volcano of a short (<10 km) East – West trending volcanic chain which includes the heavily eroded San Pablo Volcano (**Fig. 2.8**) (Francis et al., 1974; O'Callaghan and Francis, 1986). Activity along this volcanic chain has migrated westward through time, beginning at San Pablo (Francis et al., 1974; O'Callaghan and Francis, 1986).

San Pedro itself is a compound volcano, comprising two cones [Old and Young; Francis et al. (1974)], with a summit altitude of 6,142 m (Global Volcanism Program, accessed 2019). The two cone units were first described by Francis et al. (1974), and a more detailed petrographic and geochemical study of these units was conducted by O'Callaghan and Francis (1986). The Old Cone unit comprises basaltic andesite lavas and scoriaceous flows, which have been heavily eroded by glacial action (O'Callaghan and Francis, 1986). The Young Cone unit has been separated into four lava suites



Figure 2.8. San Pedro stratovolcano. Filled star highlights the lava from which samples were collected. Base image from Google Earth (2019).

that are generally more evolved in composition than those of the Old Cone unit, comprising dominantly andesitic and dacitic lavas and pyroclastic flows, with a single basaltic andesite lava identified in one of the earlier lava suites (O’Callaghan and Francis, 1986). Additionally, O’Callaghan and Francis (1986) demonstrated that both the Old and Young Cone units were geochemically distinct from one another. Francis et al. (1977) postulated that the lavas of San Pedro had suffered minimal crustal contamination, based on Sr isotope systematics. Francis et al. (1977) suggested that San Pedro’s elevated Sr isotope ratio compared to stratovolcanoes in Ecuador, and their situation atop considerably thicker continental crust made it likely they had been crustally contaminated.

Prior to the onset of the construction of the Young Cone, San Pedro’s Old Cone summit suffered a major collapse, associated with a Plinian eruption, possibly

evidenced by a several hundred-meter-tall amphitheatre scarp (O’Callaghan and Francis, 1986). During the Young Cone phase, San Pedro experienced numerous pyroclastic events, which have been associated with each of the four suites of lavas of the Young Cone unit (Francis et al., 1974; O’Callaghan and Francis, 1986). Francis et al. (1974) described the most common of these as hot avalanche deposits, formed through the collapse of unstable, hot, thick (100 – 200 m), andesitic lava flows, high on the flanks of San Pedro.

2.4. Summary

Overall, this thesis focusses on a suite of volcanic rock samples from eight stratovolcanoes and several SECs along the Chilean segments of the Andean Volcanic Arc. With samples collected from edifices situated on varying crustal thicknesses (i.e., 25 to ≥ 70 km), questions regarding the role of crustal thickness on the behaviour of the chalcophile elements can be investigated (e.g., Lee et al., 2012; Chiaradia, 2014). Furthermore, the range in composition of the sample suites permits comparisons to be made between the processing of the chalcophile elements in more primitive and more evolved sample suites. The current project can also investigate the processing of the chalcophile elements between the more complex plumbing systems of stratovolcanoes and the generally ‘simpler’ plumbing system beneath SECs. Finally, the sample suites define both along and across-arc (i.e., Villarrica – Quetrupillán – Lanín) transects that can be utilised to explore potential variations in slab-derived fluxes.

Chapter 3

Sample descriptions

The volcanic rock samples presented in this thesis were collected by either the author, during a field expedition to southern and northern Chile in 2016 (Villarrica, Quetrupillán, Lanín, the Caburgua – Huelemolle Complex small eruptive centres, Huililco, Ollagüe, San Pedro and La Poruñita), or by the author's supervisor (Dr S. Watt), over the course of several field seasons to southern Chile during 2007, 2008 and 2013 (Yate, Apagado, Hornopirén and Antuco). Most samples were collected from separate lava or pyroclastic units, believed to represent separate eruptions (in most cases undated), and therefore discrete batches of magma. The following sections of this chapter briefly summarise the overall petrological characteristics of each sample set (excluding samples from the Caburgua – Huelemolle Complex and Huililco, as loose scoria samples were not made into thin sections). Petrological descriptions of individual samples, based on examination of thin sections, are provided in **Appendix A**.

3.1. Southern Volcanic Zone samples

3.1.1. Antuco²

The current study made use of twenty-six volcanic rock samples (fifteen Phase 1 and eleven Phase 2 samples; see **Chapter 5** for details on each phase), each from separate lava flows or pyroclastic units. The location of each sample is highlighted on the map of Antuco in **Fig. 2.3**. Petrographically, all samples have a porphyritic texture (**Fig. 3.1a,b**). The groundmass is generally cryptocrystalline (crystals too small to identify) and varies from light grey to dark in colour. Phenocryst phases are dominated by plagioclase (most common) and olivine, usually comprising c. 10 – 20 vol.% (all phenocrysts) of thin sections (minus vesicles; can be as great as c. 40 vol.% and as low as <<5 vol.%). Opaques and clinopyroxene phenocrysts are rare. Plagioclase phenocrysts are mostly subhedral to euhedral laths, and commonly display simple and albite twinning and oscillatory zoning. Coarse and fine sieve textured plagioclases are common across the samples. Olivine phenocrysts are usually anhedral (mostly rounded) and fractured. Glomerocrysts are observed in all sections and comprise plagioclase and/or olivine. Sample An28-6 shows extensive Fe-oxyhydroxide alteration in both phenocryst phases and groundmass.

3.1.2. Yate

Ten samples (nine lava, one fall deposit) from Yate were used in the current study, collected from the northern and southern flanks of the stratovolcano (sample locations are highlighted in **Fig. 2.5**). The samples obtained for Yate are previously unpublished and have not been previously analysed for the chalcophile elements.

²Petrographic descriptions of Antuco's samples are published in *Earth Planet. Sci. Lett.* (Cox et al., 2019).

Yate samples are porphyritic in nature, with phenocrysts set in light grey to dark, fine to cryptocrystalline or glassy groundmass (**Fig. 3.1c,d**). The groundmass components are usually indiscernible; however, some sections have plagioclase microlites, and/or opaques, olivine and clinopyroxene. Phenocrysts commonly comprise c. 15 to 20 vol.% of the sections, but can be as little as 10 vol.% or as large as 40%. Plagioclase (most common), olivine and clinopyroxene dominate the phenocryst assemblage; opaques, orthopyroxene and quartz are rare. Plagioclase phenocrysts are usually lath-like, square or triangular ['broken'(?)] in form, although partially complete crystals are also common (i.e., anhedral to euhedral). They are usually 1 to 2 mm in size, but range between <1 and 4 mm throughout the sections. Twinning, both simple and albite, and oscillatory zoning are common. Dissolution textures are not extensive throughout the Yate sample set. Where dissolution textures do occur, they are mostly concentrated along crystal edges or following oscillatory zones, with a limited number of crystals having heavily dissolved cores. Olivine phenocrysts are generally smaller (~1 mm) than the plagioclase phenocrysts and show a variety of forms, from rounded (anhedral) to elongate or prismatic (euhedral), although subhedral crystals are most common. Crystals are extensively fractured, with edges commonly showing minor alteration to clays. Across the sample set, the degree of crystal completeness varies, from minor embayments to highly skeletal. Clinopyroxene phenocrysts are usually subhedral and prismatic in form and ~1 mm in length, but can be as large as ~3 mm. Twinning (simple) and oscillatory zoning are often observed. Dissolution of crystal edges is fairly common. Glomerocrysts are common and can be either mono- or polymineralic. Polymineralic glomerocrysts can be as large as 6 mm across.

3.1.3. Hornopirén

One scoria and three lava samples were analysed in the current study, collected from the volcano's summit and surrounding region (**Fig. 2.5**), respectively. Again, the samples utilised are previously unpublished and have not been previously analysed for the chalcophile elements.

Lava samples 19-1A and 30-2A have a porphyritic texture, with a fine to cryptocrystalline groundmass dominated by plagioclase laths and minor olivine and orthopyroxene. Phenocryst phases comprise ~10 vol.% of the sections, with plagioclase and olivine in roughly equal proportions. Plagioclase phenocrysts are usually lath or square in form, up to 2 mm in length, with minimal alteration or dissolution. Simple and albite twinning and oscillatory zoning are common. Olivine phenocrysts are mostly anhedral (rounded) to subhedral and ≤ 1 mm in length. Olivine phenocrysts are commonly fractured and have minimal rim alteration. Vesicles comprise <5 vol. % of the sections.

Unlike the above samples, lava sample 15-5a is weakly porphyritic and almost equigranular in nature (**Fig. 3.1e,f**). The phenocryst phases (plagioclase, olivine and orthopyroxene) comprise ≤ 1 vol.% of the section, usually as glomerocrysts (≤ 1.5 mm in length). Plagioclase and olivine phenocrysts are as above. The groundmass (<1 mm in length) of the section is dominated by plagioclase laths (>90 vol.%) that display simple and albite twinning and oscillatory zoning. Minor anhedral olivine and tabular clinopyroxene crystals are present in the groundmass, both minimally altered.

3.1.4. Apagado

Eight lava samples from Apagado were analysed in the current study, which were collected from the caldera wall and regional lavas of the older volcanic edifice (i.e., stratovolcano), rather than the young scoria cone (**Fig. 2.5**). Given the deeply eroded nature of this structure, the samples are likely Pleistocene in age and may predate volcanism at Yate. As with Yate and Hornopirén, the samples are previously unpublished and have not been previously analysed for the chalcophile elements.

With the exception of sample 20-4A, which has an ophitic texture, most lava samples have a porphyritic texture, with a light grey to dark, fine to very fine groundmass. The groundmass is dominated by plagioclase laths, with varying amounts of olivine, clinopyroxene and opaques. Phenocryst phases either form 10 – 15 vol.% or <5 vol.% of the sections, and are commonly plagioclase (dominates) and olivine, with minor amounts of clinopyroxene (usually <1 vol.%). Plagioclase crystals display a range in form, usually from anhedral to subhedral, and include forms such as laths, prisms, and partial/'broken' crystals. Crystals are usually sub-mm to 2 mm in length, but can be as large as 2.5 – 3 mm, with plagioclase glomerocrysts being as large as 4 mm. Disequilibrium textures are common throughout all sections, and include simple and albite twinning, oscillatory zoning and crystal dissolution. The degree of crystal dissolution varies across the sections, but can also vary within sections. Crystals can display little to no evidence of dissolution, while others are heavily dissolved, usually at crystal cores or along crystal edges. Olivine phenocryst form varies from anhedral to euhedral and are commonly ≤ 1 mm across, although can be as large as 1.5 mm. Crystals are usually heavily fractured and sections generally lack skeletal olivine crystals; although some are observed across the sample set. Olivine crystals

commonly form glomerocrysts. Alteration to serpentinite(?) is common at crystal edges or along fractures. Clinopyroxene is a very minor phenocryst phase, although where present forms subhedral prisms or laths that are ≤ 1 mm. Twinning is not common across the sections, neither is crystal alteration. Although not extensive, fluid and/or melt inclusions are observed in each of the phenocryst phases across the sample suite.

3.1.5. Villarrica

Three samples were obtained from very well exposed lavas on the flank of Villarrica (**Fig 2.4**). These samples may be associated with the same eruption, as it was difficult to ascertain the boundaries of individual lava flows in the field, given the high frequency of eruptions at Villarrica and large number of young lava flows.

Samples from Villarrica have a porphyritic texture, with phenocrysts set in a dark, very fine to cryptocrystalline groundmass (**Fig. 3.1g,h**). In areas of the section where the groundmass is fine, plagioclase microlites can be identified. The phenocryst assemblages are dominated by plagioclase (most abundant) and olivine, comprising c. 20 – 30 vol.% of the section (excluding vesicles). Clinopyroxene and opaques are rare phases. Plagioclase phenocrysts are generally sub- to euhedral laths and commonly 1 to 2 mm in size; however, entire size range is from <1 to ~ 6 mm. Simple and albite twinning and oscillatory zoning are common throughout the sections. Dissolution textures are fairly common, generally focussed at crystal interiors, or following oscillatory zones. Some crystals lack dissolution textures, while within some it is pervasive. Plagioclase crystals can form glomerocrysts. Olivine phenocrysts display a variety of habits, from rounded, anhedral crystals to euhedral crystals, are usually ~ 1 mm across, but range from <1 to ~ 3 mm. Some crystals can show minor

degrees of skeletal. Olivine crystal glomerocrysts are infrequent, as are plagioclase – olivine glomerocrysts.

3.1.6. Quetrupillán

Five samples were collected from Quetrupillán, from well-exposed lavas high up on the flanks of the stratovolcano (**Fig. 2.4**).

The samples from Quetrupillán have a porphyritic texture, with the phenocryst assemblage set in a generally dark, very fine to cryptocrystalline groundmass. Plagioclase microlites show a rough alignment within the groundmass, possibly highlighting a flow texture(?). The phenocryst assemblage comprises plagioclase (most common), olivine and clinopyroxene, forming c. 10 – 15 vol.% of the sections. Plagioclase phenocrysts are mostly sub- to euhedral, lath-like in form, and are commonly 1 to 2 mm in length, but range in size from <1 mm to ~3 mm. Both simple and albite twinning and oscillatory zoning are common features of plagioclase crystals across the sections. Dissolution textures are observed in the crystals; however, the degree of dissolution varies from none to extensive in individual crystals. Dissolution textures can be concentrated at crystal cores, follow oscillatory zoning or are focussed along crystal edges. Olivine phenocrysts are generally anhedral in form, ≤1 mm across (can be as large as ~2 mm) and fractured. Crystals also show varying degrees of skeletal, from minor to heavily skeletal. Clinopyroxene phenocrysts are subhedral (can be euhedral), 1 to 2 mm in length and are commonly (simple) twinned. Crystals are rarely oscillatory zoned. Glomerocrysts are common and comprise plagioclase, clinopyroxene, or both.

3.1.7. Lanín

Five samples were collected from well-exposed lavas on the Chilean flank of the stratovolcano. Samples appear to be from individual lava flows, representing discrete magma batches (**Fig. 2.4**).

Samples from Lanín have a porphyritic texture, with a dark grey to black, cryptocrystalline to glassy groundmass. The total phenocryst volume of the thin sections varies from as little as c. 15%, to as great as c. 40%. The phenocryst assemblage is dominantly comprised of plagioclase (most common) and olivine, with rare clinopyroxene and opaques. Plagioclase phenocrysts have a mostly well-formed, euhedral lath-like form, display simple and albite twinning and oscillatory zoning, and range in size from <1 to ~2 mm. Dissolution texture is not commonly observed in the sections, but where present, is usually located at the centres of larger crystals that make up glomerocrysts. The form of olivine phenocrysts varies between sections, from small (<<1 mm), anhedral crystals to larger (≤ 1 to ~2 mm), euhedral crystals. Crystals are commonly heavily fractured. One sample (16DCLan.001) from Lanín appears heavily altered in thin section, with an apparent green overprint (clays?); the outline of plagioclase and potentially olivine phenocrysts set in a fine groundmass can be observed.

3.2. Central Volcanic Zone samples

3.2.1. Ollagüe

Ten samples were collected from either well exposed lavas or hummocks of the debris avalanche deposit (**Fig. 2.7**), formed during the ~300 ka collapse event (Clavero et al., 2004) of Ollagüe's western flank. Most of the hummock population (>75%) are composed of volcanic rock (Clavero et al., 2004). Samples collected from the debris

avalanche deposits (i.e., hummocky terrane) cannot be confidently attributed to individual eruptive events.

Ollagüe's samples have a porphyritic texture, with phenocrysts set in a grey to dark grey, fine to cryptocrystalline groundmass (**Fig. 3.1i,j**). In the more coarse areas of the groundmass, plagioclase laths and opaques can be vaguely discerned. The phenocryst assemblage of the Ollagüe samples commonly comprises c. 15 – 20 vol.% of the sections, and is generally dominated by plagioclase, amphibole (hornblende) and biotite. Phenocrysts of clinopyroxene and opaques are minor constituents. The form of plagioclase phenocrysts varies between lath-like, square and partially completed/'broken' crystals. Crystals are usually ~1 mm in size, with a total range of ~0.5 to 2 mm. Simple and albite twinning and oscillatory zoning are very common features of plagioclase crystals throughout all sections. Dissolution of plagioclase crystals is generally limited across the sections, but can be extensive within individual crystals when present. Amphibole phenocrysts vary from rounded, anhedral to prismatic or lozenge, euhedral crystals; with most having a subhedral form. Crystals are generally 0.5 to 1.5 mm in length, but can be as large as 3 mm. Oscillatory zoning is uncommon throughout the sections. The crystal edges of amphibole phenocrysts commonly have a dark, oxide rim, with the degree of internal crystal alteration varying from limited to extensive. Biotite phenocrysts are of tabular or lath-like form and usually ≤ 1 mm in length. Alteration of biotite phenocrysts is observed, commonly to chlorite(?), either along crystal edges or internally, although internal alteration is less common. 'Bird's eye texture' is rare. Glomerocrysts comprising plagioclase, amphibole, or both are observed throughout all sections.

3.2.2. La Poruñita

A single sample was collected from the flank of the small La Poruñita scoria cone (**Fig. 2.7**). No visible flow(s) or extensive deposits sourced from the cone were identified in the field. Vesicles are abundant in the section, comprising ≥ 60 vol.%. The groundmass between vesicles is fine to cryptocrystalline, comprising plagioclase and olivine crystals. Plagioclase crystals dominate the groundmass (>90 vol.%), are tabular in form, $<<1$ mm in length and commonly display simple twinning. Olivine crystals are much less abundant, $<<1$ mm in length and display a range of forms, from euhedral (diamonds) to rounded, anhedral crystals.

3.2.3. San Pedro

Three samples from a well-exposed, single lava flow of San Pedro were obtained for the current study (**Fig. 2.8**). This is supported by their very similar geochemical characteristics (**Chapter 6**). Access to the lava flow was challenging, with samples being taken in addition to the more substantial Ollagüe dataset.

Samples from San Pedro have a porphyritic texture, with their phenocrysts set in a light grey, very fine groundmass comprising plagioclase laths and opaques. The phenocryst assemblage accounts for c. 15 vol.% of the sections, and is predominantly composed of plagioclase and clinopyroxene crystals, although rare amphibole, orthopyroxene, biotite and opaques are observed. Plagioclase phenocrysts are lath-like or square in form, and range in size from <1 to ~ 2 mm. Simple and albite twins are common, as is oscillatory zoning. Dissolution of plagioclase crystals can vary from very minor to extensive. Clinopyroxene crystals are rounded to prismatic (anhedral to subhedral) in form, 1 to 1.5 mm in size and are commonly twinned. The clinopyroxene

phenocrysts are generally altered throughout the sections, with dissolution of crystal centres; some show exsolution lamellae.

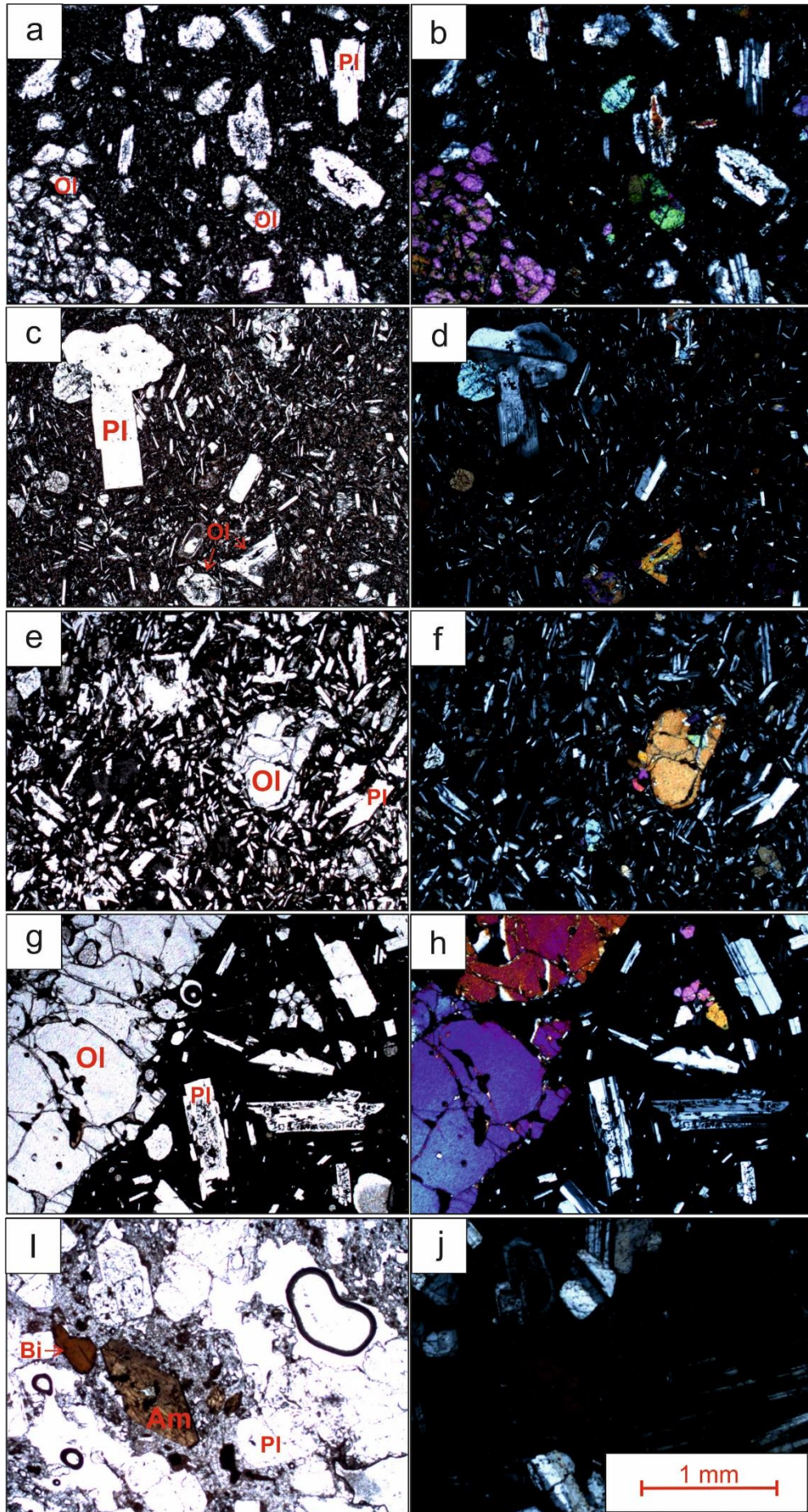
3.3. Petrographic summary

The reason for examining the petrography of the arc lavas is to ascertain whether samples represent typical arc magmas, or have been effected by complex magmatic processes during magma ascent and storage. Erupted arc magmas, including mafic through to felsic compositions, usually represent a hybrid of components of different ages and from various levels of a magma plumbing system, including amalgamations of crystal cargoes, assimilation or recycling of antecrysts and/or crustal material (i.e., xenocrysts) and mixing of other liquids (Davidson et al., 2005; Jackson et al., 2018). These components can alter the bulk composition of an arc magma, making erupted primary magmas in arc settings rare (Davidson et al., 2005). These processes are unavoidable, and thus the chalcophile element analyses presented here are unlikely to represent magmas evolving in a true closed system purely undergoing fractional crystallisation, but have likely been affected by mixing processes.

The petrography of the samples presented in this chapter are of standard arc composition and are similar to other volcanic edifices in Chile (e.g., Calbuco, Osorno, Llaima, Puyehue – Cordon Caulle); primarily comprising plagioclase, olivine and clinopyroxene phenocrysts (Gerlach et al., 1988; López-Escobar et al., 1992; Lopez-Escobar et al., 1995a; Bouvet de Maisonneuve et al., 2013). There is also little evidence of strong disequilibrium textures within the samples. The samples presented here appear to represent expected arc magma compositions, and therefore processes,

thus providing the best opportunity to investigate typical arc processing of the chalcophile elements.

Figure 3.1. Petrographic photomicrographs of select samples: Antuco (a,b), Yate (c,d), Hornopirén (e,f), Villarrica (g,h) and Ollagüe (i,j). Ol: olivine; Pl: plagioclase; Am: amphibole; Bi: biotite. Photomicrographs were taken using an AxioCam mounted on a Zeiss petrographic microscope.



Chapter 4

Method development: acquiring chalcophile element analyses through ICP-tandem mass spectrometry

4.1. Introduction

Geochemical data is an important tool used to investigate a myriad of processes in the Earth Sciences, including the genesis and subsequent evolution of ascending magmas across tectonic settings. Inductively coupled plasma optical emission spectrometry/mass spectrometry (ICP-OES/MS) and X-ray Fluorescence Spectrometry (XRF) are common analytical techniques employed by Earth Scientists to acquire such geochemical data, and each of these have been utilised over the course of the current project to acquire whole rock compositional data. This chapter covers the basic principles behind each of the above-mentioned analytical techniques, then discusses the analytical issues involved when analysing for the chalcophile elements, and the solutions that were adopted in the current project to overcome these issues. Finally, this chapter comments on the repeatability and accuracy of the analytical data acquired.

4.1.1. XRF analysis

XRF analysis, most commonly used to obtain major element analyses, involves exciting atoms of elements in unknown samples (glass beads or powdered pellets) by

exposing them to X-rays. The excitation of the samples results in the emission of secondary X-rays (X-ray fluorescence), with individual elements having characteristic wavelengths. The intensity of the emitted secondary X-rays can be translated into concentrations through reference to calibration standards [e.g., International Standard Reference Materials (ISRM)] (Rollinson, 1993).

4.1.2. ICP-OES analysis

During ICP-OES analysis, unknown sample solutions are introduced into the ICP torch as an aerosol, produced via a nebuliser. Within the ICP torch, a high-temperature (~10,000 K) Ar plasma is generated, which excites atoms (and ions) of elements within the sample. On returning to their lower energy state, the previously excited atoms emit energy in the way of photons (Hou and Jones, 2000). Each element has its own characteristic emission spectrum, which is measured in the spectrometer and translated into concentrations with reference to calibration standards (Rollinson, 1993).

4.1.3. ICP-MS and ICP-MS/MS analysis

4.1.3.1. ICP-MS analysis

ICP-MS analysis provides some of the lowest detection limits, on the order of parts per billion/trillion (ppb/t). An ICP-MS can thus be used to accurately analyse for a greater number of elements constituting the Periodic Table than ICP-OES. As in ICP-OES analysis, unknown sample solutions are introduced into the ICP torch as an aerosol during ICP-MS analysis. Within the ICP torch, the generated Ar plasma ionises atoms of the elements in the samples, converting them into positive ions (X^+ or X^{2+} , where X represents an element). These positive ions are then introduced into the mass spectrometer through small holes (~1 mm) in interface cones (located between the ICP

torch and mass spectrometer). Within the mass spectrometer, these positive ions are separated according to their mass-to-charge ratio (m/z). A detector, placed at the end of the mass spectrometer, detects ions of specific m/z (as instructed by a programmer), and using calibration standards, converts these signals into concentrations of a specific element (Rollinson, 1993).

As mentioned previously (**Chapter 1**), the chalcophile elements (**Fig. 1.1**) are an important suite of elements because of their economic value (Sillitoe, 2010; Kiseeva et al., 2017) and use as geochemical tracers of magmatic processes (Noll Jr et al., 1996; Jenner et al., 2010; Lee et al., 2012; Jenner, 2017). Despite their importance, the chalcophile elements are often not measured in published whole rock compositional analyses. This is because their very low concentrations (ppb) in igneous rocks, numerous mass interferences (May and Wiedmeyer, 1998; Sugiyama and Shikamori, 2015; Bolea-Fernandez et al., 2017) and a lack of accurate ISRM values (Jenner and Arevalo, 2016; Jochum et al., 2016), all of which make their analysis challenging.

ICP-MS is perhaps the most common analytical technique employed by Earth Scientists to analyse trace element abundances (such as the chalcophile elements) in geological materials (Balcaen et al., 2015; Bolea-Fernandez et al., 2017). However, solution ICP-MS analysis has several complications that need to be overcome in order to acquire accurate analyses. These include incomplete sample digestion (e.g., acid resistant zircon crystals) and interferences (i.e., mass interferences, instrument drift) that reduce or enhance the apparent signal of a target analyte (Evans and Giglio, 1993; Dams et al., 1995; Chen et al., 2017).

Instrument drift is common in ICP analysis, which sometimes needs to be corrected for prior to data interpretation (Salit and Turk, 1998; Chen et al., 2017; Evans et al., 2017). There are many causes of drift (e.g., deposits, temperature control), that can result in reduced instrument sensitivity and detection limits. During an analytical run, a way of monitoring instrument drift is through the use of monitors/monitor blocks (Salit and Turk, 1998; Chen et al., 2017). These monitors are usually ISRM solutions that are analysed after a set number of unknown samples (approximately five). This way the variation in instrument sensitivity to an analyte can be tracked throughout an analytical cycle.

Arguably, the most important of the complications during ICP-MS analysis are mass interferences (May and Wiedmeyer, 1998; Balcaen et al., 2015; Bolea-Fernandez et al., 2017). Mass interferences enhance the signal of a target analyte, by incorporating the signal of other ions, be it atomic or molecular, that have the same m/z as the target analyte; these interferences are termed either isobaric (atomic ions) or polyatomic (molecular ions) (Evans and Giglio, 1993; Dams et al., 1995; May and Wiedmeyer, 1998). Isobaric interferences are the result of isotopes of different elements (including doubly charged ions) with the same m/z as the analyte, whereas polyatomic interferences are the combination of \geq two isotopes of different elements (such as oxides or argides), again resulting in the same m/z as the analyte (Evans and Giglio, 1993; Dams et al., 1995; May and Wiedmeyer, 1998).

The chalcophile elements have abundant possible mass interferences during analysis; for non-exhaustive lists on these interferences see Table 1 of May and Wiedmeyer (1998) and Table 2 of Bolea-Fernandez et al. (2017). Of the chalcophile element suite, arguably the most challenging interference to remove (and the

interference that proved to be the most issue during the current project) is that of ZrO ($^{91}\text{Zr}^{16}\text{O}^+$ and $^{90}\text{Zr}^{17}\text{O}^+$) on Ag ($^{107}\text{Ag}^+$). Both $^{91}\text{Zr}^{16}\text{O}^+$ and $^{90}\text{Zr}^{17}\text{O}^+$ have the same m/z as $^{107}\text{Ag}^+$ and so 'pretend' to be $^{107}\text{Ag}^+$ during analysis. This results in an overestimation of the Ag concentration, due to the incorporation of the ZrO signal during Ag analysis. Understanding and removing this interference is an important step in understanding the processing of Ag during magmatic differentiation, as highlighted in Fig. 3 of Jenner and Arevalo (2016). Jenner and Arevalo (2016) showed that an overestimation of Ag contents in evolved back arc basin glasses could lead to a false interpretation of whether a melt is sulfide (under-) saturated, and therefore potentially result in misleading interpretations of the distribution of the chalcophile elements.

4.1.3.2. ICP-MS/MS

The latest advancement in ICP-MS technology was the release of the ICP-tandem mass spectrometer by Agilent Technologies, in 2012. Compared to the more traditional ICP-MS machine, where a collision and reaction cell (CRC) is located before a quadrupole mass analyser, the new ICP-tandem mass spectrometer machine incorporates an additional quadrupole mass analyser located before the CRC. Hence, the new configuration includes two independently controlled quadrupole mass analysers in series, either side of a CRC (**Fig. 4.1**) (Sugiyama and Shikamori, 2015; Bolea-Fernandez et al., 2017). These machines are commonly referred to as either ICP-MS/MS or ICP-QQQ. The ability to independently control each quadrupole mass analyser allows for further control on the m/z of ions that enter into the CRC, reducing the overall total number of ions entering the CRC to only the target analyte ion(s) and any interfering ion(s) (Balcaen et al., 2015; Bolea-Fernandez et al., 2017). This way, the collisions and reactions ongoing in the CRC can be better controlled, and mass

interferences on the target analyte ions can be more effectively removed (Balcaen et al., 2015; Sugiyama and Shikamori, 2015).

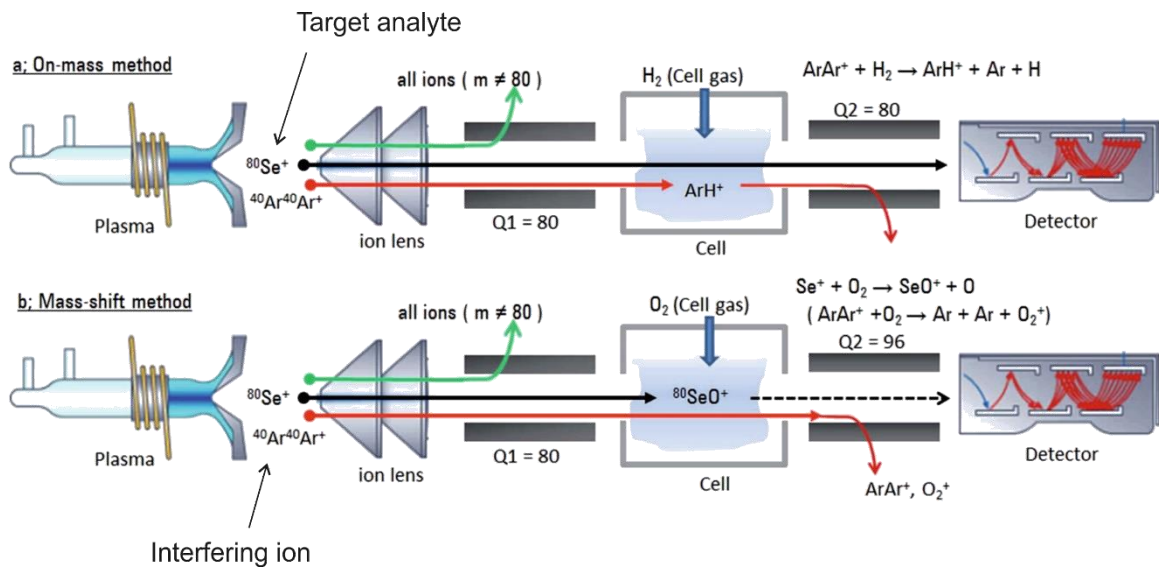


Fig. 4.1. Schematic profile highlighting the difference between, a) on-mass, and b) mass-shift methods of analysis using an ICP-tandem mass spectrometer (ICP-MS/MS, ICP-QQQ). In this example, $^{80}\text{Se}^+$ represents the target analyte. During the on-mass method, the mass of the target analyte ion remains unaltered ($m = 80$), whereas during the mass-shift method, the mass of the target analyte ion is shifted (from $m = 80$ to $m = 96$) by reaction with O_2 in the collision and reaction cell (Cell). Figure adapted from Sugiyama and Shikamori (2015).

With the exception of the analysis of monoisotopic elements, some of these mass interferences can be routinely measured by simply choosing a mass of a given element that has an inconsequential interference, or by measuring an interference rate, such as the $^{91}\text{Zr}^{16}\text{O}$ production rate, and removing the interference from the measured signal, in this case ^{107}Ag (Jenner and O'Neill, 2012b; Jenner and Arevalo, 2016). Alternatively, interferences can be removed in the CRC through either collision with a non-reactive gas (e.g., He), or by reacting away the interfering ions using reactive gases (e.g., He, NH_3 , O_2) during analysis (Balcaen et al., 2015). A good indication that an interference has been removed, or is inconsequential, is elemental concentrations being roughly equal between analyses in different gas modes.

Two methods of analysis can be conducted to more effectively remove mass interferences: either on-mass or mass-shift analysis (**Fig. 4.1**). During the on-mass method of analysis, both quadrupole mass analysers are set to select the same m/z (**Fig. 4.1a**). As such, the first quadrupole (Q1) selects only the target analyte ion and any interfering ions of the same m/z . This way, all other ions are removed. In order to isolate the target analyte ion to pass through the second quadrupole (Q2) and to the detector, any interfering ions present can be reacted to a different m/z in the CRC using the various gas modes (e.g., O_2 , He, NH_3), leaving only the target analyte ion on the mass selected.

Alternatively, the mass-shift method of analysis has the quadrupole mass analysers set to select different m/z (**Fig. 4.1b**). Again, like in the on-mass method, the first quadrupole selects only the target analyte ion and any interfering ions of the same m/z . Then, in contrast with the on-mass method of analysis, where the interfering ions are reacted to different m/z , the mass-shift method reacts the target analyte ion with

the CRC gas to change its m/z . As such, the second quadrupole is set to select the new m/z of the target analyte ion.

4.2. Analytical methods

This section outlines the analytical techniques employed in obtaining whole rock major and trace element analyses during the current project. For the complete set of raw sample analyses, see **Appendix B**.

Major and trace element analyses for all samples presented in this thesis were obtained through whole rock analysis. Prior to analysis, samples were hammered and sawn to remove weathered material. Furthermore, to avoid metal contamination, the use of a jaw crusher was avoided. As an alternative, samples were crushed and powdered using a fly press and agate planetary ball mill, respectively. The loss on ignition (LOI) of the samples was determined by baking $\sim 1.5 \pm 0.0001$ g of sample powder at 900°C in a furnace for 2 hours. Further details on rock preparatory techniques are provided in **Appendix C**.

4.2.1. ICP-OES and MS analysis, Cardiff University

Rock powder fusion of samples from Villarrica, Quetrupillán, Lanín, Yate, Hornopirén, Apagado, and select samples from Antuco, was undertaken using a Claisse Fluxy fusion system at Cardiff University. 100 mg of sample powder was fused with 600 mg of flux (lithium borate) and lithium iodide wetting agent, and subsequently dissolved in HNO_3 . A 1 ml Rh spike (of 100 ppm Rh stock solution) was added to each sample solution. Solutions were made up to 1,000-fold dilutions of the original sample powder mass using MQ H_2O , prior to analysis. Full details of the rock powder fusion process are provided in **Appendix C**.

Sample solutions were analysed for their major and trace elements (excluding Ge, As, Tl, Se, Ag, Bi, W, Mo, S, Ru, Sn and Sb) via solution ICP-OES/MS at the School of Earth and Ocean Sciences, Cardiff University, U.K. Iain McDonald, following the methods of McDonald and Viljoen (2006), undertook analysis of the sample solutions.

4.2.2. XRF analysis

Alternatively, samples from Ollagüe, San Pedro and La Poruñita (obtained later in the project) were analysed for major elements via XRF at the School of Geography, Geology and the Environment, University of Leicester, U.K. In addition, some pre-existing, unpublished XRF data was made available (courtesy of Dr S. Watt) for Antuco, Yate, Apagado and Hornopirén. The current study obtained replicate XRF analyses for selected Antuco, Yate, Apagado and Hornopirén samples from The School of Geosciences, University of Edinburgh, U.K. to further test analytical precision and reproducibility.

For analysis at the University of Leicester, ignited samples powders were fused with a Li (meta-/tetra-) borate flux, in a powder – flux ratio of 1:5, to generate glass beads. Fusion was undertaken using platinum crucibles and moulds on a Fluxana Vitriox gas bead maker. The samples were subsequently analysed for major elements using a PANalytical Axios Advanced XRF spectrometer at the Department of Geology, University of Leicester, U.K.

For analysis at the University of Edinburgh, fused glass discs were prepared by mixing ignited sample powders with a Li borate flux (Spectroflux), in a powder – flux ratio of 1:5, and fusing at 1,100°C in a muffle furnace for 20 minutes. Glass beads were

again fused over a meker burner, and the resultant glass poured onto a graphite plate to form a glass disc via compression using an aluminium plunger; completed on a hotplate at 220°C. Samples were subsequently analysed for major elements using a Philips PW2404 wavelength dispersive sequential X-ray spectrometer fitted with a Rh anode end window X-ray tube.

4.2.3. ICP-MS/MS analysis, Open University

Acid digestion of all sample powders was undertaken at the Open University. 100 mg of sample powder was digested in Perfluoroalkoxy (PFA) vials, following a multi-stage HF – HNO₃ digestion process, with interval dry down temperatures of 65°C to minimise volatile element loss. Subsequent solutions were made up to 1,000-fold dilutions of the original sample powder mass with a 2% HNO₃ solution, preceding analysis. Prior to the acid digestion process, it is important that sample powders are very fine to make sure all phases, including acid-resistant zircons, will be digested. Blanks and ISRM were prepared in the same manner. Full details of the multi-stage acid digestion process are provided in **Appendix C**.

The trace element contents (except Tm) of all samples were analysed using the Agilent 8800 Triple Quadrupole ICP-MS (Mass Spectrometry) at The School of Environment, Earth and Ecosystem Sciences, Open University, U.K. Samples were analysed across separate batches, between 2017 and 2019. Because ICP-MS/MS is still in its infancy, the gas mode in which an element was analysed and whether an element was measured using the on-mass or mass-shift method of analysis was refined during this period, therefore they were not consistent across analytical batches. However, this is not a concern, as the production of mass interferences can vary between each analytical run, as can the accuracy of a given gas mode. Hence, the

data obtained using each of the different gas modes for a given element were examined thoroughly to determine the best gas mode for an element for each batch of analyses [i.e., if three different gas modes give the same concentration data for a given element, the analysis with the lowest relative standard deviation (RSD) during analyses was chosen]. For a complete list of the gas modes under which elements were analysed during each session, see **Appendix C**. It must be noted that across all batches, Ag was analysed in a reactive NH₃ gas mode, and an offline correction was subsequently made to remove the ZrO interference (see below).

An online standard (containing Be, Bi, Rh, In and Tm) was analysed alongside unknown samples and ISRM and was used to monitor and correct for instrument drift. ISRM BHVO-2 and an unknown sample from each respective batch were consistently used as monitor blocks to track instrument drift. Additionally, each monitor block contained a measurement of pure 2% HNO₃ to monitor background build-up. Only the Rare Earth Elements (REE) were consistently drift corrected across all batches. This is because in order to drift correct an element, both the unknown and BHVO-2 monitors must drift consistently; that is, either increase or decrease in concentration with continued analysis. This was not the case for most elements across all analysed batches.

Thulium analyses were not obtained for Ollagüe and San Pedro, as their samples were solely analysed at the Open University, where the online standard used during trace element analysis contains Tm.

4.2.4. Data accuracy

Data accuracy was assessed using an extensive range of internal laboratory standards, repeat analyses and ISRM standards at all analytical stages throughout the duration of the project; the full list of which can be found in **Table 4.1** and **Appendix D**. Major and trace element analyses of the ISRM standards fell mostly within 5% of published values for all datasets. Additionally, the R^2 values of the major and trace element analyses were all better than 0.9994 (**Figs. 4.2** and **4.3**).

For ICP-MS/MS analysis at the Open University, data accuracy and precision was assessed by repeat analyses of ISRM BHVO-2 (used as a monitor). In **Table 4.1**, the average of the measured values for each of the four analytical sessions is given, together with the RSDs and a comparison over the preferred values. Subsequently, **Fig. 4.4** presents the accuracy of each element of the four analytical sessions. Accuracy is mostly better than 7%. For the elements that display greater variability, such as Mo, W, Tl and Pb, heterogeneities for BHVO-2 have been reported (Willbold and Elliott, 2017; Brett et al., 2018; Kurzweil et al., 2018). However, for elements such as Ge, As and Sb, reference values are not well characterised [e.g., Jochum et al. (2016); also see GeoRem database] and thus leads to less accurate results.

The apparent inaccuracy of some measurements of the elements listed above may in some cases reflect the accuracy of the ISRM values and/or inhomogeneity of reference powders, rather than the accuracy of the absolute values measured in this project. ISRM values for several of the chalcophile elements are not provided for some ISRM standards, and even when they are, may not be as well constrained as other trace elements (Jenner and Arevalo, 2016). For example, the As values for ISRM BHVO-2 have only been determined through a single analytical technique (Jochum et al., 2016).

Chapter 4. Method development: acquiring chalcophile element analyses through ICP-tandem mass spectrometry

Table 4.1. Average elemental concentrations of the BHVO-2 monitor analyses for the four sessions over which data was obtained for the current project

Element	PV: BHVO-2 (OU)	Session: August '17			Session: January '18 (1)			Session: January '18 (2)			Session: December '18		
		Average	RSD	Avg./PV	Average	RSD	Avg./PV	Average	RSD	Avg./PV	Average	RSD	Avg./PV
Li	4.500	4.39	2.83	1.02	4.67	1.50	0.96	4.79	0.64	0.94	4.77	1.63	0.94
S	164.000	172.31	0.86	0.95	169.31	1.66	0.97	170.37	1.04	0.96	171.51	1.28	0.96
Sc	31.830	30.85	1.58	1.03	32.42	1.08	0.98	33.57	3.72	0.95	32.93	1.65	0.97
V	318.200	321.61	1.48	0.99	327.85	0.69	0.97	319.74	1.31	1.00	333.48	0.47	0.95
Cr	287.200	287.59	1.12	1.00	297.86	1.65	0.96	287.59	1.64	1.00	299.97	0.59	0.96
Co	44.890	44.68	0.68	1.00	46.37	1.47	0.97	43.44	1.13	1.03	44.45	1.81	1.01
Ni	119.800	118.66	1.52	1.01	118.66	1.13	1.01	116.92	0.61	1.02	117.70	1.58	1.02
Cu	129.300	129.80	0.60	1.00	136.25	0.63	0.95	128.15	1.19	1.01	134.90	0.87	0.96
Zn	103.900	102.87	0.81	1.01	104.11	0.85	1.00	103.71	1.08	1.00	105.12	0.44	0.99
Ga	21.370	20.77	0.78	1.03	21.45	0.77	1.00	21.46	1.71	1.00	21.46	1.41	1.00
Ge	1.623	1.74	1.51	0.93	-	-	-	-	-	-	-	-	-
As	0.540	0.35	5.02	<u>1.54</u>	0.65	4.98	<u>0.83</u>	0.66	2.98	<u>0.82</u>	0.47	2.38	<u>1.14</u>
Se	0.169	-	-	-	0.16	8.12	1.07	0.16	5.57	1.08	0.16	3.64	1.05
Rb	9.261	9.10	1.45	1.02	8.85	0.87	1.05	9.32	0.26	0.99	9.72	1.13	0.95
Sr	394.100	393.36	1.72	1.00	399.52	0.68	0.99	401.40	1.86	0.98	397.51	0.35	0.99
Y	28.000	26.66	0.55	1.05	26.74	0.49	1.05	27.21	1.87	1.03	28.44	1.79	0.98
Zr	171.200	171.10	0.58	1.00	175.38	0.66	0.98	175.78	2.09	0.97	178.84	0.26	0.96
Nb	18.100	18.65	1.65	0.97	18.19	0.70	0.99	18.39	2.41	0.98	18.11	1.35	1.00
Mo	4.070	3.87	2.85	1.05	5.12	1.66	<u>0.79</u>	5.05	2.14	<u>0.81</u>	4.53	1.12	<u>0.90</u>
Ag	0.031	-	-	-	0.03	6.02	1.06	0.03	4.38	1.03	0.03	2.34	0.92
Cd	0.093	-	-	-	-	-	-	-	-	-	0.08	6.16	<u>1.12</u>
Sn	2.020	2.26	0.45	<u>0.89</u>	1.88	1.19	1.07	1.83	1.38	<u>1.10</u>	1.94	1.46	1.04

Chapter 4. Method development: acquiring chalcophile element analyses through ICP-tandem mass spectrometry

Table 4.1. continued

Sb	0.103	0.12	2.73	<u>0.84</u>	0.08	1.20	<u>1.25</u>	0.08	1.97	<u>1.23</u>	0.11	1.80	0.95
Cs	0.100	0.10	2.74	0.98	-	-	-	-	-	-	0.10	0.33	0.97
Ba	133.000	129.99	1.27	1.02	-	-	-	-	-	-	128.63	1.74	1.03
La	15.200	15.44	0.89	0.98	15.84	0.34	0.96	15.48	0.67	0.98	15.88	1.35	0.96
Ce	37.530	37.54	0.66	1.00	38.56	0.33	0.97	37.21	0.41	1.01	38.50	1.16	0.97
Pr	5.339	5.12	0.43	1.04	5.23	0.12	1.02	5.11	0.56	1.04	5.24	1.12	1.02
Nd	24.270	23.65	0.25	1.03	23.62	0.18	1.03	23.66	1.19	1.03	23.58	0.97	1.03
Sm	6.023	6.09	0.32	0.99	6.31	1.86	0.95	6.21	1.35	0.97	6.21	1.05	0.97
Eu	2.043	2.05	1.04	1.00	2.08	1.69	0.98	2.04	0.75	1.00	2.10	1.13	0.97
Gd	6.207	6.21	0.59	1.00	6.48	1.66	0.96	6.32	0.73	0.98	6.33	0.40	0.98
Tb	0.939	0.97	0.22	0.97	0.99	1.78	0.95	0.99	1.96	0.94	0.97	0.53	0.97
Dy	5.280	5.31	0.29	0.99	5.35	0.69	0.99	5.33	0.51	0.99	5.37	0.80	0.98
Ho	0.989	1.03	0.70	0.96	1.02	1.37	0.97	1.02	1.72	0.97	1.01	1.11	0.98
Er	2.511	2.57	0.66	0.98	2.63	1.11	0.96	2.62	1.62	0.96	2.59	1.05	0.97
Yb	1.994	2.02	0.81	0.99	1.90	1.17	1.05	2.06	3.24	0.97	2.06	3.40	0.97
Lu	0.275	0.28	0.46	0.97	0.28	1.83	0.99	0.28	1.45	0.98	0.28	1.11	1.00
Hf	4.470	4.43	0.76	1.01	4.43	1.02	1.01	4.34	0.70	1.03	4.37	0.69	1.02
Ta	1.154	1.13	1.05	1.02	1.27	2.93	0.91	1.03	0.92	<u>1.12</u>	1.14	1.00	1.01
W	0.227	0.33	6.88	<u>0.70</u>	0.30	9.36	<u>0.75</u>	0.22	1.70	1.02	0.20	0.86	<u>1.11</u>
Tl	0.022	0.02	1.90	1.03	0.02	2.84	1.06	0.02	4.39	<u>1.14</u>	0.02	2.38	1.06
Pb	1.653	1.47	0.55	<u>1.12</u>	1.44	0.80	<u>1.15</u>	1.45	0.37	<u>1.14</u>	1.53	0.99	1.08
Th	1.224	1.19	0.61	1.02	-	-	-	-	-	-	1.19	0.75	1.03
U	0.412	0.42	0.82	0.99	-	-	-	-	-	-	0.42	1.02	0.98

Analyses underlined are those anomalous to the preferred values of the International Standard Reference Material BHVO-2. PV: preferred value from the Open University (OU) laboratory; Avg.: average

Chapter 4. Method development: acquiring chalcophile element analyses through ICP-tandem mass spectrometry

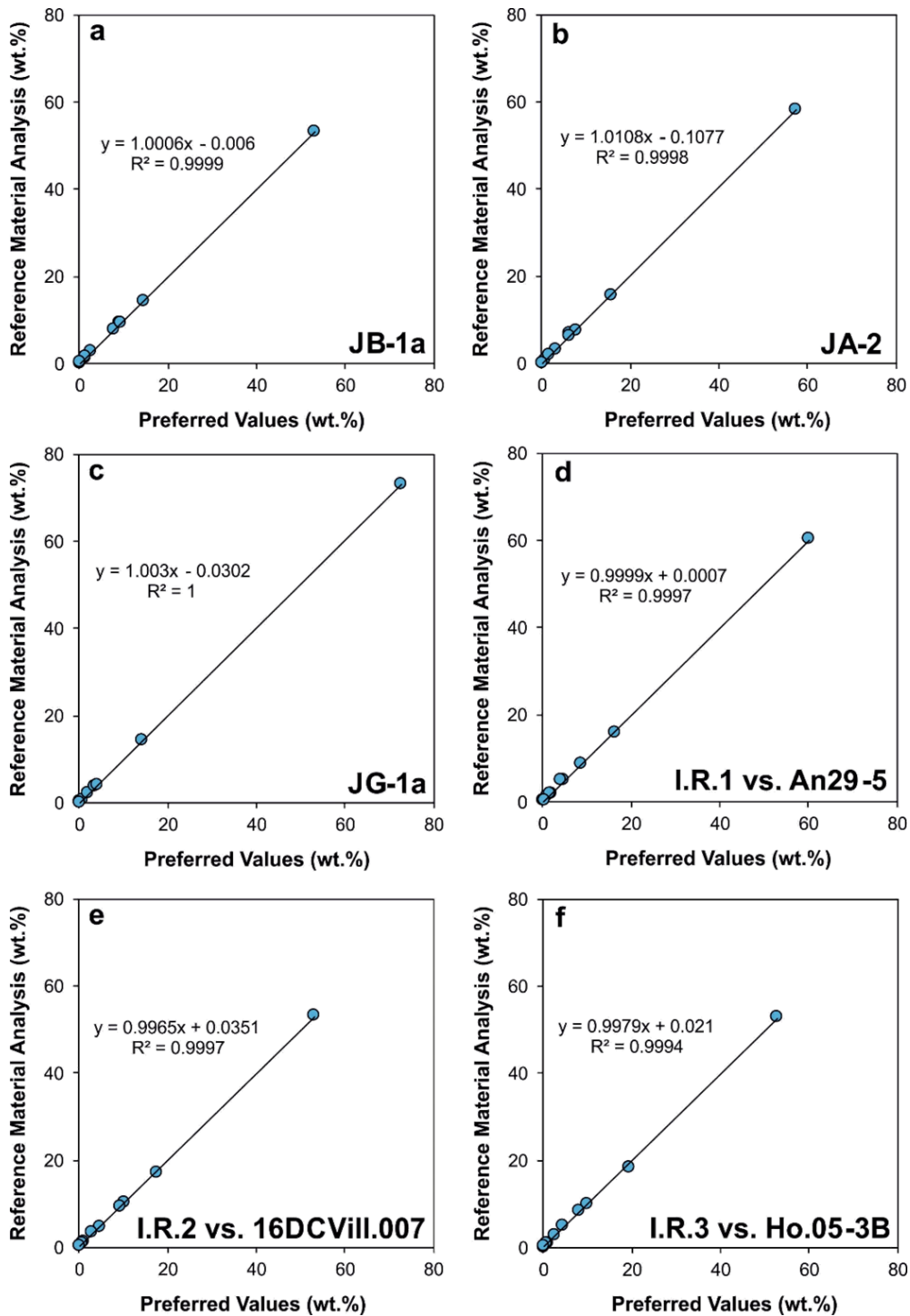


Fig. 4.2. Bivariate plots assessing the accuracy of analyses of, (a – c) International Standard Reference Materials (ISRM) JB-1a, JA-2 and JG-1a, and (d – f) Internal Repeat analyses (I.R. 1 – 3) acquired through ICP-OES at Cardiff University, in 2017. Preferred values for ISRMs JB-1a, JA-2 and JG-1a sourced from Govindaraju (1994). Samples acting as Internal References were chosen at random. All analyses show consistent results, with R^2 values ≥ 0.9994 .

Chapter 4. Method development: acquiring chalcophile element analyses through ICP-tandem mass spectrometry

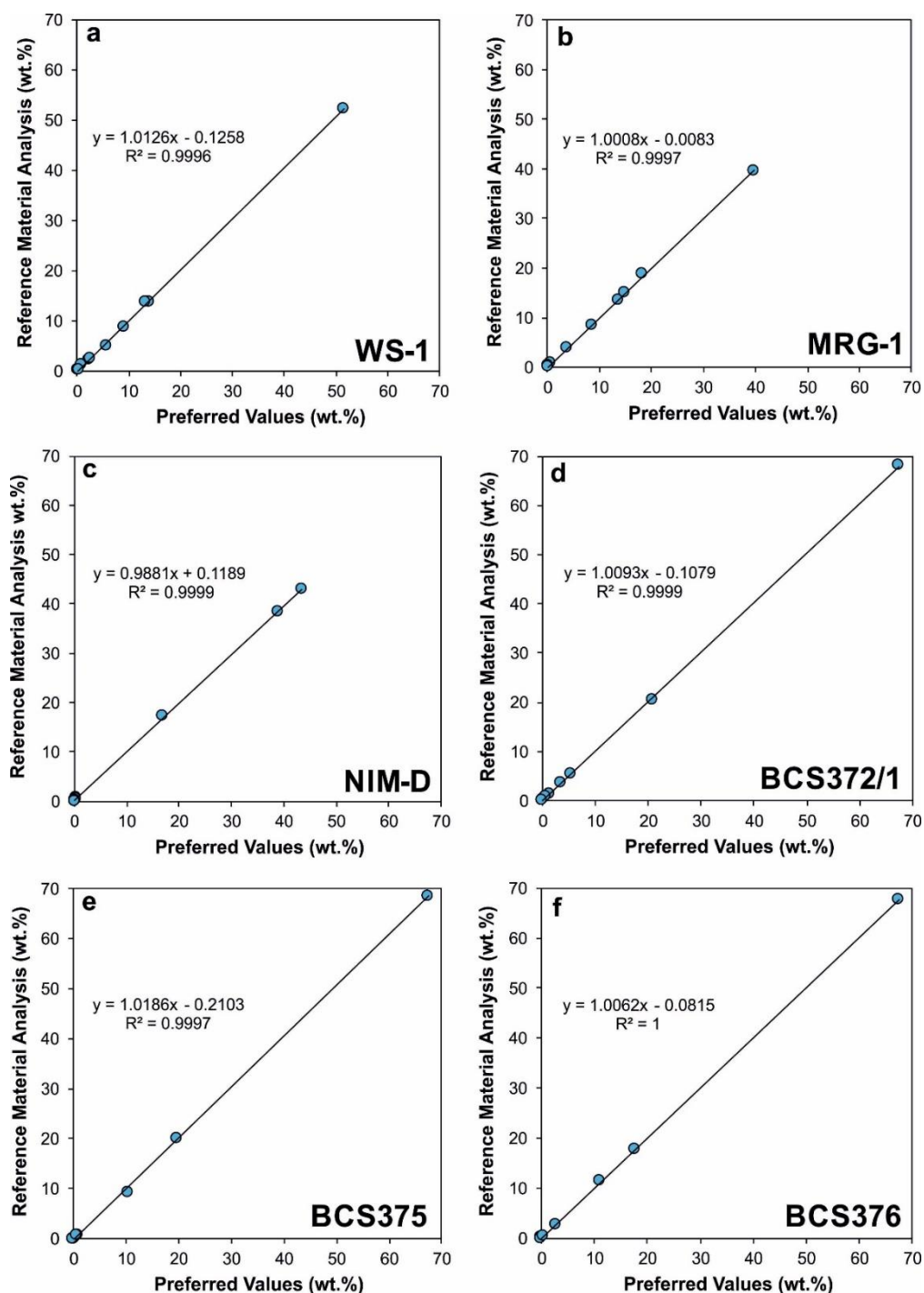


Fig. 4.3. Bivariate plots assessing the accuracy of International Standard Reference Material (WS-1, MRG-1, NIM-D, BCS372/1, BCS375, BCS376) analyses acquired through XRF analysis at the University of Leicester, in 2018. Preferred values sourced from GeoReM (georem.mpch-mainz.gwdg.de). All analyses show consistent results, with R^2 values ≥ 0.9996 .

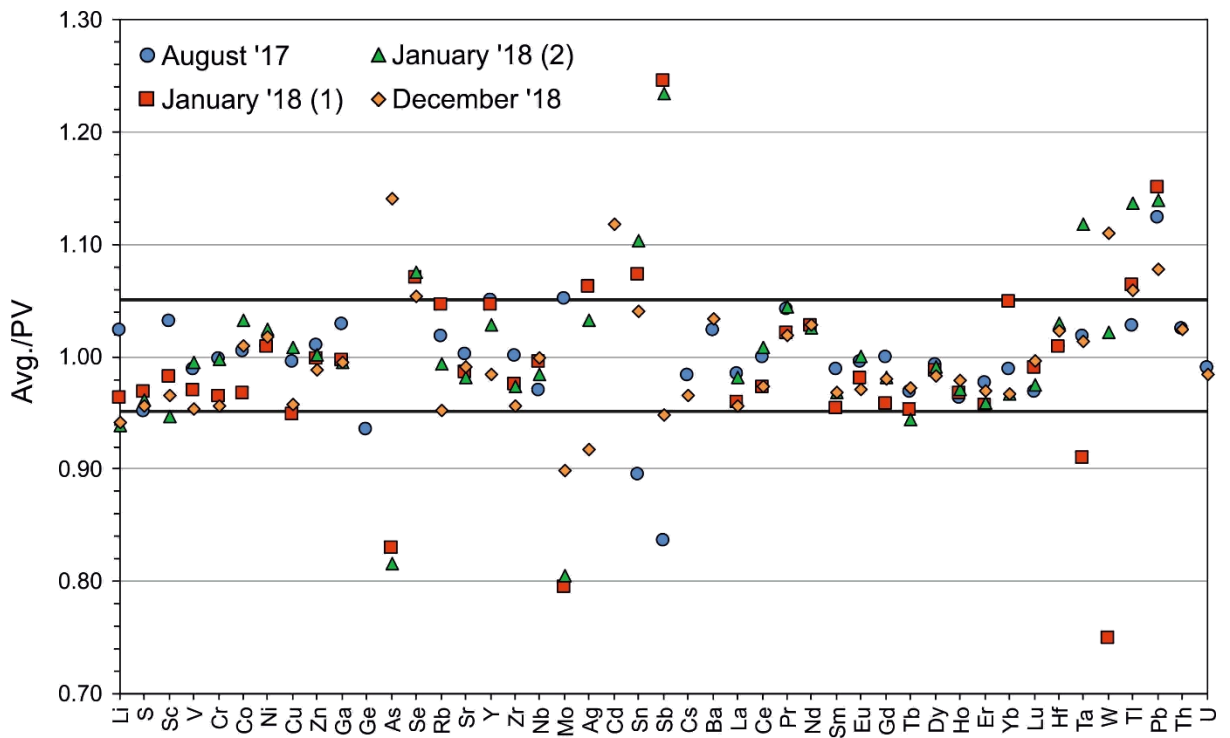


Fig. 4.4. Multi-element plot presenting the accuracy of averaged analyses of each element of the BHVO-2 monitor for each analytical session. Accuracy is mostly better than 7%. Avg.: average; PV: preferred values for BHVO-2 from the Open University; January '18 (1/2): refers to two separate sessions of analyses during January 2018.

4.2.4.1. Silver (Ag) standard addition method and subsequent offline ZrO interference correction

Silver presented a particular analytical challenge during the current project, because no suitable published Ag values exist for the ISRM samples analysed alongside these sample batches. As a result, the Ag contents determined in this project were defined using a calibration line through standard addition methods.

To undertake the standard addition method, 100 µl aliquots of specific Ag concentrations (2.5, 7.5 and 17.5 ng/g Ag solution and 2% HNO₃) were used to spike ~5 ml of selected ISRM samples (BHVO-2, BCR-2 and RGM-1). The concentrations of these solutions were calculated based on estimates, made from referring to the literature, of expected Ag contents of the unknown samples. An average of 50 ppb Ag in the 'rock' was consequently used to make these calculations. The new ZrO corrected Ag concentrations for the ISRM samples are given in **Table 4.2**. Within error, these values have since been reproduced (Kunz, 2019).

Table 4.2. Ag values for International Standard Reference Materials determined through standard addition methods

ISRM	Ag value (ppb)
BHVO-2	29.07
BIR-1	31.38
W-2	31.97
BE-N (OU)	5.63
AGV-1	44.99

ISRM: International Standard Reference Material; OU: Open University ISRM

Silver was measured in reaction mode with NH_3 as the reaction gas. However, this does not fully remove the ZrO interference, thus requiring an additional offline correction. This correction was made using a set of pure Zr standard solutions with increasing concentrations (2% HNO_3 and 25, 75, 100 and 150 ppb Zr). The production rate of ZrO on the Ag signal was calculated using the slope and y-intercept of a best-fit line calculated on the Zr standard solutions. Due to the linear nature of the ZrO production, the production rate could be used to calculate the ZrO contribution on the Ag signal depending on the Zr concentration for each analysis. The actual Ag concentration was subsequently determined by subtracting the calculated ZrO contribution from the Ag signal.

4.2.4.2. Further assessment of data repeatability

To further assess the repeatability of analyses, the major element composition of pre-existing XRF analyses of samples from Antuco, Yate, Apagado and Hornopirén were compared to those obtained through ICP-OES analysis in the current project. Repeat analyses of five samples from Antuco (An27-1, 27-8, 27-10, 28-1 and 28-9) were within 5% of each other for all major elements, with all R^2 values being ≥ 0.9998 (**Fig. 4.5**). On comparing repeat analyses of samples from Yate, Apagado and Hornopirén, the major element compositions were also mostly within 5% of each other, with all analyses having R^2 values of ≥ 0.9975 (**Fig. 4.6**). Therefore, where available, pre-existing XRF major element compositions were used.

Additionally, a combination of ten samples from Yate, Apagado, Hornopirén and Antuco were analysed for major elements by XRF at The School of Geosciences, University of Edinburgh, U.K., in 2017, again to assess the accuracy (repeatability) of the previously obtained data sets. ISRM samples used included JA-2, JR-1 and BHVO-1, with

major element analyses being mostly within 5% of preferred values [as provided by Govindaraju (1994)] and having R^2 values of ≥ 0.9998 on bivariate plots (**Fig. 4.7**). Comparing these XRF analyses with those obtained by ICP-OES at Cardiff University (in 2017), demonstrate the major elements to be mostly within 5% of each other.

Chapter 4. Method development: acquiring chalcophile element analyses through ICP-tandem mass spectrometry

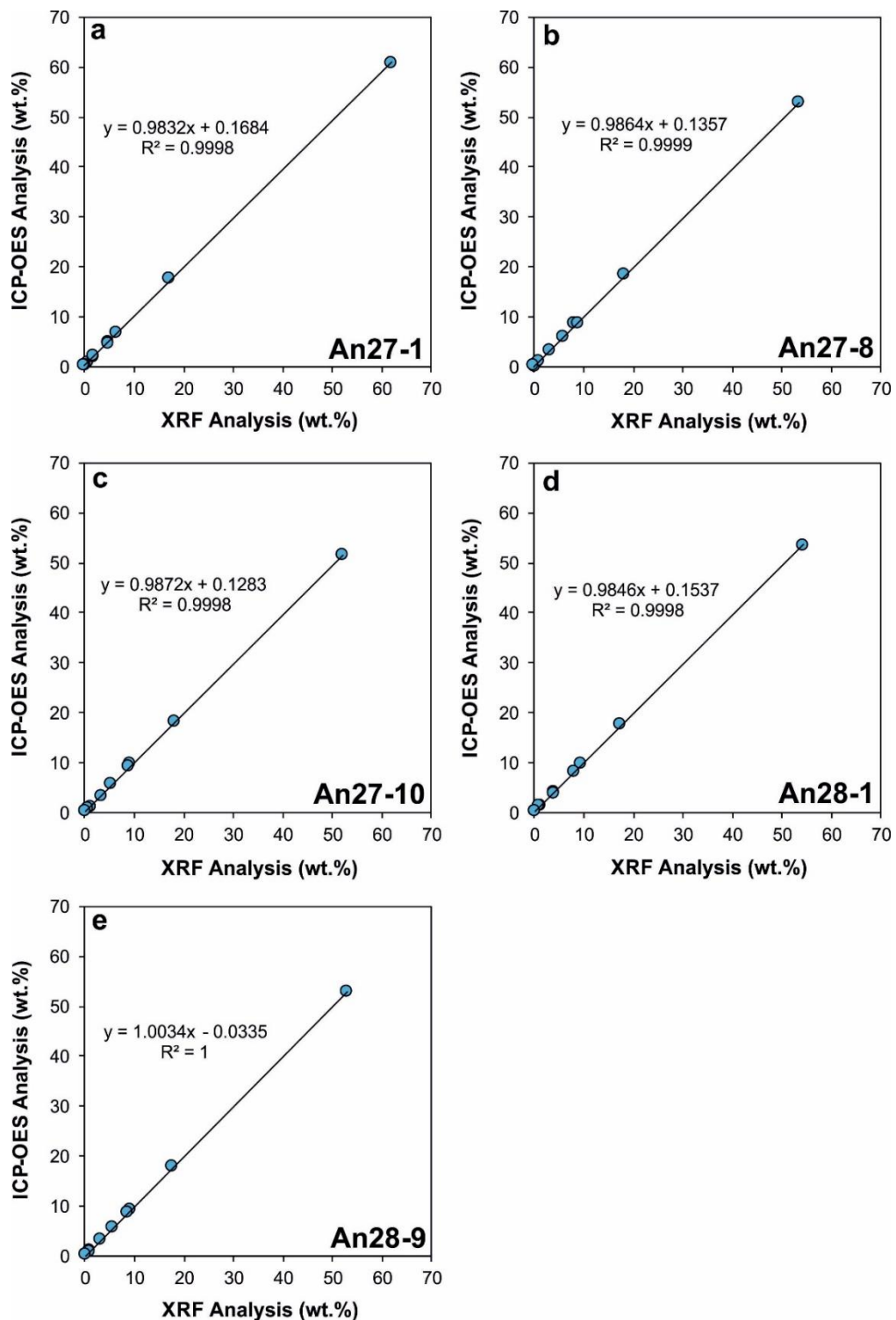


Fig. 4.5. Bivariate plots comparing pre-existing XRF analyses with new ICP-OES analyses (Cardiff University, 2017) acquired for the current project for five Antuco samples (An27-1, An27-8, An27-10, An28-1, An28-9). Analyses are consistent between analytical techniques, with R^2 values of ≥ 0.9998 .

Chapter 4. Method development: acquiring chalcophile element analyses through ICP-tandem mass spectrometry

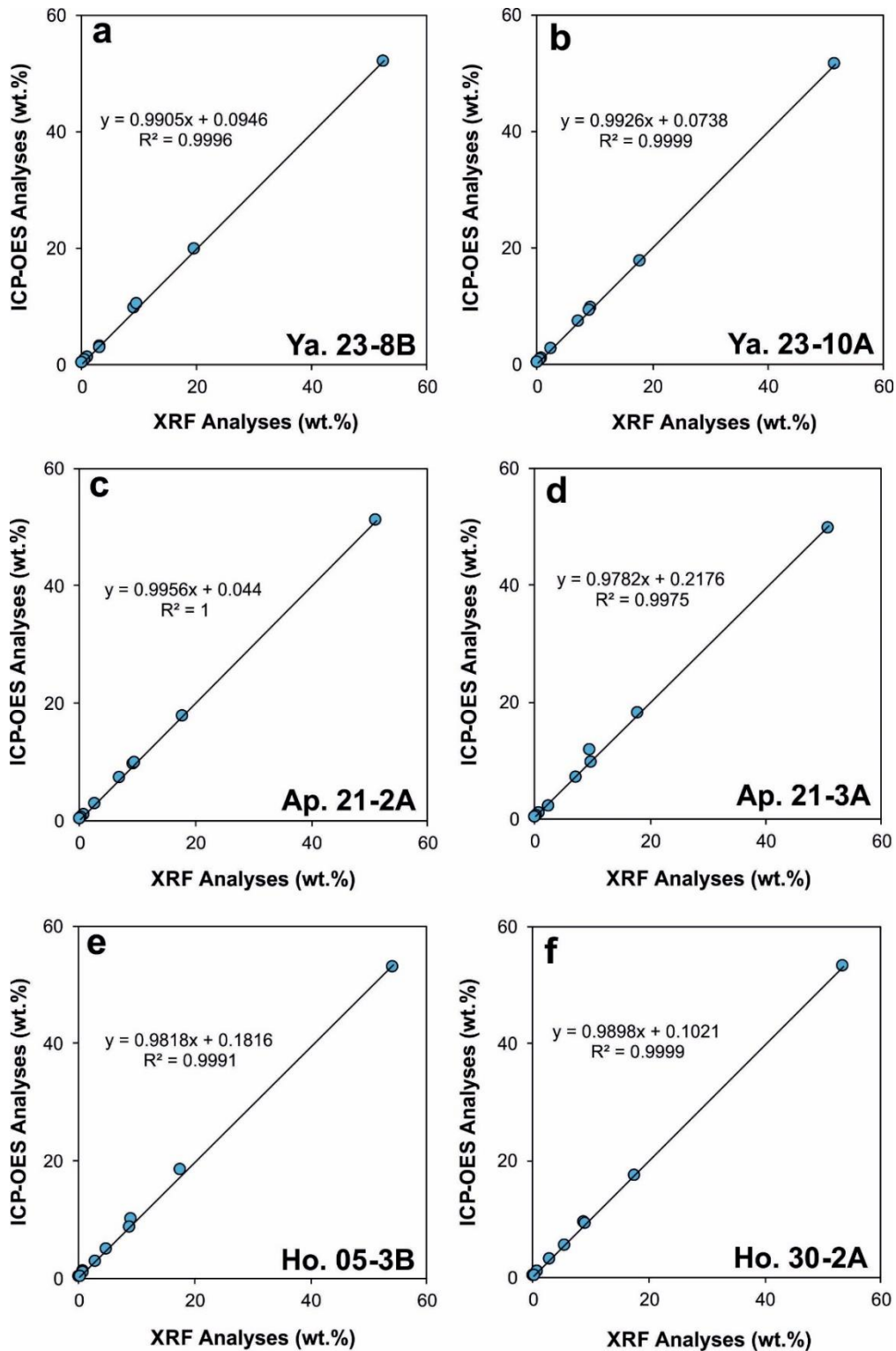


Fig. 4.6. Bivariate plots comparing pre-existing XRF analyses with new ICP-OES analyses (Cardiff University, 2017) acquired for the current project for samples from Yate (a, b), Apagado (c, d) and Hornopirén (e, f). Analyses are consistent between analytical techniques, with R^2 values of ≥ 0.9975 .

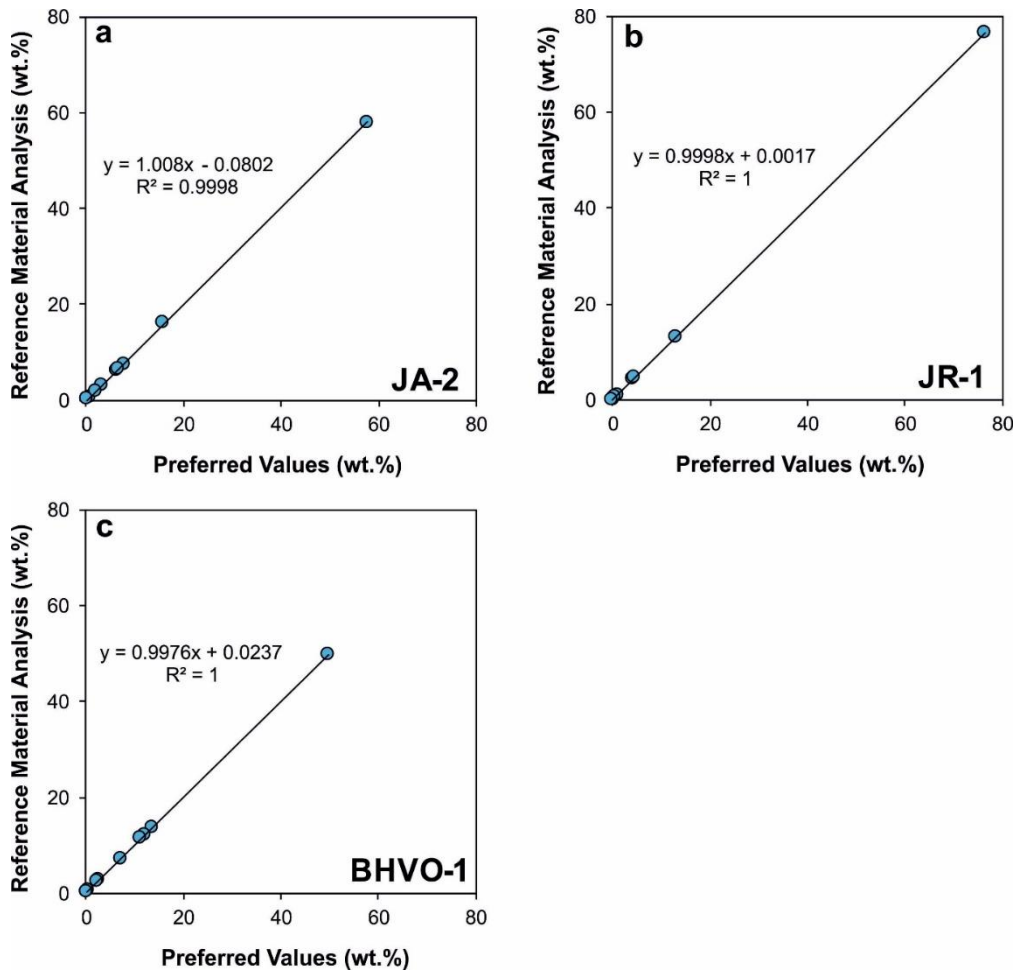


Fig. 4.7. Bivariate plots assessing the accuracy of International Standard Reference Material (JA-2, JR-1, BHVO-1) analyses acquired through XRF analysis at the University of Edinburgh, in 2017. Preferred values sourced from Govindaraju (1994). All analyses show consistent results, with R^2 values ≥ 0.9998 .

4.3. Summary

The above discussions have demonstrated that both the major and trace element data obtained in the current project are of high quality. Due to using multiple analytical techniques (XRF, ICP-OES, ICP-MS/MS) to obtain compositional data for the volcanic rock samples however, the data presented in the subsequent chapters is a combination of the above. The major element composition of volcanic rock samples

Chapter 4. Method development: acquiring chalcophile element analyses through ICP-tandem mass spectrometry

subsequently presented are those obtained through either XRF or ICP-OES, whilst most trace element analyses presented are those obtained through ICP-MS/MS analysis (exceptions include Ba, Tm, U and Th). A summary of the data sources utilised in the current project are presented in **Table 4.3**.

Table 4.3. Data sources for samples presented in the current project

Volcanic edifice	No. of samples	Major element data source	Trace element data source
Antuco	26	XRF ¹ , ICP-OES ²	ICP-MS/MS ⁴
Villarrica	3	ICP-OES	ICP-MS/MS ⁴
Quetrupillán	5	ICP-OES	ICP-MS/MS ⁴
Lanín	5	ICP-OES	ICP-MS/MS ⁴
Cab. – Huel. Complex	23	ICP-OES	ICP-MS/MS ⁴
Huililco	3	ICP-OES	ICP-MS/MS ⁴
Yate	10	XRF ¹	ICP-MS/MS ⁴
Hornopirén	4	XRF ¹	ICP-MS/MS ⁴
Apagado	8	XRF ¹	ICP-MS/MS ⁴
Ollagüe	10	XRF ³	ICP-MS/MS ⁴
San Pedro	3	XRF ³	ICP-MS/MS ⁴
La Poruñita	1	XRF ³	ICP-MS/MS ⁴

¹Pre-existing XRF analysis courtesy of S. Watt; ²ICP-OES analysis from Cardiff University; ³XRF analysis from University of Leicester; ⁴ICP-MS/MS analysis from the Open University, through which most trace elements were obtained: exceptions include Ba, Tm, U and Th, which were, in most cases, obtained from pre-existing datasets (courtesy of S. Watt) or via ICP-MS at Cardiff University (see Appendix B for further details). Cab. – Huel.: Caburgua – Huelemolle.

Chapter 5

Chalcophile element processing beneath a continental arc stratovolcano

The bulk of material presented in this chapter is published in Earth and Planetary Science Letters³, a copy of which is attached at the end of this thesis. S.W. collected the samples during fieldwork in 2013. D.C. led the analysis and interpretation. D.C. and S.J.H. undertook ICP-MS/MS analysis on the samples and processed the data. D.C., S.F.L.W., F.E.J. and A.R.H. interpreted the data. D.C. wrote the manuscript with contributions from all other authors. All authors contributed to the final edits of the manuscript.

5.1. Introduction

The chalcophiles (e.g., Cu, Ag, Se, Pb, Bi) are an important suite of elements both in terms of their economic value and their potential to investigate magmatic processes active at convergent margins (Noll Jr et al., 1996; Richards, 2009; Jenner et al., 2010; Sillitoe, 2010; Wilkinson, 2013; Jenner, 2017). Compared to the bulk continental crust, many of the economically important chalcophile elements are extremely enriched in porphyry Cu-Au deposits that are globally associated with

³ Cox et al., 2019. Chalcophile element processing beneath a continental arc stratovolcano. *Earth and Planetary Science Letters*, 522, 1-11.

convergent margins (Sillitoe, 2010; Wilkinson, 2013). Because primitive subduction-related magmas are not enriched in Cu, Ag, Se or Au relative to mid-ocean ridge basalt (MORB) magmas, there has been considerable debate regarding the crustal processes that contribute to the formation of magmatic-hydrothermal ore deposits (Richards, 2009; Jenner et al., 2010; Lee et al., 2012; Wilkinson, 2013; Chiaradia, 2014; Matjuschkin et al., 2016; Jenner, 2017). For example, although there is a global association between porphyry deposits and convergent margins (Sillitoe, 2010), the spatial distribution of these deposits is sporadic (Sillitoe, 1997) and the remainder of the bulk continental crust is notably depleted in Cu, Se and Au compared to primitive arc magmas (Lee et al., 2012; Jenner, 2017). Given that the bulk continental crust has been generated at convergent margins, these observations suggest that most arc magmas are not predisposed to fuel the formation of economically viable ore deposits (Jenner, 2017).

The way in which many chalcophile elements are processed and distributed within a magmatic system and throughout the continental crust is controlled by the stability of sulfides (Lee et al., 2012; Chiaradia, 2014; Richards, 2015). The point at which a magma becomes saturated in a sulfide phase is a function of the temperature, pressure, oxygen fugacity and composition of the magma (Mavrogenes and O'Neill, 1999; O'Neill and Mavrogenes, 2002; Wallace and Edmonds, 2011; Matjuschkin et al., 2016). Geochemical studies of volcanic glasses have demonstrated that the Cu/Ag of MORB magmas remains constant following sulfide saturation, in contrast to a decreasing post-saturation Cu/Ag in arc-related magmas (Jenner et al., 2010, 2015). These varying trends have been attributed to differences in the nature of the fractionating sulfide phase during differentiation of MORB (molten sulfide) and

subduction-related (crystalline sulfide) magmas (Jenner et al., 2010; Jenner, 2017). This interpretation is supported by experimental studies indicating that Cu and Ag have similar partition coefficients with respect to molten sulfide, but that Cu is more compatible in crystalline sulfide than Ag (Li and Audétat, 2012, 2015). During differentiation of oceanic convergent margin magmas, the decrease in Cu/Ag (marking sulfide saturation and fractionation of crystalline sulfide) coincides with a sharp decrease in Fe, V, Cu, Ag, S and Au (reversing the preceding trend of increasing concentrations with increasing SiO₂ and decreasing MgO), suggesting that magnetite fractionation 'triggers' reduction-related sulfide saturation [the 'Magnetite Crisis'; Jenner et al. (2010)] during the evolution of oceanic arc magmas (Chiaradia, 2014; Jenner, 2017). Although the 'Magnetite Crisis' potentially controls sulfide processing and the fate of chalcophile elements during island arc-magmatic evolution, such a mechanism has not been fully explored within a continental arc.

Despite the importance of the chalcophile elements for understanding both mantle and crustal processes, they are still a relatively under-studied suite of elements. This is partly because elements such as Se and Ag, which can be used in conjunction with Cu to place constraints on the timing of sulfide saturation [see Jenner (2017), and references therein], are difficult to analyse in both natural and experimental materials (Jenner and Arevalo, 2016). Thus, studies of chalcophile element processing at continental arcs have focussed mainly on whole rock Cu systematics, arguing that most arc magmas reach sulfide saturation during crustal differentiation (Lee et al., 2012; Chiaradia, 2014; Richards, 2015; Jenner, 2017). This is supported by observations of magmatic sulfide inclusions across a broad range of bulk compositions

in Ecuadorian arc volcanic rocks, hosted predominantly in magnetite but also in silicate phases (Georgatou et al., 2018).

Chiaradia (2014) used Cu systematics to argue that magmas erupting through thicker crust (>30 km) are of calc-alkaline affinity and require smaller proportions of crystallisation to reach sulfide saturation compared to tholeiitic magmas erupting through thinner crust (<20 km), as a consequence of their higher H₂O and fO_2 . This would thus influence the timing of magnetite-triggered sulfide fractionation and the resulting drop in total Fe content and fO_2 of the evolving magma. However, experimental constraints suggest an alternative explanation (Matjuschkin et al., 2016), showing that with increased pressure, and therefore depth, the sulfide stability field shifts to higher fO_2 . In conjunction with this widening of the sulfide stability field with depth, Jenner (2017) used the Cu deficit and the significantly lower Cu/Ag of the bulk continental crust compared to mantle-derived melts to argue that continental crust formation is dominated by the addition of magmas that fractionate high Cu/Ag sulfides at the base of the continental crust [i.e. in a deep crustal hot zone; cf. Annen et al. (2006)], prior to magma ascent to higher crustal levels.

Alternatively, Tang et al. (2018) argue that the Fe-depleting trend (i.e., calc-alkaline series) observed in magmas erupting through thick crust is attributable to garnet fractionation, from magmas that have initial fO_2 comparable to MORB. Furthermore, Tang et al. (2018) suggest that magmas erupting through thick continental crust inherit their high fO_2 (>MORB) as a consequence of this garnet fractionation. However, the limited overlap between the garnet stability field and the crustal depth range of magmatic differentiation (Alonso-Perez et al., 2009) suggests that garnet fractionation is unlikely to explain the higher fO_2 of all arc magmas,

particularly those erupted on thinner crust, and high fO_2 compared to MORB (Matjuschkin et al., 2016) appears to be a ubiquitous characteristic of arc magmas prior to the earliest stages of their differentiation (Kelley and Cottrell, 2012; Richards, 2015). As the solubility of S decreases with decreasing total Fe content of a magma, garnet fractionation would promote sulfide fractionation during magmatic differentiation at high pressures. Regardless of whether the 'Magnetite Crisis', a shift in the sulfide stability field with pressure (depth), garnet fractionation, or potentially a combination of the above processes are the 'trigger' for sulfide saturation, there is an emerging consensus that most continental arc volcanic rocks should fractionate sulfide in the lower crust prior to ascent. As a result, continental arc volcanic rocks should have lower Cu/Ag than primitive arc magmas and the entire oceanic crust, but there is a lack of reliable Cu/Ag in the literature to test this hypothesis.

Here, we present major and trace element volcanic rock compositions from Antuco Volcano, Chile (**Fig. 2.3**), a typical continental arc stratovolcano, in order to characterise chalcophile behaviour during the generation and subsequent processing of magmas through a continental arc. Bulk compositions at Antuco span basaltic to andesitic compositions (Lopez-Escobar et al., 1981; Martínez et al., 2018), and are interpreted to initially stall and crystallise at the base of the continental crust (~40 km) prior to ascent and shallower crystallisation [$\sim 0.9 - 1.5$ kbar ($\sim 2 - 5$ km); Martínez et al. (2018)]. This represents an ideal setting to test current models of chalcophile element processing within a continental arc, which are based on inferences drawn from oceanic arcs or datasets limited principally to Cu analyses. By generating a novel dataset that includes a near complete suite of chalcophile elements (S, Cu, Ag, Se,

As, Sb, Sn, W, Mo, Pb, Bi, Tl, Zn, Ga, Co), we seek to refine the understanding of the controls of chalcophile element distribution in continental arcs.

5.2. Geochemical results

5.2.1. Major elements

In terms of classification, both Phase 1 and Phase 2 samples from Antuco (see **Chapter 2**) span a similar range on a total alkali against silica (TAS) plot (**Fig. 5.1a**). Phase 1 samples range from basalt to andesite, with Phase 2 samples ranging from basaltic-andesite to andesite; however, two samples, one from each phase, classify as trachy-andesite. The majority of samples plot in the calc-alkaline field on an AFM (alkali – FeO – MgO) ternary plot (**Fig. 5.1b**) following the boundaries of Kuno (1968) and Irvine and Baragar (1971).

Antuco samples range from 51.6 to 62.3 wt.% SiO₂ and 1.5 to 6.7 wt.% MgO (anhydrous values) (**Figs. 5.2** and **5.3**). Titanium dioxide, Fe₂O₃ (as total Fe) and V display broadly similar trends, all increasing with increasing SiO₂, reaching a maximum of 1.6 wt.%, 10.9 wt.% and ~290 ppm, respectively at ~54-55 wt.% SiO₂, before decreasing with further increasing SiO₂ (**Fig. 5.2**). The trends in V, TiO₂ and Fe₂O₃ are also seen when plotted against MgO, reaching a maximum at ~3 wt.% MgO (**Fig. 5.2**). Many of the Phase 2 samples have higher TiO₂ and Fe₂O₃ at a given SiO₂ (and MgO) compared to Phase 1 samples. Calcium oxide shows a positive correlation with MgO; Al₂O₃ shows a peak in contents between 3 – 4 wt.% MgO; and K₂O, Na₂O and P₂O₅ show negative correlations (**Fig. 5.3**). Manganese oxide shows no correlation with MgO (**Fig. 5.3b**). Our data are consistent with the major element data discussed in detail by Martínez et al. (2018), in the most recent study of Antuco (**Figs. 5.1 – 5.3**).

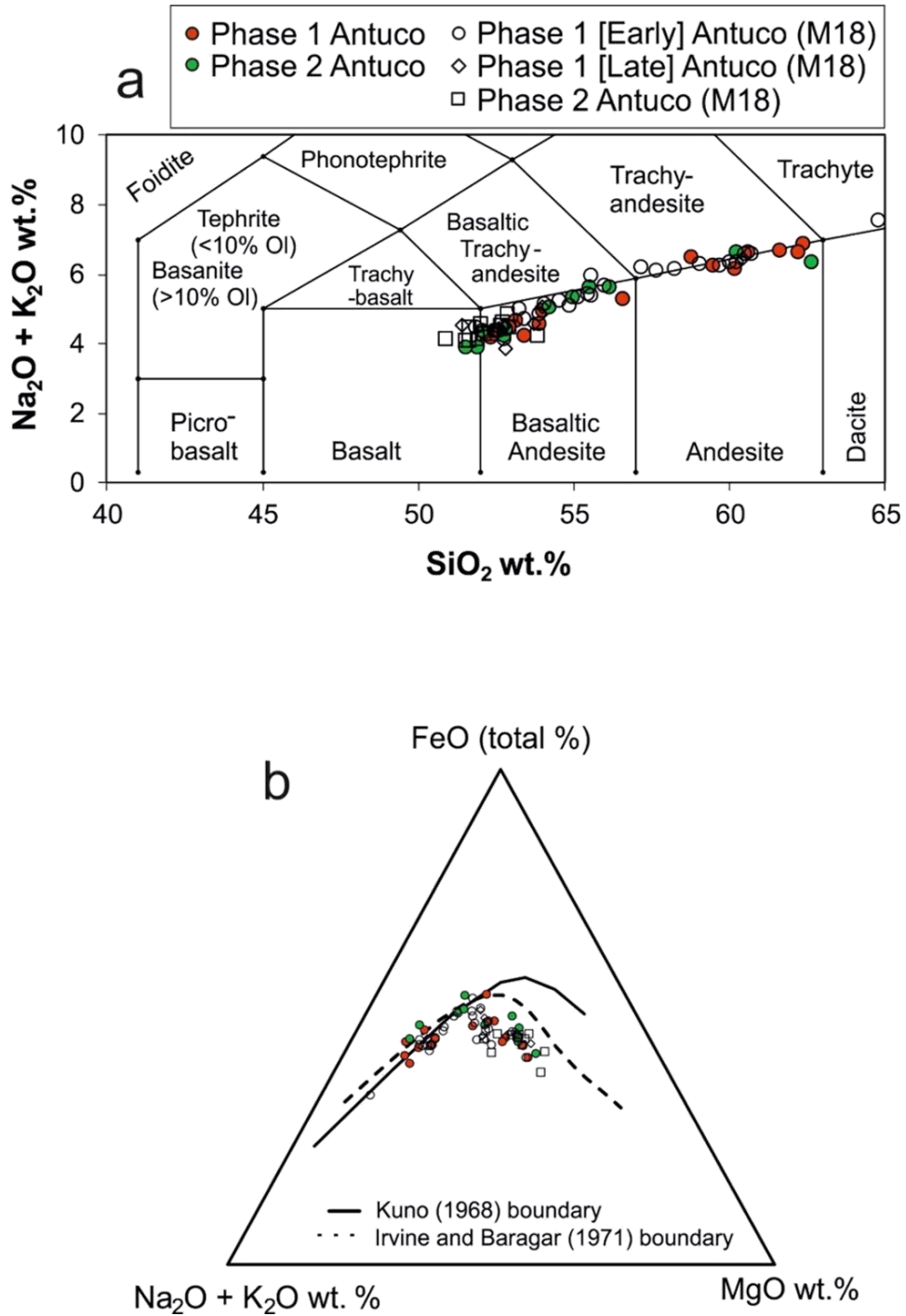


Figure 5.1. (a) Total-alkali-silica (TAS) plot of the Antuco samples. Antuco Phase 1 samples of the current study range in composition from basalt to andesite, with one classifying as a trachy-andesite. Antuco Phase 2 samples of the current study have a slightly narrower compositional range from basaltic andesite to andesite, again with one classifying as a trachy-andesite. Also plotted are samples analysed by Martínez et al. (2018) from Antuco (M18), which display very similar compositional ranges to the current study. Classification fields as of Le Bas et al. (1986). (b) Alkali-iron-magnesium (AFM) ternary plot of the Antuco samples. The majority of both Phase 1 and 2 samples plot in the calc-alkaline field. Ternary plot constructed in TernPlot (Marshall, 1996), using the boundary lines of Kuno (1968) and Irvine and Baragar (1971).

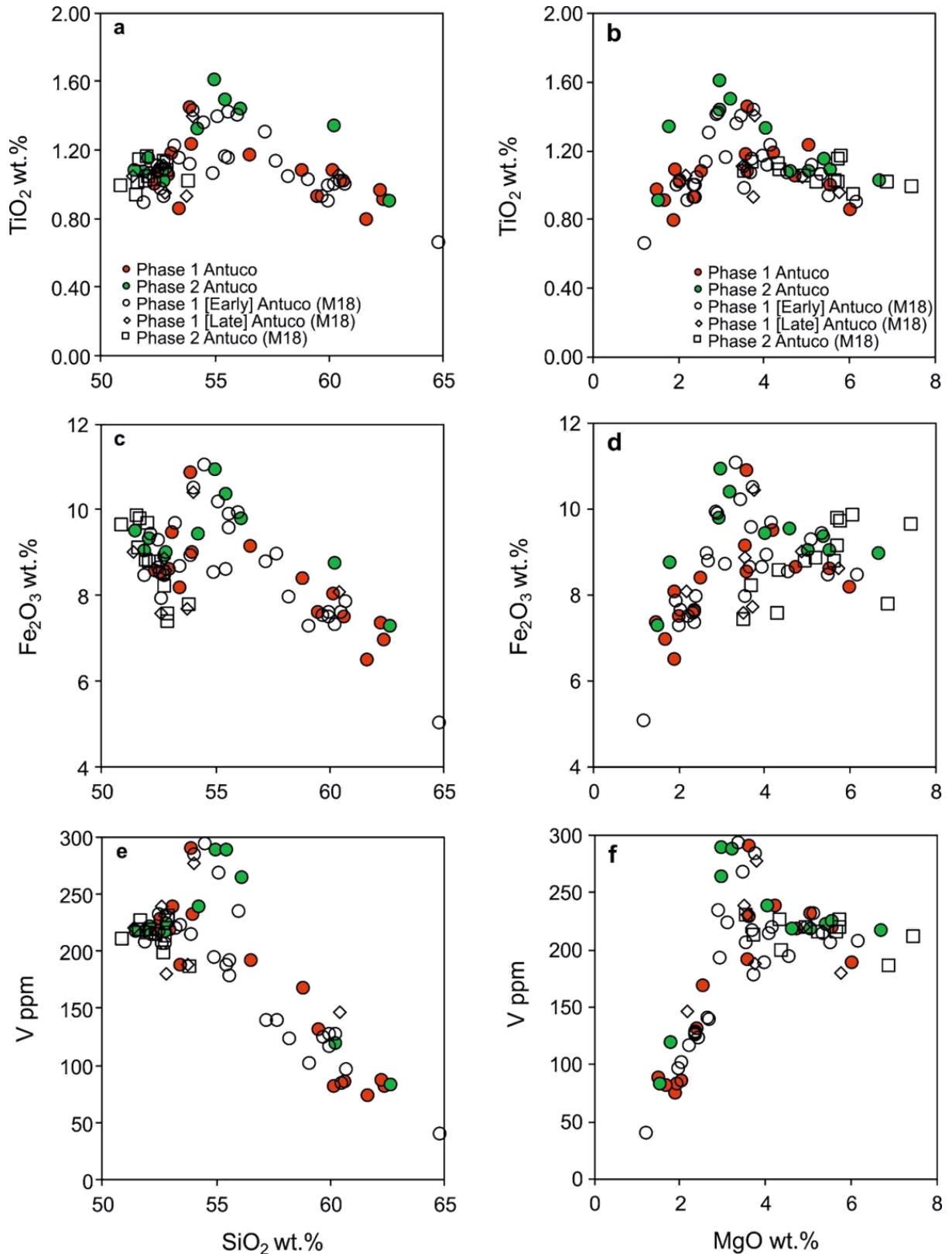


Figure 5.2. Select major element (TiO₂, Fe₂O₃) and Vanadium bivariate plots (vs. SiO₂, MgO) of the Antuco samples. Inflections in TiO₂, Fe₂O₃ and V at ~55 wt.% SiO₂ and ~3 wt.% MgO highlight the onset of magnetite fractionation in the Antuco magmas. Also plotted are samples from Antuco analysed by Martínez et al. (2018) (M18). Samples from M18 display similar concentration ranges and show inflections in TiO₂, Fe₂O₃ and V.

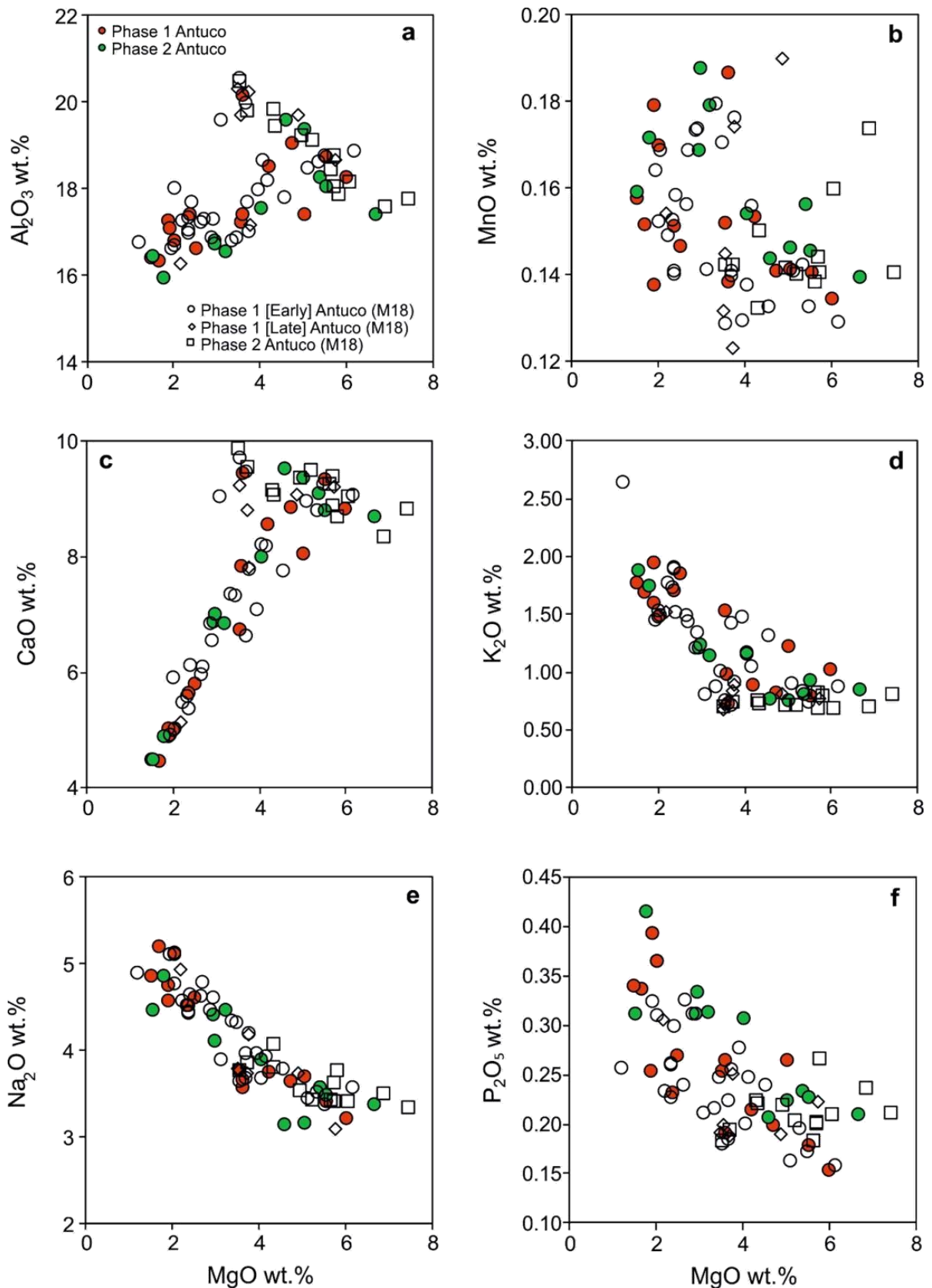


Figure 5.3. Remaining major element (Al_2O_3 , MnO, CaO, K_2O , Na_2O , P_2O_5) bivariate plots (vs. MgO) of the Antuco samples. Analyses of Antuco lavas presented by Martinez et al. (2018) (M18) have also been plotted. Samples of the current study and those presented by (M18) are very similar in terms of their major element compositions.

5.2.2. Trace elements

Most of the chalcophile elements (excluding Cu and Se) show negative correlations with MgO across the Antuco sample set (**Fig. 5.4** and **Appendix E**). Phase 1 samples show a broad overall decrease in Cu with increasing SiO₂ (and decreasing MgO), which follows the trend defined by sulfide saturated lava samples from Ecuador (Georgatou et al., 2018) (**Fig. 5.5a** and **Appendix E**). Additionally, Phase 1 samples show a decrease in Cu/Ag with increasing SiO₂ and decreasing MgO (**Fig. 5.5e** and **Appendix E**). Three of the ~59 – 62 wt.% SiO₂ (~1.5 – 2.5 wt.% MgO) Phase 1 samples have considerably lower Cu contents (5.4 – 25.0 ppm) and Cu/Ag (124 – 691) compared to other samples with a comparable SiO₂ and MgO (48.6 – 58.9 ppm Cu and 771 – 1497 Cu/Ag). The Cu contents of Phase 2 samples remain approximately constant with increasing SiO₂ and decreasing MgO (**Fig. 5.5a** and **Appendix E**).

At a given MgO, the most primitive (highest MgO) Antuco samples have higher Pb, Tl, Sb, As and similar Bi and W compared to the MORB array (**Fig. 5.4**). The contents of Mo, Sn, Cu and Ag of the most primitive Antuco samples are comparable to MORB (**Figs. 5.4** and **5.5**). The S and Se contents of the Antuco samples are considerably lower than the MORB array (**Fig. 5.5b,d**). On a Parental-MORB normalised plot (**Fig. 5.6a**), the Antuco samples display negative Nb-Ta anomalies (barring one showing only a negative Nb anomaly) compared to neighbouring elements. Samples also show substantial peaks (15 – 100 times Parental-MORB) in W, Tl, As, Pb, Sb and Bi relative to the REE.

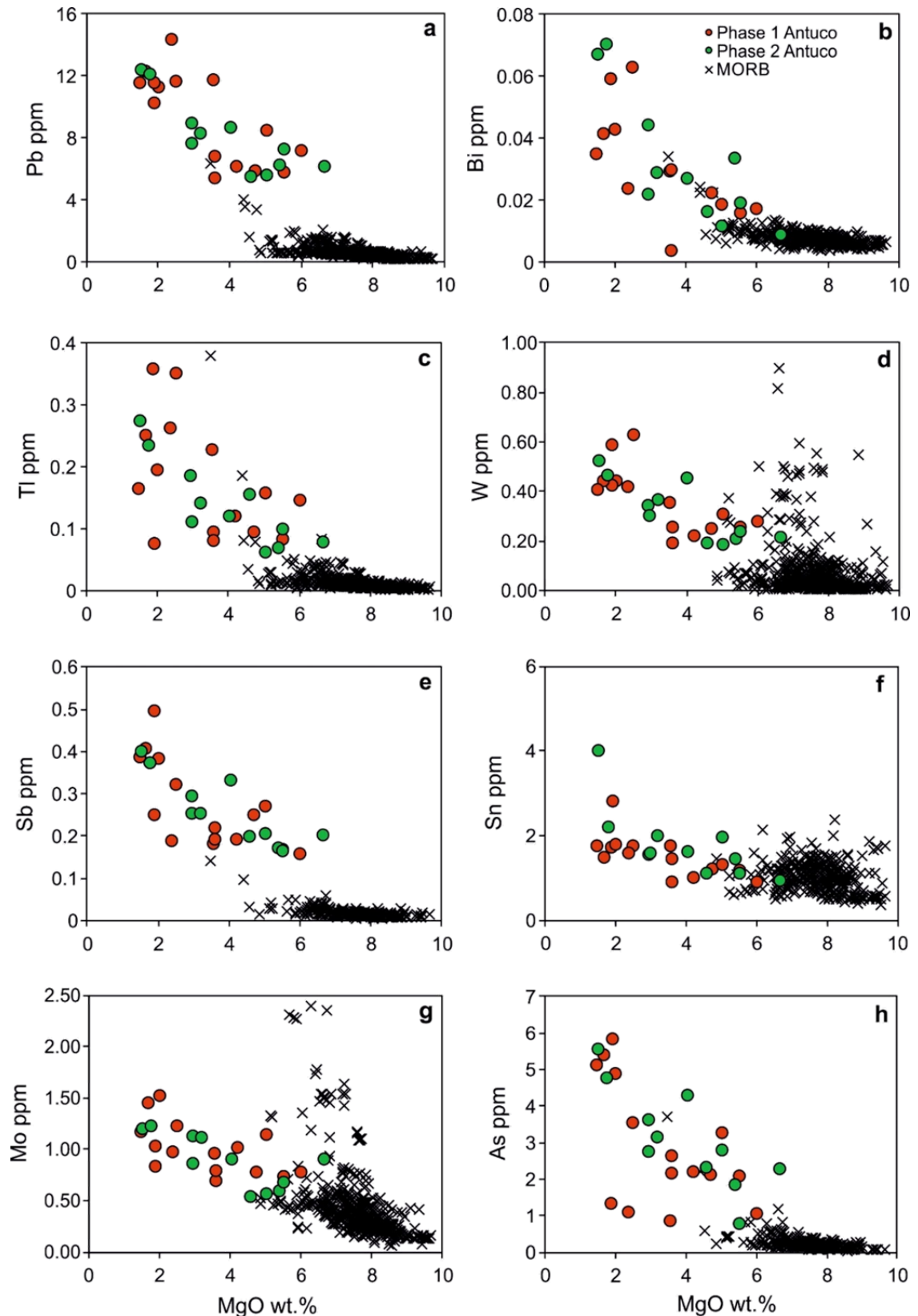


Figure 5.4. Pb, Bi, Tl, W, Sb, Sn, Mo, As bivariate plots (vs. MgO) of the Antuco samples. Unlike Cu and Se, the contents of Pb, Bi, Tl, W, Sb, Sn, Mo and As all show negative correlations against MgO. At a given MgO, the most primitive (highest MgO) Antuco samples have higher Pb, Tl, Sb and As, and similar Bi, W, Sn and Mo compared to the Global MORB array (data from Jenner and O'Neill, 2012).

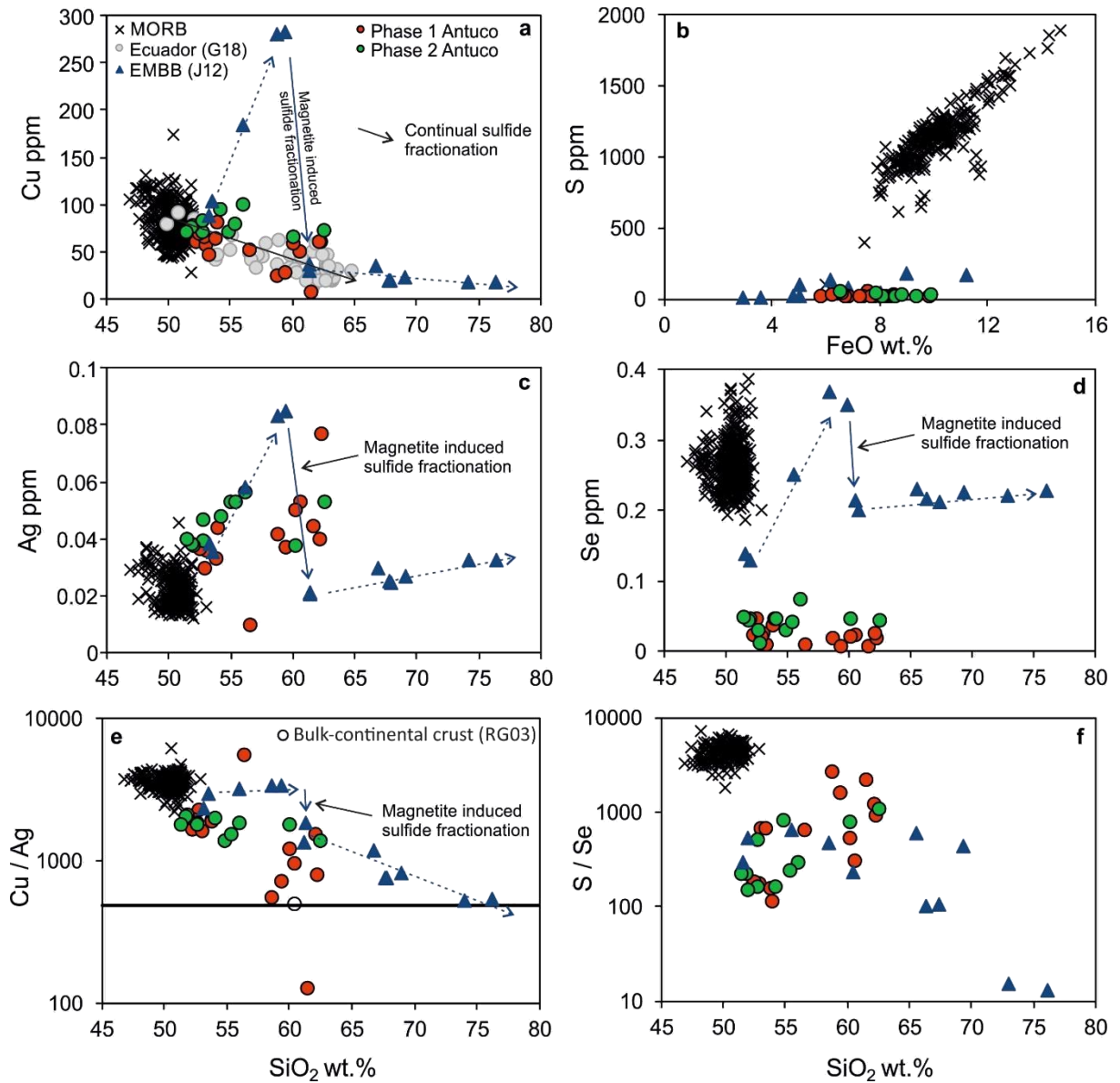


Figure 5.5. Select trace element (Cu, Ag, Se, and S) bivariate plots (vs. SiO₂, FeO) of the Antuco samples. (a) The continual decrease in Cu contents with increasing SiO₂ shown by Phase 1 samples (and Early Antuco samples of M18) is similar to that seen in Cu data from sulfide saturated Ecuadorian volcanoes [data from Georgatou et al., 2018 (G18)]. (a, c, d, e) The trends seen in Cu at Antuco and in Ecuadorian volcanoes are different to that seen in data from the Eastern Manus Backarc Basin (EMBB), where Cu (and Ag, Se) contents increase with increasing SiO₂, before rapidly decreasing after the onset of magnetite fractionation at ~58 wt.% SiO₂ [data from Jenner et al., 2012 (J12)]. (b, d, f) The S and Se contents of the Antuco samples are considerably lower than the Global (Pacific and Atlantic) MORB array [data from Jenner and O'Neill, 2012], suggesting they were both degassed from the Antuco magmas. This is unlike that seen in Se data from the Eastern Manus Backarc Basin (EMBB), where Se contents increase then decrease with increasing SiO₂, attributed to magnetite induced sulfide fractionation [data from Jenner et al., 2012 (J12)]. Bulk continental crust composition from Rudnick and Gao (2003) (RG03).

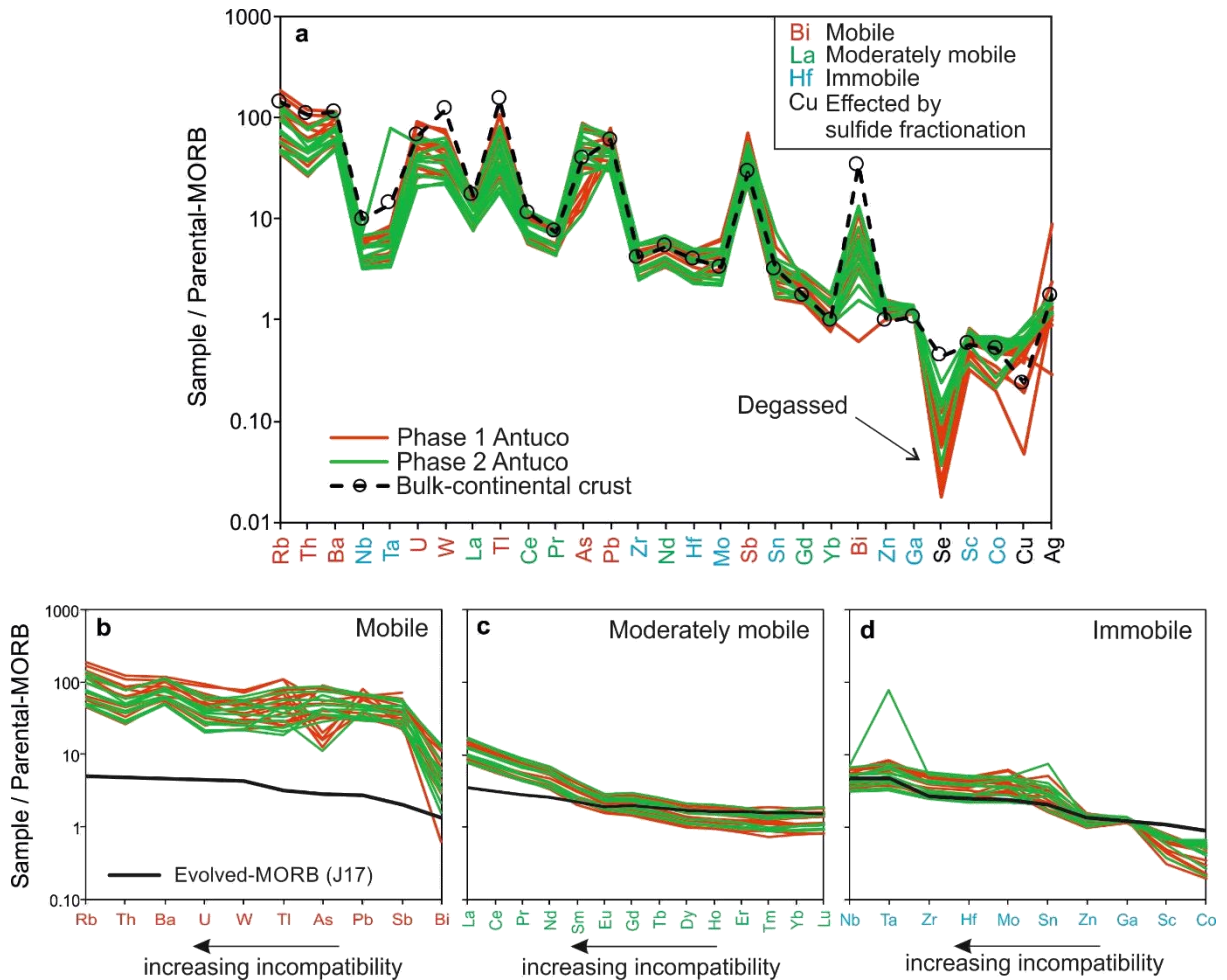


Figure 5.6. Parental-MORB normalised (values from Jenner, 2017) multi-element plots. (a) Complete multi-element plot of Antuco samples compared to the bulk-continental crust [data from Rudnick and Gao, 2003]. Element ordering reflects increasing incompatibility (from right to left) of the elements during low-pressure differentiation of MORB (see Jenner, 2017). Isolated mobile (b), moderately mobile (c) and immobile (d) Parental-MORB normalised multi-element plots show that the mobile chalcophile elements are considerably more enriched in the Antuco magmas compared to the REE and HFSE. Additionally, the relatively unfractionated patterns displayed by the Parental-MORB normalised mobile chalcophile elements, together with the slight increase in values with increasing incompatibility during MORB differentiation, indicates that these elements were added into the mantle wedge in roughly similar proportions as they are found in the upper oceanic crust [i.e., pattern comparable to Evolved-MORB, as presented by Jenner (2017) (J17)].

5.3. Discussion

5.3.1. Subduction mobile chalcophile elements

In order to distinguish which of the chalcophile elements are mobile during subduction, Jenner (2017) normalised samples to Parental-MORB (calculated). Parental-MORB represents an undifferentiated melt composition, approximating that of the bulk oceanic crust, and can therefore be used to constrain the relative differences in elemental fluxes at convergent margins compared to at MOR. On a Parental-MORB normalised plot (**Fig. 5.6a**), the Antuco samples display geochemical signatures typical of a volcano situated above a subduction zone (e.g., Pearce et al., 2005): enrichments in mobile large ion lithophile elements (LILE) compared to the moderately mobile REE, and enrichments of the moderately mobile REE compared to the high field strength elements (HFSE). All Antuco samples display enrichments in chalcophile elements W, Tl, As, Pb, Sb and Bi (**Fig. 5.6a**) compared to the REE and the HFSE, demonstrating that W, Tl, As, Pb, Sb and Bi are mobile during subduction. By comparison, other chalcophile elements (Mo, Sn, Zn, Ga, Co) appear to be immobile during subduction. These findings are in general agreement with previous geochemical studies regarding the relative mobility of chalcophile elements during the petrogenesis of convergent margin magmas (Noll Jr et al., 1996; Jenner, 2017). Parental-MORB-like Cu and Ag contents of the most primitive Antuco samples indicate that neither Cu nor Ag were mobilised in a slab flux to the mantle wedge during subduction, and were thus sourced from the mantle wedge. The minor difference in enrichment of Ag relative to Cu (**Fig. 5.6a**) is likely a result of early sulfide fractionation from the Antuco magmas, preferentially removing Cu (over Ag).

When plotted in isolation, the mobile (i.e., Rb, Th, Ba, U, W, Tl, As, Pb, Sb and Bi, **Fig. 5.6b**), moderately mobile (i.e., REE, **Fig. 5.6c**) and immobile (i.e., HFSE, Mo, Sn, Zn, Ga, Sc and Co, **Fig. 5.6d**) elements show relatively smooth patterns. Additionally, each group of elements shows a slight increase in Parental-MORB normalised values with increasing incompatibility of the element during differentiation of the oceanic crust. Detailed work on the partitioning of chalcophile and siderophile elements during the differentiation of mantle-derived melts (MORB and subduction-related volcanic rocks) conducted by Jenner (2017) has shown that the majority of chalcophile and siderophile elements are incompatible during differentiation (e.g., As, Sb, Tl, Pb, W, Bi). As such, these elements are preferentially enriched in the upper oceanic crust [e.g., Evolved-MORB (at ~7 wt.% MgO)] compared to the bulk (Parental-MORB) and lower oceanic crust, and are therefore more likely to be fluxed into the sub-arc mantle wedge during arc magma genesis, relative to Cu and Ag, which are compatible and reside in the lower oceanic crust (Jenner, 2017). Hence, the slight increase in the magnitude of the enrichments of the mobile elements in the Antuco samples, which mimics the upper oceanic crustal distributions of elements, suggests that the mobile elements have been added from the subducting slab to the mantle wedge source of the Antuco magmas in roughly the same proportions as their distributions in the upper oceanic crust.

5.3.2. Degassing of S and Se

Sulfur is commonly degassed from magmatic systems during magma ascent and/or during subaerial eruption, and consequently, determining the pre-degassing S content of magmas is challenging (Jenner et al., 2010; Wallace and Edmonds, 2011). Previous studies have demonstrated the use of Se, Cu and Ag for reconstructing the

pre-eruptive S contents (i.e., melt inclusion contents of S) of magmatic systems (Jenner et al., 2010, 2015). For example, during differentiation of backarc basin magmas from the Eastern Manus Basin, the initial increase in FeO, Cu, Ag and Se, but constant Cu/Ag with increasing SiO₂ (and decreasing MgO), followed by a sudden drop in Cu, Ag, Se and Cu/Ag at ~60 wt.% SiO₂ (**Fig. 5.5**), has been attributed to magnetite-triggered sulfide fractionation rather than Cu, Se and Ag degassing (Jenner et al., 2010, 2012, 2015). As S is an essential ingredient required for fractionation of sulfides, and also because melt inclusions from the same suite have sufficient S for the melts to be considered sulfide saturated, S degassing of the Eastern Manus Basin and other backarc basin magmas is considered to take place during eruption rather than differentiation (Jenner et al., 2010, 2015). Evidence for sulfide fractionation prior to S degassing has also been demonstrated by the presence of magmatic sulfides in convergent margin magmas (Georgatou et al., 2018; Zelenski et al., 2018), such as those from Ecuador, which show a similar range in Cu versus SiO₂ systematics to the Antuco samples (**Fig. 5.5a**). However, the behaviour of Cu, Ag and Se in the Manus Basin was investigated using glass samples erupted beneath a significant (>1600 m) water column. Thus, it is important to re-assess the behaviour of the chalcophile elements during subaerial eruptions.

Unlike Cu, Ag, Pb, Tl, Sb, Bi, W, Sn and As, which have contents that are comparable to or higher than MORB at Antuco, the behaviour of Se appears to be decoupled from the rest of the chalcophile elements, except S. The very low S and Se concentrations – considerably lower than Parental-MORB (**Fig. 5.6a**), the MORB array (**Fig. 5.5b,d**) and Eastern Manus Backarc Basin samples (**Fig. 5.5b,d**) – suggests that both S and Se were degassed from the melts during either differentiation and/or

eruption. Observations of Se enrichment in volcanic plumes at Mt Etna (Floor and Román-Ross, 2012) support this interpretation. The S/Se of the Antuco samples are similar to those observed in the Eastern Manus Backarc Basin suite, but are considerably lower than MORB (**Fig. 5.5f**), indicating that S was more volatile than Se during degassing. Interestingly, the three samples that have the highest S/Se (i.e., the least degassed samples, approaching MORB values) have the lowest Cu contents and Cu/Ag, suggesting that sulfur degassing cannot explain the trend to low Cu with increasing evolution of the Antuco samples. Given that sulfide fractionation requires the presence of S in the melt, we consider that the degassing of S (and Se) must have predominantly taken place during eruption rather than during differentiation.

5.3.3. Crustal processing of the chalcophile elements

Many of the chalcophile elements either have such low sulfide-silicate melt partition coefficients ($D^{\text{sulf-sil}}$) that they cannot be used to assess whether a melt has fractionated sulfide (e.g., As, Tl, Sb, Mo, Pb, Bi), and/or they show 'mixed affinities' (e.g., In, Ga, Sn, Zn, Cd), because their bulk partitioning is controlled by a combination of silicate, oxide and sulfide minerals (Jenner, 2017). Only a few of the chalcophile elements (e.g., Cu, Ag, Se, Au) are sufficiently compatible in sulfide phases to be of use for demonstrating sulfide fractionation from an evolving melt. For example, unlike the incompatible elements (e.g., As, Pb, Sb and Tl) which show a steep increase in contents with decreasing MgO (**Fig. 5.4**), the contents of Cu and Ag of the Antuco samples remain approximately constant and/or show a subtle decrease with increasing SiO₂ and decreasing MgO (**Fig. 5.5** and **Appendix E**). Thus, like lava samples from Ecuador (Georgatou et al., 2018), the full compositional range of Antuco's magmas have been affected by sulfide fractionation. Given the potentially limited depth range

of sulfide stability in the lower crust (Matjuschkin et al., 2016), this suggests that much of the compositional diversity of these magmas was acquired at lower crustal levels [consistent with “hot zone” models; e.g., Annen et al. (2006)].

Unlike samples from the Eastern Manus Backarc Basin, neither the Antuco nor the Ecuador samples show an initial increase in Cu with increasing SiO₂ (or decreasing MgO) prior to magnetite fractionation. Broad inflections at Antuco in the trends between TiO₂, Fe₂O₃ and V with SiO₂ and MgO indicate the onset of magnetite fractionation in these magmas at ~55 wt.% SiO₂ (~3 wt.% MgO) (**Fig. 5.2**). However, this does not correspond with a drop in Cu contents for any Phase 2 samples or for the majority of Phase 1 samples (**Fig. 5.5a** and **Appendix E**). A similar pattern is observed in Cu data presented by Martínez et al. (2018); some, but not all Early/Late Antuco samples (Phase 1 Antuco) display a drop in Cu contents post-55 wt.% SiO₂ (or post-3 wt.% MgO), but this drop is not observed in the post-collapse samples (Phase 2 Antuco). These systematics suggest that magnetite fractionation did not play a strong control on Cu partitioning in the Antuco magmas, because the melts were already sulfide saturated before magnetite saturation. A minor impact of magnetite fractionation on the proportion of sulfide fractionation is, however, suggested by the scatter to lower Cu/Ag of some of the Phase 1 samples at ~55 wt.% SiO₂ and ~3 wt.% MgO (**Fig. 5.5e** and **Appendix E**).

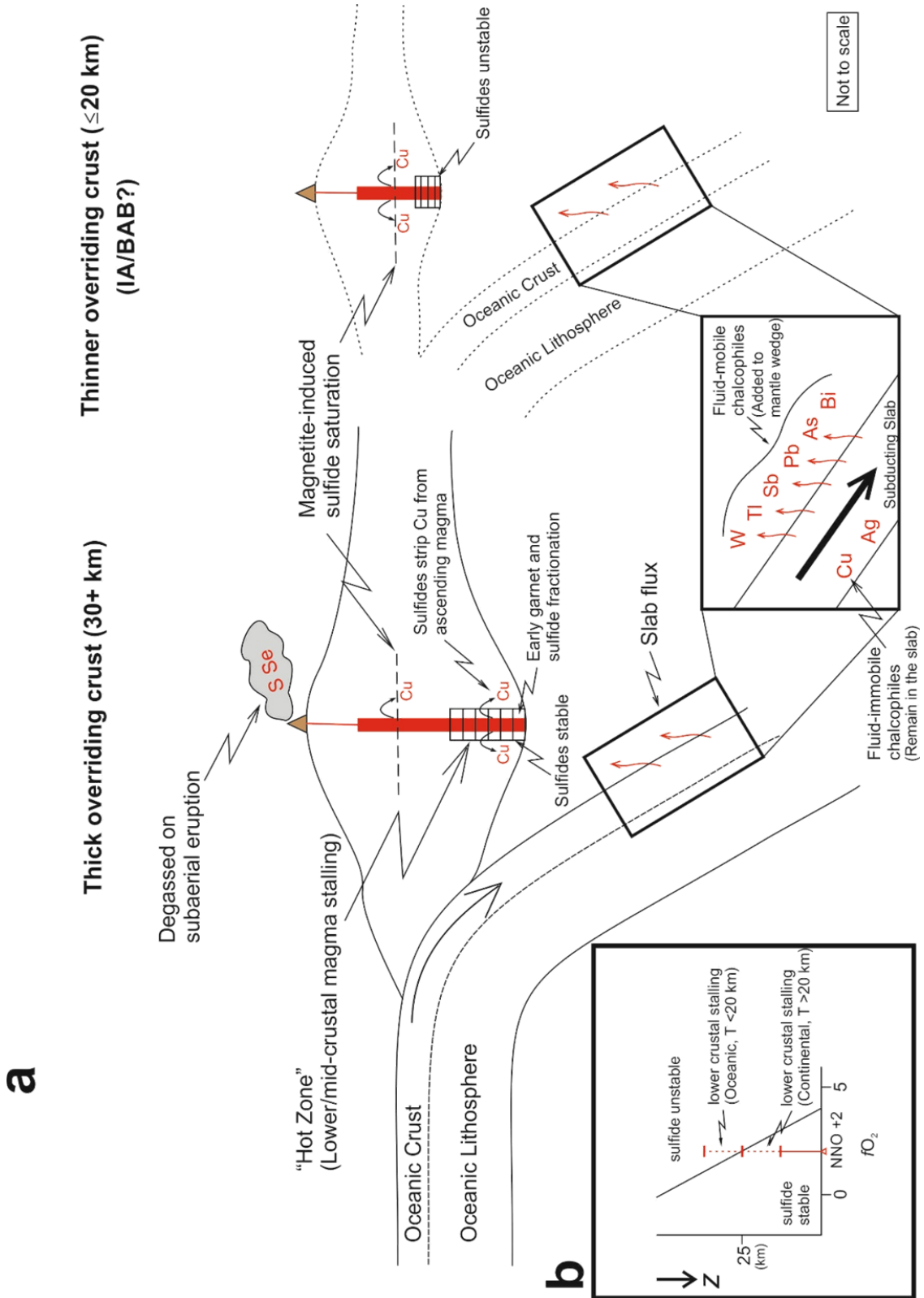
The indistinguishable Cu/Ag of MORB, oceanic island basalts, oceanic plateau basalts, primitive convergent margin magmas and mantle xenoliths has been attributed to the presence of sulfide melt in the mantle source region at each tectonic setting (Jenner et al., 2010, 2012, 2015; Jenner, 2017; Wang et al., 2018). With the exception of one sample with a Cu/Ag of 5416, the Cu/Ag of the Antuco samples are all lower

than the global MORB array (**Figs. 5.5e**), even in the most primitive Antuco magmas. This may indicate that minor amounts of Cu were removed from the parental Antuco melts at an early stage in their evolution. Cu/Ag patterns across the full Antuco sample set suggest fractionation of Cu from Ag throughout the crustal differentiation of these magmas, which is consistent with crystalline, rather than a sulfide melt, fractionation (Jenner et al., 2010; Li and Audétat, 2012). Some of the most evolved Antuco samples (lowest MgO) have Cu/Ag approaching that of the bulk-continental crust (**Fig. 5.5e**). It is unlikely that an early fractionating phase, such as olivine, could cause such a drop in Cu/Ag from mantle values, given the incompatibility of Cu and Ag in potential fractionating silicate phases (Jenner et al., 2010; Lee et al., 2012). We therefore suggest that sulfide fractionation began in the lower crust and at a very early stage in the evolution of Antuco's parental magmas, prior to ascent and low-pressure fractional crystallisation (**Fig. 5.7**). This is consistent with initial stalling and crystallisation at the base of the continental crust prior to ascent to higher crustal levels (e.g., Annen et al., 2006). Lower crustal sulfide saturation is likely a result of the increased stability of crystalline sulfides at depth (Matjuschkin et al., 2016) (**Fig. 5.7b**). Fractionation of crystalline sulfide at the base of the continental crust (*cf.* Jenner, 2017) contrasts with observations in thinner, oceanic island arc/backarc settings, where Cu and Ag systematics suggest that mantle-derived melts are sulfide undersaturated until the point of magnetite fractionation, and only fractionate sulfide after this point in their evolution [e.g., Eastern Manus Basin; Jenner et al. (2010, 2012); Chiaradia (2014)] (**Fig. 5.7**).

Consequently, for oxidised parental arc magmas [e.g., fO_2 of $\sim NNO +2$; Matjuschkin et al. (2016); *cf.* Kelley and Cottrell (2012); Richards (2015)], sulfides

would likely be stable during stalling and subsequent differentiation in 'deep crustal hot zones' (Annen et al., 2006) where the crust is $\geq \sim 20$ km (i.e., mid- to lower continental crust) (**Fig. 5.7b**). In contrast, on stalling at shallower crustal levels (i.e., < 20 km), approximating that of the lower crust of oceanic island arcs, oxidised magmas would not be within the field of sulfide stability (Matjuschkin et al., 2016) (**Fig. 5.7b**), and would thus retain their chalcophiles until their first point of sulfide fractionation was initiated by magnetite fractionation and a fO_2 -related drop in S solubility. Through this mechanism, the 'Magnetite Crisis' plays a more dominant control on the fate of the chalcophile elements in thinner, oceanic arcs than it does in arcs built on thicker crust. Crustal thickness thus exerts a fundamental control on chalcophile element distribution via its influence on initial depths of magmatic differentiation, and the stability of sulfide at these depths.

Figure 5.7. (a) Schematic illustration comparing the processing of Cu beneath thick (≥ 30 km) and thin (≤ 20 km) overriding crust at convergent margins. Fluid mobile chalcophile elements (W, Tl, Sb, Pb, As, Bi) are added to the mantle wedge via a slab flux, whereas the immobile chalcophile elements (Cu, Ag) are retained in the lower oceanic crust. Thicker overriding (continental) crust promotes early sulfide fractionation from the Antuco magmas (and removal of Cu from the ascending magma) due to the increased stability of sulfides at higher fO_2 with increased pressure (and therefore depth) (**inset b**; adapted after Matjuschkin et al., 2016). The thinner nature of the overriding crust at island arcs (IA) and backarc basins (BAB) means sulfides are less likely to be stable at the base of the crust and therefore do not fractionate, allowing Cu contents to increase as magmas ascends prior to magnetite induced sulfide fractionation.



5.3.4. A role for garnet fractionation?

Recently, Tang et al. (2018) used an inverse correlation between $[Dy/Yb]_N$ and FeO_T/MgO of global arc magmas to argue that garnet fractionation results in the simultaneous Fe depletion and increase in fO_2 of magmas, from initial fO_2 values comparable to MORB, during early differentiation of continental arc magmas. As a consequence, because the solubility of sulfur decreases with decreasing FeO_T , if primitive magmas intruding the lower continental crust were fractionating garnet, this would be expected to induce sulfide fractionation (and would also be a mechanism to increase fO_2 of the residual magma). As such, this provides an additional mechanism for deep-crustal sulfide fractionation, distinct from pressure-related effects on the sulfide stability field (e.g., Matjuschkin et al., 2016).

A direct comparison cannot be made between our data from Antuco and the trend observed between $[Dy/Yb]_N$ and FeO_T/MgO presented by Tang et al. (2018), as the FeO_T values presented for global arc magmas are for intermediate compositions (i.e., 4 ± 1 wt.% MgO) only, highlighting garnet fractionation-induced Fe depletion. However, REE systematics presented by Davidson et al. (2007, 2012) demonstrate the difference between amphibole and garnet fractionation; amphibole fractionation will result in a decrease in Dy/Yb with increasing SiO_2 , whereas garnet fractionation will result in an increase in Dy/Yb with increasing SiO_2 . Thus, the decrease in Dy_N/Yb_N with increasing SiO_2 , and positive correlation between Dy/Dy^* and Dy_N/Yb_N of the Antuco suite is consistent with amphibole, not garnet fractionation (**Fig. 5.8**). The absence of amphibole phenocrysts in the Antuco samples further supports Davidson et al.'s (2012) interpretation that these REE ratios imply “cryptic” amphibole fractionation.

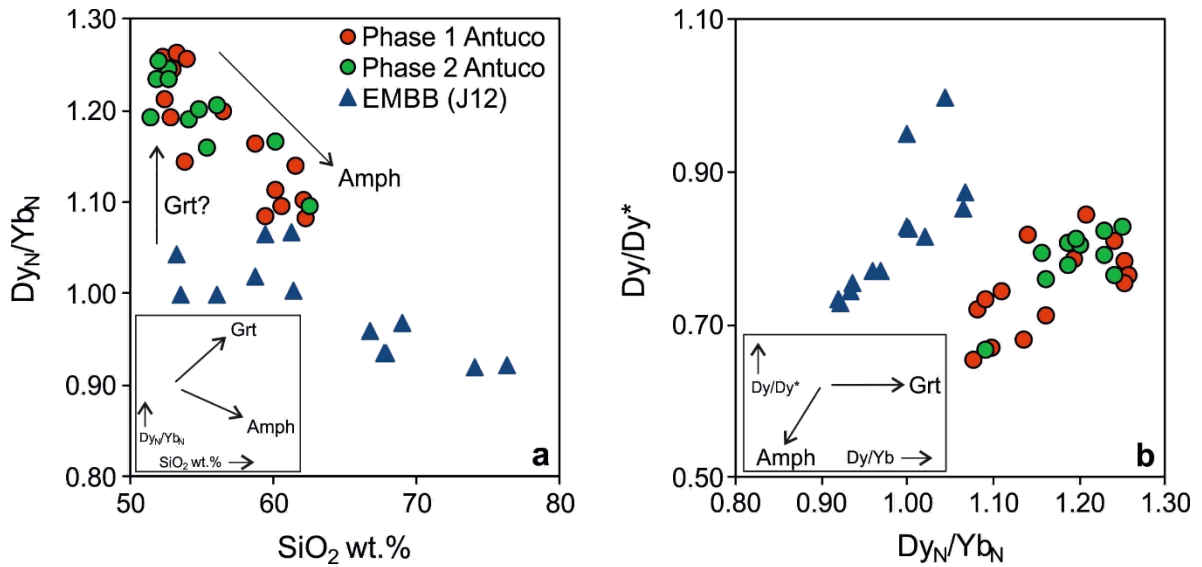


Figure 5.8. Rare Earth Element systematics of the Antuco magmas. Decreasing Dy_N/Yb_N with increasing SiO_2 (a), and a positive correlation between Dy/Dy^* and Dy_N/Yb_N (b) suggest “cryptic amphibole fractionation” from the Antuco magmas (e.g., Davidson et al., 2013, 2007). EMBB (J12): Eastern Manus Backarc Basin (data from Jenner et al., 2012). Normalising values from Sun and McDonough (1989). Grt: garnet; Amph: amphibole.

Despite arguing that at Antuco the magmas have been affected by amphibole, rather than garnet fractionation, we do not discount Tang et al.'s (2018) suggestion that the crystallising assemblage from arc magmas is likely to transition from magnetite to garnet fractionation if the crust becomes sufficiently thick. Indeed, the noticeably higher Dy_N/Yb_N of the most primitive Antuco samples compared to the Eastern Manus Backarc Basin suite is consistent with the fractionation of garnet (**Fig. 5.8**). Thus, the high Dy_N/Yb_N and low Cu/Ag of the Antuco suite could indicate that garnet and sulfide were fractionated from the most primitive Antuco magmas (during the earliest or deepest stages of magmatic differentiation), prior to ascent. Additionally, a minor initial decrease in Fe_2O_3 with increasing SiO_2 (**Fig. 5.2c**) supports an initial stage of garnet fractionation.

However, the degree of garnet fractionation from the Antuco magmas appears minimal (based on the D_{Y_N}/Y_{b_N} trends supporting a predominance of amphibole fractionation). As such, we still call upon the effect of pressure on the sulfide stability field (Matjuschkin et al., 2016) to achieve sulfide saturation in the lower continental crust and explain the overall Cu/Ag trends at Antuco, which is a satisfactory explanation especially if convergent margin magmas have a higher initial fO_2 compared to MORB or are driven to a higher fO_2 as a consequence of garnet fractionation.

5.3.5. Sulfide fractionation and Cu – Ag systematics

To place constraints on the proportion of sulfide fractionation required to explain the Cu and Ag systematics of the Antuco magmas, we have used the following fractional crystallisation equation:

$$C_i = C_o^*(F^{D_o-1})$$

where, C_i is the concentration of an element in the resultant melt, C_o is the concentration of an element in the source prior to fractional crystallisation, F is the fraction of melt remaining, and D_o is the bulk-partition coefficient of an element prior to fractional crystallisation.

Starting compositions used for Cu (68.9 ppm) and Ag (0.04 ppm) are those of the most primitive (highest MgO wt.%) Antuco sample (An27-7). Partition coefficients used for Cu and Ag in crystalline (monosulfide solid solution) sulfides ($K_{d_{Cu}^{Sul}}$: 215, $K_{d_{Ag}^{Sul}}$: 24) were those derived experimentally by Li and Audétat (2012) (average of experiments LY15 and LY17) and are chosen as they are determined under conditions that best replicated a subduction zone setting (i.e., oxidised). Available partition coefficients for Cu and Ag in plagioclase and olivine show them both to be very low at

$\ll 0.1$ (Ewart et al., 1973; Adam and Green, 2006; Lee et al., 2012). As such, both plagioclase and olivine were grouped as one in the modelling calculations. For full details on the modelling parameters, see **Table 5.1**.

With only a minor volume (0.5 to 0.6 wt.%) of sulfide fractionation, broadly flat to slightly decreasing Cu and increasing Ag trends can be produced (**Figs. 5.9a,b**). Consequently, as a result of the divergent trends in Cu and Ag, a continual decrease in Cu/Ag is also produced (**Fig. 5.9c**). These trends match those seen in Cu and Ag at Antuco and supports our conclusion that the Antuco magmas have been affected by a small degree (~0.5 wt.%) of sulfide fractionation throughout their petrogenesis.

Table 5.1 Fractional crystallisation modelling parameters

	Plagioclase / Olivine	Sulfide
Mineral proportion	0.994	0.006
Kd	Cu	Ag
Plagioclase / Olivine	0.05	0.001
Sulfide (crystalline)	215	24
Do	1.340	0.145
Co (16DCCaHu.017)	68.923	0.038

Kd: Partition coefficient for a particular element in a mineral, Do: Bulk-distribution coefficient of a particular element prior to fractional crystallisation, Co: Concentration of a particular element in the source.

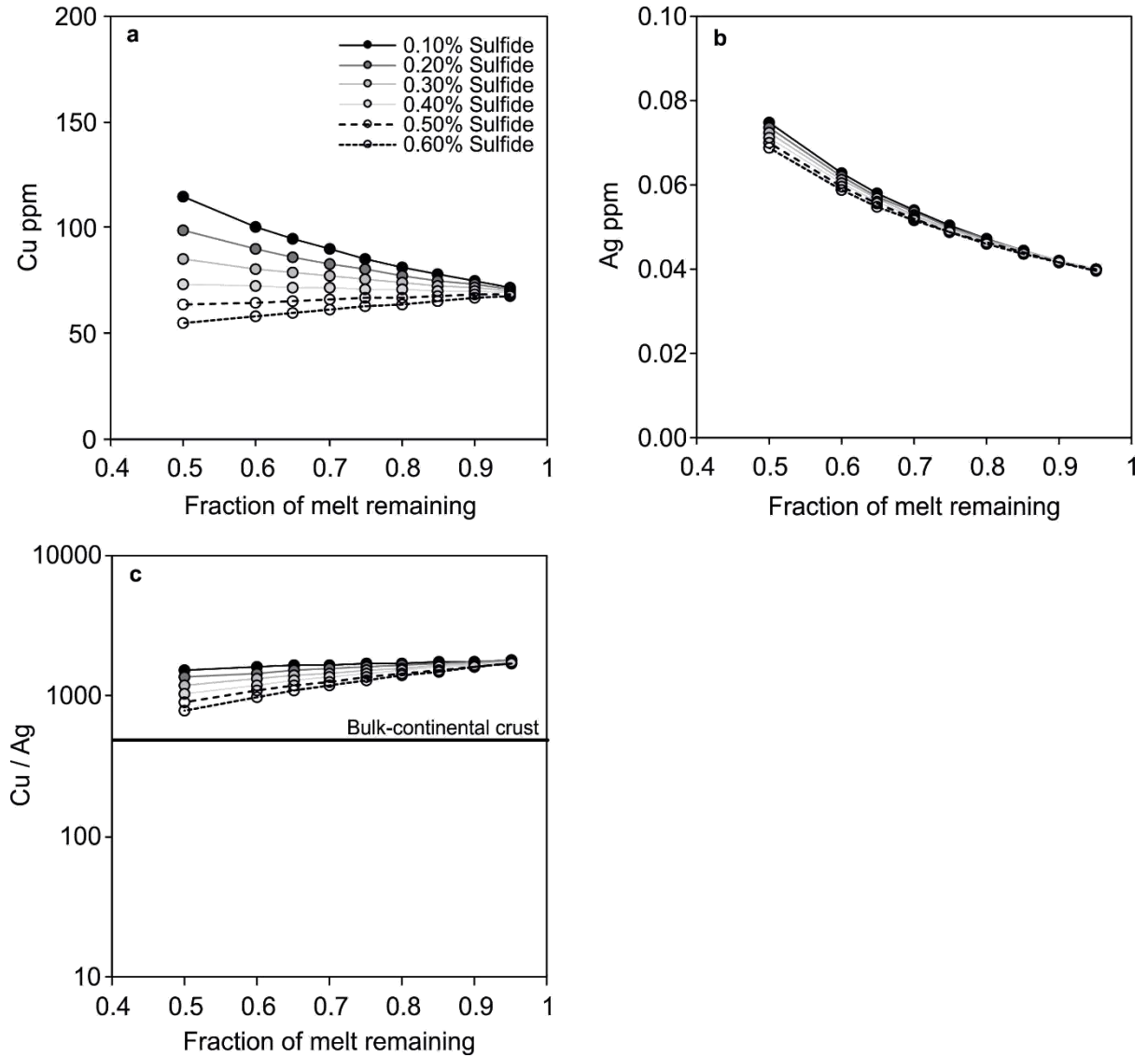


Figure 5.9. Trace element modelling of fractional crystallisation. Minimal sulfide fractionation (0.5 – 0.6 wt.%) is required to produce divergent trends in Cu (a) and Ag (b) and Cu/Ag approaching that of the bulk continental crust (c), as observed in the Antuco samples. Starting Cu and Ag compositions used were those of the most primitive (highest MgO wt.%) Antuco sample (An27-7). The composition of the bulk continental crust is plotted for comparison [data from Rudnick and Gao (2003)].

5.4. Conclusion

The near complete suite of chalcophile elements were analysed in twenty-six volcanic rock samples from Antuco Volcano, Chile, which were used to investigate their processing and distribution within the magmatic system of a typical continental arc stratovolcano. Enrichments in W, Tl, As, Pb, Sb and Bi in the Antuco volcanic rocks suggest these chalcophile elements were mobilised during subduction. Additionally, the relative enrichments of these chalcophile elements indicate that the flux of elements from the oceanic crust to the mantle wedge is determined by their prior concentration in the subducting upper oceanic crust. Cu and Ag concentrations similar to the global MORB array suggest that neither Cu nor Ag were mobilised during subduction, and that Mo, Sn, Zn, Ga and Co were also immobile. Very low Se and S concentrations relative to the global MORB array reflect low-pressure degassing of these elements during eruption, preventing the reconstruction of Se systematics from subaerial volcanic rocks.

Inflections in the TiO_2 , Fe_2O_3 and V concentrations, and a corresponding (minor) drop in Cu contents and Cu/Ag of some Phase 1 Antuco samples at ~55 wt.% SiO_2 and ~3 wt.% MgO, suggests that magnetite fractionation occurred during the crustal evolution of these magmas. However, in contrast to oceanic arc magmas, there is no strong correspondence between magnetite and sulfide fractionation. Mostly flat Cu and Ag trends indicate that the Antuco melts were already sulfide saturated from a very early stage in their crustal history, and well before magnetite fractionation. Fractionation of Cu from Ag (i.e., a decreasing Cu/Ag ratio throughout the evolutionary trend) suggests that the fractionating sulfide phase was crystalline and can be explained by 0.5 to 0.6% of fractionating sulfide during crustal differentiation. The low

Cu/Ag of the most primitive Antuco samples compared to the global MORB array suggest an early, high-pressure stage of sulfide fractionation from the Antuco magmas. This implies that sulfide fractionation began at the base of the continental crust, in primitive magmas, and that sulfide is stable at lower crustal pressures in continental arcs, which is the predominant depth range of magmatic differentiation. As such, sulfide fractionation was not strongly influenced by magnetite fractionation, as is more likely the case in thinner, oceanic arcs. In oceanic arcs, the initial depth range of magmatic differentiation may be outside the field of sulfide stability, and magnetite thus acts as a dominant control on sulfide fractionation. We have shown that crustal thickness plays an important role in controlling the differentiation of continental arc magmas and the resulting distribution of the chalcophile elements in the arc crust. Beneath continental arcs, these processes would lead to the formation of a theoretical chalcophile-rich reservoir at or near the base of the continental crust that could be tapped to fuel ore deposit formation.

Chapter 6

Arc-scale processing of the chalcophile elements: implications for the formation of ore deposits

6.1. Introduction

In the detailed study of Antuco (**Chapter 5**), a typical continental arc stratovolcano with a broad compositional range of erupted products, it was demonstrated that the Cu contents and Cu/Ag of Antuco's magmas continually decrease with differentiation indexes. This was used to suggest that Antuco's magmas had fractionated crystalline sulfide throughout their evolutionary history. Furthermore, the depleted Cu/Ag of the most primitive Antuco samples relative to the global MORB array suggested that crystalline sulfide began to fractionate at an early stage in the evolution of Antuco's magmas, likely at or near the base of the continental crust. By comparison with data from other continental arcs and oceanic arc/back-arc settings, it was also argued that the overriding crustal thickness at a convergent margin plays a dominant role in controlling the initial depth of magmatic differentiation, and therefore acts as a major control on the timing of sulfide saturation.

Although garnet was demonstrated to fractionate during the petrogenesis of Antuco's magmas, as evidenced by heavy Rare Earth Element (HREE) depletion relative to the light/middle REE (L/MREE) and elevated D_{Yb} / Yb_N relative to back arc

basin magmas, the effect of pressure on the stability field of sulfide (e.g., Matjuschkin et al., 2016) was concluded to be the dominant factor inducing sulfide saturation in Antuco's magmas. Recent experimental work has also indicated that the sulfide stability field is temperature dependant (e.g., Nash et al., 2019). This chapter expands on the detailed study presented on Antuco to test whether the same conclusions can be replicated at other arc stratovolcanoes in Chile, and to explore in more detail the importance of crustal thickness and pressure on the behaviour of the chalcophile elements during the petrogenesis of continental volcanic arc magmas. Comparisons are made between whole rock major and trace element analyses of volcanic rock samples from stratovolcanoes sat on thick (northern Chile) versus thinner (central – southern Chile) continental crust in the Chilean Andes, and the implications of these observations for the formation of ore deposits are also considered.

6.2. Geological context

Volcanic rock samples (mostly lavas) presented in this chapter were collected from several stratovolcanoes throughout the Central and Southern Volcanic Zones (C/SVZ) of the Chilean Andes, including Yate, Apagado, Hornopirén, Villarrica, Quetrupillán, Lanín (SVZ), San Pedro and Ollagüe (CVZ) (**Figs. 2.2 and 2.6**), as introduced in **Chapter 2**. The stratovolcanoes for which data are presented here are collectively referred to as the Chilean stratovolcanoes throughout this chapter.

The CVZ and SVZ represent ideal locations to investigate the importance of the depth of magma storage and modification, and therefore pressure, on the behaviour of the chalcophile elements (e.g., Lee et al., 2012; Chiaradia, 2014), as the thickness of the overriding continental crust varies along the length of Chile, thickening from the southernmost SVZ (≤ 30 km) to the CVZ of the Atacama Desert ($\geq 70 - 80$ km)

(Tassara et al., 2006; Tassara and Echaurren, 2012; Assumpção et al., 2013). The thickness of the overriding continental crust on which Yate, Apagado, Hornopirén (~25 – 30 km), Villarrica, Quetrupillán, Lanín (~ 35 – 40 km), Antuco (~40 km), Ollagüe and San Pedro (~70 – 80 km) are situated varies considerably, spanning the range defined by continental volcanic arcs globally (e.g., Syracuse et al., 2010). Thus, the suite of samples from stratovolcanoes situated on varying crustal thicknesses presented here permit an investigation into the effect of pressure on the behaviour of the chalcophile elements. Furthermore, the thickness of the continental crust on which the stratovolcanoes investigated here are situated (i.e., >25 – 30 km) overlaps well with the depth at which garnet becomes stable within most continental arcs [i.e., ≥ 25 km (Alonso-Perez et al., 2009)]. Thus, the effect of garnet fractionation on the behaviour of the chalcophile elements can also be assessed. Comparisons will also be made with a suite of lava analyses from Quaternary-aged stratovolcanoes in Ecuador that are situated on continental crust that is 50 – 70 km thick, and well within the stability field of garnet (Georgatou et al., 2018).

The studied stratovolcanoes also permit the investigation of potential variations in the processing of the chalcophile elements associated with stratovolcano location relative to the arc front or downgoing slab. Examples include Villarrica – Quetrupillán – Lanín, which define a trench-perpendicular volcanic chain at 39°S; Apagado, situated east of the arc front; and Ollagüe, which is located west of the arc front.

6.3. Geochemical Results

6.3.1. Major elements

On a total alkali versus silica (TAS) plot volcanic rock samples from the Chilean stratovolcanoes define a bi-modal distribution [i.e., the ‘Daly Gap’; Daly (1914)],

classifying as either basalts to basaltic-andesites or evolved trachy-andesites to trachytes (**Fig. 6.1a**). Of note, the sample suite from Yate displays a range in composition (51.7 – 67.0 wt.%; anhydrous values), from basalt through dacite, broadly matching the compositional range defined at Antuco (grey field). According to the AFM [alkali – FeO (as total Fe) – MgO] ternary plot, the bulk of the volcanic rock samples are of calc-alkaline affinity (**Fig. 6.1b**).

On major element bivariate plots (**Fig. 6.2**), samples from Yate display a broad range in their MgO contents (1.6 to 7.3 wt.%). Sodium negatively correlates with MgO, while K₂O, P₂O₅ and CaO have no correlation with MgO. Seven (of ten) Yate samples have CaO contents between 8 and 10 wt.%, with the remaining three having CaO contents of 3.76, 5.11 and 5.14 wt.%. Iron (as total Fe), Al₂O₃, TiO₂ and MnO generally increase with decreasing MgO, reaching maximums of 9.25, 20.21, 1.17 and 0.16 wt.% at ~3 wt.% MgO, respectively, before decreasing with further decreasing MgO. Several samples display Al₂O₃ contents that are depleted relative to other stratovolcanoes at a given MgO (**Fig.6.2b**).

Samples from Apagado cluster at either ~4 wt.% or between 6.5 and 8 wt.% MgO, with each cluster generally having similar major element contents. Hornopirén's samples cluster very tightly in terms of their major element contents, at the more primitive end of the overall trend defined by the Chilean stratovolcanoes.

Lava samples from Villarrica are all basaltic (SiO₂ and MgO contents range from 51.3 to 53.1 wt.% and 4.1 to 5.0 wt.%, respectively), and within this narrow range none of the major element contents show a strong correlation with MgO. Like Villarrica, lava samples from Quetripillán generally have a narrow range in the contents of most major

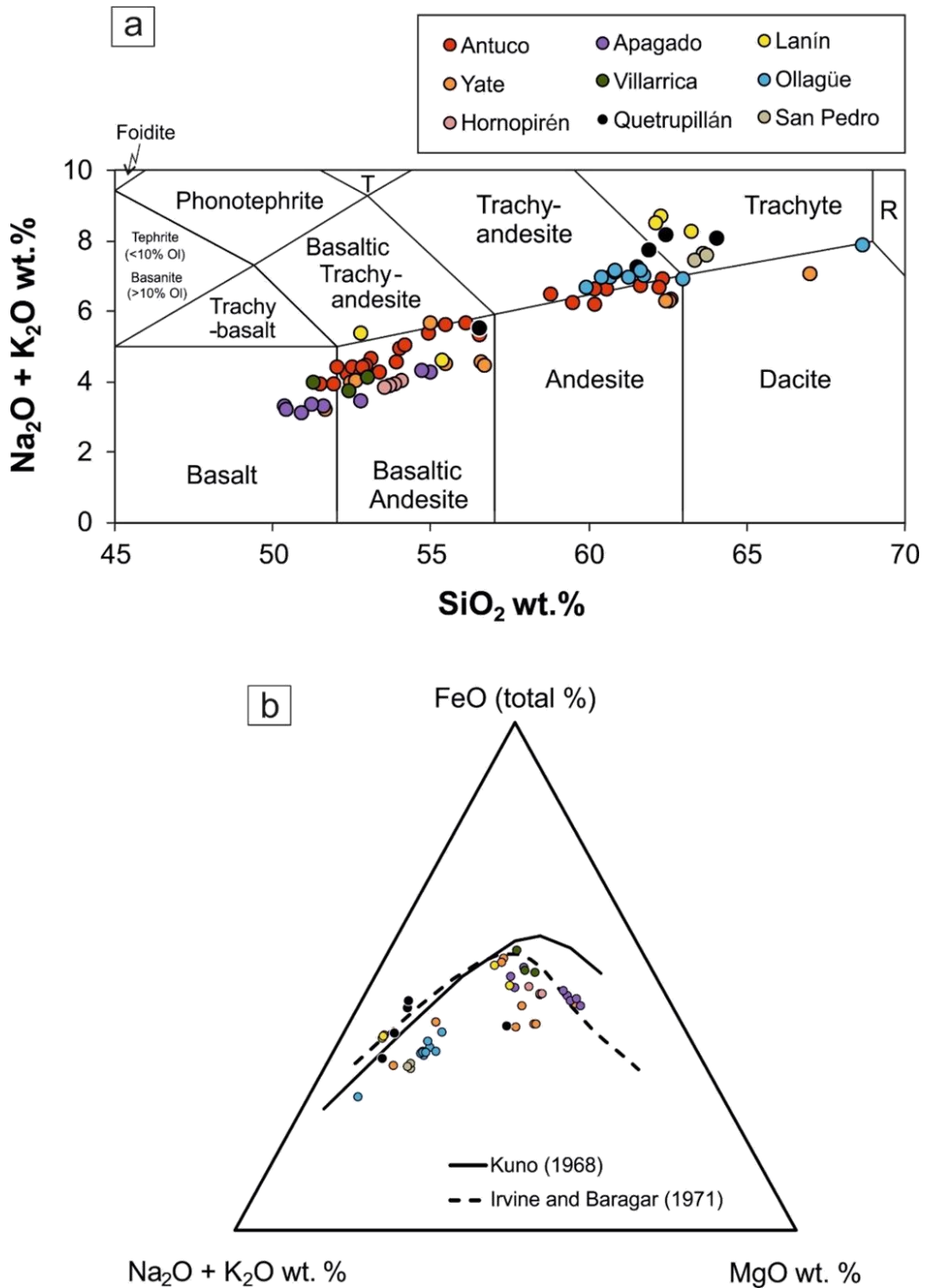


Figure 6.1. Geochemical classification of volcanic rock samples from Chilean stratovolcanoes. (a) Total – alkali – silica (TAS) plot highlighting the compositional range of volcanic rock samples. The Chilean stratovolcano samples presented here overlap with samples from Antuco presented in **Chapter 5**. Classification fields of Le Bas et al. (1986). T: Tephri-phonolite, R: Rhyolite. (b) Alkali – FeO (as total Fe) – MgO ternary plot showing most samples to be calc-alkaline in nature. Plot constructed using TernPlot (Marshall, 2006), with boundaries of Kuno (1968) and Irvine and Baragar (1971).

elements, also having no correlation with MgO. Lava samples from Lanín are bimodally distributed (52 and 55 wt.% and 62 to 63 wt.% SiO₂), with separate groups clustering tightly.

Lava samples from Ollagüe cluster tightly, showing a narrow range in all major element contents with no strong correlation with MgO. Their silica contents range from 60 to 63 wt.%, with one sample drifting to greater SiO₂ contents (68.7 wt.%). As expected, a similar pattern is observed in MgO contents, with most samples clustering in the range 2.3 to 2.8 wt.% MgO. One sample has a lower MgO content (1.12 wt.%), correlating with the sample having the highest SiO₂ content. This sample also extends to lower TiO₂, Al₂O₃, Fe₂O₃, CaO, MnO, K₂O and P₂O₅ (**Fig. 6.2**) than the remaining samples. San Pedro lava samples show a very narrow range in major element contents, clustering very tightly and at similar concentrations to samples from Ollagüe. The MnO contents of samples from both Ollagüe and San Pedro are noticeably depleted relative to the sample sets from Yate, Villarrica, Quetrupillán and Lanín (**Fig. 6.2d**).

The major element contents of samples from the Chilean stratovolcanoes presented here overlap the major element trends defined at Antuco, although some samples from Apagado extend to lower SiO₂ concentrations (**Fig. 6.1a** and **6.2**). The broad compositional range of volcanic samples from Yate follow the same trends of increasing then decreasing Fe₂O₃ and TiO₂ with decreasing MgO (**Fig. 6.2a, c**) as observed at Antuco. Additionally, the Chilean samples presented here (including those from Antuco) show similar trends in CaO, Na₂O and K₂O (**Fig. 6.2e-g**) space as a suite of volcanic rock samples from 15 Quaternary-aged stratovolcanoes in Ecuador, presented by Georgatou et al. (2018). However, similar trends between Chilean and

Ecuadorian samples are not observed in their TiO_2 , Fe_2O_3 or P_2O_5 contents (**Fig. 6.2a, c, h**). Specifically, Chilean samples display an overall increase then decrease in TiO_2 and Fe_2O_3 with decreasing MgO , whereas those samples from Ecuador show a continual decrease in TiO_2 and Fe_2O_3 with decreasing MgO .

Chapter 6. Arc-scale processing of the chalcophile elements: implications for the formation of ore deposits

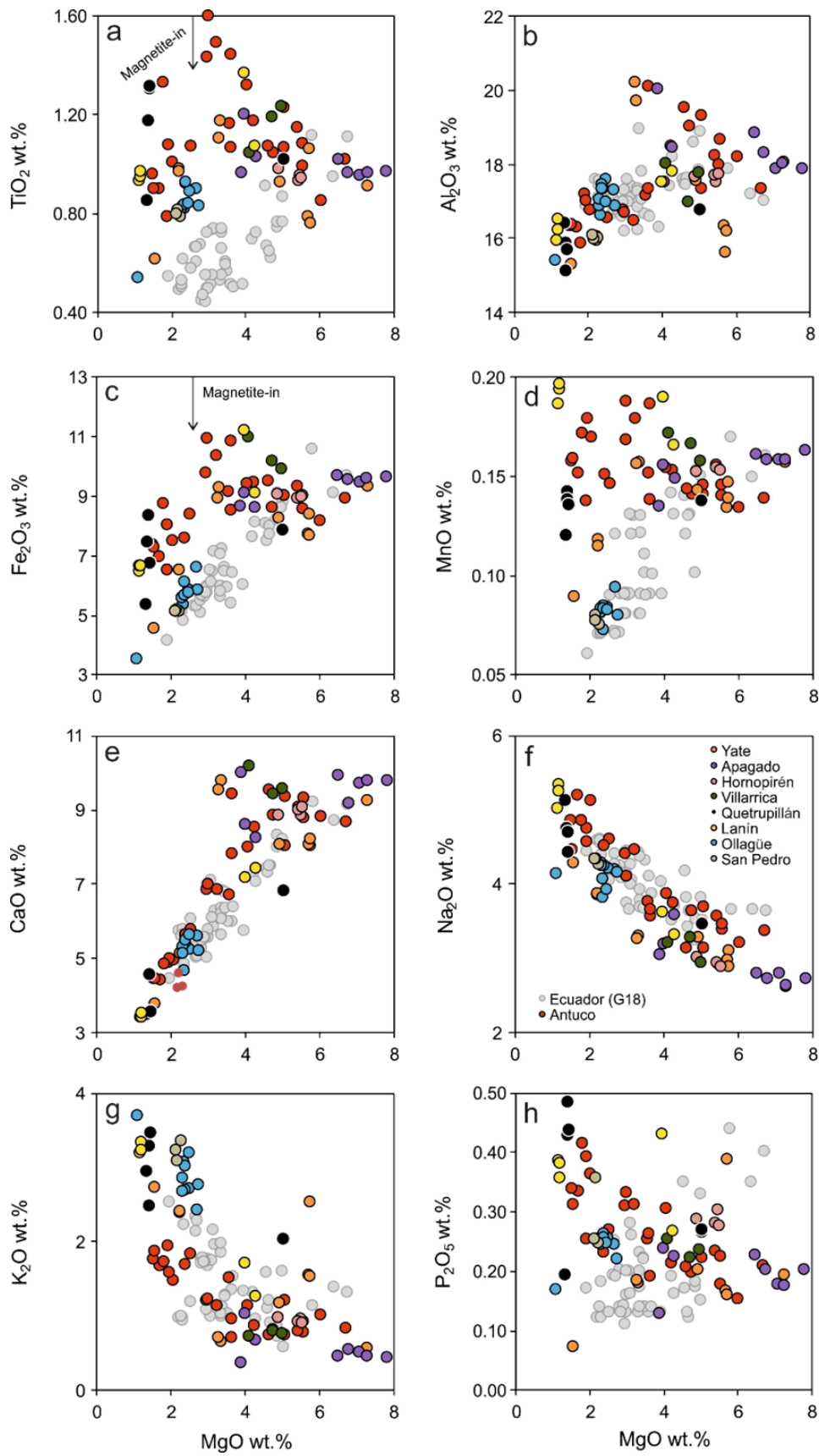


Figure 6.2. Major element bivariate plots (versus MgO) of all Chilean stratovolcano samples. (G18): major element data for Ecuadorian stratovolcanoes from Georgatou et al. (2018).

6.3.2. Trace elements

Collectively, the Cu contents of the Chilean stratovolcanoes correlate negatively with SiO₂ (**Fig. 6.3a**). Additionally, the Cu/Ag of the Chilean suite of samples display a weak negative correlation with SiO₂ (**Fig.6.3e**), with the most evolved samples scattering to lower Cu/Ag. Neither S nor Se correlate with SiO₂ for any of the Chilean stratovolcanoes (**Fig.6.3b, d**). Instead, all samples have considerably lower S and Se contents when compared to the global MORB array. However, a few samples from Ollagüe do have elevated S contents relative to the remainder of the suite of samples, with one sample displaying S contents in excess of the MORB array.

When treated separately, Yate spans the broadest range of whole rock major element compositions after Antuco, and thus makes the best comparison. The trends observed in the chalcophile element contents of volcanic rock samples from Yate are similar to those trends observed at Antuco, although the positive correlation observed in Yate's Ag contents with SiO₂ is subtler than that at Antuco; Ag contents at Antuco are greater than Yate at a given SiO₂ content (**Fig. 6.3c**). Additionally, the trend observed in Yate's Cu contents is similar to that observed in Ecuadorian stratovolcanoes (Georgatou et al., 2018), as also observed at Antuco. Cu and Ag data from the other stratovolcanoes are consistent with the trends defined by Yate and Antuco, with the exception of the Cu contents of lava samples from Villarrica, which are noticeably enriched compared to the global MORB array at a similar SiO₂ (**Fig. 6.3a**).

Chapter 6. Arc-scale processing of the chalcophile elements: implications for the formation of ore deposits

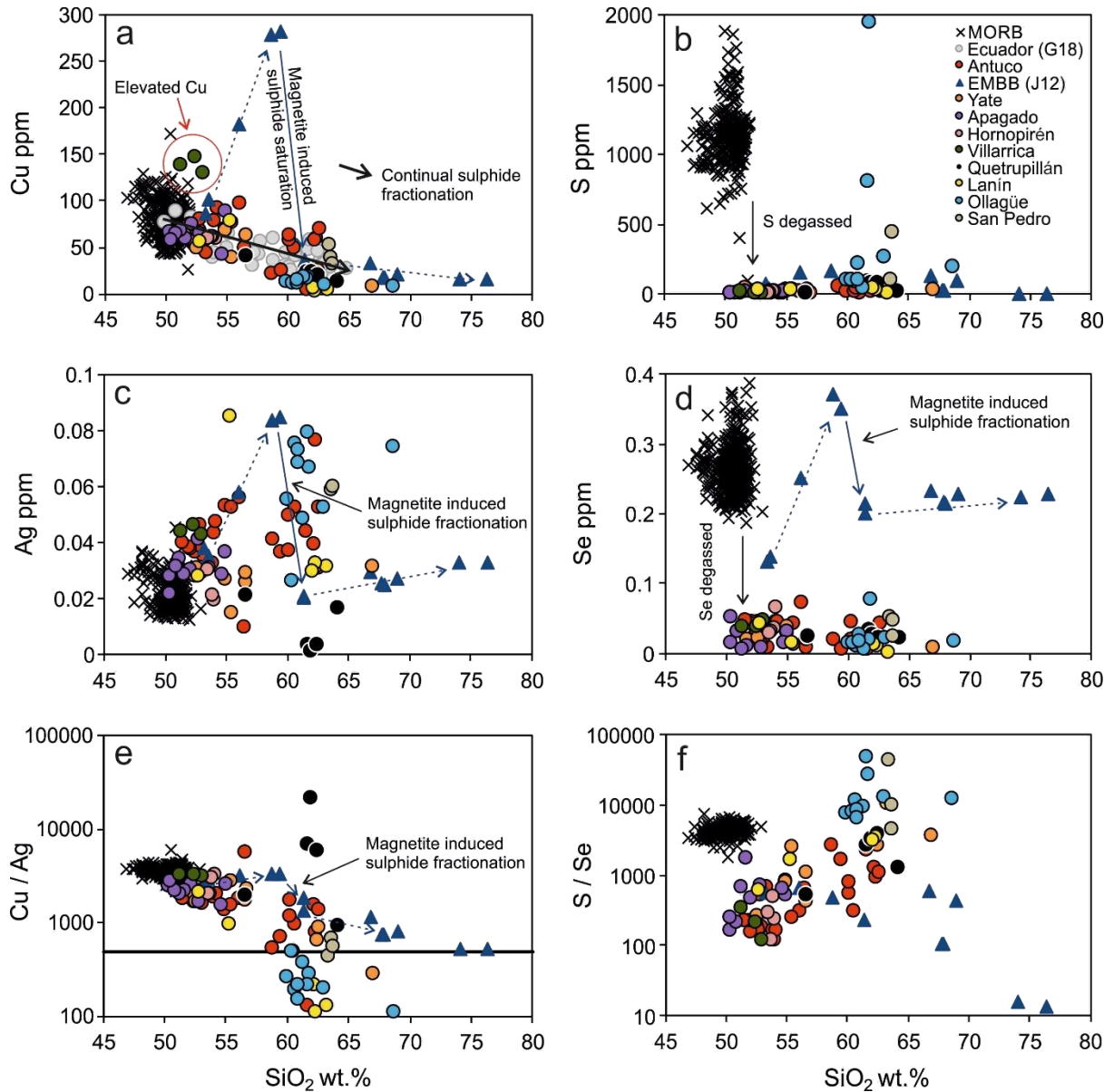


Figure 6.3. Cu, Ag, Cu/Ag, S, Se and S/Se bivariate plots (versus SiO_2) of all Chilean stratovolcano samples. (G18) Cu data for Ecuadorian stratovolcanoes from Georgatou et al. (2018); (J12): Eastern Manus Backarc Basin (EMBB) data from Jenner et al. (2012); Global MORB array from Jenner and O'Neill (2012); Cu/Ag of the bulk continental crust from Rudnick and Gao (2003).

On (C1) Chondrite normalised REE plots (**Fig.6.4**), the SVZ stratovolcanoes all display similarly smooth REE patterns: LREE enriched relative to the M/HREE $[(La/Sm)_N \sim 1.4 - 3]$ and depleted in the HREE relative to the MREE $[(Gd/Yb)_N \text{ mostly } 1.4 - 1.8]$. Those samples from Ollagüe and San Pedro have greater enrichments in the LREE relative to the M/HREE $[(La/Sm)_N \sim 3.4 \text{ to } 4]$, and are more depleted in the HREE relative to the MREE $[(Gd/Yb)_N \text{ mostly } \sim 2.1 \text{ to } 3.4]$. As a consequence of the more extensive LREE enriched and HREE depleted patterns at Ollagüe and San Pedro, their samples have considerably steeper overall REE patterns $[(La/Yb)_N \text{ mostly } \sim 18 - 22, \text{ although entire range is broader } (\sim 13 - 46)]$ than those of the SVZ stratovolcanoes $[(La/Yb)_N \sim 2.5 \text{ to } 6.5]$. Furthermore, all samples have minor to negligible negative Eu anomalies ($Eu/Eu^* \geq 0.70$). Samples from SVZ stratovolcanoes display broadly similar REE patterns to those observed at Antuco, whereas both Ollagüe and San Pedro have much greater enrichments in the LREE and depletions in the HREE when compared to Antuco.

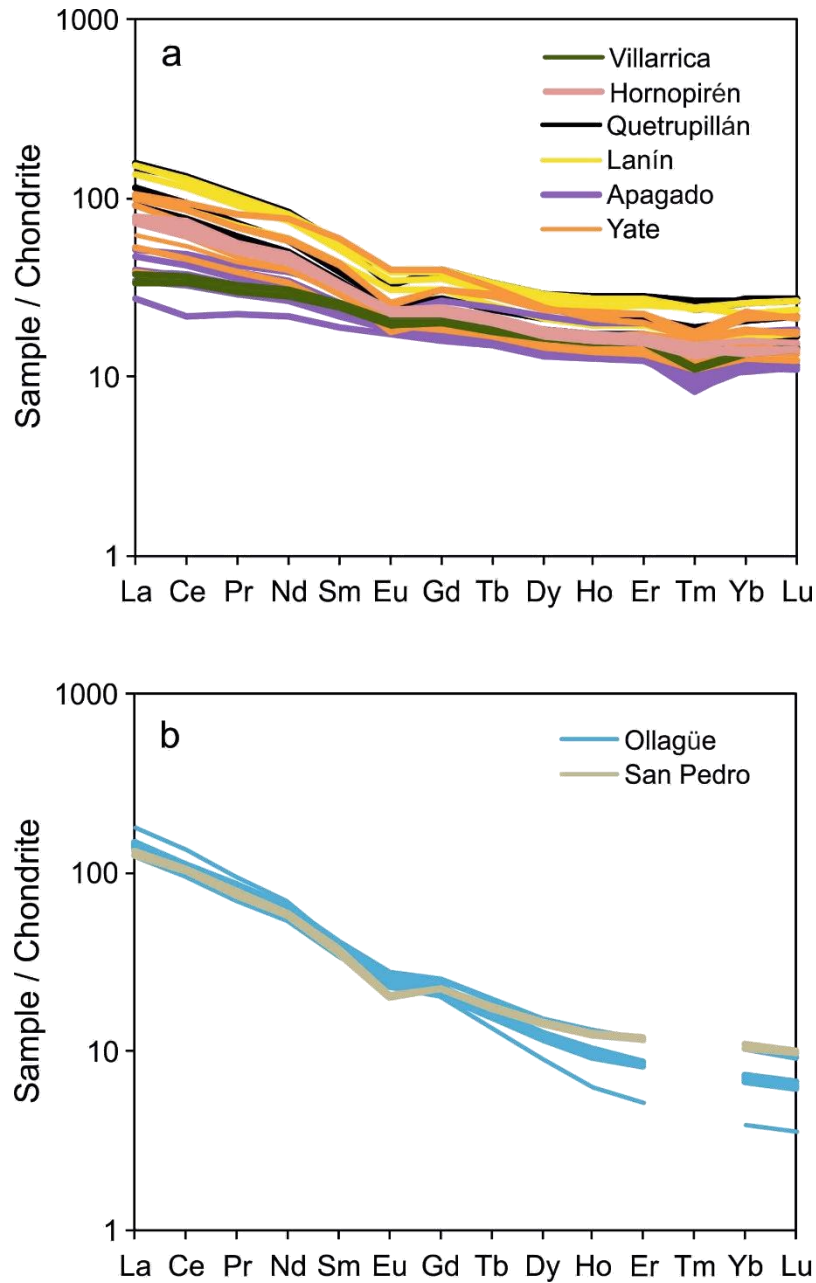


Figure 6.4. (C1) Chondrite normalised Rare Earth Element (REE) plots of all Chilean stratovolcano samples from the Southern (a) and Central (b) Volcanic Zones. Normalising values as of Sun and McDonough (1989).

6.4. Discussion

6.4.1. Crustal processing of the chalcophile elements

As discussed in **Chapter 5**, only Cu, Ag and Se [‘purely chalcophile’ end-members; *cf.* Jenner (2017)] can be used to truly investigate the behaviour of S within evolving arc magmas. This is because the remaining chalcophile elements (e.g., As, Tl, Sb, Pb, In, Ga, Zn, Sn) have either too low sulfide – silicate melt partition coefficients or have ‘mixed affinities’, meaning their behaviour is not only controlled by sulfides, but also by silicates (Jenner, 2017). However, as was the case at Antuco, the majority of the Chilean stratovolcanoes presented here have all extensively degassed S and Se, as evidenced by S and Se contents considerably lower than the global MORB array, and in the case of Se, depleted relative to Eastern Manus Backarc Basin (EMBB) magmas (**Fig.6.3**). Thus, the Se contents of the Chilean stratovolcanoes cannot be used to assess the behaviour of S during magma ascent and subsequent evolution. Further to this, the observation that S/Se is lower than the global MORB array suggests that S was more volatile than Se during degassing (**Fig. 6.3f**) across all the studied SVZ stratovolcanoes. The elevated S/Se of the CVZ stratovolcanoes relative to the global MORB array contrasts with the SVZ. However, this is unlikely to suggest increased volatility of Se over S, as the absolute Se contents of the CVZ stratovolcanoes are similar to those of the SVZ stratovolcanoes. Rather, the elevated S/Se is inferred to be a result of Ollagüe’s and San Pedro’s elevated S contents, which could reflect either assimilation of S-rich country rock during magmas ascent, as both stratovolcanoes have been effected by crustal contamination (Francis et al., 1977; Feeley et al., 1993), or the possible presence of sulfide inclusions in the samples. As the Cu contents of Ollagüe’s and San Pedro’s samples are very low, the presence of

sulfide inclusions seems unlikely. Nevertheless, to more accurately constrain the relative behaviour of S and Se, mineral-hosted melt inclusion analysis would be required.

The new Cu and Ag data presented here for Chilean stratovolcanoes generally follows the trends defined by Antuco and Ecuadorian stratovolcanoes (**Fig.6.3a,c,e**); that is, decreasing Cu and Cu/Ag and broadly increasing Ag with increasing SiO₂. Consequently, this suggests that the Chilean stratovolcano magmas were all saturated in a sulfide phase across their entire compositional range. Moreover, the continually decreasing Cu/Ag of the Chilean stratovolcanoes with increasing SiO₂, and the lower Cu/Ag of the most primitive samples relative to the global MORB array at a given SiO₂ (**Fig.6.3e**), suggests that the fractionating sulfide phase was crystalline, rather than molten, in nature (Li and Audétat, 2012, 2015).

Interestingly, samples from Villarrica prove to be an exception, having Cu contents that are elevated relative to other Chilean and Ecuadorian stratovolcanoes and the global MORB array at a given SiO₂ (**Fig.6.3a**), and lying above the trend defined by these stratovolcanoes. Furthermore, the Cu/Ag of Villarrica's samples (~3,100 – 3,200) are similar to that of the global MORB array and elevated relative to the majority of Chilean stratovolcanoes (generally <3,000) (**Fig. 6.3e**). Thus, in contrast to the other stratovolcano magmas studied here, Villarrica's magmas appear to have not lost their Cu during magma ascent and subsequent evolution. This suggests that they were sulfide undersaturated, as was the case in the more primitive samples from the EMBB (e.g., Jenner et al., 2012). It is also perplexing that the samples from Villarrica have considerably elevated Cu contents relative to Quetrupillán and Lanín,

despite their close proximity (<50 km; **Fig. 2.4**), with the latter both having lost their Cu through sulfide fractionation (**Fig.6.3a**).

6.4.1.1. The role of pressure on the chalcophile elements during the petrogenesis of continental arc magmas

As previously discussed in **Chapter 5**, Antuco's magmas were demonstrated to have fractionated garnet during their petrogenesis [elevated $(Dy/Yb)_N$ relative to low pressure back arc magmas], although amphibole was shown to be the more dominant fractionating phase, and thus pressure was argued to play a more significant role than garnet fractionation in achieving sulfide saturation. The suite of samples from Chilean stratovolcanoes presented here, situated on a broad array of crustal thicknesses (25 – ≥ 70 km), allow the role of pressure on the behaviour of the chalcophile elements to be explored more thoroughly.

All Chilean stratovolcanoes display evidence of garnet fractionation, having $(Gd/Yb)_N > 1$ and elevated $(Dy/Yb)_N$ compared to low pressure-derived EMBB magmas (**Fig.6.5**). However, those stratovolcanoes situated in the CVZ (i.e., Ollagüe and San Pedro), where the continental crust is extremely thick (≥ 70 km), display stronger garnet signatures [$(Gd/Yb)_N > 2$; $(La/Yb)_N$, 12 – 46; lower MnO contents than SVZ stratovolcanoes] than those stratovolcanoes located in the SVZ [$(Gd/Yb)_N \leq 1.7$; $(La/Yb)_N$, 2.5 – 6.0], where the crust is ≤ 40 km. In addition to garnet fractionation, positive correlations of $(Dy/Yb)_N$ and Dy/Dy^* with SiO_2 suggest that amphibole also fractionated from the evolving magma suites (**Fig.6.5a, b**). Thus, this advocates that the Chilean sample suite experienced initial garnet fractionation at minimum depths of ~ 0.8 GPa/ ~ 25 km (Alonso-Perez et al., 2009) prior to amphibole fractionation.

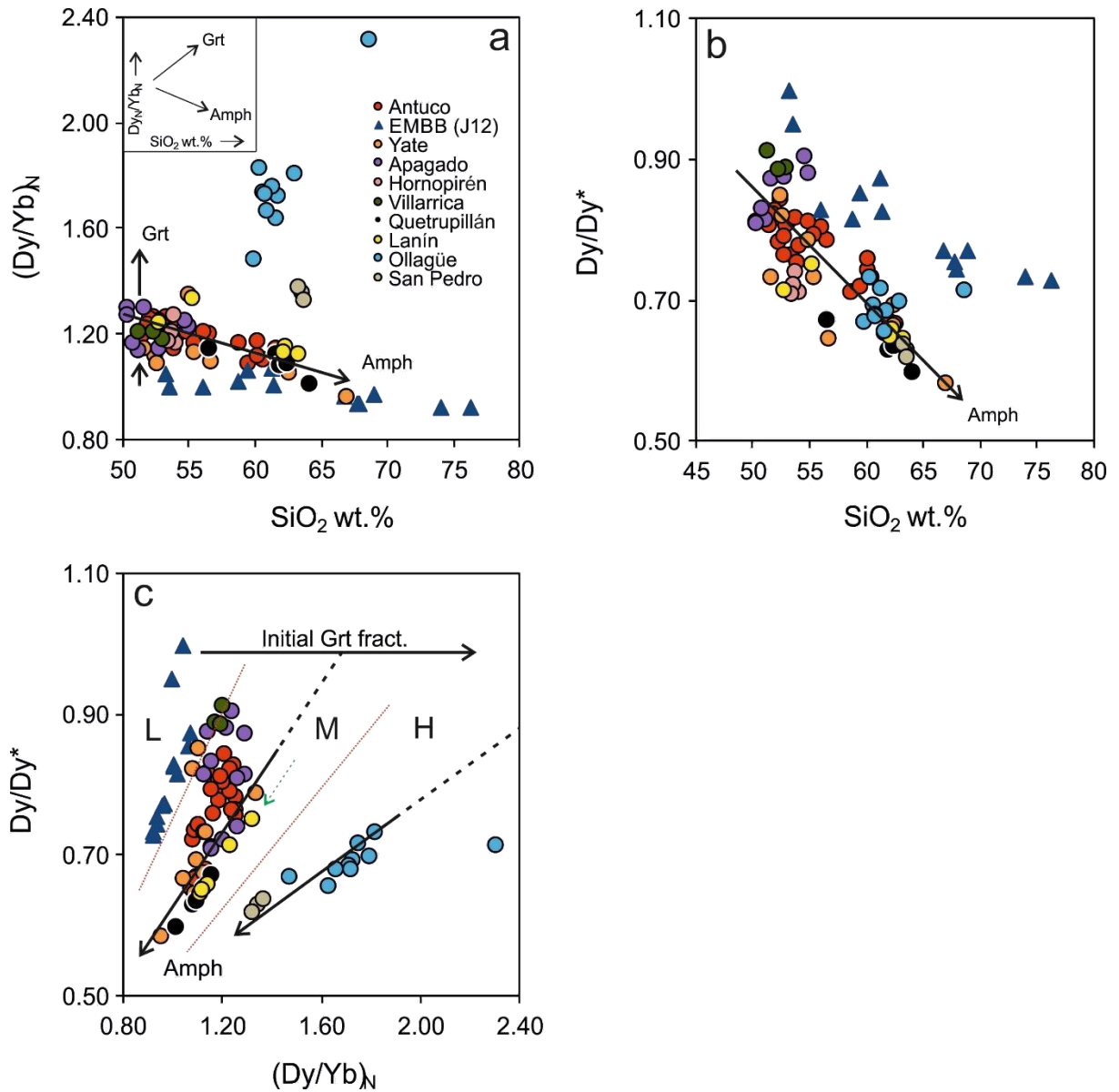


Figure 6.5. Rare Earth Element (REE) systematics of the Chilean stratovolcano samples [after Davidson et al. (2007, 2013)]. Normalising values as of Sun and McDonough (1989). Amph: amphibole; Grt: garnet; L/M/H: low, medium, high (referring to low, medium and high pressure fractionation in the main text); Dy/Dy^* defined as $Dy_N/((La_N^{4/13}) * (Yb_N^{9/13}))$.

Furthermore, when the relationship between $(Dy/Yb)_N$ and Dy/Dy^* of the Chilean stratovolcanoes is assessed in conjunction with that in magmas from the EMBB, three separate trends are apparent; these trends can roughly be attributed to low (L), medium (M) and high (H) pressure fractionation trends, and represent increasing degrees of initial garnet fractionation (**Fig.6.5c**). Consequently, initial garnet fractionation, likely during magma storage in the lower crust, seems to be the driver of stratovolcano parental magmas to greater $(Dy/Yb)_N$ (e.g., see arrows on **Fig. 6.5c**).

Of note is the positioning of the cluster of samples from Villarrica (**Fig.6.5c**). Considering the close proximity (<50 km) of each of the stratovolcanoes in the Villarrica – Quetrupillán – Lanín volcanic chain and the similar crustal thickness on which they are situated, samples from Villarrica again appear offset toward the low pressure fractionation trend defined by EMBB samples, away from both Quetrupillán and Lanín, which themselves produce a well-defined positive correlation between Dy/Yb and Dy/Dy^* . The dashed, green arrow in **Fig. 6.5c** highlights the trajectory along which samples from Villarrica would be expected to plot, if they followed a similar trend to the other stratovolcanoes in the chain, whereas they lie at a much lower-pressure position.

An alternative way of assessing the REE patterns of a sample suite is through ‘shape coefficients’ (e.g., O’Neill, 2016), which can be used to evaluate the linear slope (λ_1) and curvature (λ_2) of a REE pattern, as annotated in **Fig. 6.6**. The vectors ‘Amph’ and ‘Grt’ highlight the trends that would be expected from amphibole and garnet fractionation, respectively. The red, dashed tramlines highlight the trend defined by the bulk of ocean floor basalt (OFB) analyses, which include analyses of spreading ridges, fracture zones, seamounts, aseismic ridges and back arc basins. As an example, a suite of analyses from the Hawaiian plume are plotted to exemplify the offset related

to garnet fractionation. This figure has been used to compare interpretations drawn using the REE systematics of Davidson et al. (2007, 2012). The bulk of the Chilean stratovolcano dataset cluster tightly within a narrow range of λ_1 (5 to 11), at slightly higher λ_1 at a given λ_2 relative to the OFB array and EMBB suite. This is suggestive of minimal garnet fractionation; although, the cluster defines a trend that would be expected for amphibole fractionation. However, samples from Ollagüe and San Pedro plot noticeably to the right of the OFB array and other Chilean stratovolcanoes, demonstrating a stronger garnet signature that is consistent with the patterns seen in the REE systematics (**Fig. 6.5**) and their location on significantly thicker continental crust.

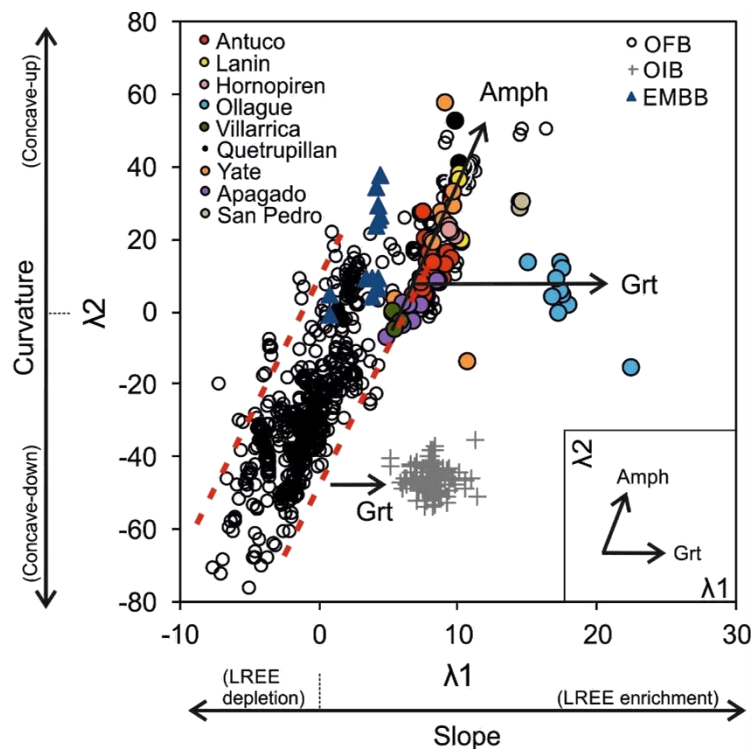


Figure 6.6. ‘Shape coefficients’ used to describe the Rare Earth Element (REE) patterns of the Chilean stratovolcano samples [after O’Neill (2016)]. λ_1 describes the overall slope of the REE pattern, while λ_2 describes the curvature of the REE pattern. Red, dashed tramlines define the trend of the bulk of OFB data. OFB: ocean floor basalt [data from Jenner and O’Neill (2012)]; OIB: ocean island basalt (Hawaii) [data from Feigenson et al. (2003)]; EMBB: Eastern Manus Backarc Basin samples [data from Jenner et al. (2012)]; Amph: amphibole; Grt: garnet.

Overall, the fractionation of garnet appears to be a widespread process in the genesis of the Chilean continental volcanic arc magmas, but much more extensive at stratovolcanoes situated atop thicker crust. Consequently, this supports recent work by Tang et al. (2018), who argued for the importance of crustal thickness in producing calc-alkaline differentiation series magmas (i.e., Fe depleting), generally associated with the continental crust and continental volcanic arcs. Tang et al. (2018) demonstrated that arcs situated on thicker crust are systematically more depleted in Fe, because of an earlier onset of Fe depletion associated with garnet fractionation, favoured at higher pressures, than arcs situated on thinner crust. However, what this means for the Cu contents and Cu/Ag of continental arc stratovolcanoes is yet to be fully explored.

The samples with the strongest garnet signature (i.e., those from Ollagüe and San Pedro) have some of the lowest Cu/Ag values (<660, mostly <400) in the Chilean stratovolcano datasets (**Fig. 6.3e**). This is consistent with the conclusions drawn by Tang et al. (2018), that garnet fractionation from continental arc magmas would induce sulfide saturation through the depletion of a magma in Fe, because of the strong dependence of S solubility on the FeO content of a magma (O'Neill and Mavrogenes, 2002). However, Tang et al. (2018) also argued that in addition to depleting a magma in Fe, garnet fractionation would simultaneously oxidise the magma. Increased fO_2 of a magma would be expected to destabilise sulfides and release Cu back into the magma, thus acting against the effects of Fe depletion. Ollagüe and San Pedro have some of the lowest Cu contents of the Chilean stratovolcanoes, which suggests they have lost much of their Cu and implies that sulfides must have been stable at the base of the continental crust. This is hard to reconcile with Fe depletion, and a consequent

increase in magma fO_2 , being the dominant control on lower-crustal sulfide stability and chalcophile element processing. Therefore, it is concluded that the pressure, and potentially temperature effect on the sulfide stability field (Matjuschkin et al., 2016; Nash et al., 2019) appears to play a more important role in stabilising sulfides in the lower continental crust than the effects of garnet fractionation.

Furthermore, the trace element systematics demonstrate that all Chilean stratovolcanoes display a garnet signature, although this signature is noticeably stronger in the CVZ. Nevertheless, all stratovolcanoes evolve to similarly low Cu contents, and therefore garnet fractionation appears unlikely to be the dominant control (and perhaps even not a significant control) on the stability or behaviour of sulfides. This supports the earlier conclusion that pressure plays a dominant role in controlling the behaviour of the chalcophile elements during the evolution of continental arc magmas. Although it is not considered to be an overriding control on sulfide fractionation, the competing effects of Fe-depletion versus increased magma oxidation on sulfide stability, associated with garnet fractionation, warrant further investigation.

In terms of the Ecuadorian stratovolcano dataset, although decreasing Fe_2O_3 (with MgO) could be a consequence of olivine fractionation, when viewed in conjunction with decreasing MnO (**Fig. 6.2**), these trends are more likely to be a consequence of garnet fractionation. Thus, observations from Ecuador also suggest that those samples that have fractionated the most garnet (i.e., lowest Fe_2O_3 and MnO) also display the lowest Cu. Although, this is not necessarily a causal relationship: both the low Cu, and the strong garnet signature, are rather interpreted as a consequence of evolution at high pressures.

Unlike in oceanic arc-like settings (e.g., EMBB), where the ‘Magnetite Crisis’ has been demonstrated to play a dominant role in controlling the behaviour of the chalcophile elements, by inducing sulfide saturation (e.g., Jenner et al., 2010; Williams et al., 2018; Valetich et al., 2019), the data presented here for continental arc stratovolcanoes demonstrates that sulfide saturation was reached prior to the onset of magnetite fractionation. Inflexions in the overall trends of Fe_2O_3 and TiO_2 in the Chilean dataset at ~3 wt.% MgO highlight the onset of magnetite fractionation (**Fig.6.2a,c**), but show that this occurred later than the onset of sulfide saturation. Furthermore, although Georgatou et al. (2018) demonstrated that magmatic sulfide inclusions were most common in magnetite phenocrysts of Ecuadorian stratovolcano lava samples, their identification in pyroxene phenocrysts supports sulfide saturation prior to magnetite fractionation. Hence, this new data, and findings presented by Georgatou et al. (2018) for Ecuadorian stratovolcanoes, supports the argument that the thickness of the overriding crust at a convergent margin plays the dominant role in controlling the behaviour of the chalcophile elements during magma genesis, by controlling the initial depth of magmatic differentiation, as proposed at Antuco (**Chapter 5**). This conclusion supports the idea of the presence of a theoretical Cu-rich ‘reservoir’, resulting from sulfide fractionation, at or near the base of the continental crust, possibly in the form of Cu-rich cumulates (Lee et al., 2012; Holwell et al., 2019).

6.4.2. Implications for the formation of ore deposits

As discussed above, the elevated Cu contents of Villarrica’s samples relative to other Chilean and Ecuadorian stratovolcanoes is very interesting, especially because nearby Quetrupillán and Lanín stratovolcanoes follow the Cu depleting trends observed at Antuco and Ecuadorian stratovolcanoes. Furthermore, recently published

analyses of lava samples from Villarrica presented by Hickey-Vargas et al. (2016) also have elevated Cu contents, similar to those presented here (**Fig.6.7a**). However, the Cu contents of Villarrica's samples are not unique in Chile, based on an analysis of whole rock data in the GeoROC database (Geochemistry of Rocks of the Oceans and Continents: <http://georoc.mpch-mainz.gwdg.de>, accessed 2019). Of the stratovolcanoes across Chile, for which data is available in the GeoROC database, samples from Llaima (e.g., Reubi et al., 2011) and the Puyehue – Cordon Caulle Volcanic Complex [PCCVC; e.g., Singer et al. (2008)] have similar Cu values to those at Villarrica, although this is not the case for all samples from these stratovolcanoes (**Fig. 6.7a**). However, samples from other stratovolcanoes are within the 'normal' range observed at the other stratovolcanoes studied here.

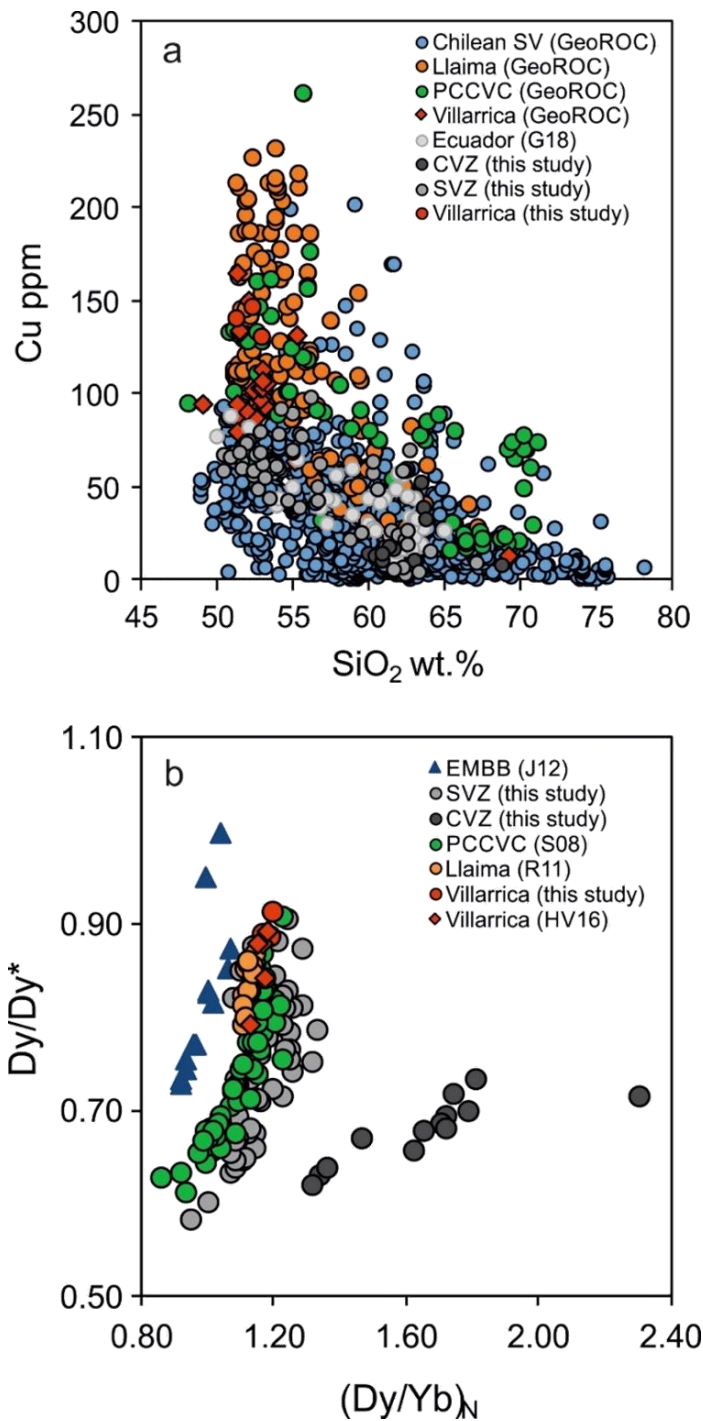


Figure 6.7. (a) Cu-SiO₂ bivariate plot comparing the Cu contents of stratovolcanoes (SV) from the Central and Southern Volcanic Zones (Chile). (b) Dy/Dy*-(Dy/Yb)_N bivariate plot comparing the high-Cu stratovolcanoes with data from the current study. Normalising values as of Sun and McDonough (1989). GeoROC data: Cu and SiO₂ data for stratovolcanoes from the Central/Southern Volcanic Zones from the Andean Arc GeoROC databases. The databases were filtered to only contain whole rock Cu and SiO₂ analyses of volcanic rocks (excluding ignimbrites and porphyry deposits) from stratovolcanoes [PCCVC: Puyehue – Cordon Caulle Volcanic Complex]; (G18): Cu data for Ecuadorian stratovolcanoes from Georgatou et al. (2018); (HV16): Further Cu data from Villarrica from Hickey-Vargas et al. (2016); (R11): Dy and Yb data for Llaima stratovolcano from Reubi et al. (2011); (S08): Dy, and Yb data for the PCCVC from Singer et al. (2008); (J12): Dy and Yb data for the Eastern Manus Backarc Basin (EMBB) from Jenner et al. (2012).

Significantly, Villarrica, Llaima and the PCCVC have been shown to be the three most active volcanic systems in the SVZ of Chile, based on both historical (Global Volcanism Program: <https://volcano.si.edu>, accessed 2019) and geological timescales (Volker et al., 2011). Volker et al. (2011) demonstrated these edifices to have volumes well in excess of 300 km³, considerably greater than the average edifice volume (~100 km³) in the SVZ. As a consequence of its very high activity, Villarrica ranks as Chile's highest risk volcano [SERNAGEOMIN: <http://www.sernageomin.cl/>, accessed 2019]. Therefore, both the historical records and longer-timescale observations suggest that Villarrica, Llaima and the PCCVC have the greatest magma flux or throughput in the SVZ, raising the possibility that there is a link between high levels of magma productivity or crustal flux and the Cu contents of an erupted magma. It must be noted however, that not all magmas from Llaima and the PCCVC have similarly elevated Cu contents to Villarrica. At the same SiO₂ content, some of the primitive Llaima and PCCVC samples have Cu contents that lay on the trend defined by other Chilean and Ecuadorian stratovolcanoes (**Fig.6.7a**). Thus, it appears that some, but not all, magmas at Llaima and the PCCVC have the capability to ascend without losing their Cu.

Villarrica is situated on the Liquiñe-Ofqui Fault Zone (LOFZ), which throughout the SVZ has been postulated to facilitate magma ascent (Lopez-Escobar et al., 1995a; Cembrano and Lara, 2009). Several other volcanic edifices across the SVZ [e.g., Yate, Minchinmavdia, Calbuco, Osorno; Cembrano and Lara (2009)] are situated on the LOFZ, however, they do not have a high magma flux or elevated Cu contents similar to what is observed at Villarrica, Llaima or the PCCV. Thus, the cause of elevated Cu contents at Villarrica, Llaima and the PCCVC may be rooted in controls on

productivity/magmatic flux. Magmas of several small eruptive centres (SECs) also lie on the LOFZ (Cembrano and Lara, 2009), and those from the Caburgua – Huelemolle Complex, ~20 – 30 km to the north of Villarrica, have been proposed to have ascended rapidly (Morgado et al., 2015, 2017; Hickey-Vargas et al., 2016b). However, the Cu contents of these SECs (discussed in more detailed in **Chapter 7**) are depleted relative to Villarrica and are more similar to those of the global MORB array and the most primitive Chilean and Ecuadorian stratovolcano magmas (**Fig. 7.4**). It is therefore not clear that the high Cu values at Villarrica are simply a consequence of rapid ascent or the volcano's position on the LOFZ. It is perhaps conceivable that a high magma flux or throughput (perhaps ultimately a result of deeper, mantle processes), enables a more rapid crustal transit and inhibits deep crustal storage, facilitated by crustal scale faults (e.g., LOFZ), thus reducing the volume of garnet fractionated and limiting the effect of pressure on sulfide saturation. Thus, the observations across the SVZ suggest that at a small number of high-flux volcanic systems, the processing of the chalcophile elements may differ to that at more typical arc stratovolcanoes. This could be a result of the more rapid magma throughput beneath these systems, possibly preserving the primary Cu content of the magmas, and transporting Cu to shallower environments, where ore deposits are situated.

Further support for the observations at Villarrica comes from the PCCVC. Here, samples have similar $(Dy/Yb)_N$ as the samples from Villarrica, suggesting a similarly minor degree of garnet fractionation (**Fig. 6.7b**), which is plausible given the similar crustal thickness (30 – 40 km) on which they are situated (Tassara and Echaurren, 2012). Moreover, the heavily faulted nature of the area surrounding the PCCVC,

associated with the LOFZ, suggests that some magmas may have ascended rapidly (Lara et al., 2006; Singer et al., 2008).

6.4.2.1. Summary of the potential mechanism(s) for ore deposit formation

The findings presented here for the behaviour of the chalcophile elements within a continental volcanic arc has profound implications for the generation of porphyry Cu deposits. Observations from stratovolcanoes across the CVZ and SVZ demonstrate that continental arc magmas generally achieve saturation in a sulfide phase early in their evolutionary history, thus losing sulfides and their primary Cu at depth, possibly generating a Cu-rich 'reservoir' at or near the base of the continental crust. Therefore, in order to transport Cu to shallower depths, where ore deposits are usually situated, secondary processes would be required. Alternatively, such shallow ore deposits are possibly generated in more atypical scenarios, where the magma throughput is highest (e.g., Villarrica, Llaima and the PCCVC), preserving the primary Cu content of a magma.

6.5. Conclusions

The majority of Chilean stratovolcanoes presented here adhere to the Cu trends defined at Antuco and Ecuadorian stratovolcanoes, suggesting that sulfide fractionated across their entire compositional range. Moreover, the Cu/Ag values of the most primitive samples are lower than that of the global MORB array, as observed at Antuco, suggesting sulfide saturation was reached early in their evolutionary history, and before magnetite fractionation, which occurred later at ~3 wt.% MgO. Consequently, most of the Chilean stratovolcanoes support the interpretation presented in **Chapter 5** that the thickness of the overriding crust at a convergent margin plays a dominant role in the behaviour of the chalcophile elements. However, the Cu contents of samples

from Villarrica are elevated relative to the global MORB array at a given SiO₂, suggesting their magmas to have been sulfide undersaturated.

Rare Earth Element systematics show that all stratovolcanoes initially fractionated garnet, although to varying degrees, prior to amphibole fractionation. This suggests that initial garnet fractionation drove parental magma composition. Those stratovolcanoes situated on thicker crust (i.e., Ollagüe and San Pedro) have the strongest garnet signature and generally the lowest Cu contents and Cu/Ag. This is consistent with recent work presented by Tang et al. (2018) who suggested that garnet fractionation could induce sulfide saturation by depleting magma of its Fe. However, Tang et al. (2018) also argued that garnet fractionation would simultaneously increase the fO_2 of the magma, thus destabilising and resorbing sulfides, releasing Cu back into the magma. This is not the case at either Ollagüe nor San Pedro, suggesting that the pressure (or temperature) effect on the stability field of sulfides plays an important role in overriding the effects of garnet fractionation.

Villarrica's high Cu contents are not unique in Chile, as similar Cu contents at a similar SiO₂ are observed in samples from Llaima and the Puyehue – Cordón Caulle Volcanic Complex (PCCVC). These three systems are the most active in Chile, thus suggesting a possible link between elevated magmatic flux and high Cu contents within erupted products. Additionally, because Villarrica has higher Cu contents and Cu/Ag than small eruptive centres just to the north, whose magma ascent is postulated to have been fast, this suggests that fast ascent alone is not adequate to explain Villarrica's elevated Cu contents. Consequently, high absolute levels of crustal magma flux (presumably ultimately reflecting higher levels of melt productivity beneath these

volcanic systems), possibly coupled with fast ascent, may have the potential to allow high-Cu content magmas to reach shallower crustal environments.

Overall, the samples studied here are situated on a range of crustal thicknesses that span the global range of continental arc crustal thicknesses. Thus, although Villarrica has proven to be an exception, the general trends observed in the chalcophile elements at multiple Chilean stratovolcanoes are argued to be applicable to continental arcs in general.

Chapter 7

Chalcophile element systematics beneath small eruptive centres

7.1. Introduction

Building on the initial work conducted in **Chapter 5** at Antuco, the detailed study of Chilean stratovolcanoes presented in **Chapter 6** demonstrated that most stratovolcano magmas achieve saturation in a crystalline sulfide phase early during their evolutionary history. This was evidenced by their continually decreasing Cu contents and Cu/Ag with increasing SiO₂, and lower Cu/Ag of the most primitive samples relative to the global mid-ocean ridge basalt (MORB) array. Hence, these findings supported the conclusions presented at Antuco, that the thickness of the overriding crust at a convergent margin plays an important, and arguably dominant role in controlling the behaviour of the chalcophile elements. Furthermore, the increasing garnet signature and lower Cu contents and Cu/Ag of stratovolcanoes situated on thicker crust (i.e., Ollagüe and San Pedro) supports the conclusions of Tang et al. (2018) that garnet fractionation could induce sulfide saturation by depleting a magma in Fe. However, the simultaneous oxidation of a magma, as a consequence of such garnet fractionation, would cause resorption of sulfide and the subsequent release of Cu back into the magma. Despite this, the low Cu contents of the stratovolcanoes

situated on thicker crust suggest that sulfides were still stable and it was therefore concluded that the pressure (e.g., Matjuschkin et al., 2016), or temperature (e.g., Nash et al., 2019) effect on the stability of sulfides is a more significant lower crustal process than garnet fractionation in the evolution of these magmas, allowing sulfides to remain stable and be fractionated from the magmas, thus depleting evolving melts in Cu.

Interestingly, samples from Villarrica proved to be an exception to the above, having Cu contents that were elevated (~140 ppm) relative to the other Chilean stratovolcanoes, but also elevated relative to Ecuadorian stratovolcanoes and the global MORB array. Consequently, this suggests that the magmas from which these samples were sourced were sulfide undersaturated. Moreover, the Cu contents of samples from Villarrica were demonstrated to not be unique in the Chilean Andes, with analyses from Llaima (Reubi et al., 2011) and the Puyehue – Cordon Caulle Volcanic Complex (Singer et al., 2008) also having Cu contents similar to those at Villarrica. As these three systems are the most active in the Southern Volcanic Zone of Chile, a link between elevated magma flux and Cu contents, with possible fault assisted ascent, was postulated.

Although **Chapters 5** and **6** have begun to address the lack of chalcophile element analyses in a continental volcanic arc setting, they have only focused on volcanic rock samples from stratovolcanoes. However, extremely little attention has been paid to the processing and distribution of the chalcophile elements beneath monogenetic volcanic centres. This is despite monogenetic volcanic centres being the most common type of volcano on Earth, found throughout convergent, divergent and intraplate settings (Valentine and Gregg, 2008; Kereszturi and Nemeth, 2012; Le Corvec et al., 2013). Monogenetic volcanic centres commonly erupt among the most

primitive magmas in arc settings (Churikova et al., 2013; Watt et al., 2013; Walowski et al., 2016), and have thus been used to investigate deep magmatic processes. In spite of this, the relationship between magmas erupted at monogenetic centres and those at nearby stratovolcanoes is incompletely understood. Although monogenetic centres and stratovolcanoes are commonly within close proximity with one another, and erupted products of monogenetic centres have been used to infer arc magmatic genetic processes, they may not be directly related to magmas parental to stratovolcanoes (Hickey-Vargas et al., 2016b). Consequently, this chapter furthers the previous work offered in this thesis by presenting a new and near complete suite of chalcophile element analyses for a suite of small eruptive centres in the volcanic zones of Chile (Caburgua – Huelemolle Complex, Huililco and La Poruñita), and addresses the relationship between the processing history of these magmas and those erupted at stratovolcanoes. This new dataset allows further investigation into the behaviour of the chalcophile elements in a continental volcanic arc, testing proposed hypotheses that crustal thickness, and consequently pressure, plays a dominant role in their processing.

7.2. Monogenetic volcanic centres

Monogenetic volcanic centres, commonly referred to as small or minor eruptive centres (SECs), are generally defined as erupting once from a vent or fissure, with eruptions lasting from days to several years (Wood, 1979; Nemeth, 2010). In contrast, the eruptive history of polygenetic volcanic centres (i.e., stratovolcanoes) generally lasts for prolonged periods, on the order of 10^5 – 10^6 years, and is characterised by the development of a long-lived crustal plumbing and storage system, with the ascent and eruption of several discrete batches of magma throughout the lifetime of the

volcano (Kereszturi and Nemeth, 2012; Smith and Németh, 2017). Although monogenetic volcanic centres are usually of small volume (Nemeth, 2010), they occur in fields or alignments, sometimes comprising tens to hundreds of centres (Nakamura, 1977; Le Corvec et al., 2013), with an eruptive history lasting up to millions of years, on par with their polygenetic equivalents (Németh, 2010).

Monogenetic volcanic centres form through either effusive or explosive (pyroclastic) events (Smith and Németh, 2017), and display a broad range in morphology; from small cones (e.g., lava cones, scoria cones, pyroclastic cones, maars) to larger shield centres (Wood, 1979; Valentine and Gregg, 2008). These volcanic centres are most commonly basaltic in composition, although they can erupt a broader compositional range of volcanic products, from basaltic to andesitic (Valentine and Gregg, 2008; Smith and Németh, 2017). Detailed reviews on the origin, structure and composition of monogenetic volcanism are provided by Nemeth (2010), Kereszturi and Nemeth (2012) and Smith and Németh (2017).

The commonly more primitive nature (i.e., basaltic) of the eruptive products of monogenetic volcanic centres has led to these types of samples being regarded as “windows to the mantle” [(McGee et al., 2015), p. 420], providing access to near-primary mantle melt compositions. This is because their magmas are generally regarded to have had a more rapid ascent or shorter crustal residence time than polygenetic volcanic centres, therefore having mostly avoided intra-crustal processes capable of modifying magma composition (e.g., magma storage, fractional crystallisation and/or crustal assimilation) (McGee and Smith, 2016; Smith and Németh, 2017). ‘Simpler’ plumbing systems (e.g., Smith and Németh, 2017) and their association with fault systems (e.g., Lara et al., 2006; Cembrano and Lara, 2009) are usually thought to aid

this more rapid ascent. Therefore, as monogenetic volcanic centres have the potential to investigate near-primary mantle melts, acting as good comparators to larger stratovolcanoes which generally have more complex plumbing systems, they provide the ideal opportunity to explore the effects of early and deep magmatic processes on the behaviour of the chalcophile elements. However, there may not be a direct relationship between SEC magmas and those parental to stratovolcanoes (Watt et al., 2013; Hickey-Vargas et al., 2016b). For example, Hickey-Vargas et al. (2016) conclude that SECs near Villarrica have distinct ascent pathways compared to the neighbouring stratovolcano, and have a different melting origin (i.e., mantle lithosphere pyroxenites).

7.2.1. Geological context of the Chilean small eruptive centres

Small eruptive centres are commonplace in the Chilean Andes, with hundreds scattered across the Central and Southern Volcanic Zones of Chile (Stern, 2004). Within the Central Southern Volcanic Zone (CSVZ), the Caburgua – Huelemolle Complex (CHC) comprises several SECs that are located ~10 – 30 km north of the stratovolcano Villarrica (**Fig. 2.4**). The apparent association of the CHC SECs, and SECs [and many other SECs further south; Watt et al. (2013)], with the main structure of the LOFZ, or sub-parallel faults or oblique tension cracks (**Fig. 2.4**), suggests that their location is controlled by this large fault system (Lara et al., 2006; Cembrano and Lara, 2009; Sánchez et al., 2013). Recent geochemical and mineralogical (e.g., olivine) studies of the CHC SECs have inferred that their magmas originate from a deep-seated (>30 – 40 km) source (Morgado et al., 2015, 2017; Hickey-Vargas et al., 2016b). Furthermore, it has been suggested that lithospheric mantle pyroxenites contribute to the CHC magmas, either as direct partial melts or through assimilation by ascending asthenospheric mantle-derived melts (Hickey-Vargas et al., 2016b). Either way,

studies agree on a deep source for the CHC magmas, although possibly not the sub-arc mantle wedge as is typically assumed beneath stratovolcanoes, and that their association with the LOFZ has facilitated magma ascent.

The inferred deep source from which the CHC magmas are postulated to have been derived allows this chapter to further investigate the roles of pressure and garnet fractionation on the evolution of their magmas and the subsequent implications for the controls on the behaviour of the chalcophile elements. Furthermore, their association with the LOFZ, and fast magma ascent, permits comparisons to be made with magmas at Villarrica, whose ascent was postulated to be rapid, due to their minimal garnet signature and elevated Cu contents.

Although Huililco (**Fig. 2.4**) is not situated along a fault or tension crack associated with the LOFZ (Mcgee et al., 2015), it has been suggested that its eruptive products are equivalent in composition to the parental magmas of the neighbouring stratovolcano Quetrupillán (Brahm et al., 2018). Consequently, samples from Huililco may potentially be viewed as near-primary magmas, that can be used to investigate the early behaviour of the chalcophile elements in arc settings.

The scoria cone of La Poruñita, located ~11 km to the west of Ollagüe's summit, has received very little attention in the literature, with its relationship to Ollagüe having not been investigated. Although this thesis presents only a single geochemical analysis from La Poruñita, the extreme crustal thickness on which it is situated makes it an interesting comparison to the SECs of the CHC.

7.3. Geochemical results

7.3.1. Major elements

In terms of geochemical classification, all SEC samples classify as either basalts or basaltic andesites on a total alkali versus silica (TAS) plot (**Fig. 7.1a**). The CHC sample suite define a somewhat bimodal distribution; with most samples clustering in one of two groups, at ~47 – 49 wt.% or ~54 – 55 wt.% SiO₂. The CHC samples with greater SiO₂ are generally from fall deposits nearer vents around the southern shoreline of Lake Caburgua, whereas the samples with lower SiO₂ contents are located near the stratovolcano Villarrica. Additionally, the sample from La Poruñita has a significantly higher total alkali content than the CHC samples. On an AFM [alkali, FeO (as total Fe), MgO] ternary plot, samples from the SECs generally classify as calc-alkaline, although this is boundary dependent (**Fig. 7.1b**).

On major element bivariate plots (vs. MgO) (**Fig. 7.2**), samples from the CHC have a MgO range (3.6 – 9.7 wt.%) that extends to more primitive compositions than the Chilean (CVZ and SVZ) and Ecuadorian stratovolcanoes. Concerning the remaining major elements, samples generally show narrow ranges in their contents [e.g., TiO₂ (1.0 – 1.3 wt.%), Al₂O₃ (18.0 – 21.5 wt.%), Fe₂O₃, as total Fe (9.7 – 11.3 wt.%), CaO (7.0 – 9.6 wt.%)]. The Na₂O and K₂O contents of the samples show very weak negative correlations with MgO; Fe₂O₃ has a subtle positive correlation; and TiO₂, Al₂O₃, MnO, CaO and P₂O₅ do not display any correlation.

The major element contents of samples from Huililco resemble, to some extent, those of the more primitive samples from the CHC. However, at a given MgO content, the Huililco samples have slightly lower K₂O, MnO, Fe₂O₃ and Al₂O₃, and slightly greater CaO than the CHC samples. The sample from La Poruñita has similar MgO,

SiO₂, TiO₂ and CaO contents to the more evolved CHC samples, but higher Na₂O, K₂O and P₂O₅, and lower Al₂O₃, Fe₂O₃ and MnO at given MgO contents. In addition to extending to greater MgO contents than the Chilean and Ecuadorian stratovolcanoes, the CHC samples generally have higher TiO₂, Al₂O₃, Fe₂O₃ and P₂O₅ contents, and similar to lower CaO, Na₂O, K₂O and MnO contents. Samples from Huililco generally have major element contents similar to the Chilean stratovolcanoes at a similar MgO content.

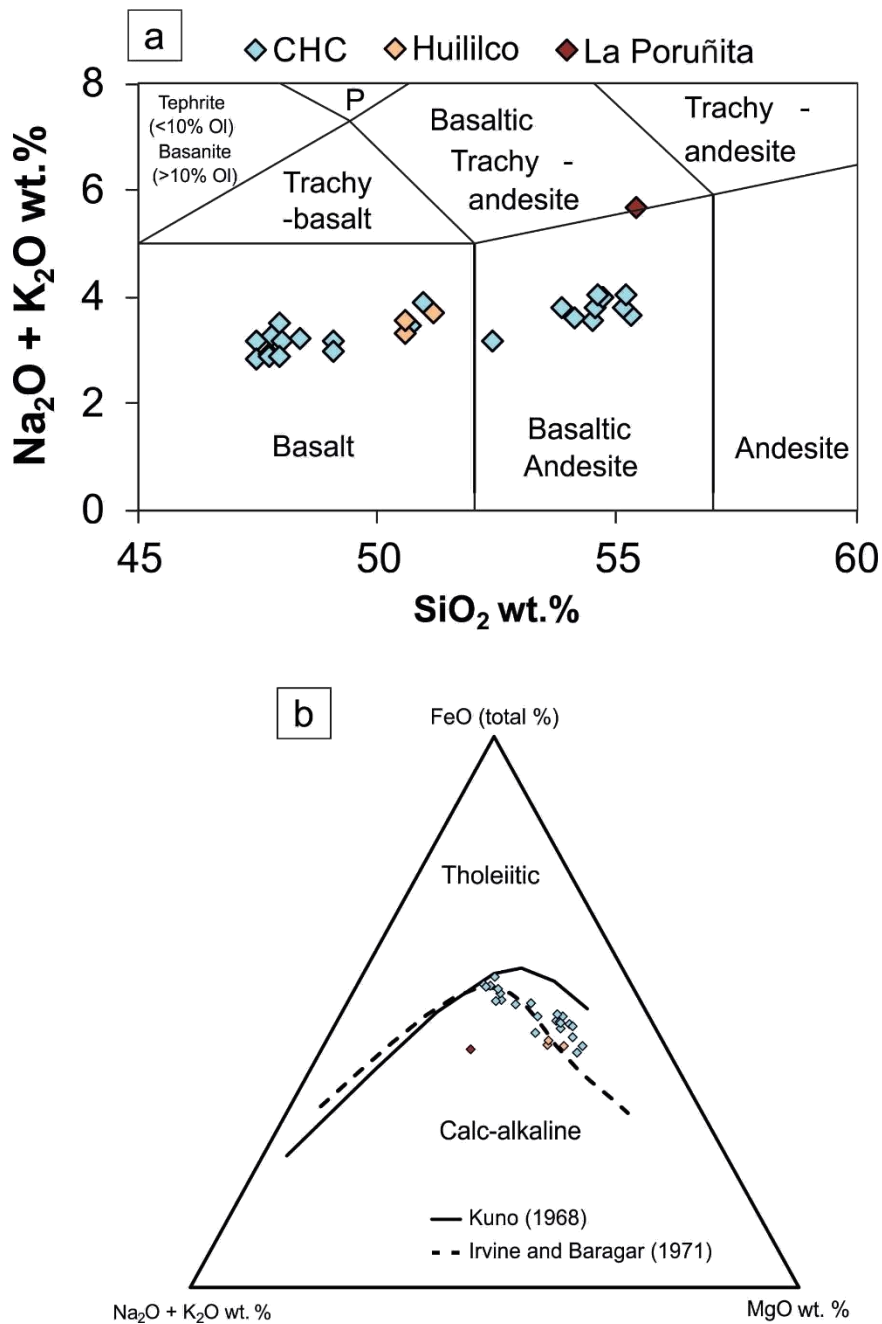


Figure 7.1. Geochemical classification of the small eruptive centres (SEC; diamonds). (a) On a total alkali versus silica (TAS) plot, the SEC classify as either basalts or basaltic andesites. Classification fields of Le Bas (1986). (b) Using the alkali – total Fe – MgO (AFM) plot, the SEC are generally of calc-alkaline affinity.

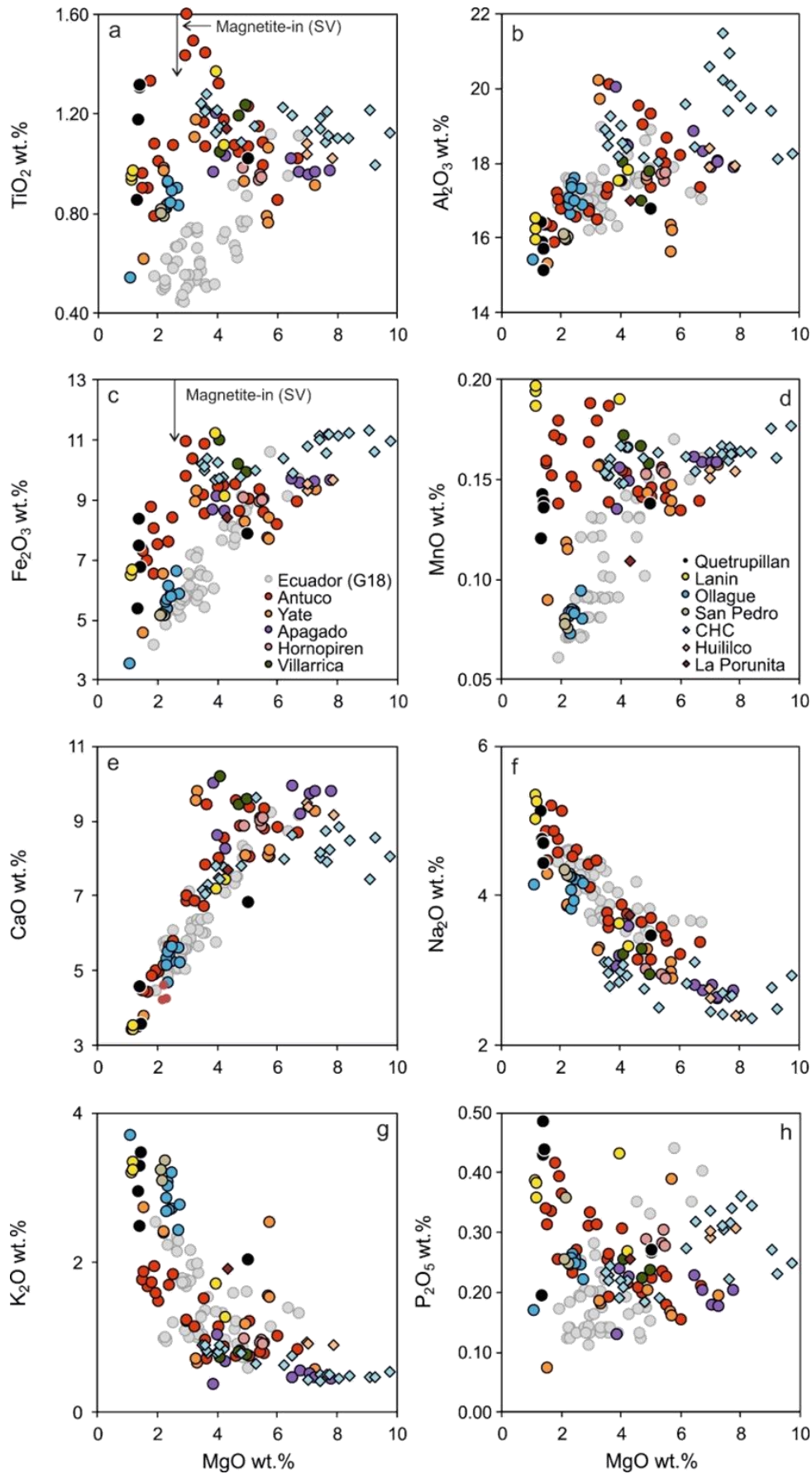


Figure 7.2. Major element bivariate plots (versus MgO) of all Chilean small eruptive centre samples (diamonds). Stratovolcano (SV) samples of this study are also presented. (G18): major element data for Ecuadorian stratovolcanoes from Georgetou et al. (2018).

7.3.2. Trace elements

The S and Se contents of samples from the CHC and Huililco are considerably depleted relative to the global MORB array (**Fig. 7.3**). Additionally, the Se contents of all SECs are depleted relative to samples from the oceanic arc-like Eastern Manus Backarc Basin [EMBB; Jenner et al. (2012)], although samples from the CHC and Huililco approach Se contents similar to those of the most primitive EMBB samples (**Fig. 7.3b**). With the exception of the sample from La Poruñita, which has a S content well in excess of the other SECs, the global MORB array and Chilean stratovolcanoes, but consistent with neighbouring stratovolcano Ollagüe, the S contents of the samples from the CHC and Huililco are similar to those of the Chilean stratovolcanoes. The CHC and Huililco SECs generally have elevated Se contents when compared to the Chilean stratovolcanoes. Again, the sample from La Poruñita differs from the other SECs, in that its Se content is similar to that of the Chilean stratovolcanoes.

At a given SiO₂, the Cu and Ag contents of the CHC samples are similar to samples from Chilean and Ecuadorian stratovolcanoes (**Fig. 7.4a,b**). The Ag contents of samples from the CHC show no correlation with SiO₂, although do display more scatter than the Cu contents. The Cu contents of the samples display a subtle increase with increasing SiO₂ (~≤5 ppm), in contrast with the stratovolcanoes, where Cu decreases with increasing SiO₂. The Cu contents of the most primitive CHC samples are similar to the global MORB array, whereas the Ag contents are similar to slightly elevated relative to the upper echelons of the global MORB array.

Samples from Huililco have similar Cu and Ag contents to the more primitive CHC samples, however, due to the limited dataset, no trends can be borne out with SiO₂. Interestingly, the sample from the La Poruñita has a slightly lower Cu, but

considerably elevated Ag content, relative to other SECs and the Chilean and Ecuadorian stratovolcanoes at a similar SiO₂ content. As was the case with the stratovolcanoes, the CHC SECs display different trends to those observed in the EMBB sample set, which show an initial increases in Cu and Ag with increasing SiO₂, before decreasing with continually increasing SiO₂ (e.g., Jenner et al., 2012).

The Cu/Ag of samples from the CHC and Huililco remain relatively constant with increasing SiO₂ (in contrast to the decreasing trend demonstrated by the stratovolcanoes), although the Cu/Ag of the most primitive CHC and Huililco samples are slightly depleted relative to the global MORB array at a given SiO₂ (**Fig. 7.4c**), which is similar to that observed in the stratovolcano datasets. The sample from La Poruñita shows a noticeably depleted Cu/Ag relative to other samples at the same SiO₂ concentration, which is attributable to its strongly elevated Ag content, noted above.

On a (C1) Chondrite normalised Rare Earth Element (REE) plot, SEC samples have very smooth patterns, all enriched in the Light REE (LREE) relative to the Middle and Heavy REE (M/HREE) (**Fig. 7.5**). The sample from La Poruñita has a greater enrichment in the LREE [(La/Sm)_N, 3.1] compared to the samples from the CHC and Huililco [(La/Sm)_N, 1.5 – 2.5]; where N denotes (C1) Chondrite normalised values. Additionally, all samples show depletions in the HREE relative to the MREE. Again, the sample from La Poruñita has a greater depletion in the HREE [(Gd/Yb)_N, 2.4] compared to those from the CHC and Huililco [(Gd/Yb)_N, 1.4 – 2.0]. Negative Eu anomalies are minor to negligible across all sample sets [Eu/Eu*, >0.80], although a few samples display insignificant positive Eu anomalies [Eu/Eu*, <1.05].

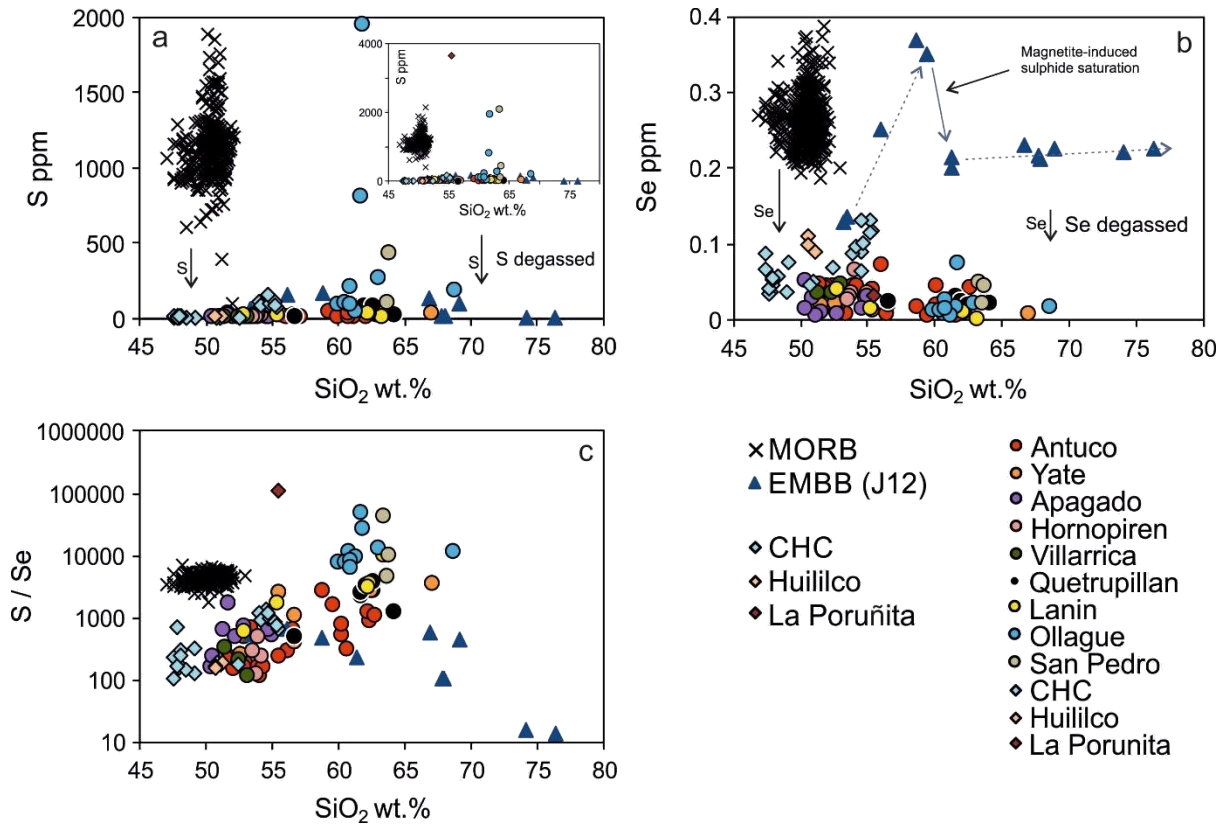


Figure 7.3. S, Se and S/Se bivariate plots (versus SiO₂) of all Chilean small eruptive centre samples (diamonds). (J12): Eastern Manus Backarc Basin (EMBB) data from Jenner et al. (2012); Global (Pacific and Atlantic) mid-ocean ridge basalt (MORB) array from Jenner and O'Neill (2012).

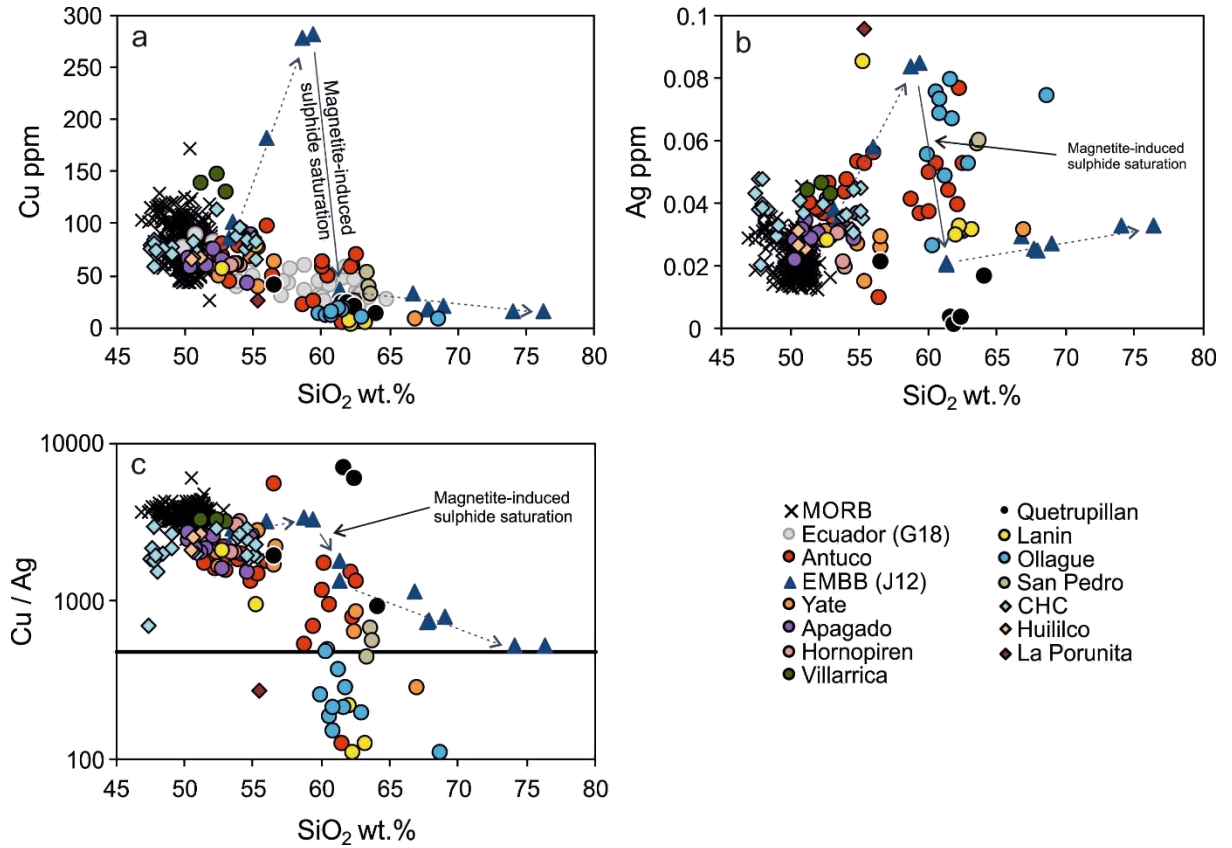


Figure 7.4. Cu, Ag and Cu/Ag bivariate plots (versus SiO₂) of all Chilean small eruptive centre samples (diamonds). (G18): Cu data for Ecuadorian stratovolcanoes from Georgatou et al. (2018); (J12): Eastern Manus Backarc Basin (EMBB) data from Jenner et al. (2012); Global MORB array from Jenner and O'Neill (2012); Cu/Ag of the bulk continental crust from Rudnick and Gao (2003).

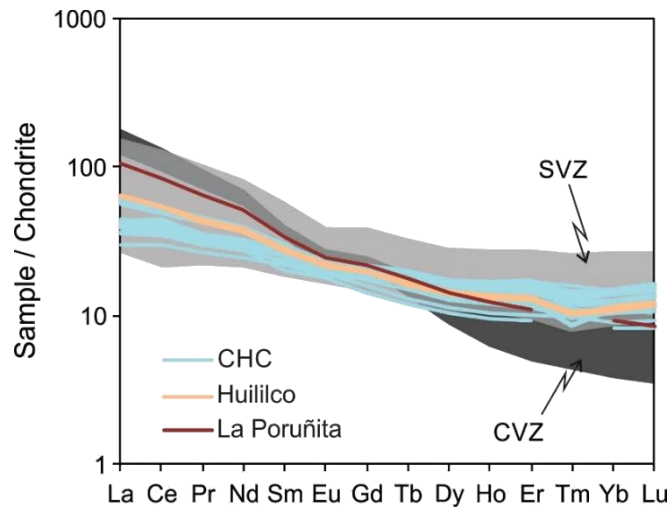


Figure 7.5. (C1) Chondrite normalised Rare Earth Element (REE) plot of all Chilean small eruptive centre samples. Light and dark grey fields define the REE patterns of stratovolcanoes from the Southern (SVZ) and Central Volcanic Zones (CVZ), respectively. Normalising values as of Sun and McDonough (1989).

7.4. Discussion

7.4.1. A similar crustal processing beneath small eruptive centres and stratovolcanoes

The S and Se contents of the SECs presented here are mostly considerably depleted relative to the global MORB array and Eastern Manus Backarc Basin (EMBB) samples (**Fig. 7.3a,b**), thus suggesting both to have been extensively degassed. However, the Se contents are generally elevated relative to the Chilean stratovolcanoes, thus suggesting a lower degree of Se degassing from the SEC magmas. Additionally, the lower S/Se of the SEC samples compared to the global MORB array implies that, as was the case for the majority of stratovolcanoes, S behaved in a more volatile manner than Se during degassing (**Fig. 7.3c**). The behaviour of S and Se appear decoupled in the La Poruñita sample, having a S content significantly higher than the global MORB array. Interestingly, this is similar to the observed S contents of samples from neighbouring stratovolcano Ollagüe. The assimilation of S (as sulfides) seems an unlikely cause of elevated S contents, as it would be expected to also result in elevated Cu contents. Thus, further investigation into S and Se at both La Poruñita and Ollagüe is required to shed light on this potential decoupling.

As was the case with the stratovolcanoes, the degassing of Se from the SEC magmas means that Se contents cannot be used to investigate the behaviour of S during magma evolution, in the way that it has been in glasses from subaqueous environments [MOR, oceanic plateaus and back arc basins; Jenner et al. (2010); Reekie et al. (2019)]. The loss of Se from all the sub-aerial volcanics studied here, in

contrast to subaqueous settings, suggests that Se is generally lost during eruption through degassing at extremely low pressures.

7.4.1.1. Sulfide saturation beneath small eruptive centres

New Cu and Ag analyses presented for the CHC and Huililco SECs define subtly increasing and flat trends with increasing SiO₂, respectively, from values similar to the global MORB array (**Fig. 7.4a,b**). In the case of Cu, this is different to what is observed in the Chilean stratovolcano datasets, where their Cu contents display an overall decrease with increasing SiO₂, although there is considerable overlap in the Cu concentrations of the two datasets. That being said, the generally flat to subtly increasing Cu trend suggests that Cu did not behave entirely incompatibly during magma evolution and was instead buffered by a fractionating phase (e.g., sulfide). Furthermore, the Cu/Ag of the CHC and Huililco SECs also define a flat trend, lower than the global MORB array (**Fig. 7.4c**), thus suggestive of a crystalline, rather than molten, fractionating sulfide phase (Li and Audétat, 2012, 2015).

The depleted Cu and enriched Ag contents of the La Poruñita sample suggest a greater degree of sulfide fractionation relative to the CHC. The Cu content and Cu/Ag are similar to Ollagüe, but displaced to lower SiO₂. This suggests that despite a likely faster magma ascent beneath La Poruñita, its magma has experienced a similar degree of sulfide fractionation to those from Ollagüe.

7.4.1.2. Quantifying the degree of sulfide fractionation from small eruptive centre magmas

To quantify the volume of sulfide fractionation required to replicate the observed Cu, Ag and Cu/Ag trends of the CHC dataset, the fractional crystallisation modelling

presented in **Chapter 5** has been used to remodel sulfide fractionation using a primitive CHC sample as a starting composition. The starting compositions of Cu (72.3 ppm) and Ag (0.04 ppm) used were those of the most primitive CHC sample [16DCCaHu.017; 9.74 wt.% MgO (anhydrous)]. The remaining model parameters (**Table 7.1**), including the partition coefficients of Cu and Ag in crystalline sulfide and silicate (olivine and plagioclase) phases, were kept the same as those used in **Chapter 5**, as they remain the most suitable for the conditions under discussion (i.e., oxidised).

The model results presented in **Fig. 7.6** confirm the hypothesis postulated above that only a minor volume (≤ 0.3 wt.%) of crystalline sulfide fractionation, and low degrees of fractional crystallisation, are required to replicate similar trends in the behaviour of Cu, Ag and Cu/Ag to those observed in the CHC dataset: i.e., subtle increase in Cu and relatively consistent Ag and Cu/Ag with SiO₂. Due to the slight scatter in the Cu and Ag trends, the degree of sulfide fractionation cannot be further constrained. Furthermore, the modelling presented here assumes that all the CHC magmas have the same source; however, as Hickey-Vargas et al. (2016) demonstrated, individual SECs can have their own discrete ascent pathways. Thus, this modelling merely serves to provide an estimate of the degree of sulfide fractionation beneath the CHC SECs. Additionally, as hypothesised above, the volume of sulfide fractionating from the CHC magma is less than that estimated for Antuco (i.e., 0.5 – 0.6 wt.%), and therefore the other Chilean stratovolcanoes in general. This could be a consequence of shorter crustal residence times (at higher pressure) of the CHC magmas compared to magmas transiting generally more complex plumbing systems associated with stratovolcanoes.

Table 7.1 Fractional crystallisation modelling parameters

	Plagioclase / Olivine	Sulfide
Mineral proportion	0.998	0.002
Kd	Cu	Ag
Plagioclase / Olivine	0.05	0.001
Sulfide (crystalline)	215	24
Do	0.480	0.049
Co (16DCCaHu.017)	72.326	0.039

*Kd: Partition coefficient for a particular element in a mineral, Do: Bulk-distribution coefficient of a particular element prior to fractional crystallisation, Co: Concentration of a particular element in the source. Excluding starting composition, the modelling parameters are the same as **Chapter 5**.*

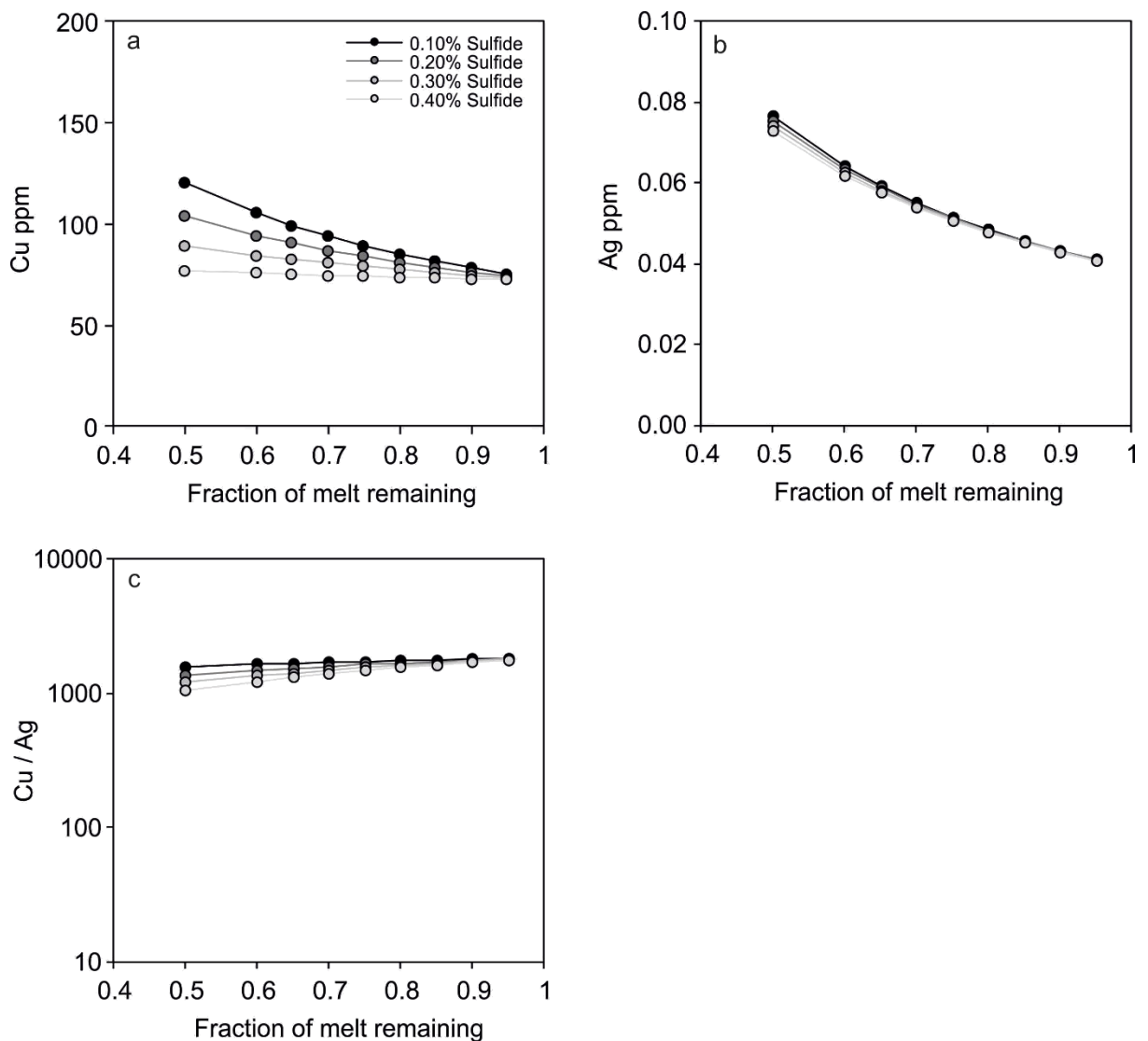


Figure 7.6. Trace element modelling of fractional crystallisation. Modelling demonstrates that only a minimal volume (≤ 0.2 vol. %) of sulfides are required to fractionate in order to replicate the trends observed in the Cu, Ag and Cu/Ag data of the small eruptive centre (SEC) samples (e.g., **Fig. 7.4**). Starting composition used was that of the most primitive SEC sample 16DCCaHu.017. Complete model parameters are outlined in **Table 7.1**.

7.4.1.3. *Pressure induced sulfide saturation in SEC magmas*

Chapters 5 and **6** argued the importance of pressure, over garnet fractionation, in inducing sulfide saturation during the petrogenesis of the Chilean stratovolcano magmas, demonstrating that those magmas erupting through the thickest overriding continental crust have amongst the lowest Cu contents. REE systematics are also used here to investigate the controls on sulfide saturation beneath the Chilean SECs.

All SECs investigated here have $(\text{Gd}/\text{Yb})_N > 1$ and at a given SiO_2 have elevated $(\text{Dy}/\text{Yb})_N$ relative to the EMBB dataset (**Fig. 7.7a**), suggesting fractionation of garnet from their magmas. Furthermore, the greater $(\text{Gd}/\text{Yb})_N$ and $(\text{Dy}/\text{Yb})_N$ of the La Poruñita sample (2.4 and 1.55, respectively), relative to the CHC and Huililco samples (1.4 – 2.0 and 1.1 – 1.3, respectively), suggests that its magma experienced a greater degree of garnet fractionation, similar to the CVZ stratovolcanoes (i.e., Ollagüe and San Pedro). This is consistent with the greater crustal thickness in the CVZ (≥ 70 km) compared to the area of the SVZ where the CHC and Huililco SECs are situated (~35 – 40 km).

Additionally, the CHC and Huililco samples define a subtle, negative correlation between $(\text{Dy}/\text{Yb})_N$ and SiO_2 , overlapping, and extending to lower SiO_2 , the trend defined by the SVZ stratovolcanoes. Therefore, this suggests amphibole was part of the fractionating assemblage from the evolving CHC and Huililco magmas, although amphibole fractionation is not clearly borne out on a plot of Dy/Dy^* against SiO_2 (**Fig. 7.7b**). A lower degree of fractionation is not unexpected, given the relatively primitive nature of the SEC magmas and that they were unlikely to be subjected to prolonged crustal storage. As was the case for the SVZ stratovolcanoes, the CHC and Huililco

SECs appear to have experienced initial garnet fractionation, likely in conjunction with sulfide fractionation, prior to amphibole fractionation.

Moreover, when $(Dy/Yb)_N$ and Dy/Dy^* are plotted against one another, the CHC and Huililco samples define a near-vertical trend within the low to medium pressure fractionation fields defined in **Chapter 6**, whereas the sample from La Poruñita plots in the high pressure fractionation field, nearer to the CVZ stratovolcanoes (**Fig. 7.7c**). Although only one sample from La Poruñita is reported, the data here appear to support the hypothesis presented in **Chapter 6** that initial garnet fractionation drives parental magma compositions to higher $(Dy/Yb)_N$, prior to the onset of amphibole fractionation.

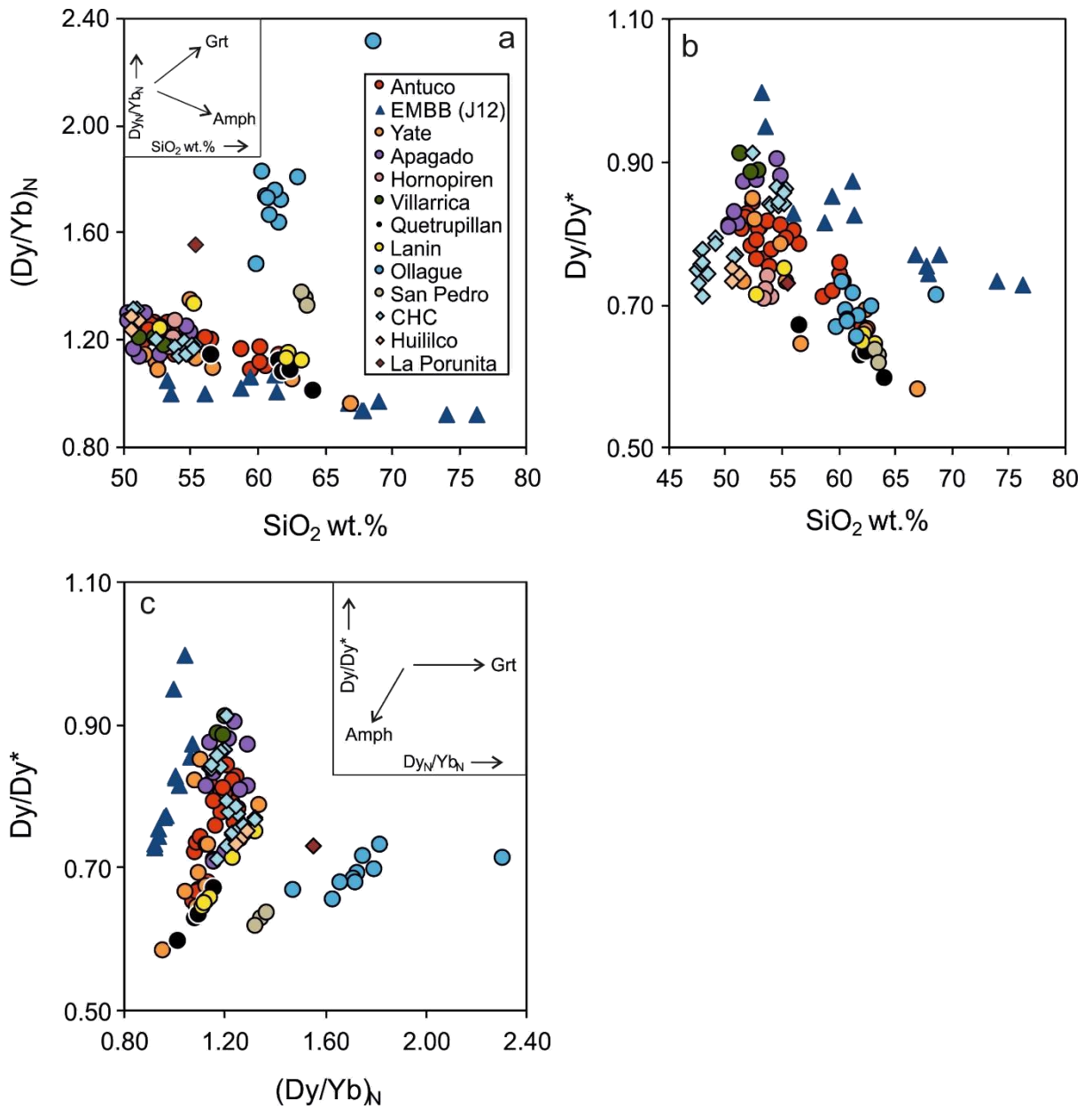


Figure 7.7. Rare Earth Element (REE) systematics of the Chilean small eruptive samples (diamonds) [after Davidson et al. (2007, 2013)]. Normalising values as of Sun and McDonough (1989). (J12): Eastern Manus Backarc Basin (EMBB) data from Jenner et al. (2012); Amph: amphibole; Grt: garnet; Dy/Dy^* defined as $Dy_N/((La_N^{4/13}) * (Yb_N^{9/13}))$.

In addition to the above, the ‘shape coefficients’ of the REE patterns (O’Neill, 2016) of samples from the CHC and Huililco overlap with those of SVZ stratovolcanoes, at slightly greater λ_1 (slope of REE pattern) than the ocean floor basalt (OFB) array at a given λ_2 (curvature of REE pattern), suggestive of minimal garnet fractionation (**Fig. 7.8**). Moreover, the subtle positive correlation between λ_1 and λ_2 observed in the CHC dataset suggest a minimal amount of amphibole fractionation also. The sample from La Poruñita, however, plots nearer those of stratovolcanoes in the CVZ, noticeably offset to the right of the OFB array, implying increased garnet fractionation, although less than at Ollagüe. The slightly weaker garnet signature in the La Poruñita sample compared to those from Ollagüe, observed in both $(\text{Dy}/\text{Yb})_N - \text{Dy}/\text{Dy}^*$ and $\lambda_1 - \lambda_2$ space, is consistent with a faster rate of magma ascent beneath La Poruñita and a shorter magma residence time in the garnet stability field.

The SEC datasets presented here support the conclusions of Tang et al. (2018) in that garnet fractionation is a common occurrence in the genesis of continental arc magmas. However, the same pattern observed in the stratovolcano and SEC datasets – i.e., depleted Cu and Cu/Ag of those samples with the strongest garnet signatures and situated on thickest overriding continental crust – supports the suggestion that the effect of pressure on the stability field of sulfides is important in inducing sulfide saturation, by overriding the effect of garnet fractionation and the subsequent oxidation of evolving magmas postulated by Tang et al. (2018).

The CHC SECs display no evidence of magnetite fractionation from their magmas (i.e., sudden depletions in Fe or Ti), but this is unsurprising, since they do not extend to the SiO_2 concentrations at which magnetite was observed to fractionate from

the Chilean stratovolcano magmas (**Fig. 7.2a,c**). This further supports the less dominant role of the ‘Magnetite Crisis’ on the behaviour of the chalcophile elements in a continental arc setting, showing that sulfide can fractionate before magnetite, and supporting the hypothesis that crustal thickness is the dominant control on their behaviour. The depletion of Fe through early garnet fractionation potentially limits the proportion of magnetite fractionating from magmas erupting through thick crust, compared to tholeiitic magmas erupting through thinner (island arc) crust.

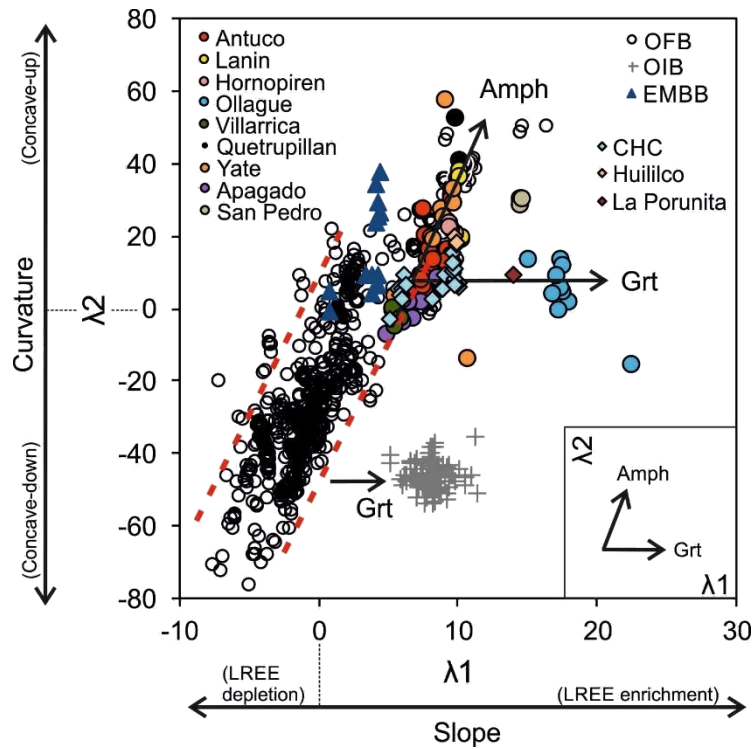


Figure 7.8. ‘Shape coefficients’ defining the Rare Earth Element (REE) patterns of the Chilean small eruptive centres (diamonds) [after O’Neill (2016)]. λ_1 describes the overall slope of the REE pattern, with λ_2 describing the curvature of the REE pattern. Red, dashed tramlines define the trend of the bulk of OFB data. OFB: ocean floor basalt [data from Jenner and O’Neill (2012)]; OIB: ocean island basalt (Hawaii) [data from Feigenson et al. (2003)]; EMBB: Eastern Manus Backarc Basin samples [data from Jenner et al. (2012)]; Amph: amphibole; Grt: garnet.

7.4.2. Consistent Cu-rich (ore?) source at the base of the continental crust

Although the magmas of the SECs are generally assumed to ascend rapidly, with ascent facilitated by the LOFZ (Morgado et al., 2015; Hickey-Vargas et al., 2016b), their Cu contents and Cu/Ag are similar to most of the Chilean stratovolcanoes. Thus, alongside the stratovolcano datasets, all the magmas studied here support deep sulfide fractionation and potential formation of a Cu-rich 'reservoir'(?), at or near the base of the continental crust (e.g., Lee et al., 2012; Jenner, 2017; Holwell et al., 2019).

7.4.2.1. A deep, pyroxenite source for Cu

Lee et al. (2012) suggested that the low Cu contents of evolved arc magmas implied that Cu has been lost from them, and by implication may reside in lower crustal or lithospheric mantle Cu-rich (pyroxenite) cumulates. This was supported by demonstrating that the Cu contents of pyroxenite xenoliths from basaltic volcanoes in eastern California, although scattered, were generally greater than primitive mantle and primitive arc basalts. Consequently, Lee et al. (2012) suggested that lower crustal pyroxenites could be the only Cu-rich source in an arc setting, and that extensive partial melting of these pyroxenites, exhausting sulfides and liberating Cu, could be an important step in providing the high Cu concentrations necessary for generating upper crustal ore deposits.

Across the SVZ, two types of basalt have been identified; those erupted at arc front stratovolcanoes (Type 1) and those predominantly erupted at SECs (Type 2) (Lopez-Escobar et al., 1995a; Hickey-Vargas et al., 2016b). Further to this, Hickey-Vargas et al. (2016b) demonstrated that Type 1 basalts represent asthenospheric mantle-derived melts, whereas Type 2 basalts have incorporated melts of lithospheric mantle pyroxenites during their petrogenesis; either solely through the partial melting

of such pyroxenites, or by mixing of pyroxenite melts with ascending asthenospheric mantle-derived magmas (i.e., Type 1). Interestingly, in defining these sources, Hickey-Vargas et al. (2016b) demonstrated that basalts of the vast majority of the CHC SECs were of the Type 2 classification, and thus had incorporated melts of lithospheric mantle pyroxenites during magma genesis. In contrast, Type 1 basalts were erupted at arc stratovolcanoes (e.g., Villarrica).

Samples from SECs of the CHC presented here are consistent with being of Type 2 origin, having similar Sc, Sr and MgO contents and La/Yb, used by Hickey-Vargas et al. (2016b) to differentiate between Type 1 and Type 2 basalts. This means that the CHC magmas may not be genetically related to those feeding the stratovolcanoes (i.e., Type 1), supporting discrete ascent pathways beneath stratovolcanoes and the SECs (Watt et al., 2013; Hickey-Vargas et al., 2016b). Furthermore, the Cu contents and Cu/Ag of the SECs presented here are lower than those at Villarrica, thus supporting the idea, previously hypothesised in **Chapter 6**, that enhanced magmatic throughput beneath volcanic systems, in conjunction with fault assisted ascent, is possibly required to transport Cu to near-surface environments where ore deposits are usually situated, and that there is not a direct relationship between basalts at Villarrica and those erupted at nearby SECs.

Although the Type 2 magmas of the CHC are thought to have either originated from mantle lithosphere pyroxenites, or at least assimilated them, there is no evidence to suggest that they mobilised Cu-rich material. The Cu-rich pyroxenites Lee et al. (2012) refer to likely occur at shallower, lower crustal levels, and that both Type 1 and Type 2 magmas may stall in this region and contribute Cu this potential 'reservoir'. Therefore, either secondary, or later, processes are required to transport elevated Cu

concentrations to shallower crustal levels, or atypical scenarios are needed, such as what may be occurring beneath Villarrica.

7.5. Conclusion

This chapter has demonstrated that despite the postulated fast ascent rate of magmas beneath SECs, magmas of the CHC, Huililco and La Poruñita achieved sulfide saturation early during their evolutionary history, likely near the base of the continental crust, and were still affected by sulfide fractionation. However, the subtle increase in Cu and relatively consistent Ag contents observed in the CHC magmas suggest a lesser degree of sulfide fractionation compared to the Chilean stratovolcanoes. This was supported by fractional crystallisation modelling where it was demonstrated that ≤ 0.3 wt.% of crystalline sulfide fractionation is required to replicate the Cu, Ag and Cu/Ag trends observed in the CHC dataset. As was concluded for the stratovolcano datasets, the SEC datasets presented here support a crustal thickness control on the behaviour of the chalcophile elements. Moreover, the datasets presented demonstrate that La Poruñita, situated on very thick continental crust (>70 km), has a greater garnet signature and lower Cu contents relative to the CHC and Huililco SECs. This supports the role of pressure being important in inducing sulfide saturation in a continental arc setting.

The Cu contents and Cu/Ag values of the CHC SECs are depleted relative to the global MORB array and Villarrica. Although the SECs are postulated to have a more simple and rapid magma ascent history, they still display evidence of S and Cu loss, thus suggesting that rapid magma ascent alone is not enough to transport elevated Cu concentrations into the upper crust. This also supports previous conclusions that the SECs near Villarrica are not closely genetically related to the

parental magmas of nearby stratovolcanoes, potentially having a different source. Therefore, this has implications for how SEC magmas are used to infer broader arc processes.

Regardless of this, the data presented here suggests that nearly all magmas in the SVZ, be it from stratovolcanoes or SECs, achieved sulfide saturation early during their evolutionary history, consistent with a strong crustal thickness control on the behaviour of the chalcophile elements.

Chapter 8

Subduction mobile chalcophile elements

8.1. Introduction

Up until this chapter, this thesis has mainly focused on investigating the processing and distribution of those trace elements that behave in a strongly chalcophile manner (i.e., Cu, Ag and Se), and has commented on the implications their processing has on constraining the cycling of S in a subduction zone and the generation of ore deposits. This is because the remaining chalcophile elements (As, Sb, Sn, W, Mo, Pb, Tl, Zn, Ga and Co) are not as instructive on the behaviour of sulfides, due to either their low sulfide – silicate melt partition coefficients ($K_d^{\text{sul-sil}}$) and/or 'mixed affinity', meaning their bulk partitioning is controlled by a combination of sulfide, silicate and oxide phases (Jenner, 2017). It is the goal of this chapter, therefore, to discuss their behaviour in a continental convergent margin setting in more detail.

In a recent study, Jenner (2017) calculated the bulk distribution coefficients for a large suite of trace elements during the differentiation of mid-ocean ridge basalts (MORB). Jenner (2017) demonstrated that many of the chalcophile elements (e.g., W, Mo, Tl, As, Pb, Sb and Bi) are incompatible during the differentiation of MORB and are thus preferentially enriched in the upper oceanic crust (i.e., Evolved-MORB; 7.6 wt.% MgO) compared to the lower and bulk oceanic crust. When this oceanic lithosphere is

subducted, these chalcophile elements are more susceptible to be added to the mantle wedge via a slab-derived fluid or flux. Comparatively, Jenner (2017) demonstrated that Cu, Ag and Se behaved in a compatible manner during MORB differentiation, and therefore reside in the lower oceanic crust where they are less likely to be liberated into the mantle wedge during subduction as part of the slab-derived flux.

Although variations in slab addition to the arc-magma source have been documented in both along- and across-arc transects in the SVZ of Chile (e.g., Jacques et al., 2013, 2014; Watt et al., 2013; Holm et al., 2014; Hickey-Vargas et al., 2016), the wider literature is lacking how these variations manifest themselves in the chalcophile element contents of convergent margin magmas in general (Savov et al., 2007). For example, Noll Jr et al. (1996) investigated a subset of the chalcophile element suite in lavas from subduction zones globally, including the Central American, Chilean, Kamchatka, Kurile, Cascades, Japan, Mariana and Aleutian arcs. In this pioneering study, they argued for the mobilisation of As, Sb and Pb in a slab-derived fluid, relative to other chalcophile elements (e.g., Sn, W, Mo), and that the addition of these chalcophile elements via a slab fluid decreased with increased distance from the arc front. More recently, Timm et al. (2012) presented data on a slightly broader set of chalcophile element analyses of lavas from 15 Kermadec arc volcanoes, arguing for the mobilisation of Cu, Sb, As, Bi, Tl and Zn into the sub-arc mantle wedge via hydrous fluids, derived from either subducted sediments or altered oceanic crust.

Further to these studies, **Chapter 5** demonstrated that the chalcophile elements Tl, As, Pb, W, Sb and Bi were enriched in samples from Antuco, highlighted by substantial peaks on a Parental-MORB normalised multi-element plot, suggesting them to be subduction mobile. Antuco sample compositions were normalised to

Parental-MORB [calculated by Jenner (2017); except for Mo, Sn and Se, revised by Reekie et al. (2019)] as it represents an undifferentiated melt composition, akin to that of the bulk oceanic crust, permitting comparisons between elemental fluxes at convergent margins and MOR to be made.

This chapter builds on the work presented in **Chapter 5** by presenting new whole rock analyses of As, Sb, Sn, W, Mo, Pb, Tl, Zn, Ga and Co for both the Chilean stratovolcano and small eruptive centre (SEC) datasets previously discussed, in order to assess the mobility of these elements during subduction and convergent margin magma generation. The array of samples presented permits investigation of both along- and across-arc (e.g., Villarrica – Quetrupillán – Lanín) transects and between stratovolcanoes and SECs (**Fig. 8.1**).

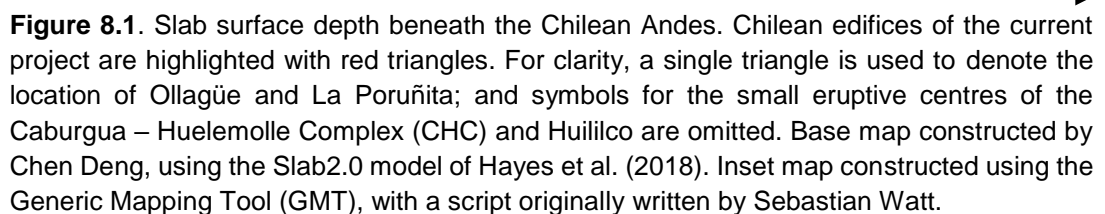
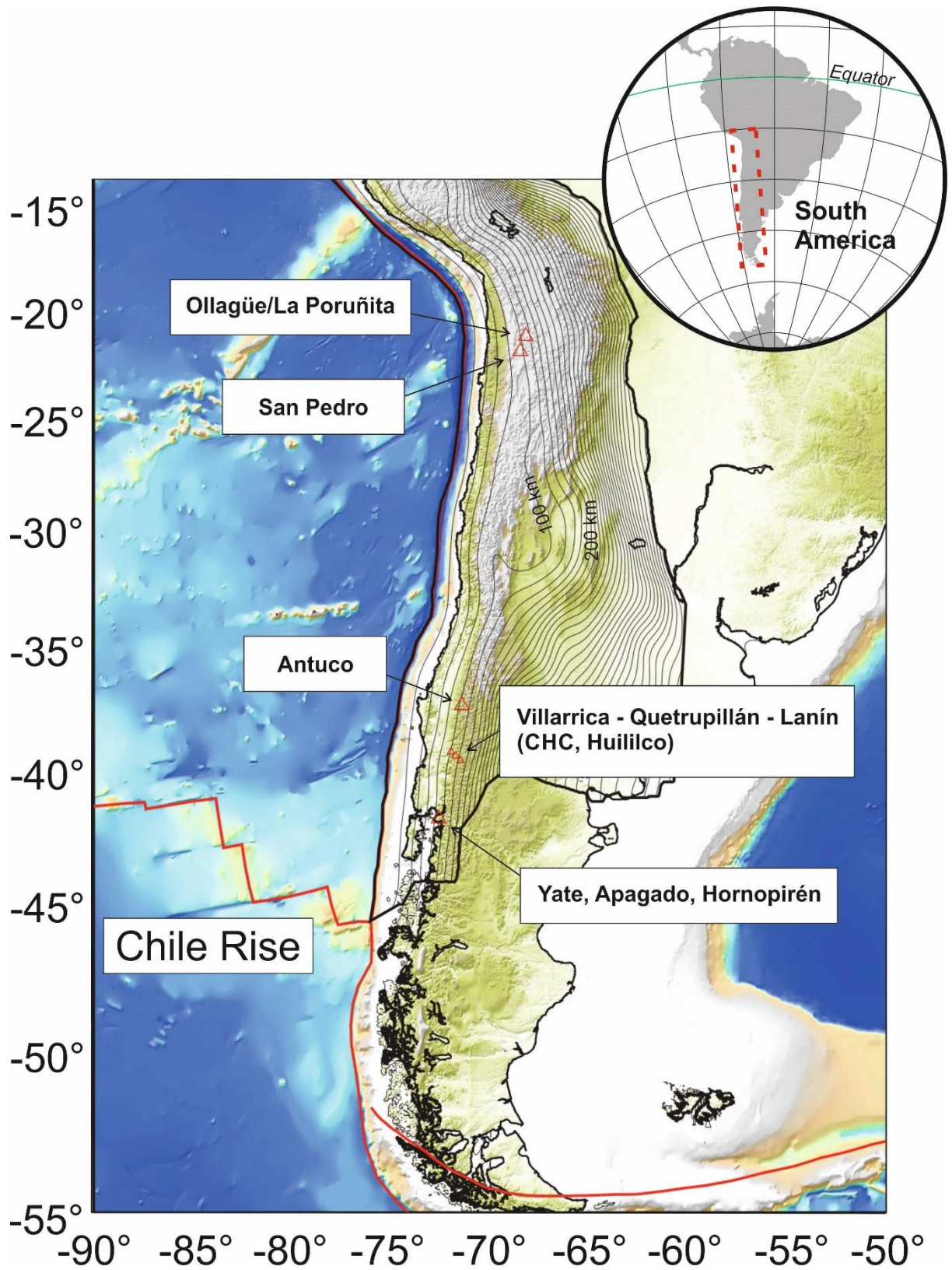


Figure 8.1. Slab surface depth beneath the Chilean Andes. Chilean edifices of the current project are highlighted with red triangles. For clarity, a single triangle is used to denote the location of Ollagüe and La Poruña; and symbols for the small eruptive centres of the Caburgua – Huelemolle Complex (CHC) and Huilico are omitted. Base map constructed by Chen Deng, using the Slab2.0 model of Hayes et al. (2018). Inset map constructed using the Generic Mapping Tool (GMT), with a script originally written by Sebastian Watt.



8.2. Geochemical results

Collectively, the As, Mo, Sb, Sn, Tl, W and Pb contents of Chilean stratovolcanoes and SECs broadly define positive correlations with SiO₂ (**Figs. 8.2**). In terms of the stratovolcanoes, these correlations become more scattered at greater SiO₂ concentrations (i.e., 60 – 65 wt.%). For example, samples from Ollagüe display a broad range in As, Tl, and Mo concentrations at a given SiO₂. However, the two clusters of CHC samples, roughly defined in **Chapter 7** based on their SiO₂ contents, define clear clusters in terms of their As and Sb contents (**Fig. 8.2a,e**). Additionally, at a given SiO₂, the SECs have Tl, Mo, W, Sn and Pb contents similar to the Chilean stratovolcanoes, although the CHC (and in the case of As, La Poruña) have elevated As and Sb contents. Moreover, the As, Tl, Mo, Pb, and Sb contents of the stratovolcanoes, and Tl and Pb contents of the SECs, are generally elevated relative to the global MORB array (e.g., Jenner and O'Neill, 2012) at a given SiO₂. With the exception of Pb (and Tl in the case of the CHC), the As, Mo, W, Sb, Sn and Tl contents of the CHC and Apagado are similar to the global MORB array. As an entire suite, the W and Sn contents of the stratovolcanoes and SECs are similar to (at a given SiO₂) and define a broad continuum with the global MORB array (**Fig. 8.2d,f**). One sample from Lanín (16DCLan.001, 55.39 wt.% SiO₂) displays elevated Tl and Sb and depleted Mo relative to other stratovolcanoes at a given SiO₂, falling off the general trend defined by the Chilean stratovolcanoes (**Fig. 8.2b,c,e**). This is possibly due to post-eruption mobilisation of these elements, as evidenced by extensive alteration in thin section (see description of 16DCLan.001 in **Appendix A** for further details).

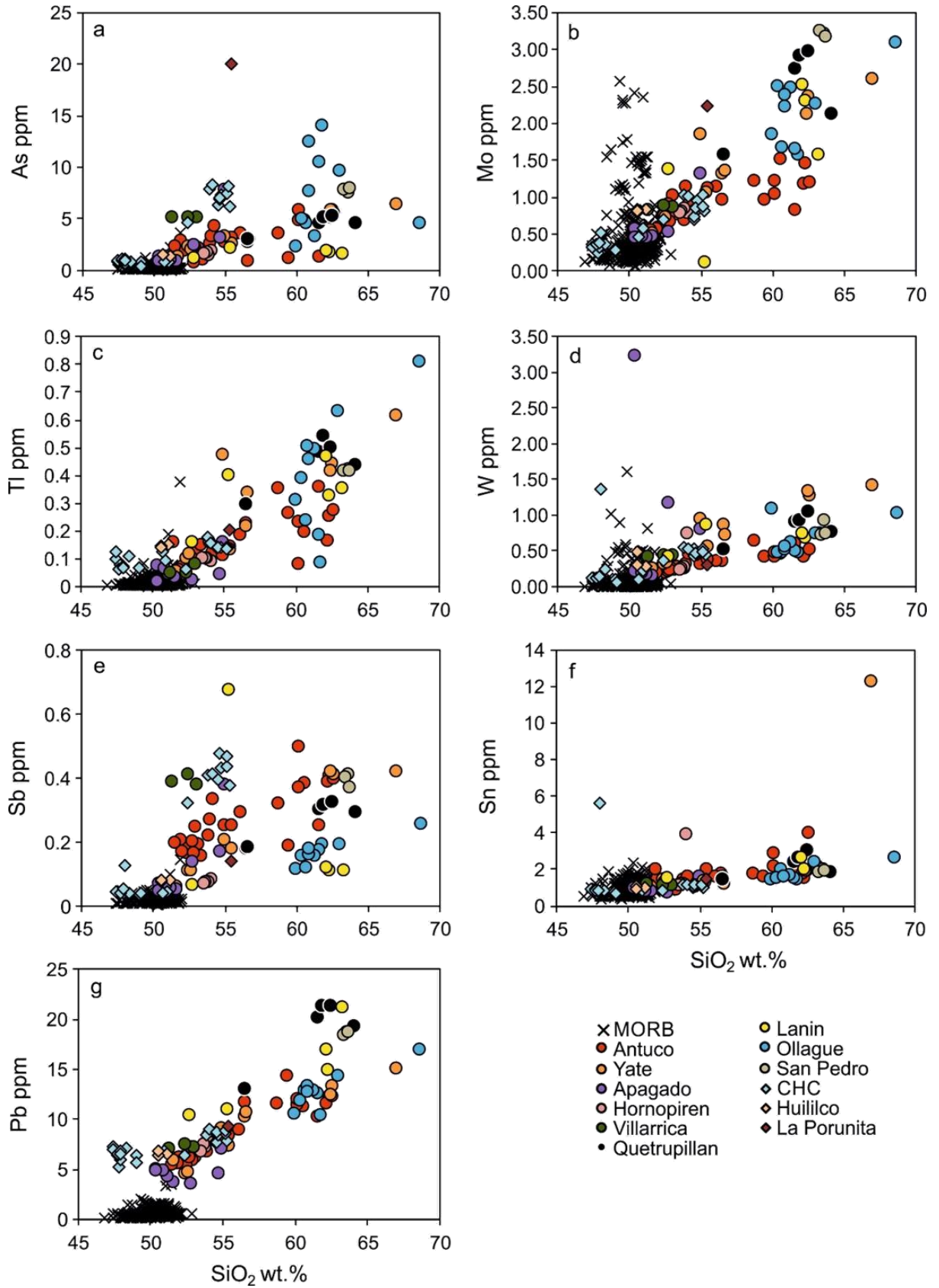


Figure 8.2. Select chalcophile element bivariate plots (vs. SiO_2) for all Chilean edifices studied in this thesis. Global MORB array data from Jenner and O'Neill (2012).

In terms of Parental-MORB normalised multi-element plots, stratovolcano (**Fig. 8.3**) and SEC (**Fig. 8.4**) samples are plotted separately for clarity. All samples display an overall increase in their Parental-MORB normalised trace element concentrations with increasing incompatibility (i.e., from right to left) during the differentiation of MORB magmas (Jenner, 2017). Negative Nb-Ta anomalies, relative to neighbouring elements, are observed in the vast majority of samples; one sample from each of Villarrica, Hornopirén, Apagado, Antuco and San Pedro, however, have only negative Nb anomalies. Significant peaks in the abundances of W, Tl, As, Pb and Sb are observed in most samples, as are substantial depletions in Se. Generally, the Zn, Ga, Mo and Sn contents of the samples are similar to very slightly elevated relative to Parental-MORB, whereas the Co contents are marginally depleted. The Ag contents of the stratovolcanoes are generally similar to Parental-MORB, whereas their Cu contents are similar to slightly depleted. In terms of the SECs, their Cu and Ag contents are mostly similar to Parental-MORB, although La Poruñita is slightly depleted in terms of its Cu contents.

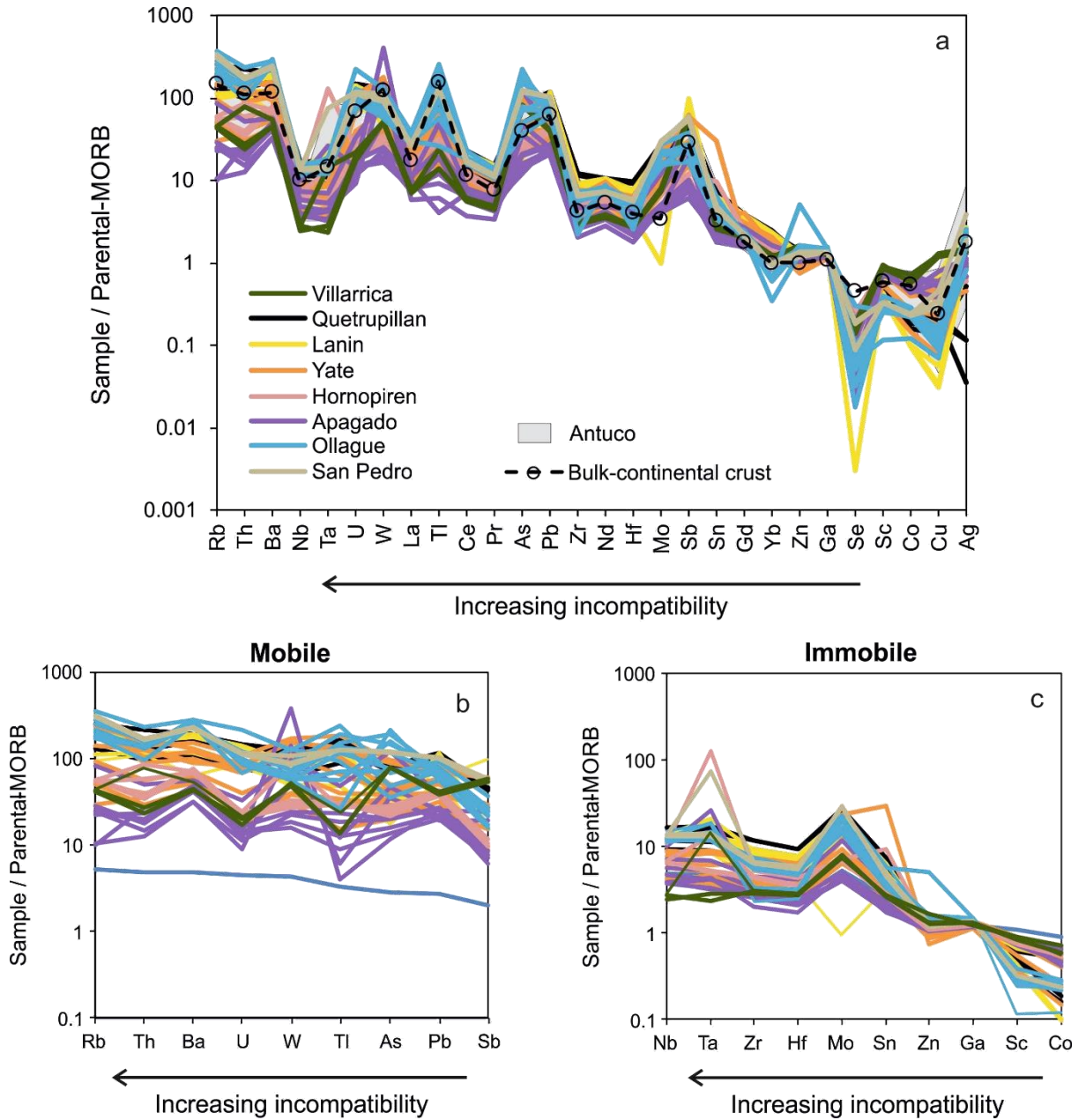


Figure 8.3. Parental-MORB (mid-ocean ridge) normalised multi-element plots of samples from Chilean stratovolcanoes. (a) Complete multi-element plot ordered in terms of trace element compatibility during the low-pressure differentiation of MORB (e.g., Jenner, 2017). Isolated mobile (b) and immobile (c) Parental-MORB normalised multi-element plots compared to their respective distribution on the upper oceanic crust (i.e., Evolved-MORB; Jenner, 2017). Normalising values as of Jenner (2017); exceptions include Mo, Sn and Se (Reekie et al., 2019). Data for the bulk-continental crust from Rudnick and Gao (2003).

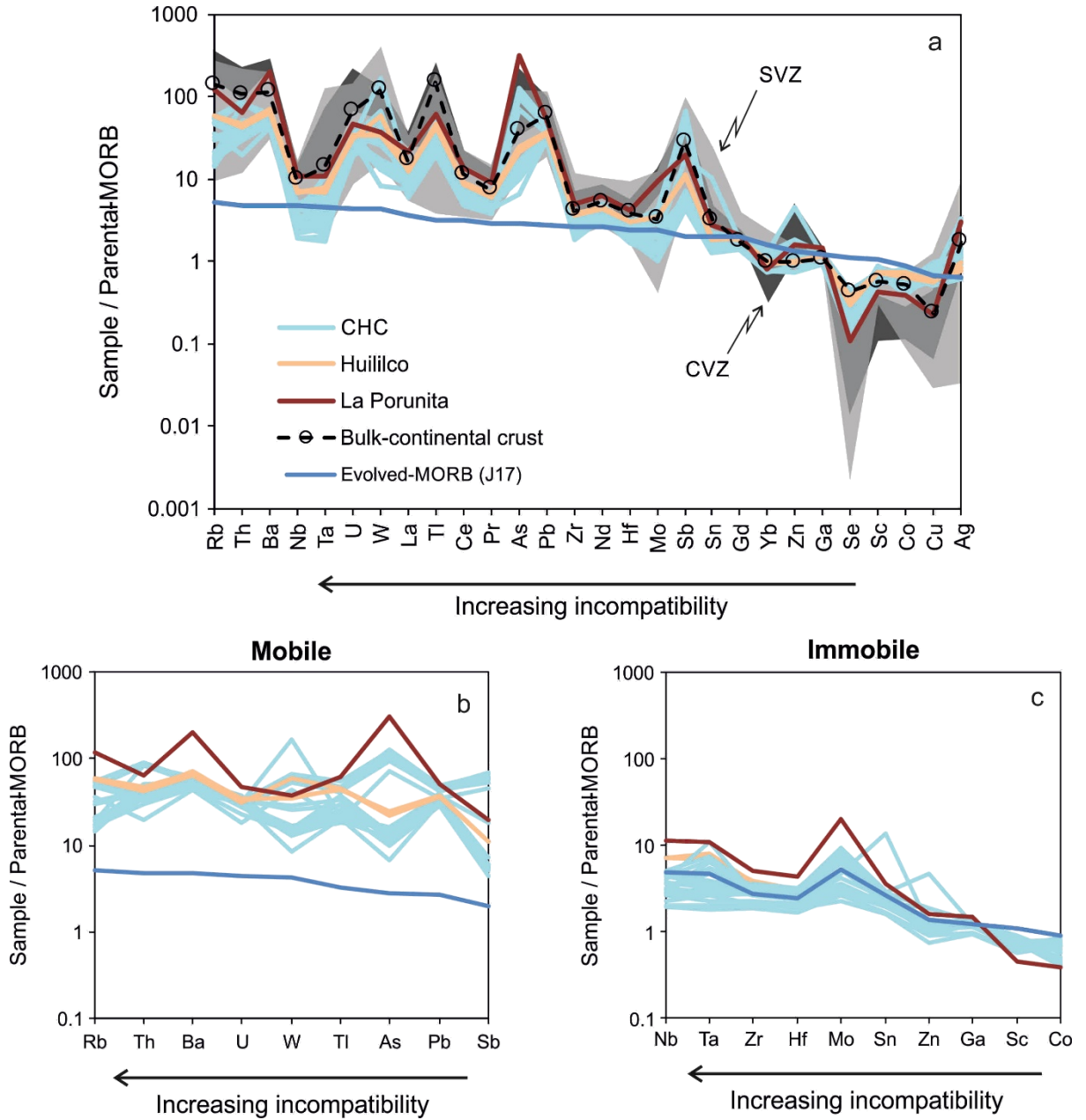


Figure 8.4. Parental-MORB (mid-ocean ridge) normalised multi-element plots of samples from Chilean small eruptive centres. (a) Complete multi-element plot ordered in terms of trace element compatibility during the low-pressure differentiation of MORB (e.g., Jenner, 2017). Isolated mobile (b) and immobile (c) Parental-MORB normalised multi-element plots compared to their respective distribution on the upper oceanic crust (i.e., Evolved-MORB; Jenner, 2017). Normalising values as of Jenner (2017); exceptions include Mo, Sn and Se (Reekie et al., 2019). Data for the bulk-continental crust from Rudnick and Gao (2003).

8.3. Discussion

To assess the mobility of the chalcophile elements during subduction, the trace element contents of the Chilean edifices have been normalised to Parental-MORB (calculated), representative of an undifferentiated melt composition, approximating that of the bulk oceanic crust (Jenner, 2017). This way, the relative differences in elemental fluxes between a subduction zone and MOR can be established.

All samples display trace element signatures characteristic of volcanoes situated above subduction zones (e.g., Pearce et al., 2005): enrichment of the mobile large ion lithophile elements (LILE) relative to the moderately mobile REE, and enrichment of the REE relative to the generally immobile high field strength elements (HFSE) (**Figs. 8.3** and **8.4**). Additionally, the majority of samples display negative Nb – Ta anomalies, also characteristic of subduction zone magmas. Most samples from both the stratovolcano and SEC datasets display significant peaks in their W, Tl, As, Pb and Sb concentrations relative to the REE and HFSE, thus demonstrating W, Tl, As, Pb and Sb to be mobile during subduction. Comparatively, the remaining chalcophile elements (e.g., Mo, Sn, Zn, Ga, Co) have concentrations similar to neighbouring REE and HFSE and to Parental-MORB, therefore suggesting that they were not mobile during subduction. Moreover, the data suggest that neither Cu nor Ag were subduction mobile, and were instead derived from the mantle wedge component. These conclusions are in general agreement with previous studies on the mobility of the chalcophile elements (e.g., Noll Jr et al., 1996; Jenner, 2017). Slight depletions of Cu relative to Ag in many samples is likely due to early sulfide fractionation, preferentially sequestering Cu (over Ag) from evolving magmas.

When plotted in isolation, the mobile (i.e., Rb, Th, Ba, U, W, Tl, As, Pb and Sb; **Figs. 8.3 and 8.4**) and immobile (i.e., HFSE, Mo, Sn, Zn, Ga, Sc and Co; **Figs. 8.3 and 8.4**) trace elements produce trends that are relatively smooth, at concentrations enriched relative to (i.e., mobile trace elements) or similar to (i.e., immobile trace elements) Evolved-MORB. However, the trends observed in the mobile and immobile trace elements are generally more scattered than those observed in the Antuco dataset (**Fig. 5.6; Chapter 5**). Nevertheless, each group displays an overall increase in Parental-MORB normalised values with increasing incompatibility of an element during the differentiation of MORB, mimicking that of their distribution in Evolved-MORB, thus suggesting that the mobile elements were fluxed into the mantle wedge in roughly similar proportions as they are distributed in the upper oceanic crust. However, those samples from Villarrica and La Poruñita have somewhat more scattered Parental-MORB normalised trace element patterns, therefore suggesting that the mobile element flux did not replicate the distribution of these elements in the upper oceanic crust.

8.3.1. Estimating the flux of the subduction mobile chalcophile elements

Above, the chalcophile elements W, Tl, As, Pb and Sb were demonstrated to be subduction mobile, evidenced by substantial peaks in their Parental-MORB normalised values relative to neighbouring elements of similar bulk distribution coefficients during the differentiation of MORB (e.g., Jenner, 2017). However, variations in the fertility of the sub-arc mantle wedge, as demonstrated by differences in the Nb/Zr of the edifices when plotted against edifice – trench distance or slab depth (**Fig. 8.5**), make it difficult to accurately establish a relative order of flux of these elements across the arc. Instead, the percentage contribution of W, Tl, As, Pb and Sb

derived from the slab component beneath each individual edifice has been estimated (Fig. 8.6 and Table 8.1).

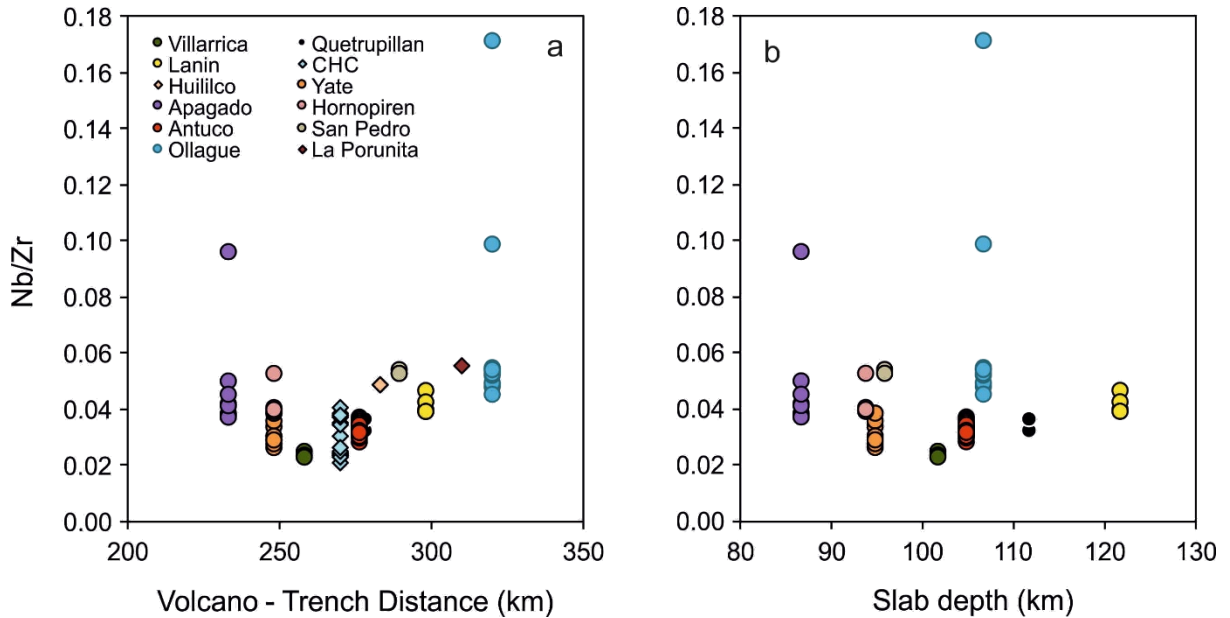


Figure 8.5. An assessment of mantle fertility (Nb/Zr) versus volcano – trench distance and slab depth (km). Volcano – trench distance estimated using the measuring tool on Google Earth (2019). Depth to slab for each edifice calculated by Chen Deng, using the Slab2.0 model of Hayes et al. (2018). CHC: Caburgua – Huelemolle Complex small eruptive centres.

Using the Parental-MORB normalised multi-element plots, baselines separating the mantle wedge (below baseline) and slab-derived (above baseline) components were constructed for each edifice by connecting the ‘conservative’ (i.e., generally immobile) elements Nb, Ta, Zr, Hf, Yb, Zn and Ga (e.g., Pearce and Peate, 1995; Pearce and Stern, 2006). Additionally, the baselines were extended to include Cu and Ag, as both Cu and Ag were demonstrated above to be immobile during subduction, having concentrations similar to Parental-MORB and neighbouring ‘conservative’ elements (i.e., the HFSE and HREE). The baselines were constructed based on

average Parental-MORB normalised values of each dataset, taking into consideration only those samples displaying both negative Nb and Ta anomalies. This is because these samples represent the dominant trace element pattern within each dataset. Those samples that display solely negative Nb anomalies, of which there are very few (one from each of the Villarrica, Hornopirén, Apagado, Antuco and San Pedro datasets), were omitted as their incorporation skewed the constructed baseline, increasing the mantle wedge component and noticeably reducing the estimated flux of W and TI. As examples, baselines constructed with the Antuco and Yate datasets are presented in **Fig. 8.6**, with the remaining constructed baselines presented in **Appendix F**.

Table 8.1 Estimated percentage contribution of W, TI, As, Pb and Sb derived from the slab component (as demonstrated in **Fig. 8.6** and **Appendix F**)

Edifice	W	TI	As	Pb	Sb	Volcano – trench*	Slab depth*
Antuco	86	89	90	91	93	277	105
Villarrica	95	80	96	93	96	259	102
Quetrupillán	88	92	86	90	88	279	112
Lanín	87	90	69	90	87	299	122
CHC	91	89	94	92	94	270 (avg.)	-
Huillico	85	88	81	89	82	283	-
Yate	94	94	91	90	92	249	95
Hornopirén	77	80	79	87	77	249	94
Apagado	92	79	92	88	90	234	87
San Pedro	86	92	94	93	95	290	96
Ollagüe	87	93	94	91	92	321	107
La Poruña	76	87	98	89	89	310	-

*Measurements in km; CHC: Caburgua – Huelemolle Complex; avg.: volcano – trench distance of the CHC is an average of the centres in the area; volcano – trench distance measured using Google Earth; Slab depth determined by Chen Deng using the model Slab2.0 (Hayes et al., 2018).

Qualitative estimations of the contributions of W, Tl, As, Pb and Sb derived from the slab component were calculated from **Fig. 8.6** and are presented in **Table 8.1**. The percentage contribution of W, Tl, As, Pb and Sb derived from the slab component is typically >85% for most of the Chilean edifices. No strong correlations are apparent between the subduction mobile chalcophile elements and volcano – trench distance or slab depth on an arc segment scale (i.e., C/SVZ) (**Fig. 8.7**), although the Villarrica – Quetrupillán – Lanín chain displays decreases in the flux of W, As, Pb and Sb with distance from the trench, with the variations in slab-derived flux generally decreasing by <10 % (**Fig. 8.7a,e,g,i**). This is consistent with a decreasing contribution of slab-derived fluids behind the arc front, as demonstrated by Hickey-Vargas et al. (1989). Moreover, no obvious along-arc variations in the estimated contributions of the subduction mobile chalcophile elements are observed.

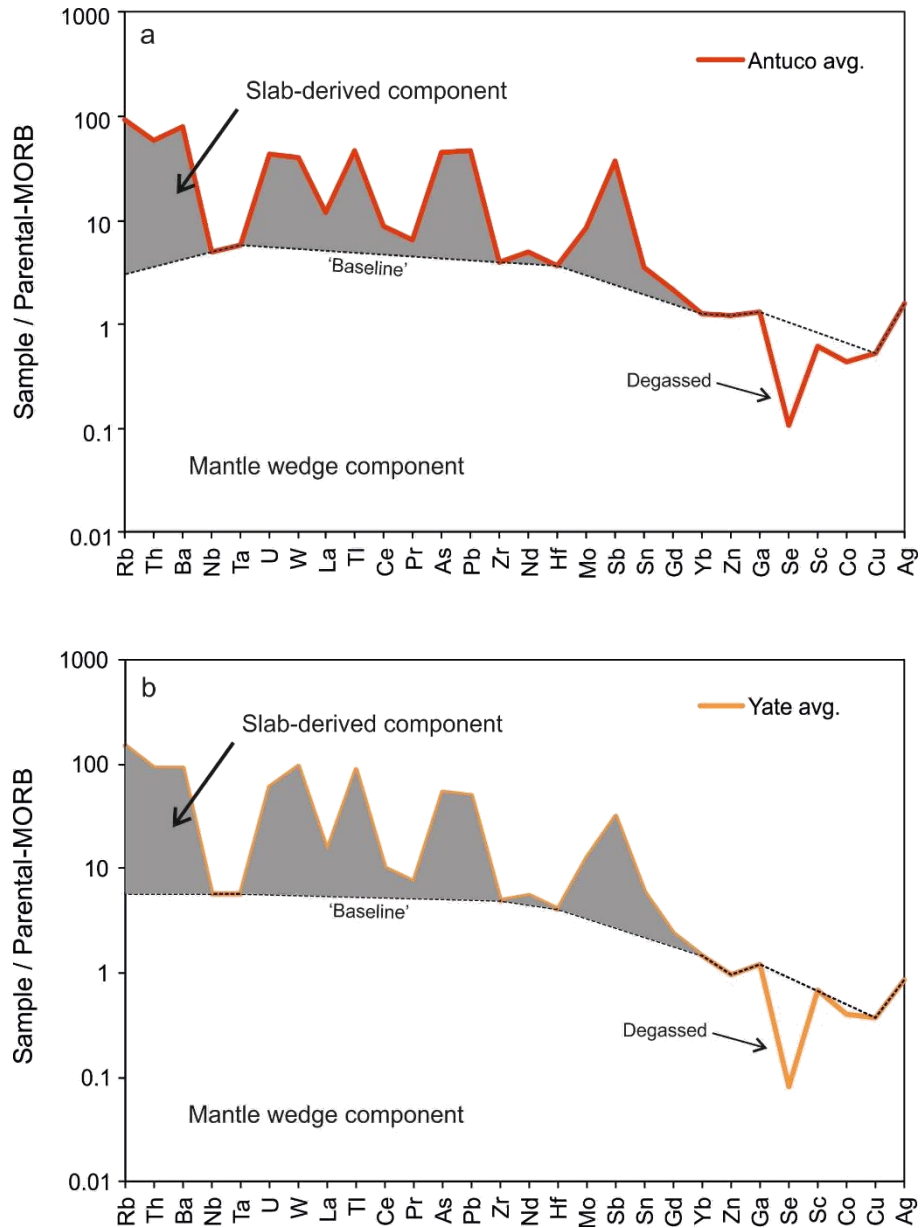
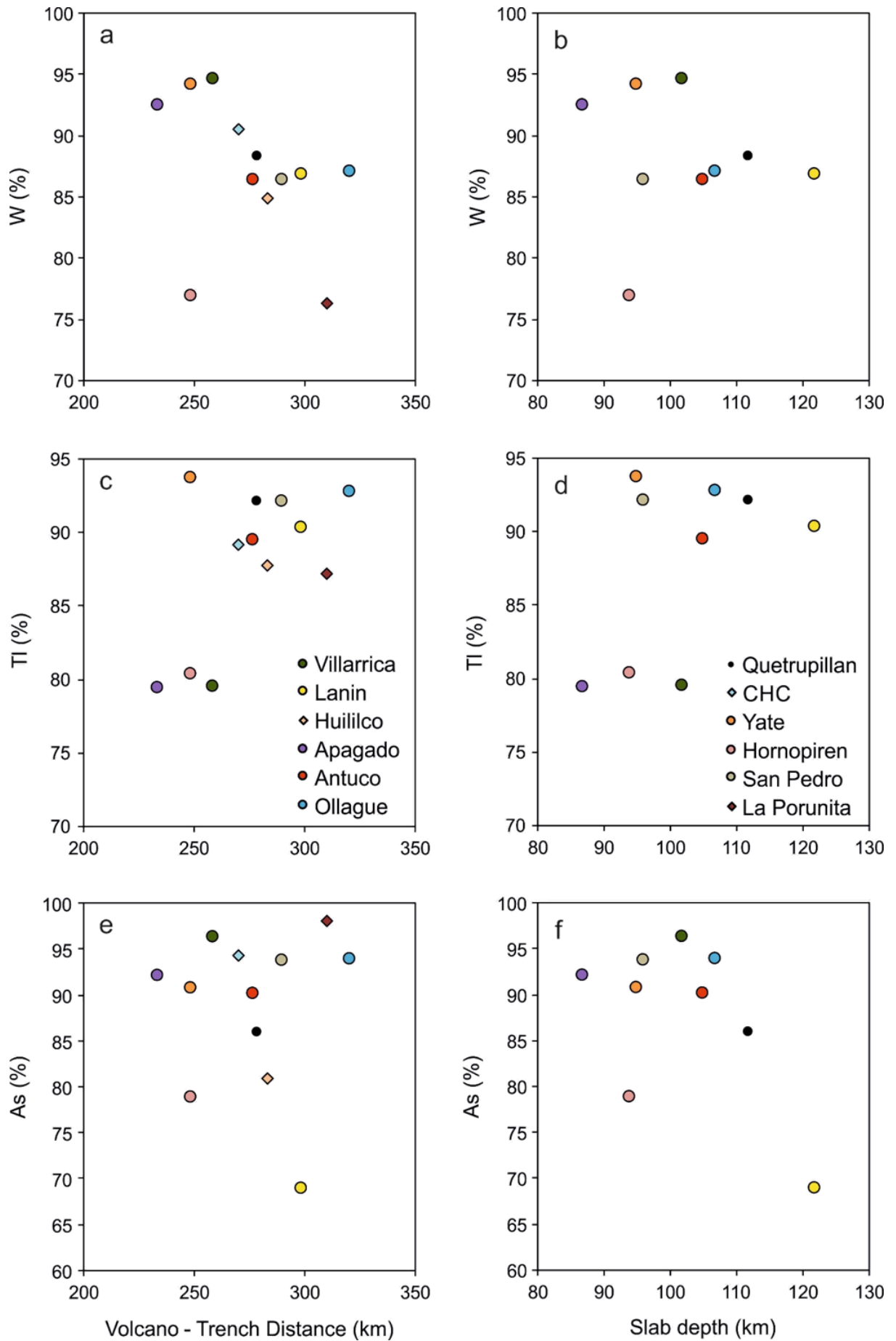


Figure 8.6. Constructed baselines separating mantle wedge and slab-derived components (e.g., Pearce and Stern, 2006) of samples from Antuco (a) and Yate (b) stratovolcanoes. Baselines were constructed by connecting the ‘conservative’ (i.e., generally immobile) elements Nb, Ta, Zr, Hf, Yb, Zn and Ga (Pearce and Peate, 1995). The baseline has been extended to include Cu and Ag, as both have been demonstrated to be immobile.

Chapter 8. Subduction mobile chalcophile elements



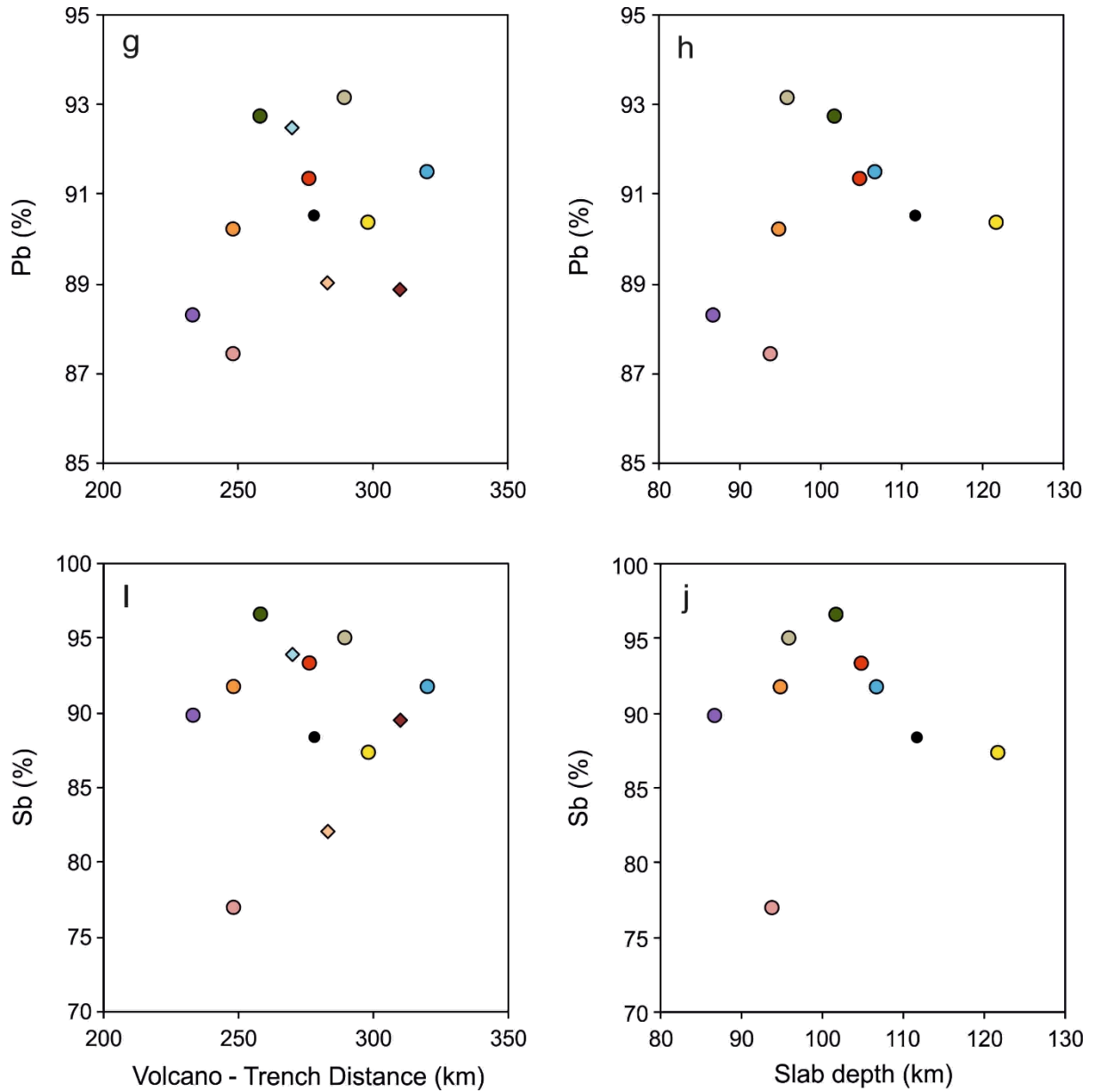


Figure 8.7. Estimated percentage contribution of W, TI, As, Pb and Sb from the slab-derived component beneath the Chilean Arc. No strong correlations are apparent between the estimated percentage flux of these elements and volcano – trench distance or slab depth. Volcano – trench distance estimated using the measuring tool on Google Earth (2019). Depth to slab for each edifice calculated by Chen Deng, using the Slab2.0 model of Hayes et al. (2018). CHC: Caburgua – Huelmolle Complex small eruptive centres.

8.4. Conclusion

This chapter focussed on investigating the chalcophile elements that are not as instructive on the behaviour of sulfides as Cu, Ag and Se (i.e., W, Tl, As, Pb, Sb, Sn, Zn, Ga and Co), with the aim of constraining how these elements are mobilised during subduction. Through normalising sample compositions to a calculated Parental-MORB composition, an undifferentiated melt composition akin to the bulk oceanic crust, the relative flux of elements at a subduction zone, compared to at MORs, can be established. Thus, this chapter has demonstrated that W, Tl, As, Pb and Sb are subduction mobile across the Chilean arc segments, compared to Mo, Sn, Zn, Ga, Co, Cu and Ag which are immobile, having contents more similar to Parental-MORB and neighbouring immobile trace elements (i.e., the HFSE and HREE). Moreover, the flux of W, Tl, As, Pb and Sb has been demonstrated to be roughly similar to their distributed proportions in the upper oceanic crust (i.e., Evolved-MORB). These findings are consistent with previous studies on the mobility of the chalcophile elements within convergent margins (e.g., Noll Jr et al., 1996; Jenner, 2017). Further to this, the percentage contributions of W, Tl, As, Pb and Sb from the slab-derived component was estimated to be >85% for most edifices, with some evidence for across-arc variations in fluid input at Villarrica – Quetrupillán – Lanín.

Chapter 9

A synthesis of the processing and distribution of the chalcophile elements in a continental volcanic arc setting

This thesis has presented novel whole rock analyses of the near complete suite of chalcophile elements (S, Cu, Ag, Se, As, Sb, Sn, W, Mo, Pb, Bi, Tl, Zn, Ga, Co) for several volcanic edifices, including both stratovolcanoes and small eruptive centres (SECs), in a continental volcanic arc setting (the Chilean Andes). Investigations into these new datasets has further constrained the behaviour of the chalcophile elements during magma genesis and subsequent evolution in a continental volcanic arc. The thesis initially focussed on studying the processing and distribution of the chalcophile elements beneath a typical continental arc stratovolcano in southern Chile (Antuco). Subsequent comparisons have been made with other stratovolcanoes situated on varying crustal thicknesses (~ 25 to ≥ 70 km) and with SECs along the Chilean volcanic arc. The insights provided into chalcophile element processing at convergent margins have implications for the cycling of S through a subduction zone and the generation of porphyry Cu ore deposits, which are globally associated with continental volcanic arcs (see **Section 9.2.** below). The results offered here also provide the basis for further study into the behaviour of the chalcophile elements.

9.1. Overall crustal processing of the chalcophile elements

Across the stratovolcano and SEC datasets, Cu and Ag were the most useful of the chalcophile elements in constraining the onset of sulfide saturation within the Chilean arc magmas. This is because both S and Se were demonstrated to have been extensively degassed, with their contents considerably depleted relative to the global MORB array and oceanic arc-like magmas. The degassing of both S and Se likely occurred during either low-pressure magmatic differentiation or sub-aerial eruption, and therefore at a much later stage of the arc-magma evolutionary process than sulfide saturation.

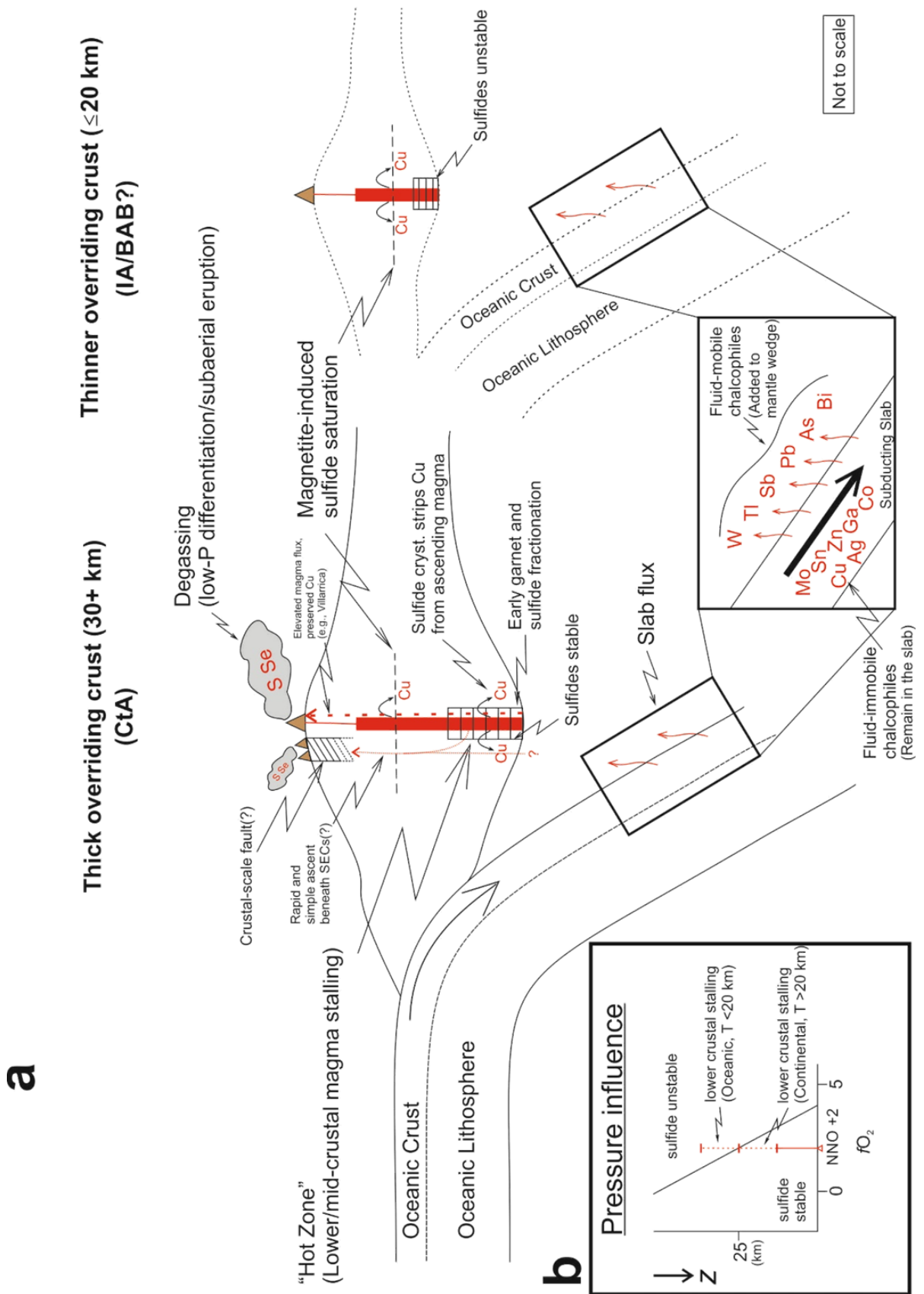
Overall, the continental arc magmas were saturated in a crystalline sulfide phase across their entire compositional range (i.e., basalt through to dacite), beginning early in their evolutionary history, and prior to ascent and low-pressure fractional crystallisation. This is consistent with the initial stalling and crystallisation of magmas in MASH (mixing, assimilation, storage, homogenisation) or 'deep crustal hot zones' within the lower continental crust (Hildreth and Moorbath, 1988; Annen et al., 2006). Additionally, the results presented here show that stratovolcano magmas evolve to depleted Cu contents and lower Cu/Ag ratios, a result of the greater partition coefficient of Cu, over Ag, for crystalline sulfide (Li and Audétat, 2012, 2015). These findings corroborate previous studies that have demonstrated continual sulfide saturation in continental volcanic arcs (e.g., Lee et al., 2012; Chiaradia, 2014; Georgatou et al., 2018). Furthermore, modelling of fractional crystallisation, using both primitive stratovolcano and SEC magmas as starting compositions, has demonstrated the volume of fractionated sulfide required to replicate the trends observed in the Cu and Ag contents of the stratovolcano and SEC magmas to be minimal (≤ 0.6 wt.%).

Unlike in oceanic arc-like settings, where magnetite fractionation has been inferred to play a dominant role in inducing sulfide saturation (e.g., Jenner et al., 2015; Williams et al., 2018; Valetich et al., 2019), sulfide saturation in the Chilean arc magmas was attained prior to the onset of magnetite fractionation. The pressure and potentially temperature of magma storage is inferred to be the dominant control on sulfide saturation in the Chilean arc magmas, rather than garnet fractionation. Although garnet fractionation would deplete a magma in Fe, subsequently inducing sulfide saturation because of the dependence of S solubility on melt Fe content (O'Neill and Mavrogenes, 2002), the simultaneous oxidation of the magma would compete against this effect, destabilising fractionated sulfides and releasing Cu back into the magma (e.g., Tang et al., 2018). However, samples with the strongest garnet signature (i.e., Ollagüe and San Pedro) have amongst the lowest Cu contents and Cu/Ag values, indicating that sulfide was stable. Excluding Villarrica, the effects of sulfide fractionation are observed across all magmas studied here, regardless of the strength of their garnet signature. It is therefore suggested that the effect of pressure and temperature on the stability of sulfides overrides any influence of garnet fractionation.

The early onset of sulfide saturation in the Chilean arc magmas, in contrast to magmas generated in oceanic arc-like settings, and the identification of magmatic sulfide inclusions in a broad range of phenocryst phases (olivine, pyroxene, plagioclase, amphibole and magnetite) in continental arc lavas (e.g., Kamenetsky et al., 2017; Georgatou et al., 2018; Zelenski et al., 2018), implies that the thickness of the overlying crust at a convergent margin plays a dominant role in controlling the saturation of sulfides and the behaviour of the chalcophile elements. That is, the crustal thickness regulates the initial depth of magmatic differentiation and is therefore the

primary control on initial sulfide saturation. The formation of a Cu-rich sulfide ‘reservoir’ at or near the base of the continental crust is expected to be the consequence of this process, potentially in the form of lower crustal cumulates [e.g., pyroxenites; Lee et al. (2012)] or within the metasomatised sub-continental lithospheric mantle (e.g., Holwell et al., 2019). **Figure 9.1** (modified after **Chapter 5**) summarises these results and presents an overall schematic model for the processing and distribution of the chalcophile elements within a continental and an oceanic volcanic arc.

Figure 9.1. (a) Schematic model of the processing and distribution of the chalcophile elements beneath thick (≥ 30 km) and thin (≤ 20 km) overriding crust at convergent margins. The fluid mobile chalcophile elements (W, Tl, As, Pb, Sb, Bi) are enriched in the upper oceanic crust (e.g., Jenner, 2017) and are therefore preferentially fluxed from the subducting slab to the mantle wedge in a fluid phase, whereas the subduction immobile Cu, Ag, Mo, Sn, Zn, Ga and Co are retained in the lower (to mid) oceanic crust. Thus, the Cu, Ag, Mo, Sn, Zn, Ga and Co contents of the continental arc magmas are derived from the mantle wedge component. Thicker overriding crust (i.e., continental volcanic arcs) promotes early (and deep) sulfide fractionation from both stratovolcano and small eruptive centre (SEC) magmas because of the increased stability of sulfides to greater fO_2 with increased pressure, and therefore depth [e.g., inset b; Matjuschkin et al. (2016)]. Additionally, the effect of temperature likely plays a role in stabilising sulfides in this region (e.g., Nash et al., 2019). Thus, the fraction of crystalline sulfide sequesters Cu from evolving magmas, depositing it at or near the base of the continental crust, likely in lower crustal cumulates. Alternatively, elevated levels of magma throughput (heavy dashed, red line; e.g., Villarrica) could maintain a hotter system and aid in a more rapid magma ascent beneath the most active stratovolcanoes, thus limiting the residence times of magmas in the garnet and sulfide fields, preserving their primary Cu contents and transporting them to upper crustal levels, where ore deposits are usually situated. In the case of thinner overriding crust [i.e., island arcs (IA) or back arc basins (BAB)], sulfides are unlikely to be stable at the base of the crust due to the shallow pressures (e.g., inset b) and therefore Cu will behave incompatibly until magnetite fractionation induces sulfide saturation. Both S and Se degas from the ascending continental arc magmas, however, this likely occurs post-sulphide saturation during either low pressure differentiation or sub-aerial eruption. Modified after **Chapter 5**.



9.2. On the formation of ore deposits

Although the spatial association of porphyry Cu deposits with continental volcanic arcs is well established (Sillitoe, 2010; Sun et al., 2015), the process(es) required in generating such mineralisation is/are still hotly debated (e.g., Mungall, 2002; Richards, 2009; Jenner et al., 2010; Lee et al., 2012; Wilkinson, 2013; Chiaradia, 2014; Matjuschkin et al., 2016; Tang et al., 2018; Holwell et al., 2019). Furthermore, whilst the majority of data presented in this thesis supports the idea of a Cu-rich 'reservoir' at or near the base of the continental crust (e.g., Lee et al., 2012; Wang and Becker, 2015; Georgatou et al., 2018; Tang et al., 2018; Holwell et al., 2019), the question as to how large Cu concentrations are transferred to mid to upper crustal levels remains unconstrained. The investigation of the typical processes involved in processing the chalcophile elements in a continental volcanic arc presented in this thesis suggest that Cu would be sequestered in the lower continental crust. It therefore remains unclear how or whether mid to upper crustal concentrations of Cu are generated as a consequence of typical arc-magmatic processes (this would require a form of secondary process, evidence of which was not found here), or if their formation requires a more atypical process or set of circumstances. The latter is potentially more in-line with the sporadic global distribution of porphyry Cu deposits (Sillitoe, 1997).

For example, the remobilisation of Cu from such deep 'reservoirs' (e.g., lithospheric or crustal pyroxenites), by either hybridisation of ascending magmas through the assimilation of sulfides or the partial melting of this 'reservoir' and exhaustion of sulfides, represents a potential mechanism for generating high Cu content magmas for forming an ore deposit (e.g., Lee et al., 2012). No evidence of such melting processes were observed in the samples studied here. For example,

although the Caburgua – Huelemolle Complex (CHC) SECs are potentially derived from lithospheric mantle pyroxenites (e.g., Hickey-Vargas et al., 2016), there is no evidence of them mobilising Cu. Rather, their magmas display evidence of early sulfide fractionation (i.e., flat Cu trend with SiO₂ and Cu/Ag values depleted relative to the global MORB). This suggests that later processes may be required to generate and transport Cu-rich magmas to upper crustal levels, where ore deposits are usually situated. Alternatively, atypical circumstances may provide an alternative process to transport elevated Cu concentrations to shallower depths (see **Section 9.2.1.** below).

9.2.1. Elevated Cu contents at Villarrica

The Cu-enriched nature of samples from Villarrica could potentially provide an insight into mechanisms of achieving high Cu concentrations in the upper crust. In conjunction with similarly elevated Cu contents at Llaima and the Puyehue – Cordon Caulle Volcanic Complex (PCCVC) (Singer et al., 2008; Reubi et al., 2011), the elevated Cu contents of samples from Villarrica were used to propose a potential link between sites of enhanced magmatic flux (or throughput) and the preservation of elevated magmatic Cu contents. The heightened magmatic flux at these centres, based on their high historical rates of activity (Global Volcanism Program, accessed 2019) and large volumes (Volker et al., 2011), could potentially inhibit magma storage by maintaining relatively hot systems that insulate ascending magmas, allowing mafic magmas to ascend more rapidly. The potential importance of a role for an elevated temperature (e.g., Nash et al., 2019) of the system is supported by the fact that SEC magmas also ascend rapidly, although do not have the same elevated Cu contents as these three volcanic centres. Furthermore, Morgado et al. (2015) demonstrated that the pre-eruptive temperatures of a deep-seated reservoir beneath Villarrica, as

recorded by olivine and augite phenocrysts, was potentially hotter than that beneath the nearby SECs. Although this is speculative, the observations suggest a clear distinction in the Cu content of erupted magmas at these three volcanic centres versus all others of the C/SVZ, and these same systems are the most active in the arc. Rapid ascent and high temperatures would limit the effects of garnet and sulfide fractionation on their magmas, thus preserving their primary Cu contents and transporting these high-Cu magmas to shallower crustal levels, where ore deposits are usually situated.

Nevertheless, what is clear is that more work is required in order to decipher the process(es) involved in generating economically viable ore deposits. Data presented here suggests that the typical processing of the chalcophile elements in continental arc magmas, whether erupted from stratovolcanoes or SECs, do not offer a mechanism through which high-Cu content magmas may reach shallower crustal levels. This is because they generally achieve saturation in a sulfide phase early and deep during their evolutionary history. Thus, either later processes are required to remobilise Cu to shallow levels, or processes that fall outside of the typical set of arc magmatic conditions (e.g., elevated magma throughput; Villarrica).

9.3. Subduction mobile chalcophile elements

Parental-MORB normalised multi-element plots consistently displayed substantial peaks in the W, Tl, As, Pb and Sb contents of the Chilean edifice samples, relative to neighbouring elements with similar bulk distribution coefficients during the differentiation of MORB (e.g., Jenner, 2017). Thus, W, Tl, As, Pb and Sb were mobilised during subduction, added to the mantle wedge in a slab-derived fluid or flux, in similar proportions to their distribution in the upper oceanic crust. In the case of the Antuco, Bi was also demonstrated to be subduction mobile, with samples displaying

considerable peaks in their Parental-MORB normalised Bi contents. This is compared to the contents of Mo, Sn, Zn, Ga and Co, which are similar to Parental-MORB and other immobile trace elements, suggestive of them being immobile during subduction. Bismuth analyses were not obtained for samples from the other Chilean stratovolcanoes investigate here, so this thesis was unable to comment on its potential mobility elsewhere long the arc.

Furthermore, constructed baselines, drawn through the 'conservative' elements and immobile Cu and Ag, were used to approximately define the mantle and slab-derived components of each sample suite. As such, the percentage contribution of W, Tl, As, Pb and Sb from the slab-derived component was estimated at >85% for most edifices.

9.4. Avenues for further investigation

Although this thesis has gone some way in constraining the behaviour of the chalcophile elements during magmatic evolution within a continental volcanic arc, it has also highlighted areas requiring additional investigation. Further understanding of the processing and distribution of the chalcophile elements within convergent margins will continually assist in refining models of ore genesis and the cycling of the climatically important volatile S within subduction zones. Thus, future potential investigations are listed below;

- Although melt inclusion (MI) studies have their difficulties, including MI abundance, size and the re-homogenisation of partially crystallised MIs, their analysis, alongside bulk rock compositions, would provide insights into the S, Se, Cu and Ag contents of near-primary, undegassed magmas. Such MI analyses could test the depth and pressure range of sulfide fractionation within

continental arc magmas, and would potentially bypass mixing processes often observed in convergent margin magmas. Furthermore, MI could be used to investigate the ideas proposed at Villarrica regarding an elevated magma throughput resulting in its magmas preserving their primary Cu content.

- Detailed scanning electron microscopy analysis of a range of continental arc magma compositions, in conjunction with MI analysis, permits the identification of magmatic sulfide inclusions (e.g., Georgatou et al., 2018; Zelenski et al., 2018), and through characterisation of the host phases, an approximation of the timing, and potentially depth, at which sulfides begin to fractionate.
- Investigations into the behaviour of different isotopes of the chalcophile elements could further constrain their processing in a continental arc setting (e.g., slab-derived TI flux into the sub-arc mantle wedge).
- Experimental work focussed on the melting of pyroxenite lithologies has the potential to constrain pyroxenite cumulates as a Cu source at the base of the continental crust at convergent margins, by testing the nature and stability of such cumulates and how they may be assimilated (e.g., Lee et al., 2012).
- Building on the ideas proposed at Villarrica, where a potential link between elevated magma throughput and magma Cu content was drawn, this could be tested by investigating the Cu contents of magmas at other highly active arcs, such as Kamchatka, in a global-scale study.

Bibliography

Adam, J. and Green, T. (2006) Trace element partitioning between mica- and amphibole-bearing garnet lherzolite and hydrous basanitic melt: 1. Experimental results and the investigation of controls on partitioning behaviour. *Contributions to Mineralogy and Petrology*, 152: 1–17.

Aiuppa, A., Bitetto, M., Francoforte, V., et al. (2017) A CO₂-gas precursor to the March 2015 Villarrica volcano eruption. *Geochemistry, Geophysics, Geosystems*, 18: 2120–2132.

Alonso-Perez, R., Müntener, O. and Ulmer, P. (2009) Igneous garnet and amphibole fractionation in the roots of island arcs: Experimental constraints on andesitic liquids. *Contributions to Mineralogy and Petrology*, 157: 541–558.

Annen, C., Blundy, J.D. and Sparks, R.S.. J. (2006) The genesis of intermediate and silicic magmas in deep crustal hot zones. *Journal of Petrology*, 47: 505–539.

Assumpção, M., Feng, M., Tassara, A., et al. (2013) Models of crustal thickness for South America from seismic refraction, receiver functions and surface wave tomography. *Tectonophysics*, 609: 82–96.

Balcaen, L., Bolea-Fernandez, E., Resano, M., et al. (2015) Inductively coupled plasma - Tandem mass spectrometry (ICP-MS/MS): A powerful and universal tool for the interference-free determination of (ultra)trace elements - A tutorial review.

Analytica Chimica Acta, 894: 7–19.

Barazangi, M. and Isacks, B.L. (1976) Spatial distribution of earthquakes and subduction of the Nasca plate beneath South America. *Geology*, 4: 686–692.

Bolea-Fernandez, E., Balcaen, L., Resano, M., et al. (2017) Overcoming spectral overlap via inductively coupled plasma-tandem mass spectrometry (ICP-MS/MS). A tutorial review. *Journal of Analytical Atomic Spectrometry*, 32: 1660–1679.

Bouvet de Maisonneuve, C., Dungan, M.A., Bachmann, O., et al. (2013) Petrological insights into shifts in eruptive styles at Volcán Llaima (Chile). *Journal of Petrology*, 54: 393–420.

Brahm, R., Parada, M.A., Morgado, E., et al. (2018) Origin of Holocene trachyte lavas of the Quetrupillán volcanic complex, Chile: Examples of residual melts in a rejuvenated crystalline mush reservoir. *Journal of Volcanology and Geothermal Research*, 357: 163–176.

Brett, A., Prytulak, J., Hammond, S.J., et al. (2018) Thallium Mass Fraction and Stable Isotope Ratios of Sixteen Geological Reference Materials. *Geostandards and Geoanalytical Research*, 42: 339–360.

Cembrano, J. and Lara, L. (2009) The link between volcanism and tectonics in the southern volcanic zone of the Chilean Andes: A review. *Tectonophysics*, 471: 96–113.

Chen, S., Wang, X., Niu, Y., et al. (2017) Simple and cost-effective methods for precise analysis of trace element abundances in geological materials with ICP-MS. *Science Bulletin*, 62: 277–289.

Chiaradia, M. (2014) Copper enrichment in arc magmas controlled by overriding plate

Bibliography

thickness. *Nature Geoscience*, 7: 43–46.

Churikova, T.G., Gordeychik, B.N., Ivanov, B. V., et al. (2013) Relationship between Kamen Volcano and the Klyuchevskaya group of volcanoes (Kamchatka). *Journal of Volcanology and Geothermal Research*, 263: 3–21.

Clavero, J. and Godoy, E. (2010) “The Late Holocene Collapse of Antuco Volcano: a Valley Confined Debris Avalanche Flow, Southern Andes, Chile.” *In Cities on Volcanoes 6 Abstracts Volume*. 2010. p. 42.

Clavero, J., Polanco, E., Godoy, E., et al. (2004) Substrata Influence in the Transport and Emplacement Mechanism of the Ollague Debris Avalanche (Northern Chile). *Acta Vulcanologica*, 16: 59–76.

Contreras-Reyes, E. and Carrizo, D. (2011) Control of high oceanic features and subduction channel on earthquake ruptures along the Chile-Peru subduction zone. *Physics of the Earth and Planetary Interiors*, 186: 49–58.

Le Corvec, N., Spörli, K.B., Rowland, J., et al. (2013) Spatial distribution and alignments of volcanic centers: Clues to the formation of monogenetic volcanic fields. *Earth-Science Reviews*, 124: 96–114.

Van Daele, M., Moernaut, J., Silversmit, G., et al. (2014) The 600 yr eruptive history of Villarrica Volcano (Chile) revealed by annually laminated lake sediments. *Bulletin of the Geological Society of America*, 126: 481–498.

Daly, R.A. (1914) *Igneous rocks and their origin*.

Dams, R.F.J., Goossens, J. and Moens, L. (1995) Spectral and non-spectral interferences in inductively coupled plasma mass-spectrometry. *Mikrochimica Acta*,

Bibliography

119: 277–286.

Davidson, J., Turner, S., Handley, H., et al. (2007) Amphibole “sponge” in arc crust? *Geology*, 35: 787–790.

Davidson, J., Turner, S. and Plank, T. (2012) Dy/Dy*: Variations arising from mantle sources and petrogenetic processes. *Journal of Petrology*, 54: 525–537.

Davidson, J.P., Hora, J.M., Garrison, J.M., et al. (2005) Crustal forensics in arc magmas. *Journal of Volcanology and Geothermal Research*, 140: 157–170.

Delgado, F., Pritchard, M.E., Ebmeier, S., et al. (2017) Recent unrest (2002–2015) imaged by space geodesy at the highest risk Chilean volcanoes: Villarrica, Llaima, and Calbuco (Southern Andes). *Journal of Volcanology and Geothermal Research*, 344: 270–288.

Dzierma, Y., Rabbel, W., Thorwart, M., et al. (2012) Seismic velocity structure of the slab and continental plate in the region of the 1960 Valdivia (Chile) slip maximum - Insights into fluid release and plate coupling. *Earth and Planetary Science Letters*, 331–332: 164–176.

Evans, E.H. and Giglio, J.J. (1993) Interferences in inductively coupled plasma mass spectrometry A review. *Journal of Analytical Atomic Spectrometry*, 8: 1–18.

Evans, E.H., Pisonero, J., Smith, C.M.M., et al. (2017) Atomic spectrometry update: review of advances in atomic spectrometry and related techniques. *Journal of Analytical Atomic Spectrometry*, 32: 869–889.

Ewart, A., Bryan, W.B. and Gill, J.B. (1973) Mineralogy and geochemistry of the Younger Volcanic Islands of Tonga, S.W. Pacific. *Journal of Petrology*, 14: 429–465.

Bibliography

- Feeley, T.C. and Davidson, J.P. (1994) Petrology of calc-alkaline lavas at volcán ollagüe and the origin of compositional diversity at central andean stratovolcanoes. *Journal of Petrology*, 35: 1295–1340.
- Feeley, T.C., Davidson, J.P. and Armendia, A. (1993) The volcanic and magmatic evolution of Volcán Ollagüe, a high-K, late quaternary stratovolcano in the Andean Central Volcanic Zone. *Journal of Volcanology and Geothermal Research*, 54: 221–245.
- Feeley, T.C. and Hacker, M.D. (1995) Intracrustal Derivation of Na-Rich Andesitic and Dacitic Magmas : An Example from Volcán Ollagüe , Andean Central Volcanic Zone. *The Journal of Geology*, 103: 213–225.
- Feeley, T.C. and Sharp, Z.D. (1995) $^{18}\text{O}/^{16}\text{O}$ isotope geochemistry of silicic lava flows erupted from Volcán Ollagüe, Andean Central Volcanic Zone. *Earth and Planetary Science Letters*, 133: 239–254.
- Feigenson, M.D., Bolge, L.L., Carr, M.J. and Herzberg, C.T. (2003) REE inverse modelling of HSDP2 basalts: Evidence for multiple sources in the Hawaiian plume. *Geochemistry, Geophysics, Geosystems*, 4, 8706.
- Floor, G.H. and Román-Ross, G. (2012) Selenium in volcanic environments: A review. *Applied Geochemistry*, 27: 517–531.
- Francis, P.W., Moorbath, S. and Thorpe, R.S. (1977) Strontium isotope data for recent andesites in Ecuador and north Chile. *Earth and Planetary Science Letters*, 37: 197–202.
- Francis, P.W., Roobik, M.J., Walker, G.P.L., et al. (1974) The San Pedro and San

Bibliography

- Pablo volcanoes of northern Chile and their hot avalanche deposits. *Geologische Rundschau*, 63: 357–388.
- Georgatou, A., Chiaradia, M., Rezeau, H., et al. (2018) Magmatic sulphides in Quaternary Ecuadorian arc magmas. *Lithos*, 296–299: 580–599.
- Gerlach, D.C., Frey, F.A., Moreno-roa, H., et al. (1988) Recent volcanism in the Puyehue - Cordón Caulle region, Southern Andes, Chile (40-5°S): Petrogenesis of evolved lavas. *Journal of Petrology*, 29: 333–382.
- Goldschmidt, V.M. (1929) The Distribution of Chemical Elements. *Nature*, 124: 15–17.
- Goldschmidt, V.M. (1937) *The Principles of Distribution of Chemical Elements in Minerals and Rocks*. (NULL). doi:10.1039/JR9370000655.
- Govindaraju, K. (1994) 1994 Compilation of working values and descriptions for 383 geostandards. *Geostandards Newsletter*, 18: 1–158.
- Hauser Y., A. (1985) Flujos aluvionales de 1870 y 1896 ocurridos en la ladera norte del Volcan Yates, X Region: su implicancia en la evaluación de riesgos naturales. *Revista geológica de Chile*, 25–26: 125–133.
- Hayes, G.P., Moore, G.L., Portner, D.E., Hearne, M., Flamme, H., Furtney, M. and Smoczyk, G.M. (2018) Slab2, a comprehensive subduction zone geometry model. *Science*, 362, 58-61.
- Hickey-Vargas, R., Holbik, S., Tormey, D., et al. (2016a) Basaltic rocks from the Andean Southern Volcanic Zone: Insights from the comparison of along-strike and small-scale geochemical variations and their sources. *Lithos*, 258–259: 115–132.
- Hickey-Vargas, R., Roa, H.M., Escobar, L.L., et al. (1989) Geochemical variations in

Bibliography

Andean basaltic and silicic lavas from the Villarrica-Lanin volcanic chain (39.5S): an evaluation of source heterogeneity, fractional crystallization and crustal assimilation. *Contributions to Mineralogy and Petrology*, 103: 361–386.

Hickey-Vargas, R., Sun, M. and Holbik, S. (2016b) Geochemistry of basalts from small eruptive centers near Villarrica stratovolcano, Chile: Evidence for lithospheric mantle components in continental arc magmas. *Geochimica et Cosmochimica Acta*, 185: 358–382.

Hildreth, W. and Moorbath, S. (1988) Crustal contributions to arc magmatism in the Andes of Central Chile. *Contributions to Mineralogy and Petrology*, 98: 455–489.

Holm, P.M., Søgner, N., Alfatsen, M., et al. (2016) Subduction zone mantle enrichment by fluids and Zr–Hf-depleted crustal melts as indicated by backarc basalts of the Southern Volcanic Zone, Argentina. *Lithos*, 262: 135–152.

Holm, P.M., Søgner, N., Dyhr, C.T., et al. (2014) Enrichments of the mantle sources beneath the Southern Volcanic Zone (Andes) by fluids and melts derived from abraded upper continental crust. *Contributions to Mineralogy and Petrology*, 167: 1–27.

Holwell, D.A., Fiorentini, M., McDonald, I., et al. (2019) A metasomatized lithospheric mantle control on the metallogenic signature of post-subduction magmatism. *Nature Communications*, 10: 3511. doi:10.1038/s41467-019-11065-4.

De Hoog, J.C.M., Mason, P.R.D. and Van Bergen, M.J. (2001a) Sulfur and chalcophile elements in subduction zones: Constraints from a laser ablation ICP-MS study of melt inclusions from Galunggung volcano, Indonesia. *Geochimica et Cosmochimica Acta*, 65: 3147–3164.

Bibliography

- De Hoog, J.C.M., Taylor, B.E. and Van Bergen, M.J. (2001b) Sulfur Isotope Systematics of Basaltic Lavas From Indonesia : Implications for the Sulfur Cycle in subduction zones. *Earth and Planetary Science Letters*, 189: 237–252.
- Hou, X. and Jones, B.T. (2000) Inductively Coupled Plasma/Optical Emission Spectrometry. *Encyclopedia of Analytical Chemistry*. pp. 9468–9485.
- Irvine, T.N. and Baragar, W.R.A. (1971) A guide to the chemical classification of the common volcanic rocks. *Canadian Journal of Earth Sciences*, 8: 523–548.
- Jackson, M.D., Blundy, J. and Sparks, R.S.J. (2018) Chemical differentiation, cold storage and remobilization of magma in the Earth's crust. *Nature*, 564: 405–409.
- Jacques, G., Hoernle, K., Gill, J., et al. (2013) Across-arc geochemical variations in the Southern Volcanic Zone, Chile (34.5-38.0°S): Constraints on mantle wedge and slab input compositions. *Geochimica et Cosmochimica Acta*, 123: 218–243.
- Jacques, G., Hoernle, K., Gill, J., et al. (2014) Geochemical variations in the Central Southern Volcanic Zone, Chile (38-43°S): The role of fluids in generating arc magmas. *Chemical Geology*, 371: 27–45.
- Jenner, F.E. (2017) Cumulate causes for the low contents of sulfide-loving elements in the continental crust. *Nature Geoscience*, 10: 524–529.
- Jenner, F.E., Arculus, R.J., Mavrogenes, J.A., et al. (2012) Chalcophile element systematics in volcanic glasses from the northwestern Lau Basin. *Geochemistry, Geophysics, Geosystems*, 13. doi:10.1029/2012GC004088.
- Jenner, F.E. and Arevalo, R.D. (2016) Major and Trace Element Analysis of Natural and Experimental Igneous Systems using LA–ICP–MS. *Elements*, 12: 311–316.

Bibliography

Jenner, F.E., Hauri, E.H., Bullock, E.S., et al. (2015) The competing effects of sulfide saturation versus degassing on the behavior of the chalcophile elements during the differentiation of hydrous melts. *Geochemistry Geophysics Geosystems*, 16: 1490–1507.

Jenner, F.E. and O'Neill, H.S.C. (2012a) Analysis of 60 elements in 616 ocean floor basaltic glasses. *Geochemistry, Geophysics, Geosystems*, 13 (1): 1–11.

Jenner, F.E. and O'Neill, H.S.C. (2012b) Major and trace analysis of basaltic glasses by laser-ablation ICP-MS. *Geochemistry, Geophysics, Geosystems*, 13: 1–17.

Jenner, F.E., O'Neill, H.S.C., Arculus, R.J., et al. (2010) The magnetite crisis in the evolution of arc-related magmas and the initial concentration of Au, Ag and Cu. *Journal of Petrology*, 51: 2445–2464.

Jochum, K.P., Weis, U., Schwager, B., et al. (2016) Reference Values Following ISO Guidelines for Frequently Requested Rock Reference Materials. *Geostandards and Geoanalytical Research*, 40: 333–350.

Johnson, J.B. and Palma, J.L. (2015) Lahar infrasound associated with Villarrica's March 3, 2015 eruption. *Geophysical Research Letters*, 42: 6324–6331.

Johnson, J.B., Watson, L.M., Palma, J.L., et al. (2018) Forecasting the Eruption of an Open-Vent Volcano Using Resonant Infrasound Tones. *Geophysical Research Letters*, 45: 2213–2220.

Kamenetsky, V.S., Zelenski, M., Gurenko, A., et al. (2017) Silicate-sulfide liquid immiscibility in modern arc basalt (Tolbachik volcano, Kamchatka): Part II. Composition, liquidus assemblage and fractionation of the silicate melt. *Chemical*

Bibliography

Geology, 471: 92–110.

Kelley, K.A. and Cottrell, E. (2012) The influence of magmatic differentiation on the oxidation state of Fe in a basaltic arc magma. *Earth and Planetary Science Letters*, 329–330: 109–121.

Kereszturi, G. and Nemeth, K. (2012) “Monogenetic basaltic volcanoes: genetic classification, growth, geomorphology and degradation.” *In Updates in volcanology - New advances in understanding volcanic systems*. InTech. pp. 1–89.

Kiseeva, E.S., Fonseca, R.O.C. and Smythe, D.J. (2017) Chalcophile elements and sulfides in the upper mantle. *Elements*, 13: 111–116.

Kuno, H. (1968) “Differentiation of basalt magmas.” *In Basalts: The Poldervaart Treatise on Rocks of Basaltic Composition*. New York: John Wiley and Sons. pp. 623–688.

Kunz, B.E. (2019) Telephone conversation with Barbara Kunz, 05 September 2019.

Kurzawa, T., König, S., Alt, J.C., et al. (2019) The role of subduction recycling on the selenium isotope signature of the mantle: Constraints from Mariana arc lavas. *Chemical Geology*, 513: 239–249.

Kurzweil, F., Münker, C., Tusch, J., et al. (2018) Accurate stable tungsten isotope measurements of natural samples using a ^{180}W - ^{183}W double-spike. *Chemical Geology*, 476: 407–417.

Lara, L.E., Lavenu, A., Cembrano, J., et al. (2006) Structural controls of volcanism in transversal chains: Resheared faults and neotectonics in the Cordón Caulle-Puyehue area (40.5°S), Southern Andes. *Journal of Volcanology and Geothermal Research*,

Bibliography

158: 70–86.

Lara, L.E., Naranjo, J.A. and Moreno, H. (2004) Lanín volcano (39.5°S), Southern Andes: geology and morphostructural evolution. *Revista geológica de Chile*, 31: 241–257.

Le Bas, M.J., Le Maitre, R.W., Streckeisen, A. and Zanettin, B. (1986) A chemical classification of volcanic rocks based on the total alkali-silica diagram. *Journal of Petrology*, 27, 745–750.

Lee, C.T.A., Luffi, P., Chin, E.J., et al. (2012) Copper systematics in arc magmas and implications for crust-mantle differentiation. *Science*, 336: 64–68.

Li, Y. and Audétat, A. (2012) Partitioning of V, Mn, Co, Ni, Cu, Zn, As, Mo, Ag, Sn, Sb, W, Au, Pb, and Bi between sulfide phases and hydrous basanite melt at upper mantle conditions. *Earth and Planetary Science Letters*, 355–356: 327–340.

Li, Y. and Audétat, A. (2015) Effects of temperature, silicate melt composition, and oxygen fugacity on the partitioning of V, Mn, Co, Ni, Cu, Zn, As, Mo, Ag, Sn, Sb, W, Au, Pb, and Bi between sulfide phases and silicate melt. *Geochimica et Cosmochimica Acta*, 162: 25–45.

Lohmar, S., Lopez-Escobar, L., Moreno, H., et al. (1999) “Antuco Volcano: One of the isotopically most primitive stratovolcanoes of the Southern Andes (37°25’S).” *In Fourth International Symposium on Andean Geodynamics*. 1999. pp. 437–440.

Lohmar, S., Lopez-Escobar, L. and Moreno, H. (2005) *Preliminary Comparison Between Antuco and Sierra Velluda Volcanoes (Southern Andes)*. pp. 385–388.

Lopez-Escobar, L., Cembrano, J. and Moreno, H. (1995a) Geochemistry and tectonics

Bibliography

of the Chilean southern Andes basaltic Quaternary volcanism (37-46°S). *Revista Geologica de Chile*, 22: 219–234.

Lopez-Escobar, L., Kilian, R., Kempton, P.D., et al. (1993) Petrography and geochemistry of Quaternary rocks from the Southern Volcanic Zone of the Andes between 41 30' and 46 00'S, Chile. *Revista Geológica de Chile*, 20: 33–55.

López-Escobar, L. and Moreno R., H. (1994) “Geochemical characteristics of the southern andes basaltic volcanism associated with the liquiñe-ofqui fault zone between 39° and 46°.” In *VII Congreso Geológico Chileno (Concepción) 1994*. pp. 1388–1393.

Lopez-Escobar, L., Parada, M.A., Hickey-Vargas, R., et al. (1995b) Calbuco Volcano and minor eruptive centres distributed along the Liquine-Ofqui Fault Zone, Chile (41-42S): contrasting origin of andesitic and basaltic magma in teh Southern Volcanic Zone of the Andes. *Contributions to Mineralogy and Petrology*, 119: 345–361.

Lopez-Escobar, L., Vergara, M. and Frey, F.A. (1981) Petrology and geochemistry of lavas from Antuco Volcano, a basaltic volcano of the Southern Andes (37 25'S). *Journal of Volcanology and Geothermal Research*, 11: 329–352.

López Escobar, Á., Parada, M., Moreno, H., et al. (1992) A contribution to the petrogenesis of Osomo and Calbuco volcanoes, Southern Andes (41 °00'-41 °30'8): comparative study. *Revista geológica de Chile: An international journal on andean geology*, 19: 211–226.

Martínez, P., Singer, B.S., Roa, H.M., et al. (2018) Volcanologic and petrologic evolution of Antuco-Sierra Velluda, Southern Andes, Chile. *Journal of Volcanology and Geothermal Research*, 349: 392–408.

Bibliography

- Matjuschkin, V., Blundy, J.D. and Brooker, R.A. (2016) The effect of pressure on sulphur speciation in mid- to deep-crustal arc magmas and implications for the formation of porphyry copper deposits. *Contributions to Mineralogy and Petrology*, 171: 66. doi:10.1007/s00410-016-1274-4.
- Mattioli, M., Renzulli, A., Menna, M., et al. (2006) Rapid ascent and contamination of magmas through the thick crust of the CVZ (Andes, Ollagüe region): Evidence from a nearly aphyric high-K andesite with skeletal olivines. *Journal of Volcanology and Geothermal Research*, 158: 87–105.
- Mavrogenes, J.A. and O'Neill, H.S.C. (1999) The relative effects of pressure, temperature and oxygen fugacity on the solubility of sulfide in mafic magmas. *Geochimica et Cosmochimica Acta*, 63: 1173–1180.
- May, T.W. and Wiedmeyer, R.H. (1998) A table of polyatomic interferences in ICP-MS. *Atomic Spectroscopy*, 19: 150–155.
- McDonald, I. and Viljoen, K.S. (2006) Platinum-group element geochemistry of mantle eclogites: a reconnaissance study of xenoliths from the Orapa kimberlite, Botswana. *Applied Earth Science*, 115: 81–93.
- McGee, L.E., Brahm, R., Rowe, M.C., et al. (2017) A geochemical approach to distinguishing competing tectono-magmatic processes preserved in small eruptive centres. *Contributions to Mineralogy and Petrology*, 172: 1–26.
- McGee, L.E., Morgado, E., Handley, H.K., et al. (2015) “The individuality of ascent paths in small volcanic systems: Small eruptive centres near Villarrica volcano, Chile.” In *Congreso Geológico Chileno XIV*. 2015. pp. 420–423.

Bibliography

McGee, L.E. and Smith, I.E.M. (2016) Interpreting chemical compositions of small scale basaltic systems: A review. *Journal of Volcanology and Geothermal Research*, 325: 45–60.

Mella Barra, M.A. (2008) *Petrogêneses Do Complexo Vulcânico Yate (42,30°S), Andes Do Sul, Chile.*

Moreno R., H., Clavero, J. and Lara, L.P. (1994a) “Actividad explosiva postglacial del Volcan Villarrica, Andes del Sur (3925’S).” *In VII Congreso Geológico Chileno, Concepción, Chile.* 1994. pp. 329–333.

Moreno R., H., López-Escobar, L. and Cembrano, J. (1994b) “The Villarrica-Quetrupillan-Lanin volcanic chain: A review and probable significance in the southern andes, 39.4° S, Chile.” *In VII Congreso Geológico Chileno, Concepción, Chile.* 1994. pp. 339–341.

Morgado, E., Parada, M.A., Contreras, C., et al. (2015) Contrasting records from mantle to surface of Holocene lavas of two nearby arc volcanic complexes: Caburgua-Huelemolle Small Eruptive Centers and Villarrica Volcano, Southern Chile. *Journal of Volcanology and Geothermal Research*, 306: 1–16.

Morgado, E., Parada, M.A., Morgan, D.J., et al. (2017) Transient shallow reservoirs beneath small eruptive centres: Constraints from Mg-Fe interdiffusion in olivine. *Journal of Volcanology and Geothermal Research*, 347: 327–336.

Mungall, J.E. (2002) Roasting the mantle: Slab melting and the genesis of major Au and Au-rich Cu deposits. *Geology*, 30: 915–918.

Mutschler, F.E., Ludington, S. and Bookstrom, A.A. (2010) *Giant Porphyry-Related*

Bibliography

Metal Camps of the World—A Database.

Nakamura, K. (1977) Volcanoes as possible indicators of tectonic stress orientation - Principle and proposal. *Journal of Volcanology and Geothermal Research*, 2: 1–16.

Nash, W.M., Smythe, D.J. and Wood, B.J. (2019) Compositional and temperature effects on sulfur speciation and solubility in silicate melts. *Earth and Planetary Science Letters*, 507: 187–198.

Nemeth, K. (2010) Monogenetic volcanic fields: Origin, sedimentary record, and relationship with polygenetic volcanism. *The Geological Society of America Special Paper*, 470: 43–66.

Noll Jr, P.D., Newsom, H.E., Leeman, W.P., et al. (1996) The role of hydrothermal fluids in the production of subduction zone magmas: Evidence from siderophile and chalcophile trace elements and boron. *Geochimica et Cosmochimica Acta*, 60: 587–611.

O'Callaghan, L.J. and Francis, P.W. (1986) Volcanological and petrological evolution of San Pedro volcano, Provincia El Loa, North Chile. *Journal of the Geological Society*, 143: 275–286.

O'Neill, H.S.C. (2016) The smoothness and shapes of chondrite-normalized rare earth element patterns in basalts. *Journal of Petrology*, 57: 1463–1508.

O'Neill, H.S.C. and Mavrogenes, J.A. (2002) The Sulfide Capacity and the Sulfur Content at Sulfide Saturation of Silicate Melts at 1400°C and 1 bar. *Journal of Petrology*, 43: 1049–1087.

Pearce, J. a and Peate, D.W. (1995) Tectonic Implications of The Composition of

Bibliography

- Volcanic Arc Magmas. *Annual Review of Earth and Planetary Sciences*, 23: 251–285.
- Pearce, J.A. and Stern, R.J. (2006) Origin of Back-Arc Basin Magmas : Trace Element and Isotope Perspectives. *Geophysical Monograph - American Geophysical Union*, 166: 63–86.
- Pearce, J.A., Stern, R.J., Bloomer, S.H., et al. (2005) Geochemical mapping of the Mariana arc-basin system: Implications for the nature and distribution of subduction components. *Geochemistry, Geophysics, Geosystems*, 6: 1–27.
- Ramos, V.A. and Folguera, A. (2009) Andean flat-slab subduction through time. *Geological Society, London, Special Publications*, 327: 31–54.
- Rawson, H., Keller, T., Fontijn, K., et al. (2016) Compositional variability in mafic arc magmas over short spatial and temporal scales: Evidence for the signature of mantle reactive melt channels. *Earth and Planetary Science Letters*, 456: 66–77.
- Reekie, C.D.J., Jenner, F.E., Smythe, D.J., et al. (2019) Sulfide resorption during crustal ascent and degassing of oceanic plateau basalts. *Nature Communications*, 10: 1–11.
- Reubi, O., Bourdon, B., Dungan, M.A., et al. (2011) Assimilation of the plutonic roots of the Andean arc controls variations in U-series disequilibria at Volcan Llaima, Chile. *Earth and Planetary Science Letters*, 303: 37–47.
- Richards, J.P. (2009) Postsubduction porphyry Cu-Au and epithermal Au deposits: Products of remelting of subduction-modified lithosphere. *Geology*, 37: 247–250.
- Richards, J.P. (2015) The oxidation state, and sulfur and Cu contents of arc magmas: implications for metallogeny. *Lithos*, 233: 27–45.

Bibliography

- Rollinson, H.R. (1993) *Using Geochemical Data: Evaluation, Presentation, Interpretation*.
- Rudnick, R.L. and Gao, S. (2003) Composition of the continental crust. In: *Treatise on Geochemistry: The Crust*, pp, 1-64.
- Salit, M.L. and Turk, G.C. (1998) A Drift Correction Procedure. *Analytical Chemistry*, 70: 3184–3190.
- Sánchez, P., Pérez-Flores, P., Arancibia, G., et al. (2013) Crustal deformation effects on the chemical evolution of geothermal systems: The intra-arc Liquiñe-Ofqui fault system, Southern Andes. *International Geology Review*, 55: 1384–1400.
- Savov, I.P., Ryan, J.G., D'Antonio, M., et al. (2007) Shallow slab fluid release across and along the Mariana arc-basin system: Insights from geochemistry of serpentized peridotites from the Mariana fore arc. *Journal of Geophysical Research*, 112: 1–30.
- Selles, D., Carolina Rodriguez, A. and Dungan, M.A. (2004) Geochemistry of Nevado de Longavi Volcano (36.2S): a compositionally atypical arc volcano in the Southern Volcanic Zone of the Andes. *Andean Geology*, 31: 293–315.
- Sillitoe, R.H. (1988) Epochs of intrusion-related copper mineralization in the Andes. *Journal of South American Earth Sciences*, 1: 89–108.
- Sillitoe, R.H. (1997) Characteristics and controls of the largest porphyry copper-gold and epithermal gold deposits in the circum-Pacific region. *Australian Journal of Earth Sciences*, 44: 373–388.
- Sillitoe, R.H. (2003) Iron oxide-copper-gold deposits: An Andean view. *Mineralium Deposita*, 38: 787–812.

Bibliography

- Sillitoe, R.H. (2010) Porphyry Copper Systems. *Economic Geology*, 105: 3–41.
- Sillitoe, R.H., Tolman, J. and Van Kerkvoort, G. (2013) Geology of the Caspiche Porphyry Gold-Copper Deposit, Maricunga Belt, Northern Chile*. *Economic Geology*, 108: 585–604.
- Singer, B.S., Jicha, B.R., Harper, M.A., et al. (2008) Eruptive history, geochronology, and magmatic evolution of the Puyehue-Cordón Caulle volcanic complex, Chile. *Bulletin of the Geological Society of America*, 120: 599–618.
- Singer, D.A., Berger, V.I. and Moring, B.C. (2002) *Porphyry Copper Deposits of the World: Database, Maps, and Preliminary Analysis*.
- Smith, I.E.M. and Németh, K. (2017) Source to surface model of monogenetic volcanism: a critical review. *Geological Society, London, Special Publications*, 446: 1–28.
- Spandler, C. and Pirard, C. (2013) Element recycling from subducting slabs to arc crust: A review. *Lithos*, 170–171: 208–223.
- Stern, C.R. (2004) Active Andean volcanism: its geologic and tectonic setting. *Revista geológica de Chile*, 31: 161–206.
- Sugiyama, N. and Shikamori, Y. (2015) Removal of spectral interferences on noble metal elements using MS/MS reaction cell mode of a triple quadrupole ICP-MS. *Journal of Analytical Atomic Spectrometry*, 30: 2481–2487.
- Sun, S.-S. and McDonough, W.F. (1989) Chemical and isotopic composition systematics of oceanic basalts: implications for mantle composition and processes. *Geological Society of London, Special Publications*, 42, 313-345.

Bibliography

- Sun, W., Arculus, R.J., Kamenetsky, V.S., et al. (2004) Release of gold-bearing fluids in convergent margin magmas prompted by magnetite crystallization. *Nature*, 431: 975–978.
- Sun, W., Huang, R. fang, Li, H., et al. (2015) Porphyry deposits and oxidized magmas. *Ore Geology Reviews*, 65: 97–131.
- Sun, W., Wang, J., Zhang, L., et al. (2017) The formation of porphyry copper deposits. *Acta Geochimica*, 36: 9–15.
- Sun, W.D., Liang, H.Y., Ling, M.X., et al. (2013) The link between reduced porphyry copper deposits and oxidized magmas. *Geochimica et Cosmochimica Acta*, 103: 263–275.
- Syracuse, E.M., van Keken, P.E. and Abers, G.A. (2010) The global range of subduction zone thermal models. *Physics of the Earth and Planetary Interiors*, 183: 73–90.
- Tang, M., Erdman, M., Eldridge, G., et al. (2018) The redox “filter” beneath magmatic orogens and the formation of continental crust. *Science Advances*, 4: 1–7.
- Tassara, A. and Echaurren, A. (2012) Anatomy of the Andean subduction zone: Three-dimensional density model upgraded and compared against global-scale models. *Geophysical Journal International*, 189: 161–168.
- Tassara, A., Götze, H.J., Schmidt, S., et al. (2006) Three-dimensional density model of the Nazca plate and the Andean continental margin. *Journal of Geophysical Research*, 111: 1–26.
- Thiele, R., Moreno, H., Elgueta, S., et al. (1998) Evolución geológico-geomorfológico

Bibliography

cuaternaria del tramo superior del valle del río Laja. *Revista Geológica de Chile*, 25: 229–253.

Timm, C., De Ronde, C.E.J., Leybourne, M.I., et al. (2012) Sources of chalcophile and siderophile elements in Kermadec arc lavas. *Economic Geology*, 107: 1527–1538.

Valentine, G.A. and Gregg, T.K.P. (2008) Continental basaltic volcanoes - Processes and problems. *Journal of Volcanology and Geothermal Research*, 177: 857–873.

Valetich, M.J., Mavrogenes, J., Arculus, R., et al. (2019) Evolution of chalcophile elements in the magmas of the Bonin Islands. *Chemical Geology*, 508: 234–249.

Vezzoli, L., Tibaldi, A., Renzulli, A., et al. (2008) Faulting-assisted lateral collapses and influence on shallow magma feeding system at Ollagüe volcano (Central Volcanic Zone, Chile-Bolivia Andes). *Journal of Volcanology and Geothermal Research*, 171: 137–159.

Volker, D., Kutterolf, S. and Wehrmann, H. (2011) Comparative mass balance of volcanic edifices at the southern volcanic zone of the Andes between 33 S and 46 S. *Journal of Volcanology and Geothermal Research*, 205: 114–129.

Wallace, P.J. (2005) Volatiles in subduction zone magmas: Concentrations and fluxes based on melt inclusion and volcanic gas data. *Journal of Volcanology and Geothermal Research*, 140: 217–240.

Wallace, P.J. and Edmonds, M. (2011) The Sulfur Budget in Magmas: Evidence from Melt Inclusions, Submarine Glasses, and Volcanic Gas Emissions. *Reviews in Mineralogy and Geochemistry*, 73: 215–246.

Walowski, K.J., Wallace, P.J., Clyne, M.A., et al. (2016) Slab melting and magma

Bibliography

formation beneath the southern Cascade arc. *Earth and Planetary Science Letters*, 446: 100–112.

Wang, Z. and Becker, H. (2015) Abundances of Ag and Cu in mantle peridotites and the implications for the behavior of chalcophile elements in the mantle. *Geochimica et Cosmochimica Acta*, 160: 209–226.

Wang, Z., Becker, H., Liu, Y., et al. (2018) Constant Cu/Ag in upper mantle and oceanic crust: Implications for the role of cumulates during the formation of continental crust. *Earth and Planetary Science Letters*, 493: 25–35.

Watt, S.F.L. (2010) *Records of volcanism and controls on volcanic processes in southern Chile*.

Watt, S.F.L., Pyle, D.M., Mather, T.A., et al. (2013) Arc magma compositions controlled by linked thermal and chemical gradients above the subducting slab. *Geophysical Research Letters*, 40: 2550–2556.

Watt, S.F.L., Pyle, D.M., Naranjo, J.A., et al. (2009) Landslide and tsunami hazard at Yate volcano, Chile as an example of edifice destruction on strike-slip fault zones. *Bulletin of Volcanology*, 71: 559–574.

Watt, S.F.L., Pyle, D.M., Naranjo, J.A., et al. (2011) Holocene tephrochronology of the Hualaihue region (Andean southern volcanic zone, ~42° S), southern Chile. *Quaternary International*, 246: 324–343.

Wehrmann, H., Hoernle, K., Garbe-Schonberg, D., et al. (2014) Insights from trace element geochemistry as to the roles of subduction zone geometry and subduction input on the chemistry of arc magmas. *International Journal of Earth Sciences*, 103:

Bibliography

1929–1944.

Wilkinson, J.J. (2013) Triggers for the formation of porphyry ore deposits in magmatic arcs. *Nature Geoscience*, 6: 917–925.

Willbold, M. and Elliott, T. (2017) Molybdenum isotope variations in magmatic rocks. *Chemical Geology*, 449: 253–268.

Williams, H.M., Prytulak, J., Woodhead, J.D., et al. (2018) Interplay of crystal fractionation, sulfide saturation and oxygen fugacity on the iron isotope composition of arc lavas: An example from the Marianas. *Geochimica et Cosmochimica Acta*, 226: 224–243.

Witter, J.B., Kress, V.C., Delmelle, P., et al. (2004) Volatile degassing, petrology, and magma dynamics of the Villarrica Lava Lake, Southern Chile. *Journal of Volcanology and Geothermal Research*, 134: 303–337.

Wood, C.A. (1979) Monogenetic volcanoes of the terrestrial planets. *Proceedings of the Lunar and Planetary Sciences Conferences*, 10: 2815–2840.

Worner, G., Hammerschmidt, K., Henjes-Kunst, F., et al. (2000) Geochronology (Ar-40/Ar-39, K-Ar and He-exposure ages) of Cenozoic magmatic rocks from Northern Chile (18-22 degrees S): implications for magmatism and tectonic evolution of the central Andes. *Revista Geologica De Chile*, 27: 205–240.

Zelenski, M., Kamenetsky, V.S., Mavrogenes, J.A., et al. (2018) Silicate-sulfide liquid immiscibility in modern arc basalt (Tolbachik volcano, Kamchatka): Part I. Occurrence and compositions of sulfide melts. *Chemical Geology*, 478: 102–111.

Zellmer, G.F., Edmonds, M. and Straub, S.M. (2015) Volatiles in subduction zone

Bibliography

magmatism. *Geological Society, London, Special Publications*, 410 (1): 1–17.
doi:10.1144/SP410.13.

Appendix A

Petrographic thin section descriptions

All thin sections were analysed in transmitted light using a Zeiss Primo Star petrographic microscope. Individual thin section descriptions have been collated in **Table A1** below. Those descriptions relating to samples collected from Antuco stratovolcano* (starred) are published in *Earth and Planetary Science Letters*⁴.

Table A1 Individual thin section descriptions of the samples used in the current project

Sample ID	Description
<i>Antuco stratovolcano</i>	
A27-1*	Porphyritic texture, with a light grey, cryptocrystalline groundmass. Phenocryst phases comprise ~10 – 15 vol. % ⁺ of the section, and include plagioclase (~10 vol. %) and olivine (<5 vol. %). Plagioclase phenocrysts are lath in form, and are mostly ≤1 mm, with some up to 1.5 to 2 mm. Simple and albite twinning is common, as is oscillatory zoning. Coarse and fine sieve textured plagioclase crystals are not overly common, however, some plagioclase crystals have overgrowths. Olivine phenocrysts are mostly rounded and ≤0.5 mm. Olivine crystals are also fractured. Both plagioclase and plagioclase and olivine glomerocrysts are seen in section.
A27-2*	Porphyritic texture, with a light grey, cryptocrystalline groundmass. Phenocryst phases make up ~30 vol. % of the section and include plagioclase (~20 vol. %) and olivine (~10 vol. %). Plagioclase phenocrysts are mostly ≤1 mm, occasionally up to ~2 mm, and in the form of sub- / euhedral laths. Simple and albite twinning is common throughout the section, with many crystals also showing oscillatory zoning. Plagioclase

⁴ Cox et al., 2019. Chalcophile element processing beneath a continental arc stratovolcano. *Earth and Planetary Science Letters*, **522**, 1-11.

Appendix A. Petrographic thin section descriptions

	<p>phenocrysts commonly show coarse and fine sieve texture, however, the degree varies from minor to major. Olivine phenocrysts are mostly rounded, usually ≤ 1 mm and heavily fractured. Some olivine crystals show skeletal form. Glomerocrysts are seen throughout the section, and are comprised of either plagioclase, olivine, or plagioclase and olivine.</p>
A27-3*	<p>Porphyritic texture, with a light grey, cryptocrystalline groundmass. Phenocryst phases make up ~15 – 20 vol. % of the section and include plagioclase (~10 – 15 vol. %), olivine (<5 vol. %) and opaques (<<1 vol. %). Plagioclase phenocrysts form sub- / euhedral laths, ranging from <1 to 2 mm. Both simple and albite twins are common, as is oscillatory zoning. Plagioclase crystals display coarse and fine sieve texture; however, it is not extensive in section. Overgrowths on plagioclase are rare. Olivine phenocrysts are generally small (<1 mm), round crystals, commonly fractured. Very few skeletal forms are present in section. Opaques are likely oxides. Glomerocrysts are present within the section, and are comprised of either plagioclase or plagioclase and olivine.</p>
A27-5*	<p>Porphyritic texture, with a dark, cryptocrystalline groundmass. Phenocryst phases comprise ~20 vol. % of the section, and include plagioclase (~15 vol. %), olivine (~5 vol. %) and clinopyroxene (rare). Plagioclase phenocrysts form sub- / euhedral laths, usually ≤ 1 mm, commonly displaying simple and / or albite twinning. Oscillatory zoning is also seen in some crystals. Sieve texture and overgrowths are not common. In some instances, plagioclase phenocrysts make up glomerocrysts. Olivine phenocrysts are commonly <<1 mm, however, some can be 1 – 2 mm. Crystals are mostly rounded, with some having skeletal forms. Olivine crystals are commonly fractured. Clinopyroxene is anhedral and <<1 mm.</p>
A27-7*	<p>Porphyritic texture, with a dark, very fine to cryptocrystalline groundmass. Groundmass is very dark in comparison to other Antuco thin sections, likely due to a greater volume of glass in section. Phenocryst phases comprise ~25 – 30 vol. % of the section, and include plagioclase (~20 vol. %) and olivine (~10 vol. %). Plagioclase phenocrysts are mostly <1 mm, however, can range to between 1 and 3 mm. Crystals form laths, that are mostly sub- / euhedral. Simple and albite twinning is common, oscillatory zoning less so. Coarse and fine sieve texture of the crystals is not extensive in section. Plagioclase overgrowths are common.</p>

Appendix A. Petrographic thin section descriptions

	<p>Glomerocrysts of plagioclase are present in section. Olivine phenocrysts are rounded, and mostly $\ll 1$ mm, but can range between 1 to 2 mm. Crystals are fractured. Skeletal forms are not common. Glomerocrysts of olivine are also present in section.</p>
A27-8*	<p>Porphyritic texture, with a light grey, fine to cryptocrystalline groundmass. The groundmass is generally coarser than other Antuco thin sections. Phenocryst phases include plagioclase and olivine. Plagioclase phenocrysts are generally ≤ 1 mm, but can be up to 3 mm. Crystals take the form of laths, displaying simple and / or albite twinning. Some form glomerocrysts. Coarse and fine sieve textured crystals are extensive. Plagioclase overgrowths are common. Olivine phenocrysts are commonly rounded (some show a subhedral form) and < 1 mm. Crystals are commonly fractured. Glomerocrysts of olivine are present in section. There is a lack of skeletal forms in section. Within the groundmass, plagioclase laths and rounded olivine crystals can be made out.</p>
A27-9*	<p>Porphyritic texture, with a light grey, fine to cryptocrystalline groundmass (plagioclase and minor olivine). Phenocryst phases make up ~ 15 vol. % of the section, and include plagioclase (5 – 10 vol. %), olivine (~ 5 vol. %) and opaques ($\ll 1$ vol. %). Plagioclase phenocrysts range in size from < 1 mm to 2.5 mm and are mostly lath in form. Simple and albite twinning is common, as is oscillatory zoning. Sieve textured plagioclase crystals are not common; however dissolution of crystal edges can be seen in some crystals. Olivine phenocrysts are rounded, mostly < 1 mm and fractured. Glomerocrysts are present in section, and are comprised of either plagioclase or plagioclase and olivine. Opaques are also included in a few of the glomerocrysts.</p>
A27-10*	<p>Porphyritic texture, with a dark, very fine to cryptocrystalline groundmass. Phenocryst phases make up ~ 40 vol. % of the section, and include plagioclase (~ 30 vol. %) and olivine (~ 10 vol. %). Plagioclase phenocrysts are mostly lath in form, and range in size from < 1 mm to 3 mm, commonly between 1 to 1.5 mm. Simple and albite twinning is common, with oscillatory zoning also seen in many crystals. Plagioclase glomerocrysts are observed. Sieve texture (coarse and fine) in plagioclase crystals is common throughout the section. Plagioclase overgrowths are not</p>

Appendix A. Petrographic thin section descriptions

	common. Olivine phenocrysts are mostly rounded, and range from <<1 mm up to 2 mm. Crystals are fractured. Some skeletal forms are present.
A27-11*	Porphyritic texture, with a light grey, cryptocrystalline groundmass. Phenocryst phases comprise ~30 vol. % of the section, and include plagioclase (~20 – 25 vol. %), olivine (~5 – 10 vol. %) and opaques (rare). Plagioclase phenocrysts are largely lath in form, and mostly <1 mm, but larger crystals are present (up to 2 / 3 mm). Simple and albite twinning is common, with some crystals showing oscillatory zoning. Glomerocrysts are observed. Coarse and fine sieve textured plagioclase crystals are common, however, the degree varies from lightly to heavily sieve textured. Plagioclase overgrowths are rare. Olivine phenocrysts are mostly <<1 mm, with only very few between 1 to 1.5 mm. Glomerocrysts are observed. Mostly rounded, with very few skeletal in form. Most are heavily fractured.
A28-1*	Porphyritic texture, with a dark, almost completely glassy groundmass. Phenocryst phases comprise 35 – 40vol. % of the section, and include plagioclase (~20 – 25vol. %) and olivine (~10 – 15vol. %). Olivine phenocrysts are few and far between. Crystals are mostly rounded, ≤1 mm (generally ≤0.5 mm) and fractured. Some olivine crystals form glomerocrysts, whereas some show a skeletal form. Plagioclase phenocrysts are mostly lath in form, and commonly 0.5 to 1.5 mm, some up to 2 mm. Simple and albite twinning is common throughout the section, with oscillatory zoning seen in fewer crystals. Sieve texture (coarse and fine) is seen throughout the section, with the larger phenocrysts (~2 mm) displaying a heavily sieved texture. Plagioclase overgrowths are not common in section. Plagioclase crystals have formed glomerocrysts.
A28-3*	Porphyritic texture, with a dark, cryptocrystalline groundmass. Phenocryst phases are less common than most other sections, making up ≤10 vol. % of the section, and include plagioclase (>5 vol. %), olivine (<<5 vol. %) and opaques (<<1 vol. %). Phenocrysts of the section show a rough alignment. Plagioclase phenocrysts are lath in form, and mostly <<1 mm (few crystals are ~1 mm). Simple and albite twinning, and oscillatory zoning are common. Limited sieve texture is observed in the section. Plagioclase glomerocrysts are present in section. Olivine phenocrysts are mostly rounded to subhedral, fractured and <<1 mm.

Appendix A. Petrographic thin section descriptions

A28-4*	Porphyritic texture, with a light grey, cryptocrystalline texture. Overall, the phenocryst population is generally coarser than other Antuco sections. Phenocryst phases make up ~40 vol. % of the section, and include plagioclase (~30 vol. %) and olivine (≤ 10 vol. %). Olivine phenocrysts are generally rounded and ≤ 1 mm. Crystals show fracturing. Plagioclase phenocrysts are on average coarser than other sections; commonly ≥ 1 mm, and up to 2 mm. Crystals are lath in form, show simple and albite twinning and commonly display oscillatory zoning. Sieve texture (coarse and fine) is common, with some crystals having plagioclase overgrowths. Plagioclase crystals often form glomerocrysts.
A28-6*	Porphyritic texture, with a mostly dark, cryptocrystalline to glassy groundmass. Unlike other Antuco sections, this section displays pervasive red staining, attributed to Fe-oxyhydroxide alteration of both phenocryst phases and groundmass. Phenocryst phases comprise ~15 vol. % of the section, and include plagioclase (~10 vol. %) and olivine (~5 vol. %). Plagioclase phenocrysts are lath in form, and no more than 1 mm. Despite pervasive Fe-oxyhydroxide alteration, little sieve texture is observed. Simple and albite twinning, and oscillatory zoning are common. Olivine phenocrysts are rounded, small ($\ll 1$ mm) and fractured. Glomerocrysts comprised of either plagioclase or plagioclase and olivine are observed in section.
A28-8*	Porphyritic texture, with a light grey, cryptocrystalline groundmass. Phenocryst phases make up a greater volume (~40 vol. %) of the section than other sections, and include plagioclase (~30 – 35 vol. %) and olivine (5 – 10 vol. %). Plagioclase phenocrysts are lath in form, and mostly ≤ 1 mm, however, some are between 1 to 1.5 mm. Plagioclase crystals also form glomerocrysts. Both simple and albite twinning are common, with oscillatory zoning seen in many crystals. Coarse and fine sieve texture is common, but not extensive. Plagioclase overgrowths are common. Some of the larger plagioclase phenocrysts are heavily sieve textured. Glomerocrysts of plagioclase are observed. Olivine phenocrysts are rounded, fractured and ≤ 1 mm. Some crystals have a skeletal form.
A28-9*	Porphyritic texture, with a light grey, cryptocrystalline groundmass. Similar to A28-8. Phenocryst phases comprise ~30 – 35 vol. % of the section, and include plagioclase (~20 vol. %) and olivine (~15 vol. %). Olivine

Appendix A. Petrographic thin section descriptions

	phenocrysts are mostly <1 mm, but can be up to 1.5 mm. Most are rounded, some show a more formed crystal shape (subhedral). Crystals are commonly fractured. Skeletal forms are also present, albeit only a minor number of the crystals. Olivine glomerocrysts are observed. Plagioclase phenocrysts are mostly ≤ 1 mm, however some approach 2 mm. Most plagioclase crystals are lath in form, and commonly display simple and albite twinning. Oscillatory zoning is less common. Sieve texture (coarse and fine) is extensive in section. Glomerocrysts comprised of either plagioclase or plagioclase and olivine are observed in section.
A29-1*	Porphyritic texture, with a dark, cryptocrystalline groundmass. Phenocrysts comprise ≤ 10 vol. % of the section, and include plagioclase (~10 vol. %) and olivine ($\ll 1$ vol. %). Plagioclase phenocrysts are the dominant phenocrysts phase and are commonly 0.5 to 1 mm, with some up to 2 mm. They are commonly lath in form, display simple and albite twinning, with many crystals displaying oscillatory zoning. Sieve texture is common in larger crystals. Overgrowths are rare. Olivine phenocrysts are rare, but where present, are rounded, fractured and ≤ 1 mm. Plagioclase – olivine glomerocrysts are observed.
A29-4*	Porphyritic texture, with a light grey, cryptocrystalline groundmass. Phenocrysts are only a minor constituent of the section ($\sim \ll 5$ vol. %), with a number of large (1 to 2.5 mm) phenocrysts (euhedral plagioclase and anhedral olivine, opaques and clinopyroxene) amalgamating (as a glomerocryst) on one side of the section. Most of the phenocrysts distributed in the groundmass are plagioclase, with only a few olivine crystals. Plagioclase phenocrysts are mostly well formed laths, all ≤ 1 mm, generally ≤ 0.5 mm. Crystals show simple and / or albite twinning and lack sieve texture. One plagioclase glomerocryst is observed in section. Olivine phenocrysts are a very minor constituent component of the section ($\ll 1$ vol. %). Crystals are rounded, fractured and $\ll 1$ mm.
<i>Yate stratovolcano</i>	
Ya.26-6A	Porphyritic texture, with phenocrysts (~20 vol. %) of plagioclase, olivine, clinopyroxene and opaques set in a fine, dark grey groundmass comprising plagioclase microlites and opaques. Plagioclase crystals are the most abundant phenocryst phase, generally forming sub to euhedral laths up to 1 mm in length. Simple and albite twinning and oscillatory

zoning are common. Dissolution of crystals is infrequent, but where found follows out oscillatory zones. Olivine phenocrysts are sub to euhedral in form, usually between ½ and 1.5 mm in length. Crystals are commonly fractured. Some crystals display moderately skeletal form. Clinopyroxene phenocrysts are generally anhedral in form and usually <1 mm in length, although are as large as 2 – 3 mm in length. Crystal edge alteration is uncommon. The opaque phenocrysts are anhedral in form, up to ½ mm in length, and show no association with a particular phase. Glomerocrysts (5 – 6 mm across) are present in the section and comprise solely plagioclase or all phenocryst phases.

Ya.23-12B A porphyritic texture, with phenocrysts (~40 vol. %) of plagioclase, olivine, clinopyroxene and opaques set in a very fine, dark grey groundmass comprising dominantly plagioclase microlites. The groundmass defines a vague flow texture. Plagioclase phenocrysts form sub to euhedral laths or squares between ½ and 1.5 mm in length. Crystals commonly display simple and albite twinning and oscillatory zoning. Dissolution texture is not pervasive, with crystal edges mostly intact. Plagioclase phenocrysts commonly form glomerocrysts up to ~4 mm across. Olivine phenocrysts are generally fine (<1 mm in length), fractured and rounded (anhedral). Some crystal edges are altered, having a very thin alteration rim. The clinopyroxene phenocrysts are subhedral in form, up to 1 mm in length. Crystals are slightly fractured with some displaying minimal alteration to crystal edges. Clinopyroxene phenocrysts can comprise small (~1 mm across) glomerocrysts. The opaques are ≤ ½ mm in length, of irregular form and not associated with a particular phase.

Ya.26-7A Porphyritic texture, with plagioclase, olivine, clinopyroxene and opaque phenocryst phases (~10 vol. %) hosted in a dark, fine groundmass comprised of plagioclase (dominant), olivine, clinopyroxene and opaques. Plagioclase phenocrysts display a broad range of forms (rounded to lath-like) between ½ and 2 mm in length. Twinning (simple/albite) and oscillatory zoning common. Dissolution of crystal centres minimal, although alteration to crystal edges more common. Plagioclase crystals commonly form glomerocrysts. Olivine phenocrysts are usually subhedral and between ½ and 1 mm in length, although can be as large as 3 mm in length. Crystal edge alteration (to clay?) common, as are skeletal crystals.

Appendix A. Petrographic thin section descriptions

	<p>Oscillatory zoning is rare. Clinopyroxene crystals are sub to euhedral in form and <1 mm in length. Simple twinning is observed, although is uncommon. Crystal edge dissolution is fairly common. Clinopyroxene crystals can form glomerocrysts. The opaque phenocrysts are very minor constituents of the section, irregular in form and < ½ mm in length.</p>
Ya.26-4A	<p>A porphyritic texture, with phenocrysts (~15 vol. %) of plagioclase, olivine, clinopyroxene and opaques sat in a black, cryptocrystalline groundmass. Opaque phenocrysts are a small (<<1 mm in length), minor phase, irregular in form. Plagioclase phenocrysts are well formed, euhedral laths, ranging between ½ and 2 mm in length, with minimal dissolution texture. Simple and albite twins are common, as is oscillatory zoning. Plagioclase crystals commonly form glomerocrysts. Olivine phenocrysts are commonly sub to euhedral, elongate crystals, ~1 to 2 mm in length. Anhedral and skeletal crystals are of minor volume. Clinopyroxene phenocrysts are usually sub to euhedral elongate prisms, ~1 mm in length. Dissolution of crystal edges fairly common. Simple twinning commonly observed.</p>
Ya.23-8B	<p>Section has a porphyritic texture, with phenocrysts (~20 vol. %) of plagioclase (heavily dominant), olivine and clinopyroxene hosted in a light grey, mostly cryptocrystalline groundmass, although few plagioclase microlites are observed. Plagioclase phenocrysts form sub to euhedral lath, usually 1 to 1.5 mm in length, although are observed as large as 4 mm in length. Twinning (simple and albite) and oscillatory zoning are common. Dissolution of crystals is uncommon, although where present, is generally focussed near crystal edges following oscillatory zoning. Both olivine and clinopyroxene phenocrysts are minor (≤1 vol. %) constituents of the section and commonly ≤1 mm in length.</p>
Ya.26-3A	<p>A porphyritic texture, with phenocrysts (~10 vol.%) of plagioclase, clinopyroxene, olivine and opaques sat in a dark grey, cryptocrystalline to glassy groundmass. Plagioclase range from anhedral, mostly 'broken' crystals, to euhedral laths, ~1 mm in length. Simple and albite twinning is common, as is oscillatory zoning. Crystals display varying degrees of dissolution, from absent to heavily dissolved, usually concentrated at the cores of crystals. Plagioclase crystals very commonly form glomerocrysts, which are up to 3 mm across. Clinopyroxene phenocrysts are sub to euhedral prisms between ½ and 1 mm in length, although are as large as 3</p>

Appendix A. Petrographic thin section descriptions

	<p>mm in length. Simple twins are common. Dissolution to crystal edges is frequent. Olivine is a very minor phenocryst phase (<<1 vol. %), having a generally anhedral form, ~1 mm in length, and commonly fractured. Opaque phenocrysts are rare, <<1 vol. % and irregular in form. Glomerocrysts are very common throughout the section, usually comprising plagioclase, clinopyroxene, or both.</p>
Ya.02-3A	<p>Porphyritic texture, with phenocrysts (~30 vol. %) of plagioclase (heavily dominant), clinopyroxene, olivine and orthopyroxene (rare) hosted in a light grey, cryptocrystalline groundmass. Plagioclase phenocrysts display lath-like or triangular forms, usually ~1 mm in length. Simple and albite twins and oscillatory zoning are common. Dissolution texture is not common. Commonly forms glomerocrysts up to 3 mm across. Clinopyroxene crystals are mostly prismatic in form and ≤1 mm in length. Crystals can form glomerocrysts with plagioclase. Olivine crystals are minor constituents (<1 vol. %) and generally anhedral (rounded) and <1 mm in length. Glomerocrysts of all phases are observed.</p>
<hr/> <p style="text-align: center;"><i>Hornopirén stratovolcano</i></p>	
Ho.15-5A	<p>Holocrystalline in nature and weakly porphyritic, with phenocrysts of plagioclase, olivine and orthopyroxene (rare) comprising <1 vol. % of the section. Plagioclase phenocrysts are lath-like in form, ~1 mm in length and generally lack alteration/dissolution. Twinning (simple/albite) and oscillatory zoning are common. Olivine phenocrysts are commonly anhedral (rounded), fractured and ~1 mm across. The groundmass in which the phenocrysts are set is dark and dominated by crystals <<1 mm in length, with plagioclase crystals being the main constituent (>90 vol. %) over olivine. Plagioclase and olivine groundmass crystals display very similar features to their phenocryst equivalents. Vesicles are present, although not abundant.</p>
Ho.19-1A	<p>A holocrystalline and porphyritic texture, with phenocrysts (~10 vol. %) of plagioclase and olivine hosted in a black, fine to cryptocrystalline groundmass. Identifiable crystals in the groundmass are plagioclase microlites (dominant) and rounded olivine crystals, generally <<1 mm in length. Plagioclase phenocrysts are lath-like or square in form, up to 1.5 mm in length (usually ~1 mm in length), and commonly display twinning (simple/albite) and oscillatory zoning. Dissolution texture of crystals is</p>

Appendix A. Petrographic thin section descriptions

	minimal. Olivine phenocrysts are mostly subhedral, up to 1 mm in length, and display minimal alteration to crystal edges. Vesicles comprise ~5 vol. % of the section.
Ho.30-2A	Holocrystalline and porphyritic texture, with phenocrysts (~10 vol. %) of plagioclase and olivine hosted in a fine to cryptocrystalline groundmass dominated by plagioclase laths. Plagioclase phenocrysts are usually lath in form, 1 to 2 mm in length and display twinning (simple/albite) and oscillatory zoning. Dissolution of crystal cores is common. Olivine phenocrysts are generally anhedral (rounded) and <1 mm across. Thin alteration rims are common. Glomerocrysts of plagioclase, olivine or both are commonly observed.
<i>Apagado stratovolcano</i>	
Ap.21-9C	Porphyritic texture, with a fine groundmass composed of plagioclase laths, olivine, minor clinopyroxene and opaques. Phenocrysts phases include plagioclase, olivine and clinopyroxene, totalling ~10 vol. % of the section. Plagioclase crystals dominate the phenocryst assemblage, forming lath-like or square crystals, sub-mm to 2.5 mm in length. Crystals are commonly twinned (simple/albite) and zoned. Dissolution of crystal cores common, edges display dissolution to a lesser extent. Olivine phenocrysts range from anhedral (rounded) to euhedral (mostly diamond) in form, again sub-mm to ~1.5 mm in length. Crystals are commonly fractured and display thin alteration rims. Clinopyroxene crystals are a minor, phenocryst phase, forming subhedral prisms, ≤1 mm in length. Simple twins are observed. Glomerocrysts of each phenocryst phase are present in section. Plagioclase glomerocrysts can be up to 3 mm across.
Ap.21-9B	A porphyritic texture, with a fine groundmass of plagioclase (dominant) and minor olivine and opaques. Phenocryst phases include plagioclase, olivine and clinopyroxene, totalling ~10 vol. % of the section. Plagioclase crystals heavily dominate the phenocryst assemblage (~8 vol. %). Crystals are mostly lath in form, ½ to 3 mm in length, and commonly display twinning (simple/albite) and oscillatory zoning. Dissolution texture is not prevalent in section, although some crystals display an extensive dissolution texture. Plagioclase crystals commonly form glomerocrysts up to 5 mm across. Olivine phenocrysts are generally anhedral, ≤1 mm in length and fractured.

Appendix A. Petrographic thin section descriptions

	Thin alteration rims are observed. Clinopyroxene phenocrysts are mostly subhedral prisms, <1 mm in length.
Ap.21-6B	Porphyritic texture, with a fine groundmass comprised of plagioclase (dominant), opaques and minor clinopyroxene and olivine. The phenocryst assemblage includes plagioclase, olivine and clinopyroxene, totalling ~15 vol.% of the section, although plagioclase crystals heavily dominate (~10 vol. %). Plagioclase phenocrysts range from anhedral ('broken' crystals) to euhedral laths or prisms and from ½ to 2.5 mm in length. Twinning (simple and albite) and oscillatory zoning are common, as are dissolution texture of crystals. Plagioclase glomerocrysts are present and are up to 4 mm across. Olivine phenocrysts are anhedral, <1 mm across, fractured and have thin alteration rims. Clinopyroxene crystals are generally anhedral and <1 mm in length. Twinning is observed, although not common. Alteration along crystal edges is infrequent.
Ap.21-4A	A porphyritic texture, with phenocrysts (≤5 vol. %) of plagioclase, olivine and minor clinopyroxene hosted in a fine groundmass of dominantly plagioclase laths. Plagioclase phenocrysts are generally an- to subhedral prisms ≤1 mm in length. Simple and albite twinning and oscillatory zoning are common. Dissolution textures are minimal. Olivine phenocrysts are mostly anhedral and <1 mm across. Alteration along fractures and crystals edges is observed, giving crystals a red overprint. The clinopyroxene phenocrysts are subhedral prisms, <1 mm in length.
Ap.21-3A	Porphyritic texture, with phenocryst phases (≤5 vol. %) sat in a fine to cryptocrystalline groundmass. Plagioclase laths and rounded olivine crystals are identifiable in the groundmass. Olivine dominates the phenocryst assemblage (~4 vol. %), mostly forming anhedral (rounded) crystals <1 mm across, although some crystals are as large as 2 mm across. Degree of the skeletal nature of olivine crystal varies. Thin alteration rims are present. Olivine crystals commonly form glomerocrysts. Plagioclase phenocrysts are generally lath in form and ≤1 mm in length. Twinning (simple/albite) is common, oscillatory zoning less so. Dissolution texture is minimal. Clinopyroxene crystals form a very minor (rare) constituent of the phenocryst assemblage.
Ap.21-2A	Weakly porphyritic texture, with phenocrysts (<3 vol. %) of plagioclase and olivine hosted in a fine groundmass of plagioclase, olivine and opaques.

Appendix A. Petrographic thin section descriptions

	<p>Olivine phenocrysts are usually subhedral, <1 to 1.5 mm in length, fractured and display red – brown alteration along crystal edges and fractures. Olivine crystals are common as glomerocrysts. Plagioclase phenocrysts are prismatic in form and <1 mm in length. Twinning (simple/albite) and oscillatory zoning are common. Dissolution textures are minimal, but where present, usually confined to crystal edges.</p>
Ap.20-5A	<p>A porphyritic texture, with phenocrysts set in a fine groundmass of plagioclase laths, olivine and opaques. The plagioclase laths in the groundmass are aligned, evidence of flow. The phenocryst assemblage totals ≤5 vol. % of the section and is comprised of plagioclase and olivine crystals. Olivine phenocrysts are an- to subhedral in form, ½ to 2.5 mm across, with most forming glomerocrysts. Thin alteration rims are observed on many crystals. Plagioclase phenocrysts are lath in form and ≤1 mm in length. Simple and albite twinning and oscillatory zoning are common. Dissolution textures are common at crystal cores.</p>
Ap.20-4A	<p>Clear ophitic texture throughout the section, with plagioclase laths radiating from/in large, encompassing clinopyroxene crystals. Around the ophitic texture, the section is near-equigranular in nature (all ≤1 mm in length), comprising an- to subhedral crystals of plagioclase, olivine and clinopyroxene. Plagioclase crystals are commonly twinned (simple/albite) and zoned, displaying minimal dissolution texture.</p>
<hr/> <i>Villarrica stratovolcano</i> <hr/>	
16DCVill.001	<p>Porphyritic texture, with a dark, cryptocrystalline groundmass. The phenocryst assemblage comprises ~30 – 35 vol. % of the section and includes olivine, plagioclase and minor clinopyroxene crystals. Olivine crystals are generally subhedral, although anhedral and euhedral forms are present, and ~1 mm in length (range between <<1 to ~3 mm in length). A minor volume of crystals display a low degree of skeletal nature. Olivine glomerocrysts are observed on section. Plagioclase phenocrysts are commonly lath-like in form, twinned (simple/albite) and zoned. Crystals are usually 1 to 2 mm in length, although can be as large as ~5 mm in length. Dissolution textures are present and can cover entire crystals, although core dissolution is more common. Clinopyroxene phenocrysts are subhedral, 1 to 1.5 mm in length, twinned and can form glomerocrysts. Olivine and plagioclase glomerocrysts are present, although not abundant.</p>

Appendix A. Petrographic thin section descriptions

16DCVill.003 A porphyritic texture, with the phenocryst assemblage hosted in a dark, very fine to cryptocrystalline groundmass. Plagioclase microlites are identifiable in the groundmass. The phenocryst assemblage totals ~20 vol. % of the section and comprises plagioclase, olivine and minor clinopyroxene crystals. Plagioclase phenocrysts are mostly lath in form and ~1 mm in length, although they do range between <1 mm and ~6 mm in length. Simple and albite twins and oscillatory zoning are common. Dissolution textures are not abundant, but where present, are focussed along crystal zones. Olivine phenocrysts are generally anhedral (rounded) and ≤ 1 mm across, although are as large as 2 mm across. Crystals are commonly fractured. Clinopyroxene phenocrysts are minor constituents, generally of prismatic form and <1 mm in length. Both olivine and plagioclase form glomerocrysts throughout the section.

Quetrupillán stratovolcano

16DCQuet.001 Porphyritic texture, with phenocrysts (~15 vol. %) of plagioclase, olivine, clinopyroxene and opaques hosted in a black, fine to cryptocrystalline groundmass. Plagioclase laths are identifiable in the groundmass and appear to align, potentially defining a flow texture. Plagioclase crystals are the most common phenocryst phase, and generally form lath-like crystals ranging in length from ≤ 1 to 3 mm. Zoning and twinning (simple/albite) are common across plagioclase crystals. Dissolution texture is observed throughout the section, although the degree varies between crystals, from limited to extensive. Olivine phenocrysts are usually anhedral (rounded) and ≤ 1 mm across. Crystals are heavily fractured. Clinopyroxene phenocrysts are an- to subhedral prisms in form, ≤ 1 mm in length, twinned, and occasionally display oscillatory zoning. Glomerocrysts are common throughout the section, comprising individual phenocryst phases or a combination of them.

16DCQuet.003 The section has a porphyritic texture, with the phenocryst assemblage (~10 vol. %) sat in a black, glassy groundmass. The phenocrysts assemblage is comprised of plagioclase, clinopyroxene and olivine crystals that are generally <1 mm in length. Plagioclase phenocrysts are mostly lath-like in form and commonly display twinning (simple/albite) and zoning. Dissolution textures are generally limited to the centre of some crystals. Clinopyroxene phenocrysts are mostly subhedral prisms,

Appendix A. Petrographic thin section descriptions

although can be anhedral (rounded). Simple twins are common, although zoning is rare. The olivine phenocrysts are anhedral, heavily fractured and generally skeletal in nature. Glomerocrysts of plagioclase and clinopyroxene are observed, although not abundant.

16DCQuet.005 Porphyritic texture, with a phenocryst assemblage of plagioclase, clinopyroxene and olivine, totalling ~15 – 20 vol. % of the section, hosted in a very fine, almost unidentifiable, grey groundmass. There appears a vague low texture of possible plagioclase microlites(?) in the section. Plagioclase phenocrysts are mostly lath-like in form, 1 to 2 mm in length, with crystals displaying varying degrees of dissolution; from heavily dissolved to almost clear of dissolution. Simple and albite twins and zoning are common throughout the section. Olivine phenocrysts are anhedral, with some having a highly skeletal nature, and ≤1 mm across. Clinopyroxene crystals are usually subhedral prisms, ranging in size from <1 to 2 mm in length. Simple twins are common, whereas zoning is infrequent. Glomerocrysts of plagioclase, clinopyroxene, or both are observed throughout the section.

Lanín stratovolcano

16DCLan.001 This sample appears heavily altered, with an observable green overprint, possibly related to crystal breakdown to clays. The remnant outlines of plagioclase and (potentially) olivine phenocrysts hosted in a fine(?) groundmass can be made out.

16DCLan.008 Porphyritic texture, with an abundance of phenocryst phases (~40 vol. %) set in a dark, cryptocrystalline groundmass. The phenocryst assemblage is comprised of generally well-formed, euhedral plagioclase, olivine and clinopyroxene (rare) crystals that are <1 to 1 mm across, although some plagioclase crystals are as large as 2 mm in length. The plagioclase phenocrysts commonly display twinning (simple/albite) and oscillatory zoning. Dissolution textures are not common, however, where present are focussed along crystal zones. Glomerocrysts are common throughout the section, usually comprised of either plagioclase and olivine, with infrequent plagioclase and olivine glomerocrysts.

16DCLan.010 The section has a porphyritic texture, with phenocrysts (~15 vol. %) of plagioclase, olivine and rare clinopyroxene and opaques hosted in a cryptocrystalline groundmass. Plagioclase crystals dominate the

Appendix A. Petrographic thin section descriptions

phenocryst assemblage (~12 vol. %) and are mostly lath in form. Crystals are generally <1 mm in length, although are as large as 2 mm in length. Twinning (simple/albite) and oscillatory zoning are common, as is crystal dissolution. The large plagioclase crystals are generally more dissolved and commonly form glomerocrysts several mm across. Olivine phenocrysts are generally anhedral in form and <<1 mm across. Most crystals are heavily fractured.

Ollagüe stratovolcano

Ollague001 Porphyritic texture, with a phenocryst assemblage (~20 vol. %) of plagioclase, amphibole, biotite and minor opaques hosted in a light grey, cryptocrystalline groundmass. Amphibole phenocrysts are generally of lozenge form and ≤1 mm in length, although can be as large as 3 mm in length. Few amphibole crystals display oscillatory zoning. Dissolution of amphibole crystals is limited to a small percentage of crystals, and in some cases, to the point where some crystals are difficult discern. Amphibole glomerocrysts are uncommon. Plagioclase phenocrysts are mostly lath in form, <1 to 2 mm, although plagioclase glomerocrysts can be as large as 4 mm in length. Simple and albite twinning and oscillatory zoning are common. Dissolution textures are mostly lacking, although few crystals are heavily dissolved. Biotite phenocrysts are tabular in form and generally between 1 and 2 mm in length. Red – brown alteration is common within and along crystal edges, with rare ‘bird’s eye’ texture.

Ollague005 A porphyritic texture, with phenocrysts (~20 vol. %) of plagioclase, amphibole, biotite and minor opaques sat in a fine to very fine groundmass mostly composed of plagioclase laths and opaques. Plagioclase phenocrysts generally form sub to euhedral laths, ranging between ½ and 2.5 mm in length, although commonly 1 to 1.5 mm in length. Both simple and albite twinning are common, as is oscillatory zoning. Dissolution of crystals is limited, with only a small percentage of crystals displaying minimal dissolution. Biotite phenocrysts are tabular to rectangular in form, 1 to 2 mm in length and display red – brown alteration to crystal interiors and dark rims. Amphibole phenocrysts are prismatic to lozenge in form, <1 to 1.5 mm in length and generally display dark, altered rims. The opaque phenocrysts are of minor volume in the section (<1 vol. %) and of irregular form.

Appendix A. Petrographic thin section descriptions

Ollague006B	<p>Porphyritic texture, with plagioclase, amphibole, biotite and minor opaque phenocryst phases (~15 vol. %) hosted in a very fine groundmass. Plagioclase laths are potentially identifiable in the groundmass. Biotite phenocrysts are tabular or lath-like in form and usually ~1 mm in length. Biotite crystals display thicker alteration rims than previous samples, possibly altered to chlorite. Plagioclase phenocrysts form laths or square crystals, although some appear 'broken'. Crystals range between <1 and 2 mm in length, although plagioclase glomerocrysts are as large as 4 mm across. Simple and albite twins are common, as is oscillatory zoning. Dissolution of crystal interiors is limited, although most crystal edges appear to have begun being altered/dissolved. Amphibole phenocrysts are anhedral (rounded) to euhedral (prismatic/lozenge) in form, no larger than 1.5 mm in length. Twins are absent, but oscillatory zoning is common. The majority of crystals display alteration, mostly concentrated along crystal edges. The opaque phenocryst phase are small (<1 mm across) and anhedral in form. All phases comprise glomerocrysts throughout the section.</p>
Poruñita002 [§] (Ollagüe)	<p>Section has a porphyritic texture, with a phenocryst assemblage (~20 vol. %) of plagioclase (dominant), amphibole, biotite and minor clinopyroxene and opaques hosted in a light grey, fine grained groundmass, predominantly composed of plagioclase microlites. Plagioclase phenocrysts display a range of forms (lath-like, square, 'broken') and are between ½ and 1 mm in length, although some crystals are as large as 3 mm in length. Twinning (simple/albite) and oscillatory zone are both common in plagioclase crystals. Dissolution of plagioclase crystals is frequent, mostly occurring within crystal interiors. Amphibole phenocrysts are lath-like, prismatic or lozenge in form, ≤1 mm in length, and commonly have thin, dark alteration rims. Simple twinning is observed, although not common. The biotite phenocrysts are tabular in form and up to 2 mm in length. Alteration to crystal interiors and long crystal edges is common. The opaque phenocrysts are usually irregular to rounded in form, whereas clinopyroxene phenocrysts form euhedral prisms. Both are ≤ 1 mm across. Glomerocrysts of plagioclase, amphibole, or both are observed throughout the section.</p>

Appendix A. Petrographic thin section descriptions

Poruñita003 (Ollagüe)	Porphyritic texture, with phenocrysts set in a light grey to brown, very fine to cryptocrystalline groundmass. The phenocryst assemblage totals ~20 vol. % of the section, comprising crystals of plagioclase (dominant), amphibole, biotite and minor opaques. The plagioclase phenocrysts display a broad range in form, from anhedral (rounded), through subhedral, and to euhedral (laths), usually ½ to 1 mm in length. Simple and albite twins and oscillatory zoning are common. Dissolution textures are not extensive, only affecting a small percentage of crystals, usually along their edges. Both amphibole and biotite phenocrysts are extensively altered, with an apparent dark (red – brown) overprint. Crystals are generally ≤1 mm in length and an- to subhedral in form. The alteration can make discerning amphibole from biotite (and vice versa) difficult. Again, opaque phenocrysts are fine (<1 mm across) and irregular in form. Glomerocrysts are observed throughout the section and are primarily composed of plagioclase.
Poruñita004 (Ollagüe)	Porphyritic texture, with a phenocryst assemblage (~25 vol. %) of plagioclase (strongly dominant), biotite, amphibole and minor opaques hosted in a light grey to brown, cryptocrystalline groundmass. Plagioclase phenocrysts range from 'broken' crystals to lath-like in form, and are up to 1.5 mm in length. Twinning (simple/albite) and zoning are common throughout the section. Dissolution of plagioclase crystals is minimal, generally limited to crystal edges. Again, amphibole and biotite phenocrysts are altered, with an apparent overprint, although to a lesser extent than above. Nevertheless, discerning between the two is still difficult in places, although crystals are generally subhedral and ~1 mm in length. The opaque crystals are ~ ½ mm across and rounded in form.
Poruñita005 (Ollagüe)	Section has a porphyritic texture, with phenocrysts (~10 vol. %) of plagioclase, amphibole, minor biotite and clinopyroxene and opaques (rare), hosted in a fine to very fine, light grey groundmass, predominantly composed of plagioclase (where discernible). Plagioclase crystals are generally square or tabular in form and up to 1.5 mm in length. Dissolution of crystals is not extensive, but where observed, mostly focussed along crystal edges. Simple and albite twinning are common, oscillatory zoning less so. Amphibole phenocrysts are generally prismatic in form, although anhedral forms are observed. Crystals are commonly ~1 mm in length.

Appendix A. Petrographic thin section descriptions

	Dark alteration rims of varying thickness are observed on most crystals. Biotite phenocrysts are tabular in form and up to 2 mm in length. Red – brown alteration of biotite is not extensive, although is observed. Clinopyroxene crystals are either prismatic or rounded, <1 mm across and are heavily altered.
Poruñita006 (Ollagüe)	A porphyritic texture, with the phenocryst assemblage (~15 vol. %) hosted in a grey, largely cryptocrystalline groundmass. The phenocryst assemblage includes crystals of plagioclase, amphibole, biotite and (rare) opaques. Plagioclase phenocrysts are broad in their observed forms, from rounded through to tabular crystals, mostly 1 mm in length. Twinning (simple/albite) and oscillatory zoning are common throughout the section. Dissolution of crystals is minimal. Glomerocrysts of plagioclase crystals are observed as large as 3 mm across. Biotite phenocrysts are rectangular in form and ≤2 mm in length. Alteration is minimal. Amphibole crystals are largely sub to euhedral (prismatic/lozenge) in form and ½ to 1 mm across. Dark rim alteration is common on amphibole crystals. Oscillatory zoning is observed, although uncommon. The opaque crystals are irregular in form and <<1 mm across.
Poruñita006a (Ollagüe)	Section has a porphyritic texture, with phenocrysts (~15 vol. %) of plagioclase, amphibole, biotite and very minor opaques hosted in a dark grey, cryptocrystalline groundmass. Plagioclase phenocrysts range from ‘broken’/anhedral crystals to euhedral laths, largely 1 to 1.5 mm in length, although are as large as 3.5 mm in length. Twinning (simple/albite) and oscillatory zoning are common. Dissolution textures are limited. Amphibole crystals are mostly euhedral prisms and lozenges, ~1 mm across. All crystals have a thin, dark alteration rim. Biotite phenocrysts are rectangular/tabular in form, largely 1 to 2 mm in length and commonly display red – brown alteration to crystal interiors. Opaques are rounded and fine (<<1 mm across).

San Pedro stratovolcano

Samples San Pedro/San Pablo 001, 007 and 011 are near-identical in nature, hence the sample description provided in Chapter 3 is representative off all samples.

La Poruñita small eruptive centre

Poruñita001a	A highly vesicular section (≥60 vol. %), with an interstitial, dark, mostly cryptocrystalline groundmass of identifiable olivine and plagioclase
--------------	--

Appendix A. Petrographic thin section descriptions

crystals. Olivine forms either near-perfect crystals (diamond in form) or rounded, anhedral crystals, <<1 mm in length. Plagioclase dominates the groundmass and forms sub to euhedral, tabular microlites <<1 mm in length. Simple twins are commonly observed.

**Published in Cox et al. (2019); +Percentage volumes quoted are estimates using a petrographic microscope; §Except for 'Poruñita001a', sample IDs beginning with 'Poruñita' refer to those collected from the debris avalanche of Ollagüe stratovolcano.*

Appendix B

Raw sample analyses

Table B.1. Complete dataset of raw analyses obtained for the current project

Edifice	Villarrica			Quetrupillán		
ID	16DCVill.007	16DCVill.003	16DCVill.001	16DCQuet.001	16DCQuet.003	16DCQuet.005
NB						
Sample	<i>Lava flow</i>	<i>Lava flow</i>	<i>Lava flow</i>	<i>Lava flow</i>	<i>Lava flow</i>	<i>Lava flow</i>
Rock type	<i>Basaltic-andesite</i>	<i>Basaltic-andesite</i>	<i>Basalt</i>	<i>Basaltic-andesite</i>	<i>Trachy-andesite</i>	<i>Trachy-andesite</i>
Long.	-71.95	-71.94	-71.94	-71.75	-71.75	-71.75
Lat.	-39.38	-39.39	-39.38	-39.49	-39.49	-39.50
Majors	ICP-OES	ICP-OES	ICP-OES	ICP-OES	ICP-OES	ICP-OES
Traces	ICP-MS/MS	ICP-MS/MS	ICP-MS/MS	ICP-MS/MS	ICP-MS/MS	ICP-MS/MS
SiO₂ (wt.%)	53.39	52.72	51.46	61.92	61.58	56.74
TiO₂	1.20	1.24	1.05	1.19	1.30	1.03
Al₂O₃	17.10	17.87	18.05	16.02	15.09	16.88
Fe₂O₃ (t)	10.21	9.93	10.98	7.54	8.33	7.91
MnO	0.17	0.16	0.17	0.14	0.14	0.14
MgO	4.77	5.02	4.13	1.39	1.39	5.03
CaO	9.45	9.61	10.19	4.62	3.58	6.85
Na₂O	3.30	2.95	3.20	4.80	4.41	3.48
K₂O	0.80	0.76	0.72	2.51	3.27	2.05
P₂O₅	0.22	0.24	0.25	0.49	0.43	0.27
SO₃	-	-	-	-	-	-
LOI	-0.04	-0.15	-0.28	-0.04	0.00	0.04
Total	100.57	100.35	99.94	100.56	99.52	100.41
Li (ppm)	9.83	10.39	9.55	19.97	20.81	12.72
Sc	35.11	31.42	33.59	19.59	18.31	23.22
S	5.30	7.34	11.45	90.91	90.27	13.34
V	297.69	296.28	293.89	132.44	109.18	170.41
Cr	95.22	161.10	256.94	3.11	2.56	150.15
Co	27.99	29.98	35.28	10.90	9.24	25.68
Ni	29.76	62.93	89.69	2.33	1.67	65.91
Cu	130.58	146.46	139.37	26.01	24.55	41.77
Zn	90.37	94.71	118.81	101.41	87.98	70.06
Ga	18.74	19.20	18.00	19.96	19.73	17.76

Appendix B. Raw sample analyses

Ge	-	-	-	-	-	-
As	5.11	5.08	5.06	4.69	5.14	3.09
Se	0.05	0.04	0.04	0.03	0.03	0.03
Rb	15.32	15.04	14.39	75.50	85.17	45.92
Sr	454.11	469.54	431.19	317.31	297.72	429.82
Y	25.06	25.24	24.40	46.85	49.13	27.93
Zr	93.24	98.03	90.45	367.73	372.65	214.49
Nb	2.25	2.23	2.00	12.55	13.20	7.65
Mo	0.86	0.89	0.82	2.74	2.93	1.59
Cd	-	-	-	-	-	-
Ag	0.04	0.05	0.04	0.00	0.00	0.02
Sn	1.05	1.06	1.14	2.45	2.66	1.48
Sb	0.38	0.41	0.38	0.30	0.32	0.19
Cs	-	-	-	-	-	-
Ba	211.57	175.96	173.36	678.86	746.12	441.28
La	8.31	8.95	7.94	35.01	37.15	21.58
Ce	21.10	22.52	20.40	77.43	81.47	47.43
Pr	2.90	3.09	2.81	9.35	9.88	5.78
Nd	13.45	14.17	13.13	36.97	38.89	23.13
Sm	3.78	3.96	3.70	8.28	8.66	5.26
Eu	1.16	1.20	1.14	1.89	1.91	1.35
Gd	4.16	4.33	4.07	7.84	8.16	4.99
Tb	0.68	0.70	0.67	1.21	1.26	0.78
Dy	4.18	4.25	4.11	7.24	7.44	4.66
Ho	0.89	0.92	0.88	1.52	1.58	0.97
Er	2.59	2.67	2.54	4.50	4.64	2.89
Tm	0.34	0.29	0.28	0.59	0.61	0.38
Yb	2.38	2.37	2.28	4.31	4.61	2.71
Lu	0.37	0.37	0.36	0.67	0.70	0.43
Hf	2.47	2.62	2.50	8.61	8.71	5.06
Ta	0.71	0.12	0.14	0.71	0.76	0.44
W	0.42	0.42	0.40	0.92	0.93	0.53
Tl	0.08	0.04	0.05	0.49	0.54	0.30
Pb	7.16	7.48	6.96	20.20	21.41	13.08
Bi	-	-	-	-	-	-
Th	4.02	1.42	1.19	8.03	8.79	5.06
U	0.41	0.34	0.39	2.43	2.72	1.52

Appendix B. Raw sample analyses

Table B.1. continued

Edificio	Quetrupillán		Lanín			
ID	16DCQuet.006	16DCQuet.007	16DCLan.001	16DCLan.007	16DCLan.008	16DCLan.010
NB						
Sample	<i>Lava flow</i>	<i>Lava flow</i>	<i>Lava flow</i>	<i>Lava flow</i>	<i>Lava flow</i>	<i>Lava flow</i>
Rock type	<i>Trachyte</i>	<i>Trachyte</i>	<i>Basaltic-andesite</i>	<i>Trachyte</i>	<i>Basaltic trachy-andesite</i>	<i>Trachyte</i>
Long.	-71.75	-71.75	-71.49	-71.50	-71.51	-71.49
Lat.	-39.50	-39.50	-39.58	-39.60	-39.60	-39.60
Majors	<i>ICP-OES</i>	<i>ICP-OES</i>	<i>ICP-OES</i>	<i>ICP-OES</i>	<i>ICP-OES</i>	<i>ICP-OES</i>
Traces	<i>ICP-MS/MS</i>	<i>ICP-MS/MS</i>	<i>ICP-MS/MS</i>	<i>ICP-MS/MS</i>	<i>ICP-MS/MS</i>	<i>ICP-MS/MS</i>
SiO₂ (wt.%)	63.41	62.99	54.62	63.37	53.13	62.61
TiO₂	0.85	1.33	1.06	0.94	1.38	0.95
Al₂O₃	16.27	15.85	17.54	15.95	17.64	16.28
Fe₂O₃ (t)	5.32	6.83	8.95	6.46	11.26	6.67
MnO	0.12	0.14	0.16	0.19	0.19	0.19
MgO	1.32	1.43	4.22	1.18	4.01	1.20
CaO	3.48	3.62	7.29	3.40	7.22	3.42
Na₂O	5.08	4.75	3.27	5.01	3.64	5.35
K₂O	2.93	3.51	1.24	3.19	1.71	3.34
P₂O₅	0.19	0.44	0.26	0.38	0.43	0.38
SO₃	-	-	-	-	-	-
LOI	0.16	0.05	2.50	-0.11	-0.05	0.01
Total	99.14	100.96	101.11	99.96	100.56	100.41
Li (ppm)	21.05	21.50	34.51	16.33	10.92	18.37
Sc	13.49	18.37	24.65	15.99	25.02	13.87
S	30.07	85.71	22.81	7.62	23.69	30.69
V	86.18	110.20	176.03	21.96	225.61	20.36
Cr	2.19	0.83	58.70	0.06	5.14	0.19
Co	7.97	9.15	24.44	5.12	28.33	4.77
Ni	1.47	0.93	27.31	0.03	12.69	0.07
Cu	15.70	21.64	78.83	3.87	56.99	3.50
Zn	67.34	82.95	100.18	91.29	90.47	92.38
Ga	19.24	19.70	18.62	20.07	20.31	18.71
Ge	-	-	-	-	-	-
As	4.59	5.35	2.12	1.53	1.15	1.64
Se	0.02	0.02	0.01	0.00	0.04	0.01
Rb	64.60	85.48	32.96	71.55	38.51	67.95
Sr	340.60	289.68	545.60	393.55	612.27	352.25
Y	34.07	48.27	23.65	46.02	31.07	41.72
Zr	296.48	374.58	131.02	280.86	168.46	266.30
Nb	9.41	13.48	6.00	11.06	7.10	10.16
Mo	2.14	2.99	0.11	1.57	1.37	2.30
Cd	-	-	-	-	-	-

Appendix B. Raw sample analyses

Ag	0.02	0.00	0.08	0.03	0.03	0.03
Sn	1.86	3.05	1.36	2.11	1.50	2.00
Sb	0.30	0.33	0.67	0.11	0.06	0.11
Cs	-	-	-	-	-	-
Ba	632.32	782.20	258.67	752.74	473.23	767.27
La	27.21	36.91	18.51	35.92	24.30	32.47
Ce	57.89	80.61	39.97	77.22	53.38	70.64
Pr	6.88	9.74	4.90	9.43	6.69	8.57
Nd	26.76	38.43	20.20	37.69	27.82	34.50
Sm	6.00	8.65	4.80	8.58	6.58	7.80
Eu	1.45	1.90	1.34	2.22	1.77	2.01
Gd	5.58	8.08	4.61	8.02	6.24	7.24
Tb	0.89	1.24	0.70	1.23	0.93	1.12
Dy	5.37	7.43	4.10	7.23	5.34	6.51
Ho	1.15	1.57	0.83	1.53	1.11	1.38
Er	3.49	4.65	2.39	4.49	3.18	4.11
Tm	0.49	0.68	0.33	0.62	0.43	0.62
Yb	3.55	4.56	2.07	4.34	2.88	3.79
Lu	0.56	0.69	0.32	0.68	0.44	0.61
Hf	7.03	8.74	3.37	6.90	4.21	6.46
Ta	0.55	0.85	0.41	1.05	0.45	0.63
W	0.78	1.05	0.86	0.74	0.41	0.68
Tl	0.44	0.50	0.40	0.35	0.16	0.32
Pb	19.36	21.43	10.98	21.18	10.34	14.86
Bi	-	-	-	-	-	-
Th	6.49	11.15	5.62	8.74	6.03	8.94
U	2.18	2.83	1.73	2.75	1.63	2.71
Edifice	Lanín	Huillico			Caburgua-Huelemolle	
ID	16DCLan.011	16DCHui.003	16DCHui.004	16DCHui.005	16DCCaHu.002	16DCCaHu.003
NB						
Sample	<i>Lava flow</i>	<i>Fall deposit</i>	<i>Fall deposit</i>	<i>Fall deposit</i>	<i>Fall deposit</i>	<i>Fall deposit</i>
Rock type	<i>Trachyte</i>	<i>Basalt</i>	<i>Basalt</i>	<i>Basalt</i>	<i>Basaltic-andesite</i>	<i>Basaltic-andesite</i>
Long.	<i>-71.49</i>	<i>-71.55</i>	<i>-71.55</i>	<i>-71.55</i>	<i>-71.81</i>	<i>-71.81</i>
Lat.	<i>-39.59</i>	<i>-39.45</i>	<i>-39.45</i>	<i>-39.45</i>	<i>-39.33</i>	<i>-39.33</i>
Majors	<i>ICP-OES</i>	<i>ICP-OES</i>	<i>ICP-OES</i>	<i>ICP-OES</i>	<i>ICP-OES</i>	<i>ICP-OES</i>
Traces	<i>ICP-MS/MS</i>	<i>ICP-MS/MS</i>	<i>ICP-MS/MS</i>	<i>ICP-MS/MS</i>	<i>ICP-MS/MS</i>	<i>ICP-MS/MS</i>
SiO₂ (wt.%)	61.82	50.69	47.37	48.17	52.19	49.41
TiO₂	0.97	1.03	0.96	1.03	1.04	1.04
Al₂O₃	16.41	17.75	16.80	17.54	17.38	16.67
Fe₂O₃ (t)	6.58	9.22	9.05	9.09	9.36	8.82
MnO	0.20	0.15	0.14	0.14	0.15	0.15
MgO	1.20	6.92	7.35	6.67	4.58	3.81
CaO	3.48	9.39	8.56	8.94	7.48	7.04

Appendix B. Raw sample analyses

Na₂O	5.21	2.73	2.25	2.51	2.64	2.66
K₂O	3.20	0.92	0.84	0.87	0.76	0.76
P₂O₅	0.35	0.29	0.29	0.29	0.18	0.20
SO₃	-	-	-	-	-	-
LOI	0.00	0.69	7.08	4.30	5.31	9.60
Total	99.42	99.77	100.71	99.55	101.08	100.17
Li (ppm)	21.91	7.45	7.42	7.82	11.78	11.72
Sc	16.03	28.20	27.83	28.53	28.12	28.52
S	33.34	16.87	18.88	15.20	86.30	85.12
V	21.57	211.10	212.27	220.39	225.48	232.51
Cr	0.17	240.48	266.22	227.40	93.02	79.00
Co	5.10	33.95	37.60	32.76	25.12	24.71
Ni	0.05	99.92	124.80	91.26	40.40	33.75
Cu	6.24	67.37	67.73	65.77	76.78	86.93
Zn	93.28	72.42	76.54	70.93	85.95	100.56
Ga	20.68	17.34	17.38	17.86	18.30	18.90
Ge	-	-	-	-	-	-
As	1.82	1.41	1.54	1.58	6.31	6.83
Se	0.01	0.09	0.11	0.10	0.06	0.09
Rb	77.37	20.44	19.78	20.66	16.24	16.60
Sr	397.09	546.00	548.43	554.75	403.58	405.59
Y	47.65	20.80	20.54	21.14	22.63	24.13
Zr	290.20	117.11	118.33	119.77	93.23	98.27
Nb	11.09	5.72	5.73	5.81	2.18	2.30
Mo	2.52	0.84	0.84	0.82	0.69	0.75
Cd	-	-	-	-	-	-
Ag	0.03	0.03	0.03	0.03	0.03	0.03
Sn	2.63	1.01	1.06	0.96	0.98	1.11
Sb	0.12	0.08	0.08	0.08	0.39	0.39
Cs	-	-	-	-	-	-
Ba	706.94	277.53	252.46	283.74	234.86	255.65
La	36.47	14.93	14.68	15.39	8.49	9.01
Ce	78.57	33.07	32.52	33.24	20.87	22.30
Pr	9.59	4.13	4.05	4.25	2.81	3.02
Nd	38.42	17.29	16.97	17.78	12.61	13.48
Sm	8.74	4.02	4.03	4.25	3.52	3.79
Eu	2.24	1.27	1.24	1.29	1.08	1.14
Gd	8.17	4.01	3.96	4.12	3.88	4.09
Tb	1.26	0.61	0.60	0.63	0.63	0.67
Dy	7.34	3.56	3.53	3.70	3.80	4.05
Ho	1.56	0.76	0.73	0.77	0.83	0.88
Er	4.58	2.14	2.11	2.22	2.44	2.59
Tm	0.61	0.27	0.26	0.26	0.32	0.33
Yb	4.38	1.87	1.83	2.00	2.12	2.36

Appendix B. Raw sample analyses

Lu	0.68	0.30	0.29	0.31	0.35	0.37
Hf	7.04	2.82	2.81	2.89	2.53	2.59
Ta	0.69	0.38	0.40	0.34	0.13	0.15
W	0.73	0.28	0.48	0.29	0.43	0.52
Tl	0.47	0.15	0.15	0.14	0.14	0.14
Pb	16.88	6.60	6.47	6.77	7.69	7.73
Bi	-	-	-	-	-	-
Th	8.37	2.42	2.18	2.22	1.71	1.72
U	2.52	0.67	0.61	0.65	0.55	0.54
Edifice	Caburgua-Huelemolle					
ID	16DCCaHu.004	16DCCaHu.005	16DCCaHu.006	16DCCaHu.007	16DCCaHu.008	16DCCaHu.009
NB						
Sample	<i>Fall deposit</i>	<i>Fall deposit</i>	<i>Fall deposit</i>	<i>Fall deposit</i>	<i>Fall deposit</i>	<i>Fall deposit</i>
Rock type	<i>Basaltic-andesite</i>	<i>Basaltic-andesite</i>	<i>Basaltic-andesite</i>	<i>Basaltic-andesite</i>	<i>Basaltic-andesite</i>	<i>Basaltic-andesite</i>
Long.	-71.83	-71.88	-71.88	-71.88	-71.88	-71.88
Lat.	-39.32	-39.32	-39.32	-39.32	-39.32	-39.32
Majors	<i>ICP-OES</i>	<i>ICP-OES</i>	<i>ICP-OES</i>	<i>ICP-OES</i>	<i>ICP-OES</i>	<i>ICP-OES</i>
Traces	<i>ICP-MS/MS</i>	<i>ICP-MS/MS</i>	<i>ICP-MS/MS</i>	<i>ICP-MS/MS</i>	<i>ICP-MS/MS</i>	<i>ICP-MS/MS</i>
SiO₂ (wt.%)	51.76	53.38	51.38	50.71	52.82	52.66
TiO₂	1.14	1.09	1.16	1.20	1.11	1.17
Al₂O₃	17.86	17.58	18.17	18.06	17.92	17.94
Fe₂O₃ (t)	9.86	9.31	9.77	9.75	9.36	9.51
MnO	0.16	0.14	0.16	0.15	0.14	0.15
MgO	5.20	3.81	3.82	3.42	3.93	3.43
CaO	9.52	7.54	7.13	6.85	7.20	6.80
Na₂O	2.47	2.74	2.85	2.63	2.97	2.84
K₂O	0.65	0.76	0.77	0.75	0.87	0.79
P₂O₅	0.19	0.18	0.21	0.23	0.20	0.22
SO₃	-	-	-	-	-	-
LOI	1.38	3.06	4.21	4.82	3.30	4.04
Total	100.20	99.60	99.62	98.56	99.82	99.54
Li (ppm)	9.07	11.72	11.74	11.74	13.15	12.82
Sc	33.67	27.75	29.49	29.87	27.93	28.75
S	12.21	79.48	107.49	88.27	100.20	112.89
V	266.79	225.09	239.22	247.90	219.97	237.38
Cr	126.88	79.61	60.78	47.38	66.34	54.77
Co	28.55	22.58	23.43	22.66	21.15	21.62
Ni	43.06	33.11	27.86	22.59	29.26	23.81
Cu	114.50	66.85	89.58	97.79	82.36	86.75
Zn	80.87	82.98	133.31	80.81	82.81	85.17
Ga	18.39	18.08	19.43	19.64	18.34	18.73
Ge	-	-	-	-	-	-
As	4.61	6.13	7.94	8.29	7.38	7.44

Appendix B. Raw sample analyses

Se	0.07	0.12	0.09	0.10	0.10	0.13
Rb	12.42	16.92	16.61	16.51	19.06	18.45
Sr	440.43	407.76	394.65	386.32	396.36	391.21
Y	21.97	21.94	25.46	25.87	23.94	24.98
Zr	87.06	94.10	104.47	106.54	103.16	108.04
Nb	1.80	2.24	2.50	2.53	2.51	2.61
Mo	0.69	0.81	1.04	1.01	0.95	1.02
Cd	-	-	-	-	-	-
Ag	0.04	0.04	0.04	0.04	0.04	0.04
Sn	0.86	1.01	1.15	1.15	1.16	1.20
Sb	0.32	0.38	0.41	0.41	0.43	0.44
Cs	-	-	-	-	-	-
Ba	172.32	212.67	235.87	213.54	241.73	230.95
La	7.08	8.33	10.25	9.69	9.30	10.27
Ce	18.02	21.35	26.97	24.20	23.27	25.89
Pr	2.49	2.83	3.39	3.27	3.13	3.40
Nd	11.51	12.82	15.10	14.72	13.99	15.21
Sm	3.34	3.57	4.19	4.14	3.97	4.22
Eu	1.07	1.06	1.21	1.24	1.13	1.17
Gd	3.71	3.82	4.50	4.52	4.21	4.43
Tb	0.60	0.63	0.74	0.73	0.70	0.73
Dy	3.71	3.79	4.37	4.36	4.11	4.32
Ho	0.80	0.82	0.95	0.96	0.89	0.94
Er	2.34	2.38	2.76	2.85	2.64	2.76
Tm	0.30	0.30	0.41	0.36	0.34	0.37
Yb	2.06	2.14	2.49	2.56	2.40	2.45
Lu	0.33	0.34	0.40	0.41	0.38	0.39
Hf	2.36	2.47	2.77	2.85	2.76	2.85
Ta	0.13	0.16	0.26	0.31	0.23	0.27
W	0.37	0.45	0.56	0.53	0.47	0.54
Tl	0.06	0.14	0.18	0.16	0.14	0.14
Pb	6.38	7.87	8.42	9.04	8.51	8.57
Bi	-	-	-	-	-	-
Th	1.02	1.69	1.90	4.29	2.39	2.05
U	0.36	0.59	0.62	0.55	0.60	0.60

Appendix B. Raw sample analyses

Table B.1. continued

Edifice		Caburgua-Huelemolle				
ID	16DCCaHu.010	16DCCaHu.011	16DCCaHu.014	16DCCaHu.015	16DCCaHu.016	16DCCaHu.017
NB						
Sample	<i>Fall deposit</i>	<i>Fall deposit</i>	<i>Fall deposit</i>	<i>Fall deposit</i>	<i>Fall deposit</i>	<i>Fall deposit</i>
Rock type	<i>Basaltic-andesite</i>	<i>Basaltic-andesite</i>	<i>Basalt</i>	<i>Basalt</i>	<i>Basalt</i>	<i>Basalt</i>
Long.	-71.88	-71.88	-71.82	-71.82	-71.81	-71.81
Lat.	-39.32	-39.32	-39.19	-39.19	-39.21	-39.21
Majors	<i>ICP-OES</i>	<i>ICP-OES</i>	<i>ICP-OES</i>	<i>ICP-OES</i>	<i>ICP-OES</i>	<i>ICP-OES</i>
Traces	<i>ICP-MS/MS</i>	<i>ICP-MS/MS</i>	<i>ICP-MS/MS</i>	<i>ICP-MS/MS</i>	<i>ICP-MS/MS</i>	<i>ICP-MS/MS</i>
SiO₂ (wt.%)	48.42	50.77	49.57	47.82	45.60	45.15
TiO₂	1.11	1.12	1.17	1.16	1.16	1.06
Al₂O₃	16.78	17.00	17.95	18.49	18.54	17.22
Fe₂O₃ (t)	9.04	9.31	9.62	9.78	10.82	10.33
MnO	0.14	0.14	0.15	0.15	0.17	0.17
MgO	3.08	3.30	6.32	5.84	8.65	9.18
CaO	6.34	6.50	8.40	7.54	7.12	7.60
Na₂O	2.76	2.86	3.02	2.67	2.65	2.77
K₂O	0.80	0.83	0.74	0.60	0.44	0.52
P₂O₅	0.21	0.20	0.31	0.26	0.26	0.23
SO₃	-	-	-	-	-	-
LOI	12.70	8.16	3.07	6.65	4.82	6.80
Total	101.37	100.19	100.33	100.96	100.23	101.02
Li (ppm)	13.23	13.52	8.23	8.18	4.56	5.73
Sc	27.86	27.80	23.60	25.22	20.95	24.91
S	159.06	88.81	8.65	8.93	5.76	8.14
V	236.24	233.58	197.46	176.66	151.15	198.25
Cr	37.56	47.84	146.76	136.01	268.89	356.51
Co	19.80	20.29	31.10	31.30	34.19	42.65
Ni	17.27	21.78	72.68	68.48	157.21	204.95
Cu	85.48	83.69	73.72	84.10	59.25	72.33
Zn	337.18	83.26	71.51	73.79	54.35	77.59
Ga	18.06	18.35	17.34	18.04	13.99	16.67
Ge	-	-	-	-	-	-
As	6.98	8.13	0.82	0.76	0.65	0.71
Se	0.13	0.11	0.05	0.05	0.04	0.05
Rb	18.42	18.88	11.13	10.39	4.91	6.64
Sr	380.78	384.36	798.91	799.23	627.45	758.65
Y	23.66	23.89	19.88	20.61	16.77	18.61
Zr	108.95	111.48	92.77	93.87	65.37	71.07
Nb	2.48	2.54	3.48	3.52	2.27	2.14
Mo	0.85	0.88	0.58	0.46	0.25	0.33

Appendix B. Raw sample analyses

Cd	-	-	-	-	-	-
Ag	0.04	0.04	0.04	0.04	0.02	0.04
Sn	1.16	1.14	0.87	1.00	0.67	0.79
Sb	0.48	0.46	0.04	0.04	0.03	0.04
Cs	-	-	-	-	-	-
Ba	230.78	225.64	241.56	247.76	195.43	199.06
La	9.20	9.33	14.11	14.52	9.98	10.56
Ce	24.46	23.77	32.09	32.30	23.46	25.26
Pr	3.19	3.19	4.20	4.30	3.14	3.39
Nd	14.41	14.42	18.06	18.64	13.96	15.28
Sm	4.08	4.09	4.43	4.54	3.33	3.70
Eu	1.15	1.18	1.32	1.34	1.08	1.20
Gd	4.31	4.29	4.15	4.28	3.22	3.60
Tb	0.71	0.72	0.62	0.63	0.49	0.55
Dy	4.21	4.25	3.48	3.55	2.83	3.23
Ho	0.92	0.92	0.73	0.75	0.58	0.67
Er	2.70	2.67	2.09	2.13	1.64	1.88
Tm	0.35	0.33	0.25	0.25	0.25	0.25
Yb	2.47	2.43	1.77	1.80	1.51	1.78
Lu	0.39	0.39	0.29	0.30	0.24	0.27
Hf	2.95	2.99	2.25	2.29	1.72	1.92
Ta	0.14	0.14	0.32	0.18	0.13	0.11
W	0.46	0.49	0.21	0.11	0.12	0.12
Tl	0.14	0.14	0.09	0.12	0.09	0.07
Pb	8.77	8.81	6.77	6.73	5.24	5.91
Bi	-	-	-	-	-	-
Th	1.91	4.60	2.26	2.09	2.39	2.18
U	0.55	0.66	0.65	0.59	0.65	0.64
Edifice	Caburgua-Huelemolle					
ID	16DCCaHu.018	16DCCaHu.020	16DCCaHu.021	16DCCaHu.022	16DCCaHu.023	16DCCaHu.024
NB						
Sample	<i>Fall deposit</i>	<i>Fall deposit</i>	<i>Fall deposit</i>	<i>Fall deposit</i>	<i>Fall deposit</i>	<i>Fall deposit</i>
Rock type	<i>Basalt</i>	<i>Basalt</i>	<i>Basalt</i>	<i>Basalt</i>	<i>Basalt</i>	<i>Basalt</i>
Long.	<i>-71.81</i>	<i>-71.73</i>	<i>-71.73</i>	<i>-71.73</i>	<i>-71.73</i>	<i>-71.73</i>
Lat.	<i>-39.21</i>	<i>-39.22</i>	<i>-39.22</i>	<i>-39.22</i>	<i>-39.22</i>	<i>-39.22</i>
Majors	<i>ICP-OES</i>	<i>ICP-OES</i>	<i>ICP-OES</i>	<i>ICP-OES</i>	<i>ICP-OES</i>	<i>ICP-OES</i>
Traces	<i>ICP-MS/MS</i>	<i>ICP-MS/MS</i>	<i>ICP-MS/MS</i>	<i>ICP-MS/MS</i>	<i>ICP-MS/MS</i>	<i>ICP-MS/MS</i>
SiO₂ (wt.%)	48.47	45.86	45.10	44.51	44.70	43.79
TiO₂	1.08	0.93	1.07	1.14	1.12	1.04
Al₂O₃	19.20	16.93	18.86	19.64	20.26	18.89
Fe₂O₃ (t)	10.46	9.93	10.37	10.49	10.38	9.91
MnO	0.16	0.15	0.16	0.16	0.15	0.15
MgO	7.52	8.64	6.92	7.18	6.99	6.42
CaO	8.62	8.00	7.48	7.41	7.68	8.59

Appendix B. Raw sample analyses

Na₂O	2.63	2.32	2.52	2.48	2.28	2.26
K₂O	0.49	0.44	0.48	0.47	0.39	0.41
P₂O₅	0.22	0.22	0.28	0.30	0.29	0.31
SO₃	-	-	-	-	-	-
LOI	1.95	6.57	6.93	6.71	6.58	9.20
Total	100.79	99.99	100.17	100.47	100.83	100.95
Li (ppm)	5.88	5.19	6.42	6.24	5.62	5.85
Sc	24.19	23.26	23.17	24.58	26.44	30.69
S	11.92	9.95	8.64	9.03	14.81	24.55
V	205.89	178.48	184.59	188.34	192.64	201.44
Cr	228.18	428.92	256.86	258.98	284.32	134.69
Co	38.00	36.62	36.20	35.57	36.48	34.77
Ni	139.61	159.52	127.51	119.72	121.18	52.78
Cu	78.83	71.30	76.40	80.16	76.07	85.55
Zn	89.72	65.20	75.42	66.50	91.57	136.18
Ga	17.18	14.07	17.53	17.94	18.40	18.39
Ge	-	-	-	-	-	-
As	0.76	0.43	0.86	0.76	0.91	0.94
Se	0.04	0.08	0.06	0.09	0.07	0.03
Rb	6.14	5.16	6.58	6.13	5.15	5.55
Sr	854.03	667.73	848.14	802.35	738.46	683.42
Y	18.92	15.60	19.73	20.66	20.57	20.88
Zr	63.90	58.93	81.91	89.48	88.46	98.39
Nb	1.61	1.57	2.85	3.30	3.02	3.65
Mo	0.31	0.29	0.36	0.36	0.32	0.36
Cd	-	0.04	-	-	-	-
Ag	0.03	0.03	0.04	0.04	0.11	0.05
Sn	0.79	0.69	0.86	0.91	0.90	0.89
Sb	0.04	0.04	0.04	0.04	0.04	0.04
Cs	-	0.40	-	-	-	-
Ba	221.85	198.73	242.67	212.77	172.81	208.56
La	9.72	8.70	13.18	13.88	13.43	13.97
Ce	23.41	21.12	30.08	31.08	30.21	31.48
Pr	3.23	2.85	4.00	4.12	4.03	4.15
Nd	14.96	12.71	17.90	18.42	17.97	18.46
Sm	3.71	3.09	4.22	4.36	4.27	4.32
Eu	1.21	1.03	1.35	1.37	1.35	1.31
Gd	3.57	2.94	3.90	4.11	4.02	4.11
Tb	0.56	0.44	0.60	0.63	0.62	0.63
Dy	3.26	2.60	3.42	3.59	3.51	3.62
Ho	0.68	0.54	0.70	0.73	0.73	0.75
Er	1.93	1.54	2.00	2.10	2.09	2.15
Tm	0.26		0.22	0.26	0.22	0.27
Yb	1.82	1.40	1.86	1.94	1.91	1.92

Appendix B. Raw sample analyses

Lu	0.27	0.21	0.28	0.30	0.29	0.30
Hf	1.82	1.54	2.18	2.29	2.24	2.38
Ta	0.10	0.09	0.17	0.53	0.16	0.18
W	0.11	0.07	0.24	0.13	0.13	0.11
Tl	0.07	0.07	0.11	0.10	0.12	0.08
Pb	6.36	5.71	7.16	7.33	7.04	6.39
Bi	-	-	-	-	-	-
Th	2.46	2.15	4.41	2.69	2.26	1.83
U	0.73	0.59	0.64	0.67	0.59	0.53
Edifice	Caburgua-Huelemolle			Yate		
ID	16DCCaHu.025	16DCCaHu.026	16DCCaHu.027	Ya. 02-3A	Ya. 23-8B	Ya. 23-10A
NB						
Sample	<i>Fall deposit</i>	<i>Fall deposit</i>	<i>Fall deposit</i>	<i>Lava flow</i>	<i>Lava flow</i>	<i>Lava flow</i>
Rock type	<i>Basalt</i>	<i>Basalt</i>	<i>Basalt</i>	<i>Basaltic-andesite</i>	<i>Basaltic-andesite</i>	<i>Basalt</i>
Long.	<i>-71.73</i>	<i>-71.73</i>	<i>-71.73</i>	<i>-72.40</i>	<i>-72.44</i>	<i>-72.44</i>
Lat.	<i>-39.22</i>	<i>-39.22</i>	<i>-39.22</i>	<i>-41.70</i>	<i>-41.71</i>	<i>-41.72</i>
Majors	<i>ICP-OES</i>	<i>ICP-OES</i>	<i>ICP-OES</i>	<i>XRF</i>	<i>XRF</i>	<i>XRF</i>
Traces	<i>ICP-MS/MS</i>	<i>ICP-MS/MS</i>	<i>ICP-MS/MS</i>	<i>ICP-MS/MS</i>	<i>ICP-MS/MS</i>	<i>ICP-MS/MS</i>
SiO₂ (wt.%)	44.53	45.04	46.35	55.30	52.34	51.14
TiO₂	1.03	1.05	1.07	0.93	1.17	0.90
Al₂O₃	18.49	18.87	18.86	17.49	19.66	17.85
Fe₂O₃ (t)	10.39	10.48	10.87	8.20	9.22	9.21
MnO	0.15	0.15	0.16	0.14	0.16	0.16
MgO	7.50	7.25	8.12	4.92	3.33	7.22
CaO	8.25	7.73	8.20	8.03	9.73	9.15
Na₂O	2.25	2.50	2.29	3.27	3.28	2.59
K₂O	0.43	0.48	0.47	1.17	0.66	0.55
P₂O₅	0.34	0.32	0.33	0.20	0.18	0.19
SO₃	-	-	-	-	-	-
LOI	7.64	6.78	4.73	0.04	-0.21	0.63
Total	101.00	100.65	101.44	99.69	99.51	99.59
Li (ppm)	6.39	6.59	6.61	12.60	9.84	10.55
Sc	29.30	28.87	28.51	28.05	33.52	29.94
S	7.14	16.02	13.76	28.10	6.21	32.09
V	204.95	202.96	197.37	206.99	295.09	218.26
Cr	200.19	263.19	250.09	78.02	10.83	214.36
Co	38.61	37.64	39.52	24.59	20.63	33.72
Ni	88.86	90.20	107.69	38.23	6.61	107.68
Cu	82.33	72.90	75.12	39.19	55.57	63.02
Zn	74.40	85.68	86.40	73.45	83.26	75.26
Ga	17.97	17.90	17.57	18.06	20.34	17.59
Ge	-	-	-	-	-	-
As	1.04	1.05	1.00	2.48	2.17	1.27

Appendix B. Raw sample analyses

Se	0.04	0.05	0.06	0.01	0.03	0.02
Rb	5.89	7.26	7.33	32.20	17.05	10.24
Sr	669.19	633.42	620.27	401.01	448.65	443.93
Y	20.74	20.82	20.24	25.95	26.65	21.73
Zr	99.17	101.14	95.50	139.19	92.23	108.29
Nb	3.80	4.08	3.62	4.58	3.51	3.77
Mo	0.37	0.51	0.39	1.05	0.73	0.50
Cd	-	-	-	-	-	-
Ag	0.04	0.05	0.04	0.01	0.03	0.03
Sn	0.85	5.58	0.85	1.24	1.38	0.99
Sb	0.04	0.13	0.05	0.17	0.11	0.06
Cs	-	-	-	-	-	-
Ba	183.14	206.90	202.46	285.80	171.90	248.94
La	14.15	14.27	13.61	14.68	8.90	12.63
Ce	31.95	31.99	30.51	32.87	21.74	28.32
Pr	4.22	4.22	4.01	4.20	2.95	3.63
Nd	18.45	18.38	17.66	18.13	13.94	15.77
Sm	4.35	4.31	4.11	4.45	3.94	3.78
Eu	1.32	1.31	1.26	1.22	1.24	1.14
Gd	4.08	4.04	4.00	4.56	4.37	3.81
Tb	0.64	0.64	0.61	0.76	0.74	0.64
Dy	3.59	3.59	3.47	4.35	4.42	3.67
Ho	0.74	0.75	0.73	0.93	0.96	0.78
Er	2.11	2.11	2.04	2.70	2.76	2.24
Tm	0.24	0.30	0.28	0.32	0.30	0.28
Yb	1.99	2.06	1.83	2.58	2.66	2.16
Lu	0.30	0.30	0.29	0.39	0.39	0.31
Hf	2.40	2.45	2.31	3.42	2.36	2.61
Ta	0.19	0.36	0.19	0.25	0.21	0.21
W	0.12	1.37	0.14	0.55	0.31	0.25
Tl	0.06	0.07	0.07	0.13	0.10	0.05
Pb	6.54	6.80	6.59	7.25	4.53	5.83
Bi	-	-	-	-	-	-
Th	1.56	1.97	1.88	2.86	1.49	1.85
U	0.44	0.60	0.57	0.77	0.30	0.39

Appendix B. Raw sample analyses

Table B.1. continued

Edifice	Yate					
	Ya. 23-12B	Ya. 26-2A	Ya. 26-3A	Ya. 26-4A	Ya. 26-6A	Ya. 26-7A
NB						
Sample	<i>Lava flow</i>	<i>Lava flow</i>	<i>Lava flow</i>	<i>Lava flow</i>	<i>Lava flow</i>	<i>Lava flow</i>
Rock type	<i>Basaltic-andesite</i>	<i>Andesite</i>	<i>Andesite</i>	<i>Basaltic-andesite</i>	<i>Basaltic-andesite</i>	<i>Basaltic-andesite</i>
Long.	-72.46	-72.35	-72.35	-72.35	-72.36	-72.37
Lat.	-41.73	-41.82	-41.82	-41.82	-41.87	-41.88
Majors	<i>XRF</i>	<i>XRF</i>	<i>XRF</i>	<i>XRF</i>	<i>XRF</i>	<i>XRF</i>
Traces	<i>ICP-MS/MS</i>	<i>ICP-MS/MS</i>	<i>ICP-MS/MS</i>	<i>ICP-MS/MS</i>	<i>ICP-MS/MS</i>	<i>ICP-MS/MS</i>
SiO₂ (wt.%)	52.32	62.16	61.74	54.78	56.22	56.17
TiO₂	1.10	0.97	0.96	1.06	0.78	0.76
Al₂O₃	20.08	15.84	15.87	15.55	16.21	16.04
Fe₂O₃ (t)	8.87	6.43	6.42	8.35	7.65	7.59
MnO	0.16	0.12	0.11	0.15	0.13	0.14
MgO	3.27	2.22	2.21	5.72	5.67	5.70
CaO	9.45	5.10	5.05	7.97	7.98	8.11
Na₂O	3.24	3.82	3.81	3.08	2.95	2.85
K₂O	0.70	2.37	2.36	2.52	1.54	1.51
P₂O₅	0.18	0.25	0.25	0.39	0.17	0.16
SO₃	-	-	-	-	-	-
LOI	0.13	1.08	-0.15	0.06	0.14	-0.04
Total	99.50	100.36	98.63	99.62	99.43	98.98
Li (ppm)	10.25	22.81	17.31	14.42	14.50	14.60
Sc	28.02	20.70	20.35	28.91	27.88	28.65
S	5.18	61.30	44.99	26.67	19.71	9.92
V	258.72	150.47	149.42	227.21	199.92	202.64
Cr	8.18	15.87	16.30	178.84	198.01	189.24
Co	20.12	12.83	12.58	24.95	24.59	24.94
Ni	7.60	7.90	7.89	73.90	44.52	43.59
Cu	49.13	25.96	19.57	67.81	42.97	62.28
Zn	82.39	68.80	68.95	76.08	62.00	63.87
Ga	20.22	18.49	18.27	17.71	16.74	16.72
Ge	-	-	-	-	-	-
As	1.92	5.73	5.75	3.28	2.72	2.90
Se	0.02	0.02	0.02	0.04	0.02	0.02
Rb	17.85	80.48	80.21	84.92	48.90	48.36
Sr	459.10	346.24	348.11	661.49	509.42	521.05
Y	25.83	38.25	36.51	34.96	23.65	24.00
Zr	90.97	238.13	237.54	199.39	115.29	120.98
Nb	3.43	7.14	7.11	5.08	3.29	3.23
Mo	0.72	2.34	2.12	1.84	1.30	1.34

Appendix B. Raw sample analyses

Cd	-	-	-	-	-	-
Ag	0.03	0.03	0.03	0.03	0.03	0.03
Sn	1.24	1.87	1.86	1.51	1.59	1.15
Sb	0.11	0.41	0.42	0.20	0.18	0.18
Cs	-	-	-	-	-	-
Ba	210.33	515.37	479.99	402.54	374.32	357.98
La	9.08	23.94	23.29	24.68	17.57	18.30
Ce	21.97	52.28	52.20	57.42	36.94	37.56
Pr	3.00	6.58	6.46	7.82	4.53	4.61
Nd	13.97	27.58	27.25	35.46	18.99	19.25
Sm	3.86	6.58	6.47	9.00	4.45	4.44
Eu	1.25	1.48	1.48	2.31	1.16	1.18
Gd	4.25	6.40	6.35	8.22	4.23	4.24
Tb	0.73	1.07	1.06	1.19	0.69	0.69
Dy	4.25	6.08	6.02	6.21	3.94	3.87
Ho	0.91	1.30	1.29	1.21	0.84	0.83
Er	2.64	3.76	3.72	3.31	2.39	2.40
Tm	0.32	0.45	0.42	0.42	0.28	0.31
Yb	2.62	3.88	3.65	3.10	2.34	2.37
Lu	0.38	0.54	0.55	0.44	0.35	0.35
Hf	2.37	5.80	5.90	4.70	2.99	3.15
Ta	0.18	0.41	0.44	0.30	0.20	0.23
W	0.33	1.27	1.32	0.94	0.85	0.72
Tl	0.11	0.44	0.42	0.47	0.21	0.34
Pb	4.62	13.20	12.35	8.96	10.18	10.62
Bi	-	-	-	-	-	-
Th	2.03	8.44	5.34	4.63	6.71	6.58
U	0.43	1.71	1.56	1.31	1.47	1.60
Edifice	Yate	Apagado				
ID	Ya. 26-5AY	Ap. 20-4A	Ap. 20-5A	Ap. 21-2A	Ap. 21-3A	Ap. 21-4A
NB						
Sample	<i>Fall deposit</i>	<i>Lava flow</i>				
Rock type	<i>Dacite</i>	<i>Basalt</i>	<i>Basalt</i>	<i>Basalt</i>	<i>Basalt</i>	<i>Basalt</i>
Long.	<i>-72.35</i>	<i>-72.59</i>	<i>-72.61</i>	<i>-72.59</i>	<i>-72.59</i>	<i>-72.59</i>
Lat.	<i>-41.85</i>	<i>-41.88</i>	<i>-41.88</i>	<i>-41.88</i>	<i>-41.88</i>	<i>-41.88</i>
Majors	<i>XRF</i>	<i>XRF</i>	<i>XRF</i>	<i>XRF</i>	<i>XRF</i>	<i>XRF</i>
Traces	<i>ICP-MS/MS</i>	<i>ICP-MS/MS</i>	<i>ICP-MS/MS</i>	<i>ICP-MS/MS</i>	<i>ICP-MS/MS</i>	<i>ICP-MS/MS</i>
SiO₂ (wt.%)	65.54	51.35	50.12	51.25	50.65	49.20
TiO₂	0.60	0.96	1.01	0.95	0.96	0.95
Al₂O₃	14.95	18.18	18.72	17.88	17.94	17.43
Fe₂O₃ (t)	4.44	9.46	9.59	9.46	9.54	9.38
MnO	0.09	0.16	0.16	0.16	0.16	0.16
MgO	1.54	6.74	6.47	7.09	7.25	7.62
CaO	3.68	9.11	9.87	9.71	9.73	9.51

Appendix B. Raw sample analyses

Na₂O	4.18	2.70	2.78	2.79	2.61	2.66
K₂O	2.66	0.54	0.46	0.51	0.45	0.42
P₂O₅	0.07	0.20	0.23	0.18	0.17	0.20
SO₃	-	-	-	-	-	-
LOI	1.42	0.24	0.23	-0.27	-0.01	-0.03
Total	99.16	99.64	99.63	99.70	99.45	97.50
Li (ppm)	26.36	8.71	7.70	8.93	9.06	7.50
Sc	13.74	29.15	30.96	32.18	32.21	30.26
S	26.72	16.07	7.86	3.17	5.90	3.22
V	76.03	237.32	241.19	233.71	238.59	229.71
Cr	12.91	156.51	147.60	196.35	198.10	261.95
Co	7.36	32.20	32.31	32.66	32.83	36.40
Ni	3.17	76.68	66.57	80.61	83.08	114.86
Cu	8.72	60.02	66.77	67.78	65.52	57.91
Zn	53.38	78.93	80.95	76.62	75.25	78.62
Ga	16.70	17.48	18.01	17.72	17.51	17.31
Ge	-	-	-	-	-	-
As	6.29	0.87	1.30	1.02	1.26	0.76
Se	0.01	0.01	0.05	0.01	0.03	0.01
Rb	96.22	7.88	7.68	8.53	8.47	3.46
Sr	280.86	449.29	494.43	462.46	461.11	487.70
Y	28.75	20.29	22.09	20.84	20.75	20.68
Zr	226.35	82.92	93.19	78.95	80.51	85.89
Nb	6.35	3.08	3.85	2.97	2.95	8.17
Mo	2.58	0.46	0.56	0.45	0.45	0.44
Cd	-	-	-	-	-	-
Ag	0.03	0.03	0.03	0.03	0.03	0.02
Sn	12.19	0.76	0.93	0.73	0.83	0.93
Sb	0.41	0.05	0.07	0.05	0.06	0.04
Cs	-	-	-	-	-	-
Ba	607.58	175.01	192.06	164.48	128.54	168.62
La	21.69	9.21	12.59	8.27	8.21	11.34
Ce	44.12	22.83	28.39	20.09	20.22	25.87
Pr	5.17	3.06	3.70	2.72	2.72	3.39
Nd	20.37	13.54	15.96	12.68	12.62	14.60
Sm	4.60	3.53	3.91	3.35	3.38	3.64
Eu	1.03	1.13	1.27	1.08	1.09	1.16
Gd	4.29	3.69	4.10	3.52	3.58	3.75
Tb	0.74	0.58	0.64	0.60	0.59	0.59
Dy	4.38	3.51	3.83	3.42	3.45	3.56
Ho	0.96	0.73	0.80	0.74	0.73	0.74
Er	2.85	2.09	2.27	2.10	2.09	2.12
Tm	0.41	0.26	0.23	0.25	0.21	0.21
Yb	3.06	1.82	1.98	2.03	1.99	1.89

Appendix B. Raw sample analyses

Lu	0.46	0.29	0.31	0.29	0.29	0.30
Hf	5.61	2.05	2.26	1.94	1.95	2.11
Ta	0.41	0.16	0.21	0.20	0.17	1.28
W	1.41	0.13	0.20	0.15	0.18	3.22
Tl	0.61	0.03	0.08	0.04	0.06	0.01
Pb	14.97	3.67	4.93	4.14	4.73	4.81
Bi	-	-	-	-	-	-
Th	7.26	1.04	1.19	0.97	0.77	1.40
U	2.09	0.27	0.33	0.28	0.22	0.28
Edifice	Apagado			Hornopirén		
ID	Ap. 21-6B	Ap. 21-9B	Ap. 21-9C	Ho. 05-3B	Ho. 15-5A	Ho. 19-1A
NB						
Sample	<i>Lava flow</i>	<i>Lava flow</i>	<i>Lava flow</i>	<i>Fall deposit</i>	<i>Lava flow</i>	<i>Lava flow</i>
Rock type	<i>Basaltic-andesite</i>	<i>Basaltic-andesite</i>	<i>Basaltic-andesite</i>	<i>Basaltic-andesite</i>	<i>Basaltic-andesite</i>	<i>Basaltic-andesite</i>
Long.	-72.62	-72.64	-72.64	-72.43	-72.47	-72.43
Lat.	-41.87	-41.85	-41.85	-41.88	-41.89	-41.86
Majors	XRF	XRF	XRF	XRF	XRF	XRF
Traces	ICP-MS/MS	ICP-MS/MS	ICP-MS/MS	ICP-MS/MS	ICP-MS/MS	ICP-MS/MS
SiO₂ (wt.%)	54.61	52.32	54.50	52.96	53.46	53.13
TiO₂	1.19	0.96	1.02	0.96	0.95	0.92
Al₂O₃	17.39	19.83	18.36	17.29	17.38	17.51
Fe₂O₃ (t)	9.01	8.54	8.58	8.86	8.88	8.82
MnO	0.15	0.13	0.15	0.15	0.15	0.15
MgO	3.97	3.86	4.28	4.79	5.44	5.37
CaO	8.51	9.90	8.21	8.65	8.77	8.87
Na₂O	3.17	3.01	3.57	2.95	2.90	2.90
K₂O	1.02	0.36	0.67	0.95	0.95	0.91
P₂O₅	0.24	0.13	0.22	0.28	0.30	0.28
SO₃	-	-	-	-	-	-
LOI	0.47	0.35	0.23	0.35	-0.09	-0.20
Total	99.73	99.38	99.80	98.19	99.09	98.66
Li (ppm)	14.61	11.49	10.84	10.23	10.72	10.97
Sc	30.87	32.66	26.56	30.94	27.46	28.18
S	14.69	4.58	8.85	14.81	16.52	3.55
V	232.56	249.60	201.85	220.49	211.64	210.45
Cr	48.94	40.55	21.12	74.30	96.01	91.40
Co	22.30	21.26	23.66	27.35	28.52	27.68
Ni	14.91	11.02	21.81	33.87	54.78	47.78
Cu	89.06	64.67	41.96	59.25	62.02	61.79
Zn	90.79	83.14	90.33	79.57	90.48	79.57
Ga	18.91	19.76	19.45	18.86	18.34	18.27
Ge	-	-	-	-	-	-
As	7.79	2.32	3.03	1.85	1.41	1.60

Appendix B. Raw sample analyses

Se	0.03	0.01	0.01	0.06	0.04	0.03
Rb	28.57	3.62	9.69	18.60	19.31	19.66
Sr	330.05	384.80	357.37	418.81	449.46	451.24
Y	32.48	20.93	25.79	26.94	25.85	25.57
Zr	143.21	62.57	102.97	167.17	142.82	139.99
Nb	5.83	3.10	4.61	8.70	5.65	5.37
Mo	1.30	0.52	0.82	0.78	0.84	0.80
Cd	-	-	-	-	-	-
Ag	0.04	0.04	0.03	0.02	0.02	0.03
Sn	1.54	0.72	1.02	3.88	1.17	1.13
Sb	0.38	0.13	0.17	0.08	0.07	0.07
Cs	-	-	-	-	-	-
Ba	224.94	126.77	170.57	276.90	310.03	294.07
La	12.24	6.50	9.32	18.58	18.62	17.70
Ce	29.55	13.18	22.52	45.23	41.72	39.34
Pr	3.97	2.14	3.13	5.26	5.25	4.97
Nd	18.02	10.33	14.35	22.38	21.71	21.15
Sm	5.01	2.92	3.95	5.20	4.99	4.90
Eu	1.31	1.00	1.26	1.40	1.38	1.34
Gd	5.49	3.28	4.39	5.06	4.92	4.70
Tb	0.90	0.56	0.72	0.82	0.74	0.76
Dy	5.49	3.32	4.35	4.66	4.37	4.30
Ho	1.15	0.71	0.90	0.97	0.90	0.90
Er	3.32	2.04	2.60	2.76	2.59	2.57
Tm	0.42	0.24	0.28	0.38	0.36	0.36
Yb	3.01	1.95	2.34	2.69	2.31	2.39
Lu	0.46	0.28	0.37	0.40	0.36	0.36
Hf	3.83	1.61	2.63	3.96	3.32	3.20
Ta	0.34	0.21	0.26	6.20	0.65	0.26
W	0.80	1.17	0.42	0.73	0.27	0.25
Tl	0.16	0.02	0.04	0.09	0.10	0.10
Pb	7.02	3.50	4.49	7.74	7.06	7.36
Bi	-	-	-	-	-	-
Th	2.58	0.65	0.92	2.98	1.96	1.74
U	0.63	0.17	0.25	0.48	0.46	0.43

Appendix B. Raw sample analyses

Table B.1. continued

Edifice	Hornopirén	Antuco				
ID	Ho. 30-2A	An27-1	An27-2	An27-3	An27-4	An27-5
NB		<i>Phase I</i>	<i>Phase I</i>	<i>Phase I</i>	<i>Phase I</i>	<i>Phase I</i>
Sample	<i>Lava flow</i>	<i>Lava flow</i>	<i>Lava flow</i>	<i>Lava flow</i>	<i>Lava flow</i>	<i>Lava flow</i>
Rock type	<i>Basaltic-andesite</i>	<i>Andesite</i>	<i>Basaltic-andesite</i>	<i>Basaltic-andesite</i>	<i>Trachy-andesite</i>	<i>Basaltic-andesite</i>
Long.	-72.46	-71.33	-71.33	-71.35	-71.35	-71.35
Lat.	-41.87	-37.45	-37.45	-37.45	-37.45	-37.44
Majors	<i>XRF</i>	<i>XRF</i>	<i>XRF</i>	<i>XRF</i>	<i>ICP-OES</i>	<i>XRF</i>
Traces	<i>ICP-MS/MS</i>	<i>ICP-MS/MS</i>	<i>ICP-MS/MS</i>	<i>ICP-MS/MS</i>	<i>ICP-MS/MS</i>	<i>ICP-MS/MS</i>
SiO₂ (wt.%)	53.05	62.54	53.00	56.50	58.20	53.41
TiO₂	0.93	0.80	1.01	1.16	1.06	1.18
Al₂O₃	17.56	17.45	18.89	17.14	16.39	18.56
Fe₂O₃ (t)	8.87	6.57	8.66	9.11	8.27	9.49
MnO	0.15	0.14	0.14	0.15	0.14	0.15
MgO	5.48	1.95	5.63	3.58	2.52	4.26
CaO	8.96	4.94	9.42	6.69	5.72	8.56
Na₂O	2.86	4.80	3.43	3.75	4.56	3.75
K₂O	0.89	1.96	0.79	1.51	1.82	0.88
P₂O₅	0.27	0.26	0.18	0.25	0.27	0.22
SO₃	-	-	-	-	-	-
LOI	-0.22	-0.12	-0.35	-0.23	0.39	-0.40
Total	98.80	101.41	101.14	99.84	99.34	100.47
Li (ppm)	10.96	23.75	8.98	19.54	25.35	12.83
Sc	28.47	12.16	26.75	22.77	18.51	26.00
S	7.15	11.29	3.55	4.42	45.36	15.46
V	210.89	73.16	217.87	190.58	166.99	237.27
Cr	95.94	4.11	110.47	29.71	2.39	40.73
Co	28.04	9.97	29.79	23.63	17.60	25.84
Ni	49.22	2.60	48.42	16.36	3.58	23.40
Cu	60.16	5.41	58.52	49.74	21.56	54.36
Zn	80.14	83.07	73.96	86.05	79.99	83.89
Ga	18.08	19.39	18.36	18.95	19.20	19.20
Ge		1.28	1.24	1.42	1.36	1.31
As	1.55	1.28	2.04	0.80	3.51	2.16
Se	0.03	0.01	0.02	0.01	0.02	0.02
Rb	19.73	64.28	19.19	48.60	57.65	21.40
Sr	448.32	437.18	597.86	400.83	445.57	523.05
Y	24.98	26.45	16.85	30.83	26.30	22.00
Zr	135.11	139.02	82.97	157.56	157.45	98.13
Nb	5.27	5.04	2.85	4.34	5.17	3.25
Mo	0.77	0.82	0.73	0.95	1.21	1.01

Appendix B. Raw sample analyses

Cd	-	-	-	-	-	-
Ag	0.03	0.04	0.04	0.01	0.04	0.04
Sn	1.09	1.68	1.14	1.74	1.72	0.96
Sb	0.07	0.25	0.16	0.18	0.32	0.19
Cs	-	1.81	0.81	1.55	3.52	1.18
Ba	280.41	458.09	228.28	338.51	413.04	249.30
La	17.26	19.64	10.21	16.10	17.92	11.60
Ce	37.88	42.69	24.07	36.70	40.14	26.30
Pr	4.79	5.28	3.06	4.90	5.03	3.53
Nd	20.38	21.93	13.66	21.70	21.38	15.86
Sm	4.78	5.02	3.33	5.35	4.96	3.94
Eu	1.31	1.35	1.07	1.39	1.40	1.27
Gd	4.63	4.78	3.21	5.41	4.76	4.02
Tb	0.74	0.77	0.51	0.88	0.78	0.65
Dy	4.25	4.43	2.92	5.21	4.49	3.79
Ho	0.89	0.94	0.62	1.12	0.95	0.81
Er	2.53	2.66	1.69	3.13	2.64	2.23
Tm	0.33	0.34	0.24	0.44	0.36	0.31
Yb	2.44	2.61	1.56	2.92	2.58	2.04
Lu	0.37	0.40	0.23	0.44	0.39	0.31
Hf	3.17	3.91	2.27	4.35	4.16	2.63
Ta	0.25	0.39	0.22	0.31	0.43	0.19
W	0.22	0.58	0.25	0.35	0.63	0.22
Tl	0.10	0.36	0.08	0.23	0.35	0.12
Pb	6.75	10.16	5.65	11.67	11.55	6.04
Bi	-	0.06	0.02	0.03	0.06	b.d.
Th	4.41	6.24	1.94	4.38	5.59	2.29
U	0.41	1.78	0.49	1.16	1.69	0.62
Edifice	Antuco					
ID	An27-8	An27-9	An27-11	An27-12	An28-3	An28-4
NB	<i>Phase I</i>	<i>Phase I</i>	<i>Phase I</i>	<i>Phase I</i>	<i>Phase I</i>	<i>Phase I</i>
Sample	<i>Lava flow</i>	<i>Lava flow</i>	<i>Lava flow</i>	<i>Lava flow</i>	<i>Lava flow</i>	<i>Lava flow</i>
Rock type	<i>Basaltic-andesite</i>	<i>Andesite</i>	<i>Basaltic-andesite</i>	<i>Basaltic-andesite</i>	<i>Andesite</i>	<i>Basaltic-andesite</i>
Long.	<i>-71.30</i>	<i>-71.30</i>	<i>-71.32</i>	<i>-71.35</i>	<i>-71.34</i>	<i>-71.34</i>
Lat.	<i>-37.41</i>	<i>-37.41</i>	<i>-37.38</i>	<i>-37.37</i>	<i>-37.40</i>	<i>-37.40</i>
Majors	<i>XRF</i>	<i>XRF</i>	<i>XRF</i>	<i>ICP-OES</i>	<i>XRF</i>	<i>XRF</i>
Traces	<i>ICP-MS/MS</i>	<i>ICP-MS/MS</i>	<i>ICP-MS/MS</i>	<i>ICP-MS/MS</i>	<i>ICP-MS/MS</i>	<i>ICP-MS/MS</i>
SiO₂ (wt.%)	53.30	60.02	53.35	54.07	60.92	52.66
TiO₂	0.85	0.93	1.05	1.45	1.01	1.07
Al₂O₃	18.15	17.50	19.15	17.40	16.84	20.13
Fe₂O₃ (t)	8.14	7.65	8.66	10.87	7.50	8.53
MnO	0.13	0.15	0.14	0.19	0.17	0.14
MgO	6.03	2.43	4.79	3.65	2.07	3.64

Appendix B. Raw sample analyses

CaO	8.78	5.67	8.89	7.84	4.98	9.43
Na₂O	3.19	4.55	3.66	3.57	5.15	3.66
K₂O	1.01	1.71	0.81	0.96	1.47	0.71
P₂O₅	0.15	0.23	0.20	0.26	0.37	0.19
SO₃	-	-	-	-	-	-
LOI	-0.30	-0.22	-0.40	-0.02	-0.27	-0.34
Total	99.73	100.84	100.70	100.23	100.46	100.17
Li (ppm)	13.30	21.60	12.35	10.13	15.98	10.92
Sc	23.81	18.80	24.62	31.70	16.98	24.35
S	4.85	8.46	3.23	5.43	6.27	7.75
V	187.22	130.34	217.42	289.15	84.58	227.46
Cr	126.47	6.39	49.32	25.42	2.16	39.80
Co	31.92	15.25	27.62	24.80	11.44	22.72
Ni	75.24	4.81	37.89	11.34	3.28	20.72
Cu	43.96	24.97	62.67	61.38	48.60	67.43
Zn	72.85	84.39	79.08	96.99	98.79	76.19
Ga	17.09	19.54	18.69	19.95	20.04	19.33
Ge	1.18	1.34	1.26	1.50	1.45	1.27
As	1.00	1.06	2.07	2.59	4.83	2.10
Se	0.01	0.01	0.02	0.04	0.02	0.04
Rb	37.92	47.30	19.85	19.47	33.66	15.55
Sr	496.67	390.27	521.80	472.15	408.01	541.67
Y	16.16	29.54	20.63	26.95	33.74	20.06
Zr	82.54	150.34	94.72	114.44	175.52	86.10
Nb	2.68	4.63	3.05	3.43	5.28	2.69
Mo	0.77	0.96	0.77	0.68	1.51	0.79
Cd	-	-	-	-	-	-
Ag	0.28	0.04	0.03	0.03	0.05	0.04
Sn	0.86	1.55	1.18	1.42	1.74	0.88
Sb	0.15	0.18	0.24	0.22	0.38	0.19
Cs	0.81	1.27	0.81	1.03	1.36	0.87
Ba	251.13	406.04	225.77	252.10	397.96	204.71
La	10.68	15.87	9.78	11.22	17.95	8.81
Ce	23.72	35.50	23.70	27.68	41.67	21.43
Pr	2.95	4.53	3.14	3.77	5.50	2.89
Nd	12.75	19.65	14.26	17.51	24.43	13.32
Sm	3.06	4.82	3.59	4.57	5.98	3.47
Eu	0.97	1.41	1.14	1.44	1.69	1.15
Gd	3.05	4.93	3.63	4.73	5.91	3.58
Tb	0.48	0.82	0.59	0.78	0.96	0.59
Dy	2.82	4.86	3.50	4.60	5.70	3.52
Ho	0.60	1.05	0.75	0.99	1.23	0.74
Er	1.64	3.00	2.09	2.76	3.46	2.06
Tm	0.20	0.43	0.30	0.36	0.52	0.30

Appendix B. Raw sample analyses

Yb	1.50	3.00	1.97	2.70	3.49	1.95
Lu	0.23	0.46	0.30	0.40	0.52	0.29
Hf	2.30	3.98	2.53	3.08	4.61	2.37
Ta	0.23	0.41	0.19	0.22	0.36	0.20
W	0.27	0.41	0.25	0.25	0.44	0.19
Tl	0.14	0.26	0.09	0.09	0.19	0.08
Pb	7.04	14.24	5.79	6.74	11.22	5.34
Bi	0.02	0.02	0.02	0.03	0.04	0.00
Th	4.11	4.45	1.93	1.69	3.05	1.36
U	1.01	1.34	0.52	0.50	0.93	0.40
Edifice			Antuco			
ID	An28-5	An28-6	An28-7	An28-8	An27-6	An27-7
NB	<i>Phase I</i>	<i>Phase I</i>	<i>Phase I</i>	<i>Phase I</i>	<i>Phase II</i>	<i>Phase II</i>
Sample	<i>Lava flow</i>	<i>Lava flow</i>	<i>Lava flow</i>	<i>Lava flow</i>	<i>Fall deposit</i>	<i>Lava flow</i>
Rock type	<i>Andesite</i>	<i>Andesite</i>	<i>Andesite</i>	<i>Basaltic-andesite</i>	<i>Andesite</i>	<i>Basaltic-andesite</i>
Long.	<i>-71.34</i>	<i>-71.35</i>	<i>-71.35</i>	<i>-71.35</i>	<i>-71.35</i>	<i>-71.32</i>
Lat.	<i>-37.40</i>	<i>-37.39</i>	<i>-37.39</i>	<i>-37.39</i>	<i>-37.44</i>	<i>-37.46</i>
Majors	<i>ICP-OES</i>	<i>XRF</i>	<i>ICP-OES</i>	<i>XRF</i>	<i>ICP-OES</i>	<i>XRF</i>
Traces	<i>ICP-MS/MS</i>	<i>ICP-MS/MS</i>	<i>ICP-MS/MS</i>	<i>ICP-MS/MS</i>	<i>ICP-MS/MS</i>	<i>ICP-MS/MS</i>
SiO₂ (wt.%)	57.69	62.27	61.59	54.30	62.79	53.28
TiO₂	1.03	0.90	0.95	1.23	0.90	1.03
Al₂O₃	16.30	16.27	16.17	17.44	16.40	17.50
Fe₂O₃ (t)	7.69	6.91	7.26	9.03	7.27	9.00
MnO	0.17	0.15	0.16	0.14	0.16	0.14
MgO	1.86	1.71	1.51	5.09	1.56	6.76
CaO	4.78	4.42	4.41	8.06	4.46	8.75
Na₂O	4.37	5.19	4.80	3.71	4.46	3.39
K₂O	1.51	1.67	1.74	1.22	1.86	0.84
P₂O₅	0.37	0.33	0.33	0.27	0.31	0.21
SO₃	-	-	-	-	-	-
LOI	4.38	-0.13	0.33	-0.27	0.22	-0.27
Total	100.15	99.81	99.25	100.49	100.39	100.90
Li (ppm)	22.76	25.74	24.83	14.92	25.74	12.15
Sc	17.28	14.38	14.55	25.55	14.27	25.81
S	9.34	14.01	27.87	4.90	42.18	4.58
V	81.05	80.53	86.69	230.42	82.06	215.79
Cr	1.85	1.83	1.76	85.01	2.65	216.24
Co	11.61	10.74	10.90	27.95	10.82	34.23
Ni	3.31	2.75	2.13	47.80	2.80	98.87
Cu	57.23	58.91	58.64	78.45	69.65	68.92
Zn	113.81	95.44	94.71	83.42	93.06	78.89
Ga	20.11	19.71	19.97	18.92	19.69	17.89
Ge	1.44	1.35	1.34	1.37	1.32	1.29

Appendix B. Raw sample analyses

As	5.80	5.36	5.08	3.23	5.52	2.25
Se	0.02	0.02	0.02	0.04	0.04	0.03
Rb	39.80	41.63	43.11	32.92	41.78	20.29
Sr	411.35	394.48	407.81	503.14	399.28	501.64
Y	33.03	27.35	26.94	22.87	26.58	18.01
Zr	173.76	175.55	172.42	128.41	172.87	96.12
Nb	5.09	5.30	5.07	4.58	6.05	3.33
Mo	1.02	1.44	1.16	1.14	1.19	0.89
Cd	-	-	-	-	-	-
Ag	0.05	0.08	0.04	0.04	0.05	0.04
Sn	2.79	1.46	1.72	1.27	3.98	0.89
Sb	0.49	0.40	0.38	0.27	0.39	0.20
Cs	2.63	2.01	2.15	1.53	2.14	0.90
Ba	393.46	451.00	445.13	324.84	438.70	238.83
La	17.44	20.16	19.34	15.57	19.38	11.51
Ce	40.79	44.29	43.27	35.46	43.12	26.71
Pr	5.37	5.53	5.41	4.52	5.41	3.41
Nd	23.88	23.34	22.87	19.59	22.81	15.06
Sm	5.86	5.25	5.14	4.58	5.18	3.55
Eu	1.66	1.47	1.43	1.32	1.44	1.10
Gd	5.81	4.93	4.82	4.41	4.83	3.45
Tb	0.95	0.78	0.77	0.69	0.77	0.54
Dy	5.58	4.51	4.49	3.98	4.49	3.14
Ho	1.20	0.97	0.96	0.83	0.95	0.66
Er	3.40	2.73	2.72	2.31	2.71	1.81
Tm	0.40	0.41	0.38	0.34	0.35	0.26
Yb	3.36	2.80	2.73	2.13	2.75	1.69
Lu	0.51	0.42	0.42	0.32	0.42	0.26
Hf	4.54	4.47	4.45	3.36	4.44	2.54
Ta	0.33	0.35	0.34	0.29	3.87	0.22
W	0.42	0.44	0.40	0.30	0.52	0.21
Tl	0.08	0.25	0.16	0.16	0.27	0.08
Pb	11.41	12.23	11.49	8.36	12.26	6.04
Bi	b.d.	0.04	0.03	0.02	0.07	0.01
Th	3.05	4.02	3.99	3.30	4.02	2.03
U	0.93	1.12	1.10	0.86	1.11	0.52

Appendix B. Raw sample analyses

Table B.1. continued

Edifice		Antuco				
ID	An27-10	An27-13	An28-1	An28-2	An28-9	An29-1
NB	<i>Phase II</i>	<i>Phase II</i>	<i>Phase II</i>	<i>Phase II</i>	<i>Phase II</i>	<i>Phase II</i>
Sample	<i>Lava flow</i>	<i>Lava flow</i>	<i>Lava flow</i>	<i>Lava flow</i>	<i>Lava flow</i>	<i>Lava flow</i>
Rock type	<i>Basaltic-andesite</i>	<i>Basalt</i>	<i>Basaltic-andesite</i>	<i>Basalt</i>	<i>Basaltic-andesite</i>	<i>Basaltic-andesite</i>
Long.	-71.30	-71.37	-71.36	-71.35	-71.38	-71.46
Lat.	-37.39	-37.38	-37.40	-37.40	-37.38	-37.40
Majors	<i>XRF</i>	<i>ICP-OES</i>	<i>XRF</i>	<i>ICP-OES</i>	<i>XRF</i>	<i>XRF</i>
Traces	<i>ICP-MS/MS</i>	<i>ICP-MS/MS</i>	<i>ICP-MS/MS</i>	<i>ICP-MS/MS</i>	<i>ICP-MS/MS</i>	<i>ICP-MS/MS</i>
SiO₂ (wt.%)	52.27	52.13	54.38	51.92	53.28	55.95
TiO₂	1.15	1.07	1.32	1.08	1.09	1.43
Al₂O₃	18.29	19.37	17.56	19.67	18.12	16.70
Fe₂O₃ (t)	9.34	9.04	9.42	9.55	9.06	9.71
MnO	0.16	0.15	0.15	0.14	0.15	0.17
MgO	5.45	5.09	4.08	4.66	5.61	2.96
CaO	9.09	9.38	8.00	9.57	8.84	6.81
Na₂O	3.57	3.15	3.88	3.16	3.49	4.38
K₂O	0.79	0.74	1.14	0.75	0.92	1.20
P₂O₅	0.23	0.22	0.31	0.21	0.23	0.31
SO₃	-	-	-	-	-	-
LOI	-0.43	-0.06	-0.45	-0.21	-0.38	-0.17
Total	100.33	100.29	100.24	100.51	100.77	99.60
Li (ppm)	11.67	10.33	17.31	10.84	13.74	18.92
Sc	26.82	25.79	27.79	26.46	26.91	28.58
S	6.38	8.97	6.75	9.86	5.12	20.43
V	220.68	216.65	237.36	216.75	223.17	263.14
Cr	122.19	75.58	44.92	71.05	107.18	6.24
Co	31.67	28.89	25.78	27.37	31.42	20.86
Ni	58.31	41.73	23.58	33.51	61.56	7.31
Cu	74.69	73.89	91.90	67.82	79.99	97.76
Zn	80.63	76.85	91.02	74.99	80.76	102.16
Ga	18.30	18.34	19.76	18.51	18.12	20.44
Ge	1.33	1.23	1.39	1.20	1.32	1.51
As	1.79	2.73	4.24	2.29	0.73	3.56
Se	0.04	0.04	0.04	0.05	0.01	0.07
Rb	16.94	16.51	32.58	15.91	24.33	37.95
Sr	524.37	567.51	491.95	589.10	497.15	564.56
Y	21.75	18.67	27.39	18.52	21.13	29.15
Zr	93.87	81.45	131.67	78.42	102.66	139.84
Nb	2.96	2.70	4.26	2.59	3.45	4.35
Mo	0.58	0.55	0.89	0.53	0.66	1.13

Appendix B. Raw sample analyses

Cd	-	-	-	-	-	-
Ag	0.04	0.04	0.05	0.04	0.05	0.06
Sn	1.41	1.93	1.59	1.09	1.07	1.53
Sb	0.17	0.20	0.33	0.19	0.16	0.29
Cs	0.93	0.89	1.84	0.82	0.50	1.70
Ba	229.90	198.23	296.87	192.73	248.97	329.54
La	10.73	9.15	14.89	8.86	11.86	14.69
Ce	25.80	22.33	34.79	21.55	28.02	34.71
Pr	3.41	2.97	4.58	2.88	3.62	4.62
Nd	15.55	13.52	20.44	13.22	16.08	20.99
Sm	3.88	3.38	5.05	3.30	3.94	5.28
Eu	1.23	1.11	1.43	1.10	1.16	1.58
Gd	3.93	3.40	5.07	3.34	3.88	5.29
Tb	0.64	0.55	0.81	0.53	0.63	0.86
Dy	3.73	3.23	4.72	3.16	3.68	5.08
Ho	0.80	0.68	1.00	0.67	0.78	1.08
Er	2.20	1.91	2.80	1.86	2.15	3.01
Tm	0.27	0.24	0.35	0.24	0.24	0.43
Yb	2.00	1.76	2.66	1.78	2.00	2.83
Lu	0.31	0.27	0.40	0.26	0.30	0.43
Hf	2.47	2.18	3.52	2.11	2.71	3.76
Ta	0.21	0.18	0.33	0.16	0.26	0.28
W	0.20	0.18	0.45	0.18	0.23	0.34
Tl	0.07	0.06	0.12	0.15	0.10	0.18
Pb	6.14	5.46	8.59	5.35	7.14	8.85
Bi	0.03	0.01	0.03	0.02	0.02	0.04
Th	1.94	1.50	3.00	1.40	2.36	2.63
U	0.54	0.42	0.86	0.39	0.66	0.80
Edifice	Antuco			San Pedro		
ID	An29-2	An29-4	An29-5	San pedro 001	San pedro 007	San pedro 011
NB	<i>Phase II</i>	<i>Phase II</i>	<i>Phase II</i>			
Sample	<i>Lava flow</i>	<i>Lava flow</i>	<i>Lava flow</i>	<i>Lava flow</i>	<i>Lava flow</i>	<i>Lava flow</i>
Rock type	<i>Basaltic-andesite</i>	<i>Basaltic-andesite</i>	<i>Trachy-andesite</i>	<i>Trachyte</i>	<i>Trachyte</i>	<i>Trachyte</i>
Long.	<i>-71.46</i>	<i>-71.46</i>	<i>-71.46</i>	<i>-68.51</i>	<i>-68.50</i>	<i>-68.48</i>
Lat.	<i>-37.40</i>	<i>-37.40</i>	<i>-37.40</i>	<i>-21.93</i>	<i>-21.93</i>	<i>-21.93</i>
Majors	<i>ICP-OES</i>	<i>XRF</i>	<i>ICP-OES</i>	<i>XRF</i>	<i>XRF</i>	<i>XRF</i>
Traces	<i>ICP-MS/MS</i>	<i>ICP-MS/MS</i>	<i>ICP-MS/MS</i>	<i>ICP-MS/MS</i>	<i>ICP-MS/MS</i>	<i>ICP-MS/MS</i>
SiO₂ (wt.%)	54.98	56.03	59.55	63.23	62.46	63.25
TiO₂	1.60	1.50	1.32	0.78	0.80	0.79
Al₂O₃	16.68	16.65	15.70	15.90	15.72	15.95
Fe₂O₃ (t)	10.90	10.45	8.62	5.07	5.08	5.07
MnO	0.19	0.18	0.17	0.07	0.08	0.08
MgO	3.00	3.27	1.79	2.25	2.15	2.13

Appendix B. Raw sample analyses

CaO	6.97	6.89	4.80	4.22	4.54	4.20
Na₂O	4.10	4.50	4.80	4.23	4.27	4.30
K₂O	1.22	1.14	1.71	3.32	3.03	3.19
P₂O₅	0.33	0.31	0.41	0.25	0.35	0.25
SO₃	-	-	-	<0.001	0.14	0.00
LOI	-0.31	-0.40	-0.12	0.78	1.17	1.03
Total	99.64	100.93	98.75	100.09	99.80	100.24
Li (ppm)	15.43	17.48	26.55	23.12	23.72	23.99
Sc	29.86	28.47	21.67	12.05	12.09	12.07
S	22.06	9.52	32.93	96.45	2064.24	434.01
V	287.66	287.38	117.75	130.42	127.93	132.39
Cr	2.94	1.93	1.75	58.64	54.91	53.51
Co	22.69	22.34	13.42	11.91	11.89	11.53
Ni	7.88	8.07	2.53	17.41	18.54	16.25
Cu	69.22	76.98	63.20	38.50	52.13	32.53
Zn	104.32	110.10	103.60	84.90	85.99	96.86
Ga	20.28	20.76	20.62	20.15	19.83	20.23
Ge	1.56	1.59	1.49			
As	2.71	3.12	4.72	7.41	7.81	7.88
Se	0.03	0.04	0.04	0.02	0.05	0.05
Rb	26.24	25.31	46.02	109.44	105.33	110.70
Sr	445.97	425.41	383.76	474.96	472.12	484.72
Y	28.67	29.51	35.27	21.11	21.30	22.10
Zr	133.77	136.89	182.08	209.33	202.45	211.29
Nb	4.14	4.35	5.63	11.22	10.51	10.93
Mo	0.86	1.10	1.21	3.20	3.23	3.16
Cd	-	-	-	0.10	0.11	0.13
Ag	0.05	0.05	0.04	0.06	0.12	0.06
Sn	1.55	1.96	2.15	1.98	1.83	1.90
Sb	0.25	0.25	0.37	0.41	0.40	0.37
Cs	1.07	1.36	2.57	2.99	2.90	2.95
Ba	308.02	323.81	438.83	897.16	893.13	937.72
La	13.97	14.14	19.57	29.73	29.75	31.04
Ce	33.17	33.92	45.41	61.02	61.88	64.57
Pr	4.41	4.54	5.93	7.05	7.15	7.42
Nd	20.34	20.75	26.33	26.67	26.98	27.75
Sm	5.14	5.29	6.46	5.41	5.49	5.73
Eu	1.57	1.60	1.77	1.16	1.16	1.20
Gd	5.23	5.31	6.36	4.53	4.58	4.62
Tb	0.85	0.86	1.03	0.65	0.66	0.67
Dy	5.01	5.06	6.04	3.58	3.62	3.69
Ho	1.07	1.08	1.29	0.69	0.70	0.71
Er	2.97	3.00	3.57	1.90	1.91	1.95
Tm	0.38	0.43	0.44	-	-	-

Appendix B. Raw sample analyses

Yb	2.80	2.93	3.47	1.78	1.77	1.86
Lu	0.42	0.43	0.52	0.25	0.25	0.25
Hf	3.59	3.66	4.79	5.26	5.12	5.37
Ta	0.35	0.28	0.37	3.63	0.66	0.69
W	0.30	0.36	0.46	0.91	0.71	0.74
Tl	0.11	0.14	0.23	0.42	0.41	0.42
Pb	7.54	8.23	11.97	18.58	18.40	18.57
Bi	0.02	0.03	0.07	-	-	-
Th	2.36	2.45	4.00	8.83	8.55	8.81
U	0.72	0.75	1.24	2.28	2.17	2.23
Edifice	Ollagüe				La Poruña	Ollagüe
ID	Ollague 001	Ollague 003	Ollague 005	Ollague 006b	Porunita 001	Porunita 002
NB					<i>Cone</i>	<i>Aval. Dep.</i>
Sample	<i>Lava flow</i>	<i>Lava flow</i>	<i>Lava flow</i>	<i>Lava flow</i>	<i>Lava flow</i>	<i>Lava flow</i>
Rock type	<i>Dacite</i>	<i>Trachy-andesite</i>	<i>Dacite</i>	<i>Trachy-andesite</i>	<i>Basaltic-andesite</i>	<i>Trachy-andesite</i>
Long.	-68.23	-68.23	-68.23	-68.27	-68.29	-68.29
Lat.	-21.27	-21.29	-21.29	-21.30	-21.32	-21.32
Majors	<i>XRF</i>	<i>XRF</i>	<i>XRF</i>	<i>XRF</i>	<i>XRF</i>	<i>XRF</i>
Traces	<i>ICP-MS/MS</i>	<i>ICP-MS/MS</i>	<i>ICP-MS/MS</i>	<i>ICP-MS/MS</i>	<i>ICP-MS/MS</i>	<i>ICP-MS/MS</i>
SiO₂ (wt.%)	66.85	59.62	62.18	60.30	54.05	59.90
TiO₂	0.52	0.89	0.81	0.88	1.11	0.92
Al₂O₃	14.97	17.18	16.40	17.45	16.58	17.28
Fe₂O₃ (t)	3.42	6.55	5.26	5.79	8.20	6.06
MnO	0.04	0.09	0.07	0.08	0.11	0.08
MgO	1.09	2.68	2.33	2.48	4.21	2.38
CaO	2.61	5.54	4.59	5.20	7.51	5.34
Na₂O	4.03	4.16	3.75	4.17	3.65	4.21
K₂O	3.59	2.41	3.01	2.68	1.87	2.67
P₂O₅	0.16	0.24	0.24	0.25	0.25	0.26
SO₃	0.01	<0.001	0.01	<0.001	0.49	<0.001
LOI	1.80	0.45	1.19	0.73	1.53	0.80
Total	99.11	99.82	99.85	100.02	99.56	99.89
Li (ppm)	29.14	13.53	26.16	21.52	17.84	20.42
Sc	4.37	14.58	10.02	10.64	16.67	9.54
S	184.81	94.69	260.39	87.18	3655.31	96.48
V	56.28	136.46	117.47	111.66	213.15	121.86
Cr	10.45	61.53	47.40	39.55	79.80	21.66
Co	5.88	14.45	10.75	12.74	19.61	12.41
Ni	3.05	12.63	7.81	12.38	17.64	7.37
Cu	8.07	13.91	10.12	13.87	26.21	12.35
Zn	94.08	105.66	362.56	117.14	115.87	107.92
Ga	22.37	21.46	21.51	21.73	21.51	22.07
Ge	-	-	-	-	-	-

Appendix B. Raw sample analyses

As	4.45	2.29	9.57	4.51	20.02	4.87
Se	0.02	0.01	0.02	0.01	0.03	0.01
Rb	123.98	61.60	95.72	58.09	41.44	74.95
Sr	416.03	526.19	464.69	554.62	615.19	531.69
Y	11.17	22.54	16.83	16.61	20.97	17.29
Zr	71.40	217.05	104.91	205.59	162.42	232.66
Nb	12.20	10.24	10.32	10.05	9.00	10.34
Mo	3.08	1.84	2.26	1.66	2.24	2.49
Cd	0.06	0.14	0.84	0.16	0.13	0.11
Ag	0.07	0.06	0.05	0.07	0.10	0.03
Sn	2.56	1.41	2.33	1.93	1.49	1.51
Sb	0.25	0.11	0.19	0.12	0.14	0.15
Cs	5.14	1.26	3.57	1.65	1.42	2.11
Ba	1115.41	985.43	886.60	1125.94	806.97	983.16
La	42.27	32.40	35.23	33.35	24.93	31.72
Ce	81.88	61.87	67.98	66.82	50.98	64.42
Pr	9.05	7.87	8.16	7.78	6.11	7.51
Nd	32.52	30.55	30.34	29.37	24.08	28.61
Sm	6.11	6.23	6.01	5.75	5.18	5.73
Eu	1.33	1.61	1.37	1.50	1.43	1.53
Gd	4.23	5.13	4.68	4.59	4.49	4.67
Tb	0.51	0.73	0.63	0.62	0.66	0.63
Dy	2.29	3.88	3.11	3.14	3.59	3.18
Ho	0.36	0.74	0.55	0.56	0.69	0.57
Er	0.84	1.91	1.39	1.41	1.82	1.44
Tm	-	-	-	-	-	-
Yb	0.66	1.76	1.15	1.22	1.55	1.17
Lu	0.09	0.24	0.16	0.16	0.21	0.16
Hf	2.33	5.13	2.96	4.97	3.96	5.31
Ta	0.90	0.64	0.93	0.74	0.54	0.63
W	1.02	1.08	0.73	0.47	0.31	0.46
Tl	0.81	0.31	0.63	0.24	0.21	0.39
Pb	16.93	10.44	14.25	12.76	9.29	11.85
Bi	-	-	-	-	-	-
Th	12.00	5.02	8.33	7.03	3.29	6.90
U	4.19	1.36	2.42	1.66	0.93	1.78

Appendix B. Raw sample analyses

Table B.1. continued

Edifice	Ollagüe				
	Porunita 003	Porunita 004	Porunita 005	Porunita 006	Porunita 006a
ID	<i>Aval. Dep.</i>				
Sample	<i>Lava flow</i>				
Rock type	<i>Trachyandesite</i>	<i>Trachyandesite</i>	<i>Trachyandesite</i>	<i>Trachyandesite</i>	<i>Trachyandesite</i>
Long.	-68.28	-68.28	-68.28	-68.27	-68.27
Lat.	-21.32	-21.32	-21.32	-21.32	-21.32
Majors	<i>XRF</i>	<i>XRF</i>	<i>XRF</i>	<i>XRF</i>	<i>XRF</i>
Traces	<i>ICP-MS/MS</i>	<i>ICP-MS/MS</i>	<i>ICP-MS/MS</i>	<i>ICP-MS/MS</i>	<i>ICP-MS/MS</i>
SiO₂ (wt.%)	60.85	60.88	60.85	59.89	59.83
TiO₂	0.82	0.81	0.82	0.82	0.83
Al₂O₃	16.61	16.84	16.73	17.04	16.67
Fe₂O₃ (t)	5.47	5.50	5.77	5.55	5.62
MnO	0.08	0.08	0.08	0.08	0.08
MgO	2.29	2.29	2.74	2.34	2.44
CaO	5.23	5.05	5.14	5.39	5.53
Na₂O	4.21	4.19	4.12	4.00	3.85
K₂O	2.63	2.82	2.74	2.97	3.14
P₂O₅	0.25	0.24	0.22	0.25	0.24
SO₃	0.19	0.05	<0.001	0.02	0.01
LOI	0.94	0.95	0.60	1.29	1.56
Total	99.57	99.72	99.81	99.65	99.81
Li (ppm)	20.38	25.04	21.16	26.99	20.24
Sc	9.69	9.28	11.55	9.34	10.12
S	1944.70	808.13	39.72	209.60	94.06
V	93.11	90.69	125.38	112.63	115.49
Cr	33.75	33.84	73.53	34.63	43.71
Co	11.63	11.52	13.89	11.93	12.44
Ni	9.32	9.15	16.19	9.44	11.16
Cu	18.48	16.41	17.65	10.87	14.51
Zn	112.11	105.60	104.82	109.86	107.95
Ga	20.84	21.36	21.41	21.39	21.13
Ge	-	-	-	-	-
As	13.96	10.43	3.16	12.44	7.62
Se	0.07	0.02	0.00	0.03	0.02
Rb	64.42	72.24	87.50	69.67	74.47
Sr	520.16	524.30	500.44	551.01	538.06
Y	17.94	16.32	16.36	16.95	16.93
Zr	190.59	186.47	173.54	194.03	181.60
Nb	9.82	10.04	9.32	10.15	9.68
Mo	1.57	1.64	2.47	2.22	2.37

Appendix B. Raw sample analyses

Cd	0.19	0.12	0.10	0.22	0.16
Ag	0.07	0.08	0.05	0.07	0.07
Sn	1.38	1.51	1.66	1.59	1.59
Sb	0.19	0.17	0.15	0.15	0.17
Cs	2.72	2.33	3.14	2.21	2.26
Ba	1046.87	1121.21	934.65	1065.91	1016.80
La	34.93	32.85	29.40	34.15	32.15
Ce	66.20	65.73	58.37	66.91	64.59
Pr	8.05	7.53	6.77	7.75	7.55
Nd	30.44	28.16	25.70	28.76	28.39
Sm	5.89	5.43	5.29	5.54	5.58
Eu	1.46	1.39	1.34	1.40	1.45
Gd	4.74	4.24	4.28	4.42	4.50
Tb	0.64	0.57	0.59	0.59	0.60
Dy	3.22	2.94	3.01	3.03	3.08
Ho	0.59	0.53	0.54	0.55	0.55
Er	1.47	1.37	1.38	1.41	1.42
Tm	-	-	-	-	-
Yb	1.26	1.20	1.15	1.18	1.24
Lu	0.17	0.16	0.16	0.17	0.17
Hf	4.68	4.64	4.32	4.71	4.51
Ta	0.61	0.64	0.65	0.63	0.59
W	0.47	0.49	0.61	0.51	0.55
Tl	0.08	0.18	0.49	0.50	0.46
Pb	10.26	12.45	12.74	13.21	12.61
Bi	-	-	-	-	-
Th	6.98	7.11	8.58	7.35	6.72
U	1.96	1.69	2.34	1.87	1.85

(t): total. b.d.: below detection. Aval. Dep.: Ollagüe avalanche deposit [see Clavero et al. (2004) for details]. Trace element analyses mostly obtained through ICP-MS/MS analysis at the Open University, between 2017 and 2019. Exceptions include: Ba (ICP-MS, Cardiff University, 2017; excluding Antuco), Tm (ICP-MS, Cardiff University, 2017; pre-existing analyses courtesy of S. Watt); U (ICP-MS, Cardiff University, 2017; excluding Antuco); Th (ICP-MS, Cardiff University, 2017; excluding Antuco). Ag analysis of Antuco sample An27-8 omitted as it is well in excess of the remaining analyses from Antuco and is not representative of the general trend observed.

Appendix C

Extended methods

The following sections of this appendix outline the details of the preparatory methods undertaken as part of the current project, building on those presented in **Chapter 4**. Both rock preparatory techniques and sample solution preparation are included in this appendix.

C.1. Rock preparation

Not all samples used in the current study were collected by the author during fieldwork. As a result, not all samples have had the same preparation history; samples donated by Sebastian Watt (Antuco, Yate, Apagado and Hornopirén) were prepared prior to the commencement of the current project, and as such were already in powder form. For this reason, the following sub-sections refer to samples collected by the author and those from the Central Volcanic Zone of northern Chile (collected by both Ginevra Chelli and the author). Sample preparation was undertaken at both the University of Birmingham and Cardiff University, U.K. between 2016 and 2018. The below sub-sections outline the different stages of rock preparation. All efforts were made to minimise sample contamination.

C.1.1. Rock saw

Rocks saws were used to remove weathered surfaces from collected samples and cut billets suitable in size for thin sectioning. Equipment used included the Husqvarane, Heathway (University of Birmingham) and Clipper (Cardiff University) rock saws.

C.1.2. Norton fly press

Lava samples were crushed using a Norton fly press at the University of Birmingham. Scoria samples, however, did not require crushing. Prior to crushing, samples were encased in numerous sheets of scrap paper. Increasing pressure was gradually applied to the samples through the fly press, crushing samples into ≤ 1 cm fines.

The reason for covering the samples in paper is two-fold; 1) to prevent contamination from the metal of the fly press (chips to the body of the fly press are evidence of extensive use and age of the equipment) or rock dust from previous samples, and 2) to contain the crushed sample. Paper was also easily removed from the sample fines if any remained after crushing. Further efforts were made to prevent contamination by cleaning the fly press thoroughly between each sample. Lost fines were removed from surfaces using a vacuum, before being lightly cleaned with a damp (water with small volume of detergent added or acetone) blue/white paper towel.

Where possible, samples were not crushed using a jaw crusher, as it is believed shards of metal from the plates of the jaw crusher can enter the sample fines, possibly affecting the concentration of trace elements, such as the Platinum Group Elements

(PGEs). Possible contamination can more easily be controlled when using the fly press (pers comms. F. Jenner, 2016).

C.1.3. Agate planetary ball mill

All samples were milled using an agate planetary ball mill (Model RETSCH PM 400) at Cardiff University. Ball mill conditions (i.e., running time and revolutions per minute [rpm]) varied between lava (30-40 minutes at 290 rpm) and scoria (15 minutes at 250 rpm) samples. In some instances, the selected time and rpm did not result in a fine enough rock powder, therefore, those samples requiring further milling were run for a further 5-10 minutes at 290 (lavas) or 250 (scoria) rpm. It is important to make sure sample powders are very fine, making sure no crystals remain. This is because some crystal phases, such as zircon, are acid resistant, making it difficult to dissolve them for solution ICP analysis.

On a few occasions, some scoria samples were 'stuck' to pot walls. This is believed to be a result of a small amount of water in the sample, either from condensation inside the sample bag, or from hydrous phases in the sample. In extreme cases, samples 16DCCaHu.005 – 009 came out of the ball mill very wet (clay-like). These five samples were placed on glass petri dishes and into an oven at 70°C overnight to dry the sample. As a result, the calculated Loss on ignition (LOI; more details in subsection **B.1.4.**) will be a minimum for these samples.

To prevent sample contamination, agate pots and balls were cleaned thoroughly (including the removal of powder from chips in the agate) and left to dry between each run. In addition, a vacuum was used to clean up rock dust within the ball mill.

C.1.4. Loss on ignition (LOI)

The loss on ignition (LOI) of a sample represents the volatiles (including water, carbon dioxide and possibly Fluorine, Bromine and Sulfur) removed from alteration products (i.e., clay minerals and sericite) within the samples. The presence of calcite veins (calcium carbonate) can increase the LOI of a sample as carbon dioxide is released. Inductively coupled plasma optical emission spectrometry (ICP-OES) and ICP-mass spectrometry (MS) cannot analyse for water and carbon dioxide, hence the calculated LOI accounts for this.

In order to calculate LOI, samples required 'baking' in a high-temperature Vecstar furnace to "burn off" any volatiles. In some instances, the calculated LOI of samples was negative, representing a mass gain. This can be explained by the oxidation of Fe in a sample from Fe²⁺ to the more dense Fe³⁺. To prevent any moisture getting into the samples post-furnace treatment, samples were sealed in airtight sample bags and stored in desiccators until required for fusion. To prevent contamination during the LOI process, crucibles were not touched by hand, preventing the transfer of moisture to the crucibles; instead, they were carefully transferred to and from the furnace using tongs.

The method of determining the LOI was undertaken at Cardiff University and was as follows:

- Clean crucibles were first placed in the warming furnace for 1 hour to remove any volatiles collected during storage,
- Subsequently, crucibles were removed and left to cool for 15 minutes,

- Once cool, crucibles were weighed on a Sartorius research scales (accuracy ± 0.0001 g) prior to addition of ~2 g of 'wet' sample powder – the crucible and 'wet' sample masses were recorded,
- Crucibles containing 'wet' sample powders were placed in the furnace at 900°C for approximately 2 hours to 'burn off' the volatile content,
- Subsequently, crucibles were removed and left to cool, again for 15 minutes,
- Crucibles were reweighed, giving an ignited total (crucible and 'dry' sample); 'dry' sample masses were calculated by deducting the mass of the empty crucible from the ignited total for each sample,
- The LOI of each sample was calculated by dividing the mass loss (i.e., 'wet' minus 'dry' mass) of a sample by its 'wet' mass and multiplying by 100.

C.1.5. Thin sections

Polished thin sections of samples from Antuco were previously made at the University of Southampton. Thesis thin sections were purposely made for electron probe analysis, thus were not 30 microns thick, making mineral identification more difficult (sections are ~70 microns thick). Polished thin sections (x8) for Villarrica, Quetrupillan and Lanin were made at the Open University (courtesy of Michelle Higgins). Additional polished thin sections (x16) of samples collected in northern Chile (Ollague, La Porunita and San Pedro) were also made at the Open University (courtesy of Michelle Higgins). Thin section descriptions were made using a petrographic microscope at the University of Birmingham, and can be found in **Electronic Appendix B**.

C.2. Sample solution preparation

C.2.1. Claisse Fluxy fusion

In order to analyse samples by solution ICP-OES/MS, they must undergo rock powder fusion. This were undertaken at Cardiff University following the procedure outlined below. International Standard Reference Materials housed at Cardiff University were prepared in the same manner and used to assess analytical accuracy (and precision, although limited ISRM data does not promote this comparison). ISRM used included JB-1B (basalt), JA2 (andesite), JG-3 (granite) and JG1a (granodiorite).

- Within error (+/- 1%), 0.1000 g of sample and 0.6000 g of flux (lithium borate 50:50) were weighed out using a Sartorius Mettler Toledo research scales (accuracy +/- 0.0001 g) into clean platinum crucibles, where, using a clean spatula, sample and flux were mixed together,
- Added to the sample-flux mix was 5-6 drops of lithium iodide wetting agent,
- Three at a time, crucibles were placed into the Claisse Fluxy fusion machine, each having a corresponding Teflon beaker containing 20 ml 10% nitric acid, 30 ml deionised water (18.2 Mohm cm) and a magnetic stirring bar placed beneath them,
- Sample fusion and dissolving of glass in the nitric acid-deionised water solution ran for approximately 9 minutes,
- On completion, crucibles were removed and checked for remaining glass – if glass remained on the crucible walls, crucibles were placed in their respective nitric acid-deionised water mix and placed on a hotplate at ~80°C for 15 minutes to dissolve the remaining glass,

- Once all the glass had dissolved, crucibles were removed and washed with deionised water which was added to the Teflon beakers,
- The solutions were transferred into 100 ml Nalgene flasks where a 1 ml Rhodium (Rh) spike (of 100 ppm stock solution) was added,
- The solution was then made up to 100 ml using deionised water,
- The 100 ml solutions were then transferred into storage beakers ahead of ICP-OES/MS analysis.

C.2.1.1. Sources of contamination

Throughout the Fluxy fusion process, all efforts were made to minimise sample contamination. Prior to beginning the fusion process, all equipment, including crucibles, Nalgene flasks, Teflon beakers, magnetic stirring bars and funnels were washed thoroughly. Between weighing out each sample powder and flux, the spatula used was wiped clean. Loose debris was also removed from the Claisse Fluxy fusion machine to prevent contamination during the fusion process. During the preparation of sample solutions, debris from the fusion machine was observed falling into a sample crucible. The debris was removed without incident; however, it puts into question the volume of debris entering sample powders going unnoticed. Once settled in storage beakers, some sample solutions were observed to contain minimal volumes of dust on the surface, likely fallout from the laboratory atmosphere.

C.2.2. Multi-stage acid digestion

In preparation for triple quadrupole solution ICP-MS analysis, acid digestion was undertaken at the Open University following the below procedure:

Appendix C. Extended methods

- Weigh out 100 mg/0.1 g of sample powder (using a Sartorius scales) into Teflon beakers – prior to weighing out the sample powder, an attempt was made to remove static from the Teflon beakers using a Zerostat 3 Anti-static gun (this was not 100% effective),
- Add to the sample powder 0.5 ml concentrated HNO₃ and 2 ml concentrated HF – acids were added using an Eppendorf research pipette (care must be taken when using the pipette to prevent any fluid being ‘sucked’ into the body of the pipette),
- Secure lids of Teflon beakers tightly and place on a hotplate at 120 °C for a minimum 12 hours,
- During the above fluxing (in HNO₃ and HF), samples were placed (15 at a time) in an ultrasonic bath for 10 minutes (this was to make sure all sample powder was mixed in with the acid solution, as some sample powder can become trapped within pockets of HF ‘gel’, so need agitating),
- Remove Teflon beakers from hotplate and allow to cool to room temperature,
- Once cool, remove lids and place back on hotplate at 65 °C (to reduce volatile loss) and evaporate until incipient dryness (sample-acid mixtures evaporated at different rates – those samples that evaporated first were removed from the hotplate and had their lids replaced tightly until the remaining mixtures had evaporated),
- Remove Teflon beakers from hotplate and add 2 ml concentrated HCl,
- Secure lids of Teflon beakers tightly and place back on hotplate at 120 °C for a minimum 12 hours,
- Remove Teflon beakers from hotplate and allow to cool to room temperature,

Appendix C. Extended methods

- Once cool, remove lids and place back on hotplate at 65 °C and evaporate until incipient dryness,
- Remove Teflon beakers from hotplate and add 2 ml concentrated HNO₃ and 2 ml (MilliQ [18.2 Ohm]) MQ H₂O,
- Secure lids of Teflon beakers tightly and place back on hotplate at 120 °C for a minimum 12 hours,
- Remove Teflon beakers from hotplate and allow to cool to room temperature,
- Once cool, remove lids and place back on hotplate at 65 °C and evaporate until incipient dryness,
- Remove Teflon beakers from hotplate and add ~ 3 ml concentrated HNO₃ (volume added is proportional to the weight of sample powder used – calculated in Excel) and a few ml of MQ H₂O (roughly 4-5 ml of MQ H₂O was added, however, it does not have to be precise as the solutions will be made up to 100 g using MQ H₂O),
- Secure lids of Teflon beakers and place back on hotplate at 120 °C for ~4 hours, Remove Teflon beakers from hotplate and allow to cool to room temperature,
- Make up “Master Solutions” (to ~100 g) using MQ H₂O (see Excel for details on the volume of MQ H₂O required);
 - Weigh (using a Mettler Toledo scales) labelled sample bottles (Nalgene flasks) and record weight (weight of sample bottle without lid),
 - Transfer sample solutions to respectively labelled Nalgene flasks,
 - Teflon beakers and lids were swilled two/three times using MQ H₂O and added to the Nalgene flask,

- The solutions are made up to a 1000-fold dilution using MQ H₂O (see Excel for details on the volume of MQ H₂O required to produce a 1000-fold dilution).

C.2.2.1. Cleaning of Teflon beakers

The Teflon beakers used in the above preparation required thorough cleaning.

The cleaning procedure was as follows:

- An acid mix (HNO₃-HF) was added to each Teflon beaker (a few ml; enough to cover base of Teflon beaker),
- Teflon beakers were fluxed on a hotplate overnight at 120 °C,
- Teflon beakers were removed from the hotplate and allowed to cool,
- Beakers and their lids were swilled (3 times) with MQ H₂O,
- Allow to dry,
- HCl was added to each Teflon beaker (~2 ml; again, enough to cover the base of the Teflon beaker),
- Teflon beakers were fluxed on a hotplate overnight at 120 °C,
- Teflon beakers were removed from the hotplate and allowed to cool,
- Beakers and their lids were swilled (3 times) with MQ H₂O,
- Allow to dry,
- Labels on the Teflon beakers were removed using an alcohol based fluid,
- Storage.

*The acids used during the cleaning process were all of trace element grade.

C.2.2.2. Triple quadrupole inductively coupled plasma mass spectrometry (ICP-MS/MS)

Triple quadrupole solution ICP-MS was undertaken at the Open University using the Agilent 880 triple quadrupole ICP-MS machine. This analytical technique was used to overcome the plethora of spectral interferences that effect the chalcophile elements during analysis. In order to remove spectral interferences during analysis, trace elements were analysed in varying gas modes (no gas, O₂, He, NH₃). The gas modes used to analyse each trace element varied between each batch of samples analysed and detailed below.

⁵During the analysis (August 2017) of samples from Antuco, Li, Sc, Co, Ni, Rb, Sr, Y, Zr, Nb, Mo, Sn, Sb, Cs, Ta, W, Tl, Th and U were analysed in a no gas mode; the REE, S, As, Ba, Hf and Se were analysed in reactive O₂ gas mode; and V, Cr, Cu, Zn, Ga, Ge, Pb and Bi were analysed in collisional He gas mode.

During analysis (January 2018) of the samples from Yate, ten from the CHC SECs, three from Hornopirén and four from Apagado, the elements V, Ni, Ga, As, Y, Nb, Mo, Eu, Hf and Tl were analysed in a collisional He gas mode; the Rare Earth Elements (REE) (except Eu), S and Se were analysed in a reactive O₂ gas mode; Li, Sc, Cr, Co, Cu, Zn, Rb, Sr, Zr, Sn, Sb, Ta, W and Pb were analysed in a no gas mode.

During analysis (January 2018) of those samples from Villarrica, Quetrupillán, Lanín, five from Apagado and 1 from Honopirén, the elements V, Cr, Co, Ni, Cu, Zn, Ga, As, Rb, Sr, Y, Zr, Nb, Mo, Sn, Eu, Ta and W were analysed in a collisional He gas

⁵ This paragraph is published in Cox et al (2019). 'Chalcophile element processing beneath a continental arc stratovolcano', *Earth and Planetary Science Letters*, 522, 1-11.

mode; the REE (except Eu), S and Se were analysed in a reactive O₂ gas mode; Li, Sc, Sb, Hf, Tl and Pb were analysed in a no gas mode.

During analysis (December 2018) of those samples from Ollagüe and San Pedro, the elements V, Cr, Co, Ni, Cu, Zn, Ga, Rb, Sr, Y, Nb, Mo, Sn, Cs, Ba, Eu and Pb were analysed in a collisional He gas mode; the REE (except Eu), S, Se and As were analysed in a reactive O₂ gas mode; Li, Sc, Zr, Cd, Sb, Ta, Hf, W, Tl, Th and U were analysed in a no gas mode.

During analysis, twelve samples from the Caburgua – Huelemolle Complex (CHC) SECs and those from Huililco were analysed for V, Cr, Co, Ni, Cu, Zn, Ga, As, Rb, Sr, Y, Zr, Nb, Mo, Sn, Eu, Ta and W in a collisional He gas mode; S, Se and the Rare Earth Elements [REE (except Eu)] were analysed in a reactive O₂ gas mode; Li, Sc, Sb, Hf, Tl and Pb were analysed for in a no gas mode. The sample from La Poruñita SEC and a single sample from the CHC SECs were analysed for V, Cr, Co, Ni, Cu, Zn, Ga, Rb, Sr, Y, Nb, Mo, Sn, Cs, Ba, Eu and Pb in a collisional He gas mode; S, As, Se and the REE were analysed for in a reactive O₂ gas mode; Li, Sc, Zr, Cd, Sb, Ta, Hf, W, Tl, Th and U were analysed for in a no gas mode. The single sample from the CHC was analysed separately alongside the La Poruñita sample as it was previously dropped during the 1000-fold dilution stage of the acid digestion process, hence needing re-digestion.

[Sentence on Ag analysis – although mentioned in main text, reiterate here].

C.3. Existing datasets

This section briefly summarises the pre-existing datasets provided by Dr S. Watt (Ph. D. Supervisor). Existing X-ray fluorescence spectrometry (XRF) and ICP-MS data

for samples from Antuco were obtained at the University of Southampton, U.K. Preparation of these samples was also undertaken at the University of Southampton, however, preparatory techniques used differed. Samples were crushed using a fly press prior to powdering in a Tungsten Carbide Tema mill. Existing data for samples from Yate, Apagado and Hornopirén were obtained from the University of Edinburgh, U.K. (major element, XRF), the Open University (trace elements, XRF) and the University of Oxford, U.K. (trace elements, ICP-MS)

Appendix D

Raw International Standard Reference Material Analyses

Table D.1. International Standard Reference Material analyses obtained by ICP-OES/MS analysis at Cardiff University (2017)

(wt.%)	JB-1a	Cert. ¹	Cert. ²	JA-2	Cert. ¹	Cert. ²	JG-1a	Cert. ¹
SiO ₂	52.62	52.16	52.56	57.83	56.18	56.39	72.94	72.19
TiO ₂	1.32	1.30	1.29	0.68	0.67	0.67	0.24	0.25
Al ₂ O ₃	14.29	14.51	14.51	15.45	15.32	15.51	14.17	14.22
Fe ₂ O ₃	9.22	9.10	9.00	6.69	6.14	6.29	2.09	2.05
MnO	0.15	0.15	0.14	0.11	0.11	0.11	0.06	0.06
MgO	7.72	7.75	7.81	7.43	7.68	7.84	0.59	0.69
CaO	9.14	9.23	9.31	6.22	6.48	6.26	2.04	2.13
Na ₂ O	2.83	2.74	2.74	3.11	3.08	3.07	3.60	3.41
K ₂ O	1.45	1.42	1.41	1.79	1.80	1.78	4.03	4.01
P ₂ O ₅	0.25	0.25	0.26	0.16	0.15	0.15	0.07	0.08
SO ₃	-	-	-	-	-	-	-	-
LOI	0.78	0.78	-	0.80	0.80	-	0.50	0.50
Total	99.77	99.39	99.03	100.27	98.41	98.07	100.32	99.59
Sc	27.91	27.90	27.81	17.80	19.60	18.93	5.87	6.30
V	222.51	206.00	200.30	131.14	130.00	119.70	22.89	23.00
Cr	420.76	415.00	408.00	465.67	465.00	424.80	18.21	18.60
Co	40.46	39.50	38.53	28.01	30.00	28.33	6.70	5.70
Ni	139.17	134.00	139.50	150.27	142.00	136.00	5.70	6.40
Cu	51.64	55.00	54.50	32.45	28.60	29.00	1.96	1.30
Zn	79.92	82.00	88.50	66.76	62.70	64.50	35.02	38.80
Sr	445.21	443.00	443.40	254.37	252.00	245.80	174.06	185.00
Y	25.40	24.00	22.91	19.18	18.10	16.89	31.57	31.60
Zr	141.01	146.00	140.10	121.84	119.00	108.50	109.78	121.00
Ba	504.56	497.00	495.10	329.73	317.00	308.40	455.99	458.00
V	226.35	206.00	200.30	128.02	130.00	119.70	21.02	23.00
Cr	414.87	415.00	408.00	453.72	465.00	424.80	16.28	18.60

Appendix D. Raw International Standard Reference Material Analyses

Table D.1. continued

Co	43.00	39.50	38.53	28.19	30.00	28.33	5.78	5.70
Ni	139.04	134.00	139.50	167.64	142.00	136.00	3.35	6.40
Cu	54.91	55.00	54.50	28.84	28.60	29.00	1.77	1.30
Zn	80.79	82.00	88.50	68.46	62.70	64.50	40.42	38.80
Ga	18.66	18.00	18.13	16.92	16.40	16.85	16.25	17.00
Ge	-	-	1.00	-	-	1.10	-	-
Rb	40.52	42.00	38.15	70.26	68.00	69.80	174.37	180.00
Sr	466.62	443.00	443.40	251.34	252.00	245.80	176.02	185.00
Y	23.95	24.00	22.91	17.47	18.10	16.89	29.34	31.60
Zr	150.86	146.00	140.10	120.68	119.00	108.50	118.70	121.00
Nb	27.04	27.00	27.57	8.39	9.80	9.30	11.80	12.00
Cs	1.20	1.20	1.22	5.06	4.20	4.78	11.49	11.40
Ba	519.05	497.00	495.10	325.65	317.00	308.40	433.11	458.00
La	38.72	38.10	37.74	16.23	16.30	15.46	21.71	21.80
Ce	67.69	66.10	65.93	33.94	32.70	32.86	44.34	45.20
Pr	7.18	7.30	7.10	3.77	4.38	3.69	5.80	6.08
Nd	26.44	25.50	26.15	14.19	13.80	14.04	20.19	21.00
Sm	5.34	5.02	5.10	3.20	3.12	3.03	4.73	4.85
Eu	1.62	1.47	1.48	0.97	0.94	0.89	0.71	0.72
Gd	4.70	4.54	4.70	2.81	3.11	3.01	3.65	3.75
Tb	0.65	0.69	0.70	0.41	0.42	0.48	0.76	0.79
Dy	4.06	4.19	4.07	2.76	3.01	2.85	4.09	4.20
Ho	0.76	0.72	0.81	0.48	0.46	0.59	0.78	0.76
Er	2.21	2.18	2.23	1.53	1.37	1.68	2.28	2.36
Tm	0.36	0.31	0.32	0.24	0.30	0.25	0.40	0.39
Yb	2.08	2.10	2.10	1.43	1.67	1.65	2.48	2.74
Lu	0.34	0.32	0.31	0.24	0.27	0.25	0.40	0.44
Hf	3.77	3.48	3.47	2.81	2.89	2.84	3.60	3.84
Ta	1.69	1.60	1.74	0.58	0.61	0.65	1.43	1.70
Pb	7.07	7.20	6.44	18.73	19.30	18.88	21.86	27.00
Th	8.88	8.80	8.97	4.64	4.70	4.80	11.89	12.10
U	1.73	1.60	1.62	2.15	2.40	2.18	4.92	4.70

JB-1a: basalt; JA-2: andesite; JG-1a: granodiorite. ¹Govindaraju (1994); ²Jochum et al. (2016). Cert.: certified value.

Table D.2. International Standard Reference Material analyses obtained by XRF analysis at the University of Edinburgh (2017)

(wt.%)	JA2 avg.	Cert. ¹	JR1 avg.	Cert. ¹	BHVO- 1 avg.	Cert. ¹
SiO ₂	57.37	56.18	75.57	75.40	49.83	49.94
TiO ₂	0.67	0.67	0.11	0.10	2.72	2.71
Al ₂ O ₃	15.98	15.32	12.82	12.89	13.67	13.80
Fe ₂ O ₃	6.18	6.14	0.83	0.96	12.29	12.23
MnO	0.11	0.11	0.10	0.10	0.17	0.17
MgO	7.34	7.68	0.16	0.09	7.08	7.23
CaO	6.28	6.48	0.69	0.63	11.45	11.40
Na ₂ O	3.12	3.08	4.14	4.10	2.45	2.26
K ₂ O	1.85	1.80	4.48	4.41	0.52	0.52
P ₂ O ₅	0.15	0.15	0.02	0.02	0.29	0.27
SO ₃	-	-	-	-	-	-
LOI	-	-	-	-	-	-
Total	99.06	97.61	98.92	98.70	100.48	100.53

JA2: andesite; JR-1: rhyolite; BHVO-1: basalt. Avg.: average.

¹Govindaraju (1994). Cert.: certified value.

Appendix D. Raw International Standard Reference Material Analyses

Table D.3. International Standard Reference Material analyses obtained by XRF analysis at the University of Leicester (2017)

(wt.%)	BH-1	Cert. ¹	WS-1	Cert. ²	BCS375	Cert. ³	BCS376	Cert. ³
SiO ₂	68.50	-	51.27	51.07	67.11	67.10	67.07	67.10
TiO ₂	0.38	-	2.27	2.43	0.35	0.38	0.01	-
Al ₂ O ₃	14.14	-	13.57	13.77	19.71	19.80	17.59	17.70
Fe ₂ O ₃	5.76	-	13.53	13.09	0.11	0.12	0.10	0.10
MnO	0.14	-	0.18	0.17	0.00	0.00	0.00	0.00
MgO	2.46	-	4.98	5.63	0.00	0.05	-0.01	0.03
CaO	3.01	-	8.49	9.00	0.72	0.89	0.41	0.54
Na ₂ O	3.31	-	2.49	2.48	9.12	10.40	2.52	2.83
K ₂ O	0.74	-	1.15	1.00	0.67	0.79	11.23	11.18
P ₂ O ₅	0.08	-	0.31	0.30	0.03	-	0.03	-
SO ₃	0.08	-	0.14	-	0.08	-	0.07	-
LOI	-	-	-	-	-	-	-	-
Total	98.60	-	98.39	-	97.92	-	99.01	-
(wt.%)	ARSiO ₂	Cert. ⁴	ARAl ₂ O ₃	Cert. ⁴	MRG-1	Cert. ⁵	NIM-D	Cert. ⁶
SiO ₂	100.43	-	0.13	-	38.97	39.12	38.46	38.96
TiO ₂	0.01	-	0.01	-	3.84	3.77	0.03	0.02
Al ₂ O ₃	0.03	-	99.81	-	8.17	8.47	0.76	0.30
Fe ₂ O ₃	0.00	-	0.01	-	18.36	17.94	17.24	16.96
MnO	0.00	-	0.00	-	0.16	0.17	0.24	0.22
MgO	-0.01	-	-0.02	-	13.29	13.55	43.00	43.51
CaO	0.01	-	0.00	-	14.67	14.70	0.33	0.28
Na ₂ O	0.17	-	0.09	-	0.77	0.74	0.07	0.04
K ₂ O	0.01	-	0.01	-	0.18	0.18	0.03	0.01
P ₂ O ₅	0.01	-	0.01	-	0.07	0.08	0.03	0.01
SO ₃	0.05	-	0.05	-	0.23	-	0.20	-
LOI	-	-	-	-	-	-	-	-
Total	100.72	-	100.10	-	98.72	-	100.38	-
(wt.%)	BCS372/1	Cert. ³						
SiO ₂	19.76	20.30						
TiO ₂	0.25	0.27						
Al ₂ O ₃	5.06	5.37						
Fe ₂ O ₃	3.41	3.42						
MnO	0.04	-						
MgO	1.20	1.31						
CaO	65.60	65.30						
Na ₂ O	0.25	0.10						
K ₂ O	0.68	0.75						
P ₂ O ₅	0.09	0.07						
SO ₃	3.00	-						
LOI	-	-						
Total	99.35	-						

Appendix D. Raw International Standard Reference Material Analyses

BH-1: diorite; WS-1: dolerite [comparable to WS-E]; BCS375/1: soda feldspar powder; BCS376/1: potash feldspar powder; ARSiO₂:Si; ARAl₂O₃: Al; MRG-1: gabbro; NIM-D: dunite; BCS372/1: Ordinary Portland Cement. ¹University of Leicester internal standard reference material; ²In-house preparation (i.e., University of Leicester); ³Bureau of Analysed Samples; ⁴University of Leicester internal spiked sample; ⁵Canada Centre for Mineral and Energy Technology; ⁶Council for Mineral Technology, South Africa Bureau of Standards.

Appendix E

Cu, Ag, Cu/Ag systematics (versus MgO) of samples from Antuco stratovolcano, Southern Volcanic Zone, Chile

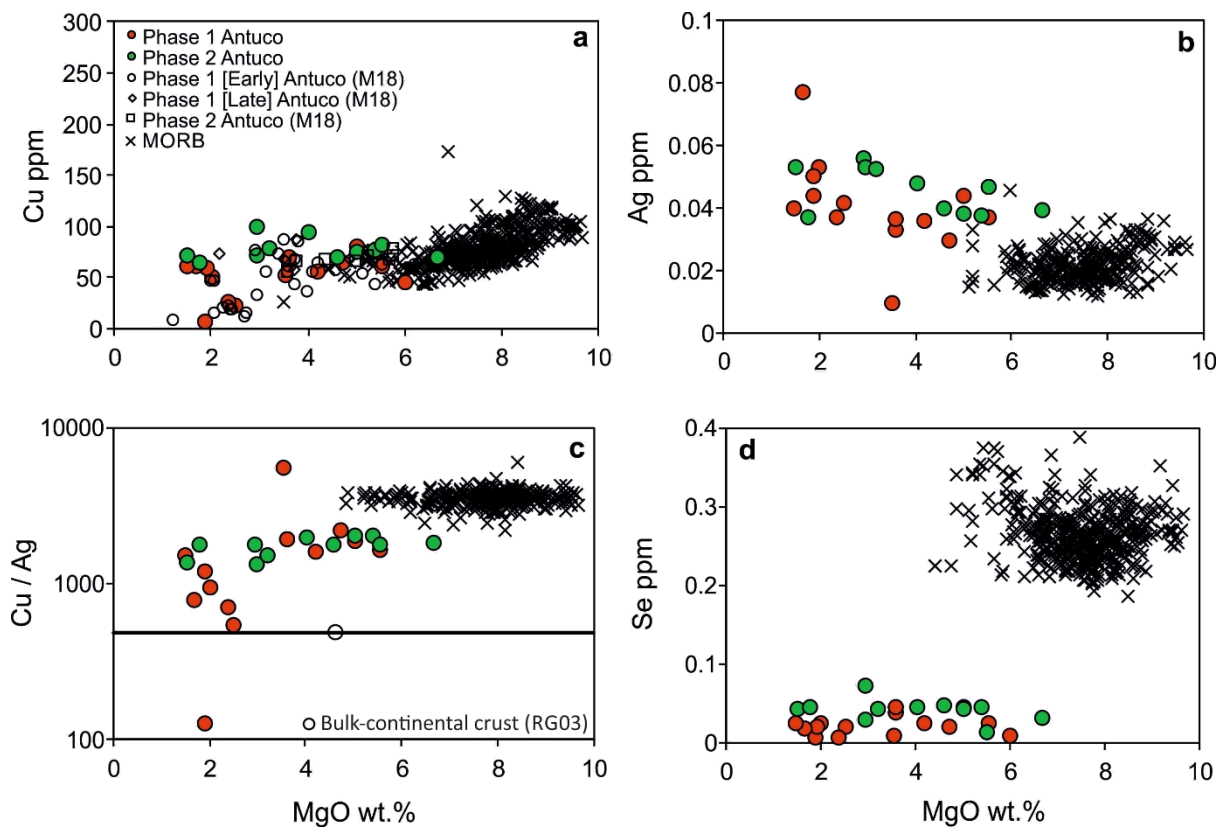


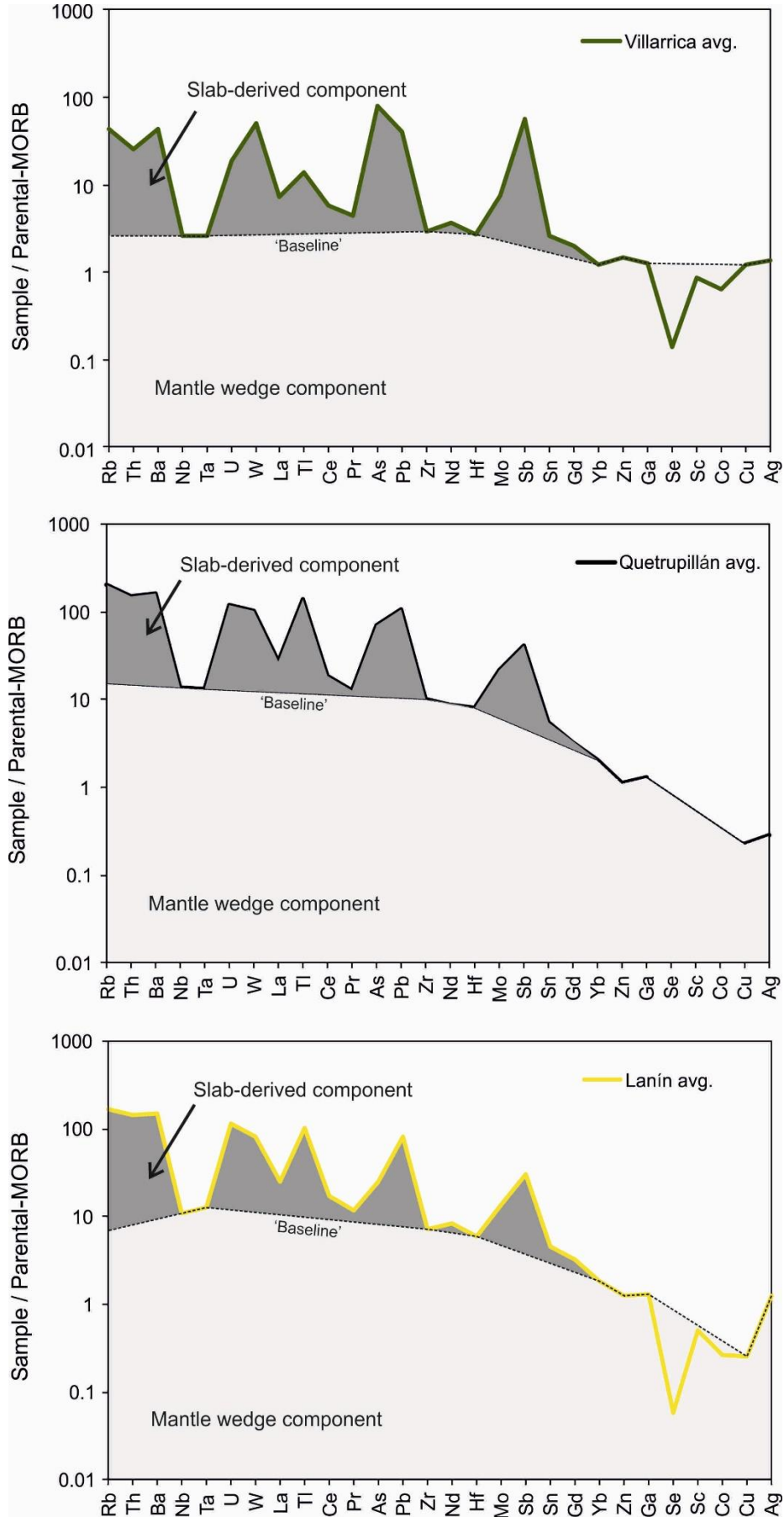
Figure E.1. Select trace element (Cu, Ag, Se) bivariate plots (vs. MgO) of the Antuco samples. (a) The pattern in the Cu data seen in the current study is very similar to that shown by data presented by Martinez et al. (2018) (M18). The Cu contents of the Phase 1 samples show an overall broad decrease with decreasing MgO, whereas those of Phase 2 remain approximately constant. (b) Ag contents show a negative correlation with MgO. (c) With the exception of one sample, the Cu/Ag of all the Antuco samples are lower than the Global (Pacific and Atlantic) mid-ocean ridge basalt (MORB) array (data from Jenner and O'Neill, 2012). Phase 1 samples show a continual decrease in their Cu/Ag with decreasing MgO, whereas the Cu/Ag of Phase 2 samples only show a slight decrease with decreasing MgO. Bulk continental crust data from Rudnick and Gao (2003) (RG03). (d) The Se contents of all the Antuco samples are considerably lower than the Global MORB array.

Appendix F

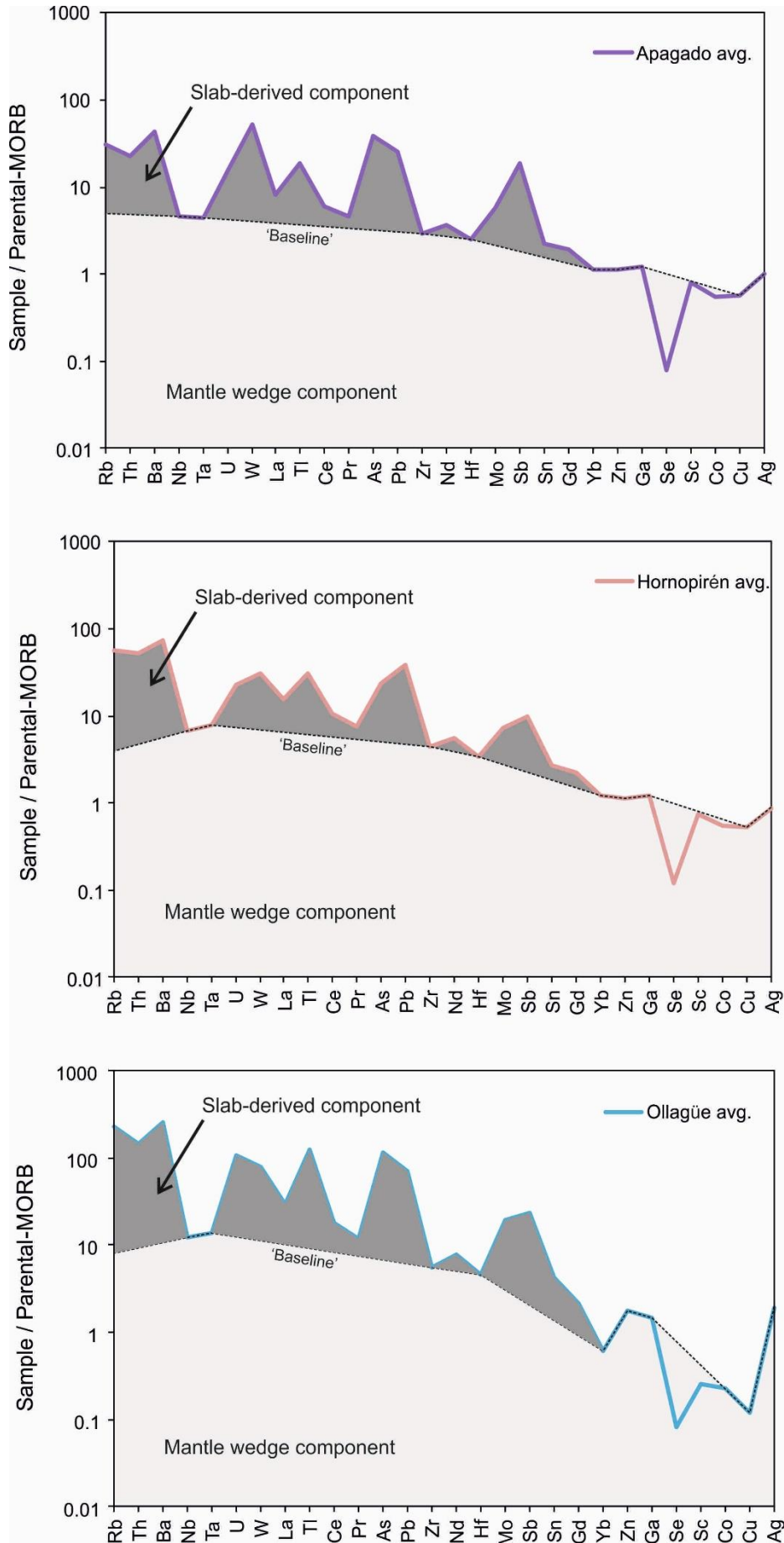
Constructed baselines for Villarrica, Quetrupillán, Lanín, Apagado, Hornopirén, Ollagüe, San Pedro, the Caburgua – Huelemolle Complex, Huililco and La Poruñita

Figure F.1. Constructed baselines (e.g., Pearce and Stern, 2006) for Villarrica, Quetrupillán, Lanín, Apagado, Hornopirén, Ollagüe, San Pedro, Huililco, the Caburgua - Huelemolle Complex and La Poruñita. Baselines have been constructed to separate the mantle wedge (below baseline) and slab-derived (above baseline) components of each edifice, allowing an estimation of the percentage contribution of subduction mobile chalcophile elements from the slab-derived component. Baselines were constructed by connecting the 'conservative' elements Nb, Ta, Zr, Hf, Yb, Zn and Ga (Pearce and Peate, 1995). The baselines were extended to include Cu and Ag, both of which have been demonstrated to be immobile. The estimated percentage contribution of each element from the slab-derived component is outlined in **Table 8.1 (Chapter 8)**.

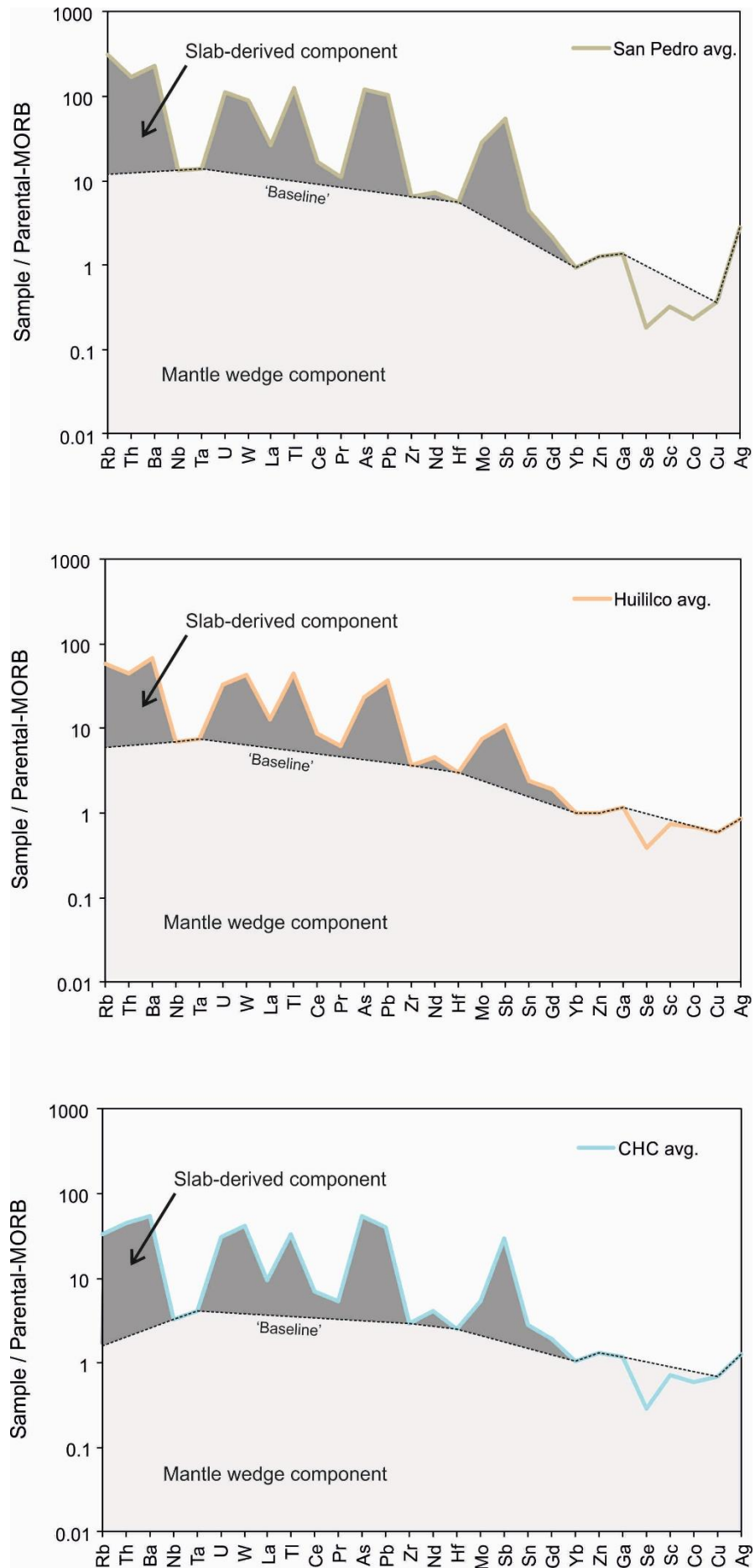
Appendix F. Constructed baselines for Chilean stratovolcanoes



Appendix F. Constructed baselines for Chilean stratovolcanoes



Appendix F. Constructed baselines for Chilean stratovolcanoes



Appendix F. Constructed baselines for Chilean stratovolcanoes

